RETURN TO DESK

JOURNAL OF THE AERONAUTICAL SCIENCES

VOLUME 12 JULY, 1945 NUMBER 3

CONTENTS

Plastic Bending—Further Considerations . . . . . WM. R. OSGOOD 253

A Consideration of Calculated Versus Flight Test Take-Off Performance . . . . . M. H. KIEHLE AND A. VANTINE 263

The Relation of Stress to Strain in Magnesium Base Alloys . . . . . E. J. EASTMAN, J. C. MCDONALD, AND A. A. MOORE 273

Design and Application of High-Pressure Coefficient Axial-Flow Fans . . . . . J. G. SAWYER 281

The Buckling of Sandwich-Type Panels . . . . . N. J. HOFF AND S. E. MAUTNER 285

The Stress-Area Method of Designing Beams . . . . . GILBERT C. BEST 298

Correction of Aluminum-Alloy Compressive Test Results for Material Properties Using Reduced Moduli . . . . . JACOB KAROL 305

Effect of Pressure Variations on Speed Runs . . . . . RICHARD M. HEAD 311

Operational Methods in Servomechanism Design . . . WILLIAM E. RESTEMEYER 313

A Review of the Aerodynamics of Flight Load Factors in Relation to the Safety Regulations . . . . . HUGH B. FREEMAN 320

The Attenuation Method for Compressible Flow Systems . . . . . LEONARD MICHAEL GREENE 329

Strength of Magnesium-Alloy Columns . . . . . F. A. RAPPLEYEA 339

Performance Methods for High-Speed Aircraft . . . . . WALLACE D. HAYES 345

A Vibration Theory Combining the Dynamic Stiffness and Mobility Methods . . . . . HUGH B. STEWART 349

Curved Aluminum-Alloy Sheets in Compression for Monocoque Constructions . . . . . GEORGES WELTER 357

Elementary Considerations of Longitudinal Stability . . MARION THOMAS HOCKMAN 370

Buckling of Plates with Intermediate Rigid Supports . . . . . ERIC REISSNER 375

Letter to the Editor 355

Copyright, 1945, by the

INSTITUTE OF THE AERONAUTICAL SCIENCES, INC.

JOURNAL OF THE AERONAUTICAL SCIENCES

VOL. 12 JULY, 1945 NO. 3

PUBLISHED QUARTERLY BY THE INSTITUTE OF THE AERONAUTICAL SCIENCES, INC.

Chairman of the Editorial Board: HUGH L. DRYDEN, *Chief of Mechanics and Sound Division, National Bureau of Standards*

Editor: ROBERT R. DEXTER *Manager:* JOSEPH J. MAITAN

The Institute of the Aeronautical Sciences publishes the JOURNAL OF THE AERONAUTICAL SCIENCES quarterly, in January, April, July, and October, and the AERONAUTICAL ENGINEERING REVIEW monthly.

The JOURNAL OF THE AERONAUTICAL SCIENCES prints papers of scientific and technical interest to Institute members and subscribers. In general, it provides an opportunity for specialists to publish articles disclosing new knowledge and new applications in the field of the aeronautical sciences. The JOURNAL restricts itself to the aeronautical aspects of advances in science and engineering, and papers printed have either been submitted directly to the JOURNAL or have been previously presented at a meeting of the Institute.

The AERONAUTICAL ENGINEERING REVIEW keeps members and subscribers informed regarding the contents of new books and current periodicals in the field of aeronautics. It reviews new developments in the aircraft industry and reports on progress from house organs and catalogues published by aircraft and engine manufacturers and other companies engaged in aeronautical activities. It publishes papers on applied engineering and aircraft production. News of Institute activities is published in the REVIEW.

Statements and opinions expressed in the JOURNAL are to be understood as individual expressions of the authors and not those of the Institute.

SUBSCRIPTION RATES

Journal of the Aeronautical Sciences
Published Quarterly

United States and Possessions		Foreign Countries Including Canada (American Currency Rates)	
1 Year	$7.00	1 Year	$9.00
Single Copies	2.00	Single Copies	2.50

Aeronautical Engineering Review
Published Monthly

United States and Possessions		Foreign Countries Including Canada (American Currency Rates)	
1 Year	$3.00	1 Year	$3.50
Single Copies	0.30	Single Copies	0.35

Notices of change of address should be sent to the Institute at least 30 days prior to actual change of address.

Manuscripts for publication, proofs, and all correspondence should be addressed to the Editorial Office of the JOURNAL.

Correspondence regarding subscriptions may be addressed to Publication Office, 20th and Northampton Sts., Easton, Pa., or to the Editorial Office of the JOURNAL OF THE AERONAUTICAL SCIENCES, 1505 RCA Building West, 30 Rockefeller Plaza, New York 20, New York.

Entered as Second-Class Matter at the Post Office, Easton, Pa., May 1, 1937. Acceptance for mailing at a special rate of Postage provided for in the Act of August 24, 1912. Authorized April 29, 1937.

JOURNAL OF THE AERONAUTICAL SCIENCES

VOLUME 12 JULY, 1945 NUMBER 3

Plastic Bending—Further Considerations

WM. R. OSGOOD*

National Bureau of Standards

ABSTRACT

The problem of plastic bending under the assumption of realistic stress-strain relations has been considered in a previous paper.[1] Since that paper was written, new ideas have occurred to the author. These ideas lead to a general relation between moment and curvature for sections the widths of which are expressible as polynomials of any order. Specific solutions are given for five symmetric cross sections, including two sections bounded laterally by arcs of parabolas, and for six unsymmetric cross sections, including the triangular section and two sections bounded laterally by arcs of parabolas.

It is planned in a subsequent paper to present an approximate solution of the problem of plastic bending.

SINCE WRITING a previous paper on plastic bending,[1] a more elegant and somewhat more practical presentation of the subject is now possible. This report may be considered a continuation of the earlier paper, but it can be read by referring to that paper without reading the latter through.

It was found that the stress-strain curve,

$$e = \sigma + K\sigma^n \tag{1}$$

where e is the strain; $\sigma = s/E$ is the ratio of the stress, s, to the modulus of elasticity E; and K and n are empiric constants, can still be used in the integrations when K and n become infinite. It is not necessary in this case to replace Eq. (1) by

$$e = s/E, \quad e \leqq S/E; \quad s = S, \quad e \geqq S/E \tag{2}$$

where S is a constant stress, as was done previously. All cases are covered by Eqs. (11) and (12) of the first paper[1] (rewritten below in a different, more general, form).

To recapitulate briefly, the equations of equilibrium of stress on which the solution of any problem in plastic bending depends are

$$\int_0^{c_1} bs\,dy = \int_{-c_2}^{0} bs\,dy \tag{3}$$

$$M = \int_0^{c_1} bsy\,dy + \int_0^{-c_2} bsy\,dy \tag{4}$$

where, as in Fig. 1, b is the width of the cross section at any distance y from the neutral axis, s is the absolute value of the stress on the cross section at the distance y, and M is the absolute value of the bending moment at the cross section. On substituting

$$y = \pm e/k \tag{5}$$

where e is the absolute value of the strain at the distance y, k is the absolute value of the curvature, and the positive sign applies when y is positive and the negative sign applies when y is negative. On introducing the nondimensional variables

$$\sigma = s/E, \quad \beta = bh/A, \quad \kappa = e_1 + e_2 \tag{38}$$

where h is the depth of the cross section, A is the area of the cross section, and e_1 and e_2 are the absolute

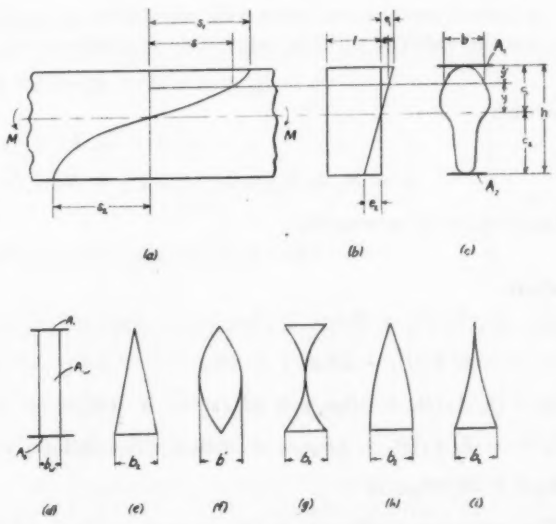

FIG. 1.

Received November 3, 1944. To have been presented at the I.A.S. Thirteenth Annual Meeting, which was canceled to cooperate with a Government appeal (January, 1945) to refrain from holding conventions and meetings.

* Materials Engineer.

values of the extreme fiber strains, Eqs. (3) and (4) become

$$(AE_1/\kappa)\int_0^{e_1}\beta\sigma\,de = (AE_2/\kappa)\int_0^{e_2}\beta\sigma\,de \quad (11)$$

$$M\kappa/h = (AE_1/\kappa)\int_0^{e_1}\beta\sigma e\,de + (AE_2/\kappa)\int_0^{e_2}\beta\sigma e\,de \quad (12)$$

The subscripts 1 and 2 refer here and throughout the paper to the material or the portions of the cross section on the two sides of the neutral axis.

The numbers of the equations below (92) in the present paper are the numbers of the same equations in the earlier paper,[1] sometimes rewritten in a different form.

It is convenient to introduce the following quantities:

$$\psi_1 = [E_1/(E\kappa)]\int_0^{e_1}\beta\sigma\,de \quad (93)$$

$$\psi_2 = [E_2/(E\kappa)]\int_0^{e_2}\beta\sigma\,de \quad (94)$$

$$\mu_1 = [E_1I_1/(EI)]\kappa \quad (95)$$

$$\mu_2 = [E_2I_2/(EI)]\kappa \quad (96)$$

$$\mu = Mh/(EI)$$

I is the moment of inertia of the cross-sectional area with respect to a centroidal axis normal to the plane of bending,

$$I_1 = (Ah^2/\kappa^3)\int_0^{e_1}\beta\sigma e\,de \quad (97)$$

$$I_2 = (Ah^2/\kappa^3)\int_0^{e_2}\beta\sigma e\,de \quad (98)$$

$$E = (E_1I_1 + E_2I_2)/(I_1 + I_2) \quad (99)$$

Reference to Eqs. (11) and (12) shows that the solution of any problem in plastic bending depends fundamentally on the two equations

$$\psi_1 = \psi_2 \quad (100)$$

$$\mu = \mu_1 + \mu_2 = [(I_1 + I_2)/I]\kappa \quad (101)$$

By introducing a reduced modulus of elasticity

$$\bar{E} = (E_1I_1 + E_2I_2)/I \quad (102)$$

Eq. (101) can be written

$$\mu = (\bar{E}/E) \quad (103)$$

Eqs. (100) and (102) will be recognized as analogous to the equations defining the double modulus in the double-modulus theory of column action.[2] For $K_1 = K_2 = 0$ and E_1 and E_2 equal to the modulus of elasticity and the tangent modulus of elasticity, Eqs. (100) and (102) reduce to the double-modulus equations.

Except in the case of a beam in which the portion subjected to tension and that subjected to compression are of unlike materials, it will be permissible to set

$$E_1 = E_2 = E$$

Considerable simplification generally results, and this assumption will be made henceforth. Then, from Eqs. (93) to (99)

$$\psi_1 = (1/\kappa)\int_0^{e_1}\beta\sigma\,de \quad (104)$$

$$\psi_2 = (1/\kappa)\int_0^{e_2}\beta\sigma\,de \quad (105)$$

$$\mu_1 = [Ah^2/(I\kappa^2)]\int_0^{e_1}\beta\sigma e\,de \quad (106)$$

$$\mu_2 = [Ah^2/(I\kappa^2)]\int_0^{e_2}\beta\sigma e\,de \quad (107)$$

If the stress-strain relations are given by Eq. (1), as will be assumed henceforth, Eqs. (104) to (107) become

$$\psi_1 = (1/\kappa)\int_0^{\sigma_1}\beta\sigma\,(1 + n_1K_1\sigma^{n_1-1})\,d\sigma \quad (104a)$$

$$\psi_2 = (1/\kappa)\int_0^{\sigma_2}\beta\sigma\,(1 + n_2K_2\sigma^{n_2-1})\,d\sigma \quad (105a)$$

$$\mu_1 = [Ah^2/(I\kappa^2)]\int_0^{\sigma_1}\beta\sigma^2\,(1 + K_1\sigma^{n_1-1})\times(1 + n_1K_1\sigma^{n_1-1})\,d\sigma \quad (106a)$$

$$\mu_2 = [Ah^2/(I\kappa^2)]\int_0^{\sigma_2}\beta\sigma^2\,(1 + K_2\sigma^{n_2-1})\times(1 + n_2K_2\sigma^{n_2-1})\,d\sigma \quad (107a)$$

Width of Section Expressible as Polynomial

A form of section that offers wide possibilities in studying the effect of shape on the moment-curvature relation is one the width of which is expressible as a polynomial, Fig. 1,

$$b = B_0 + B_1y'/h + B_2(y'/h)^2 + B_3(y'/h)^3 + \ldots + B_m(y'/h)^m \quad (108)$$

or with

$$y'/h = (c_1/h) - (y/h) = (e_1/\kappa) - (e/\kappa)$$

$$b = B_0 + B_1[(e_1/\kappa) - (e/\kappa)] + B_2[(e_1/\kappa) - (e/\kappa)]^2 + \ldots + B_m[(e_1/\kappa) - (e/\kappa)]^m \quad (109)$$

Eq. (109) may be rewritten

$$\beta = \beta_0 + \beta_1\,(e/\kappa) + \beta_2\,(e/\kappa)^2 + \beta_3\,(e/\kappa)^3 + \ldots + \beta_m\,(e/\kappa)^m \quad (110)$$

where

$$\left.\begin{aligned}
\beta_0 &= (h/A)\,[B_0 + B_1e_1/\kappa + B_2(e_1/\kappa)^2 + B_3(e_1/\kappa)^3 + \ldots + B_m(e_1/\kappa)^m]\\
\beta_1 &= -(h/A)[B_1 + 2B_2e_1/\kappa + 3B_3(e_1/\kappa)^2 + 4B_4(e_1/\kappa)^3 + \ldots mB_m(e_1/\kappa)^{m-1}]\\
\beta_2 &= (h/A)\{B_2 + 3B_3e_1/\kappa + 6B_4(e_1/\kappa)^2 + 10B_5(e_1/\kappa)^3 + \ldots + [m(m-1)/2!]\,B_m(e_1/\kappa)^{m-2}\}\\
\beta_3 &= -(h/A)\{B_3 + 4B_4e_1/\kappa + 10B_5(e_1/\kappa)^2 + 20B_6(e_1/\kappa)^3 + \ldots + [m(m-1)(m-2)/3!]\,B_m(e_1/\kappa)^{m-3}\}\\
\beta_m &= (-1)^mB_mh/A
\end{aligned}\right\} \quad (111)$$

The numerical coefficients in the expressions for the β's are the binomial coefficients.

It does not complicate the analytic treatment to add thin flanges of area A_1 and A_2 at the top and the bottom of the section, Fig. 1c. For the purposes of analysis these flanges are to be considered infinitesimally thin and infinitely wide but of finite cross-sectional areas. When the expression for β from Eq. (110) is substituted in Eq. (104a) and account is taken of the flange, one finds

$$\psi_1 = \rho_1\sigma_1 + (1/\kappa)\int_0^{\sigma_1}[\beta_0 + \beta_1(e/\kappa) + \beta_2(e/\kappa)^2 + \ldots + \beta_m(e/\kappa)^m(\sigma + n_1K_1\sigma^{n_1})d\sigma \tag{112}$$

where

$$\rho_1 = A_1/A \tag{113}$$

On substituting for e from Eq. (1) and integrating, one obtains

$$\psi_1/\kappa = \rho_1\iota_{11} + \beta_0\iota_{12} + \beta_1\iota_{13} + \beta_2\iota_{14} + \beta_3\iota_{15} + \ldots + \beta_m\iota_{1(m+2)} \tag{114}$$

where the β's are given by Eqs. (111) and where, with the use of Eq. (1),

$$\left.\begin{aligned}
\iota_{11} &= \sigma_1/\kappa \\
\iota_{12} &= (\sigma_1/\kappa)\{(1/2)(\sigma_1/\kappa) + [n_1/(1+n_1)][(e_1/\kappa) - (\sigma_1/\kappa)]\} \\
\iota_{13} &= \frac{\sigma_1}{\kappa}\left[\frac{1}{3}\left(\frac{\sigma_1}{\kappa}\right)^2 + \left(\frac{1+n_1}{2+n_1}\right)\left(\frac{\sigma_1}{\kappa}\right)\left(\frac{e_1}{\kappa} - \frac{\sigma_1}{\kappa}\right) + \left(\frac{n_1}{1+2n_1}\right)\left(\frac{e_1}{\kappa} - \frac{\sigma_1}{\kappa}\right)^2\right] \\
\iota_{14} &= \frac{\sigma_1}{\kappa}\left[\frac{1}{4}\left(\frac{\sigma_1}{\kappa}\right)^3 + \left(\frac{2+n_1}{3+n_1}\right)\left(\frac{\sigma_1}{\kappa}\right)^2\left(\frac{e_1}{\kappa} - \frac{\sigma_1}{\kappa}\right) + \left(\frac{1+2n_1}{2+2n_1}\right)\left(\frac{\sigma_1}{\kappa}\right)\left(\frac{e_1}{\kappa} - \frac{\sigma_1}{\kappa}\right)^2 + \left(\frac{n_1}{1+3n_1}\right)\left(\frac{e_1}{\kappa} - \frac{\sigma_1}{\kappa}\right)^3\right] \\
\iota_{15} &= \frac{\sigma_1}{\kappa}\left[\frac{1}{5}\left(\frac{\sigma_1}{\kappa}\right)^4 + \left(\frac{3+n_1}{4+n_1}\right)\left(\frac{\sigma_1}{\kappa}\right)^3\left(\frac{e_1}{\kappa} - \frac{\sigma_1}{\kappa}\right) + \left(\frac{3+3n_1}{3+2n_1}\right)\left(\frac{\sigma_1}{\kappa}\right)^2\left(\frac{e_1}{\kappa} - \frac{\sigma_1}{\kappa}\right)^2 + \right. \\
&\qquad \left. \left(\frac{1+3n_1}{2+3n_1}\right)\left(\frac{\sigma_1}{\kappa}\right)\left(\frac{e_1}{\kappa} - \frac{\sigma_1}{\kappa}\right)^3 + \left(\frac{n_1}{1+4n_1}\right)\left(\frac{e_1}{\kappa} - \frac{\sigma_1}{\kappa}\right)^4\right] \\
\iota_{16} &= \frac{\sigma_1}{\kappa}\left[\frac{1}{6}\left(\frac{\sigma_1}{\kappa}\right)^5 + \left(\frac{4+n_1}{5+n_1}\right)\left(\frac{\sigma_1}{\kappa}\right)^4\left(\frac{e_1}{\kappa} - \frac{\sigma_1}{\kappa}\right) + \left(\frac{6+4n_1}{4+2n_1}\right)\left(\frac{\sigma_1}{\kappa}\right)^3\left(\frac{e_1}{\kappa} - \frac{\sigma_1}{\kappa}\right)^2 + \right. \\
&\qquad \left. \left(\frac{4+6n_1}{3+3n_1}\right)\left(\frac{\sigma_1}{\kappa}\right)^2\left(\frac{e_1}{\kappa} - \frac{\sigma_1}{\kappa}\right)^3 + \left(\frac{1+4n_1}{2+4n_1}\right)\left(\frac{\sigma_1}{\kappa}\right)\left(\frac{e_1}{\kappa} - \frac{\sigma_1}{\kappa}\right)^4 + \left(\frac{n_1}{1+5n_1}\right)\left(\frac{e_1}{\kappa} - \frac{\sigma_1}{\kappa}\right)^5\right] \\
\iota_{1(m+2)} &= \ldots\ldots\ldots\ldots\ldots\ldots
\end{aligned}\right\} \tag{115}$$

In the expression for any ι the components of the numerators of the coefficients of the terms are related to the binomial coefficients in an obvious manner, and the components of the denominators form arithmetic series. The ι's are independent of the shape of the cross section.

Similarly, by substituting β from Eq. (110) in Eq. (106a), taking account of the flange, and integrating, one finds

$$\mu_1/\kappa = (Ah^2/I)[\rho_1(e_1/\kappa)\iota_{11} + \beta_0\iota_{13} + \beta_1\iota_{14} + \beta_2\iota_{15} + \ldots + \beta_m\iota_{1(m+3)}] \tag{116}$$

the β's and ι's being given by Eqs. (111) and (115), respectively.

The expressions for ψ_2 and μ_2 are the same as those for ψ_1 and μ_1, respectively, when the subscripts 1 and 2 to e, n, ρ, and σ are interchanged, and $B_0, \ldots B_m$ are replaced by $B_0', \ldots B_m'$ where

$$\left.\begin{aligned}
B_0' &= B_0 + B_1 + B_2 + B_3 + \ldots + B_m \\
B_1' &= -(B_1 + 2B_2 + 3B_3 + \ldots + mB_m) \\
B_2' &= B_2 + 3B_3 + 6B_4 + 10B_5 + \ldots + [m(m-1)/2!]B_m \\
B_3' &= -\{B_3 + 4B_4 + 10B_5 + 20B_6 + \ldots + [m(m-1)(m-2)/3!]B_m\} \\
&\ldots\ldots\ldots\ldots \\
B_m' &= (-1)^m B_m
\end{aligned}\right\} \tag{117}$$

The coefficients in Eqs. (117) are the binomial coefficients. With the changes indicated, ψ_2/κ and μ_2/κ may be written

$$\psi_2/\kappa = \rho_2\iota_{21} + \beta_0'\iota_{22} + \beta_1'\iota_{23} + \beta_2'\iota_{24} + \beta_3'\iota_{25} + \ldots + \beta_m'\iota_{2(m+2)} \tag{118}$$

$$\mu_2/\kappa = (Ah^2/I)[\rho_2(e_2/\kappa)\iota_{21} + \beta_0'\iota_{23} + \beta_1'\iota_{24} + \beta_2'\iota_{25} + \ldots + \beta_m'\iota_{2(m+3)}] \tag{119}$$

The coefficients $\beta_0', \beta_1', \beta_2', \ldots \beta_m'$ are the $\beta_0, \beta_1, \beta_2, \ldots \beta_m$, respectively, of Eqs. (111) when e_1 in those equations is replaced by e_2, and $B_0, B_1, B_2, \ldots B_m$ are replaced by $B_0', B_1', B_2', \ldots B_m'$, respectively, from Eqs. (117).

$\iota_{21}, \iota_{22}, \iota_{23}, \ldots \iota_{2(m+2)}$ are the $\iota_{11}, \iota_{12}, \iota_{13}, \ldots \iota_{1(m+2)}$, respectively, of Eqs. (115) when the subscript 1 in those equations is replaced by the subscript 2.

Parabolic Section

If $B_0 = b_1$, $B_1 = b_2 - b_1 + 4b'$, $B_2 = -4b'$, $B_3 = B_4 = \ldots = B_m = 0$, the sides of the cross section are in general parabolic arcs, the widths of the section at the extreme fibers (just inside the thin flanges) being b_1 and b_2 and the width at a point between the extreme fibers determining b'. In this case Eq. (108) becomes

$$b = b_1 + (b_2 - b_1 + 4b')(y'/h) - 4b'(y'/h)^2 \tag{120}$$

and Eq. (114) becomes

$$\frac{\psi_1}{\kappa} = \rho_1\iota_{11} + \frac{h}{A}\left\{\left[b_1 + (b_2 - b_1 + 4b')\frac{e_1}{\kappa} - 4b'\left(\frac{e_1}{\kappa}\right)^2\right]\iota_{12} - \left(b_2 - b_1 + 4b' - 8b'\frac{e_1}{\kappa}\right)\iota_{13} - 4b'\iota_{14}\right\} \tag{121}$$

and with $B_0' = b_2$, $B_1' = b_1 - b_2 + 4b'$, $B_2' = -4b'$, $B_3' = B_4' = \ldots = B_m' = 0$ according to Eqs. (117), Eq. (118) may be written

$$\frac{\psi_2}{\kappa} = \rho_2\iota_{21} + \frac{h}{A}\left\{\left[b_2 + (b_1 - b_2 + 4b')\frac{e_2}{\kappa} - 4b'\left(\frac{e_2}{\kappa}\right)^2\right]\iota_{22} - \left(b_1 - b_2 + 4b' - 8b'\frac{e_2}{\kappa}\right)\iota_{23} - 4b'\iota_{24}\right\} \tag{122}$$

By substituting in Eq. (116), one finds

$$\frac{\mu_1}{\kappa} = \left(\frac{Ah^2}{I}\right)\rho_1\left(\frac{e_1}{\kappa}\right)\iota_{11} + \frac{h^2}{I}\left\{\left[b_1 + (b_2 - b_1 + 4b')\frac{e_1}{\kappa} - 4b'\left(\frac{e_1}{\kappa}\right)^2\right]\iota_{13} - \left(b_2 - b_1 + 4b' - 8b'\frac{e_1}{\kappa}\right)\iota_{14} - 4b'\iota_{15}\right\} \tag{123}$$

and from Eq. (119)

$$\frac{\mu_2}{\kappa} = \left(\frac{Ah^2}{I}\right)\rho_2\left(\frac{e_2}{\kappa}\right)\iota_{21} + \frac{h_3}{I}\left\{\left[b_2 + (b_1 - b_2 + 4b')\frac{e_2}{\kappa} - 4b'\left(\frac{e_2}{\kappa}\right)^2\right]\iota_{23} - \left(b_1 - b_2 + 4b' - 8b'\frac{e_2}{\kappa}\right)\iota_{24} - 4b'\iota_{25}\right\} \tag{124}$$

A few specific sections will now be considered.

I-Section with Thin Flanges

If $b_1 = b_2 = b_w$ and $b' = 0$, the section becomes an I-section with thin flanges and thickness of web equal to b_w, Fig. 1d. A_w in Fig. 1d is the area of the web. In this case Eqs. (121) and (123) reduce to

$$\psi_1/\kappa = \rho_1\iota_{11} + (1 - \rho_1 - \rho_2)\iota_{12} \tag{125}$$

$$\mu_1/\kappa = (Ah^2/I)[\rho_1(e_1/\kappa)\iota_{11} + (1 - \rho_1 - \rho_2)\iota_{13}] \tag{126}$$

and ψ_2/κ and μ_2/κ may be obtained from Eqs. (125) and (126) by replacing ρ_1, ρ_2, e_1, ι_{11}, ι_{12}, and ι_{13} by ρ_2, ρ_1, e_2, ι_{21}, ι_{22}, and ι_{23}, respectively.

Triangular Section

If $b_1 = b' = \rho_1 = \rho_2 = 0$, the section becomes a triangle with base b_2, Fig. 1e. With

$$A = (1/2)b_2h,\ I = (1/36)b_2h^3$$

Eqs. (121)–(124) reduce to

$$\psi_1/\kappa = 2[(e_1/\kappa)\iota_{12} - \iota_{13}] \tag{127}$$

$$\psi_2/\kappa = 2\{[1 - (e_2/\kappa)]\iota_{22} + \iota_{23}\} \tag{128}$$

$$\mu_1/\kappa = 36[(e_1/\kappa)\iota_{13} - \iota_{14}] \tag{129}$$

$$\mu_2/\kappa = 36\{[1 - (e_2/\kappa)]\iota_{23} + \iota_{24}\} \tag{130}$$

where ψ_1 and μ_1 apply to the part of the cross section between the neutral axis and the vertex, and where ψ_2 and μ_2 apply to the part between the neutral axis and the base.

Parabolic Section, Vertices Out

If $b_1 = b_2 = \rho_1 = \rho_2 = 0$, the section is symmetric and bounded by two parabolic arcs as shown in Fig. 1f. The greatest width is b'. With

$$A = (2/3)b'h,\quad I = (1/30)b'h^3$$

Eqs. (121) and (123) reduce to

$$\frac{\psi_1}{\kappa} = 6\left\{\frac{e_1}{\kappa}\left(1 - \frac{e_1}{\kappa}\right)\iota_{12} - \left[1 - 2\left(\frac{e_1}{\kappa}\right)\right]\iota_{13} - \iota_{14}\right\} \tag{131}$$

$$\frac{\mu_1}{\kappa} = 120\left\{\frac{e_1}{\kappa}\left(1 - \frac{e_1}{\kappa}\right)\iota_{13} - \left[1 - 2\left(\frac{e_1}{\kappa}\right)\right]\iota_{14} - \iota_{15}\right\} \tag{132}$$

and ψ_2/κ and μ_2/κ may be obtained from Eqs. (131) and (132) by replacing e_1, ι_{12}, ι_{13}, ι_{14}, and ι_{15} by e_2, ι_{22}, ι_{23}, ι_{24}, and ι_{25}, respectively.

Parabolic Section, Vertices In

If $b_1 = b_2 = -b'$ and $\rho_1 = \rho_2 = 0$, the section is symmetric and bounded by two parabolic arcs as shown in Fig. 1g. The greatest width, at the top and bottom, is b_2, and the width at the middle is zero (the parabolas are tangent to each other at their vertices). With

$$A = (1/3)b_2h, \quad I = (1/20)b_2h^3$$

Eqs. (121) and (123) reduce to

$$\frac{\psi_1}{\kappa} = 3\left\{\left[1 - 2\left(\frac{e_1}{\kappa}\right)\right]^2 \iota_{12} + 4\left[1 - 2\left(\frac{e_1}{\kappa}\right)\right]\iota_{13} + 4\iota_{14}\right\} \quad (133)$$

$$\frac{\mu_1}{\kappa} = 20\left\{\left[1 - 2\left(\frac{e_1}{\kappa}\right)\right]^2 \iota_{13} + 4\left[1 - 2\left(\frac{e_1}{\kappa}\right)\right]\iota_{14} + 4\iota_{15}\right\} \quad (134)$$

and ψ_2/κ and μ_2/κ may be obtained from Eqs. (133) and (134) by replacing e_1, ι_{12}, ι_{13}, ι_{14}, and ι_{15} by e_2, ι_{22}, ι_{23}, ι_{24}, and ι_{25}, respectively.

Semiparabolic Section, Vertices Out

If $b_1 = \rho_1 = \rho_2 = 0$ and $b_2 = 4b'$, the section is bounded by two parabolic arcs as shown in Fig. 1h. The vertices are at the bottom of the section, and the greatest width, at the bottom, is b_2. With

$$A = (2/3)b_2h, \quad I = (19/480)b_2h^3$$

Eqs. (121)–(124) reduce to

$$\frac{\psi_1}{\kappa} = \frac{3}{2}\left[\frac{e_1}{\kappa}\left(2 - \frac{e_1}{\kappa}\right)\iota_{12} - 2\left(1 - \frac{e_1}{\kappa}\right)\iota_{13} - \iota_{14}\right] \quad (135)$$

$$\frac{\psi_2}{\kappa} = \frac{3}{2}\left\{\left[1 - \left(\frac{e_2}{\kappa}\right)^2\right]\iota_{22} + 2\left(\frac{e_2}{\kappa}\right)\iota_{23} - \iota_{24}\right\} \quad (136)$$

$$\frac{\mu_1}{\kappa} = \frac{480}{19}\left[\frac{e_1}{\kappa}\left(2 - \frac{e_1}{\kappa}\right)\iota_{13} - 2\left(1 - \frac{e_1}{\kappa}\right)\iota_{14} - \iota_{15}\right] \quad (137)$$

$$\frac{\mu_2}{\kappa} = \frac{480}{19}\left\{\left[1 - \left(\frac{e_2}{\kappa}\right)^2\right]\iota_{23} + 2\left(\frac{e_2}{\kappa}\right)\iota_{24} - \iota_{25}\right\} \quad (138)$$

where ψ_1 and μ_1 apply to the part of the cross section in the figure that lies above the neutral axis, and where ψ_2 and μ_2 apply to the part below the neutral axis.

Semiparabolic Section, Vertices In

If $b_1 = \rho_1 = \rho_2 = 0$ and $b_2 = -4b'$, the section is bounded by two parabolic arcs as shown in Fig. 1i. The vertices are tangent at the highest point of the section, and the greatest width is b_2, at the bottom. With

$$A = (1/3)b_2h, \quad I = (1/80)b_2h^3$$

Eqs. (121)–(124) reduce to

$$\frac{\psi_1}{\kappa} = 3\left[\left(\frac{e_1}{\kappa}\right)^2 \iota_{12} - 2\left(\frac{e_1}{\kappa}\right)\iota_{13} + \iota_{14}\right] \quad (139)$$

$$\frac{\psi_2}{\kappa} = 3\left[\left(1 - \frac{e_2}{\kappa}\right)^2 \iota_{22} + 2\left(1 - \frac{e_2}{\kappa}\right)\iota_{23} + \iota_{24}\right] \quad (140)$$

$$\frac{\mu_1}{\kappa} = 80\left[\left(\frac{e_1}{\kappa}\right)^2 \iota_{13} - 2\left(\frac{e_1}{\kappa}\right)\iota_{14} + \iota_{15}\right] \quad (141)$$

$$\frac{\mu_2}{\kappa} = 80\left[\left(1 - \frac{e_2}{\kappa}\right)^2 \iota_{23} + 2\left(1 - \frac{e_2}{\kappa}\right)\iota_{24} + \iota_{25}\right] \quad (142)$$

where ψ_1 and μ_1 apply to the part of the cross section in the figure that lies above the neutral axis, and where ψ_2 and μ_2 apply to the part below the neutral axis.

Numerical Solutions

The determination of the relation between the extreme fiber strains and the bending moment involves essentially first the location of the neutral axis by means Eq. (100). Once this has been located—that is, the relation between e_1 and e_2 found—the bending moment is obtained at once from Eq. (101).

Eq. (100) will usually have to be solved by trial—that is, for a given value of e_1 or e_2, e_2 or e_1 will have to be found by trial. This trial solution can be considerably shortened if graphs exist of $\kappa^j\iota_{ej}$ plotted against e_e, where $j = 1, 2, 3, \ldots, m + 2$, and the subscript e stands for either 1 or 2, as the case may be. Such graphs are not particularly tedious to construct. Figs. 2–4 represent graphs of this kind corresponding to four

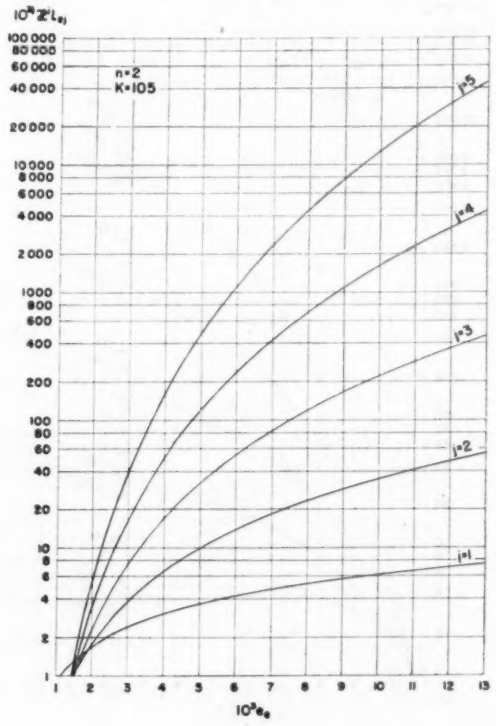

Fig. 2.

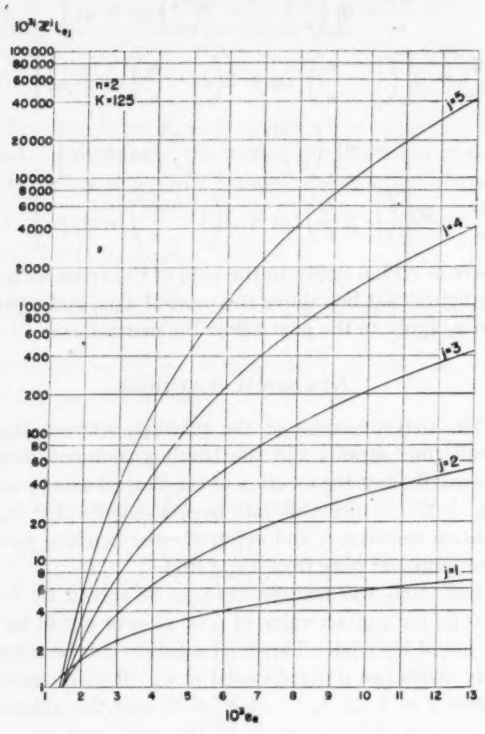

FIG. 3.

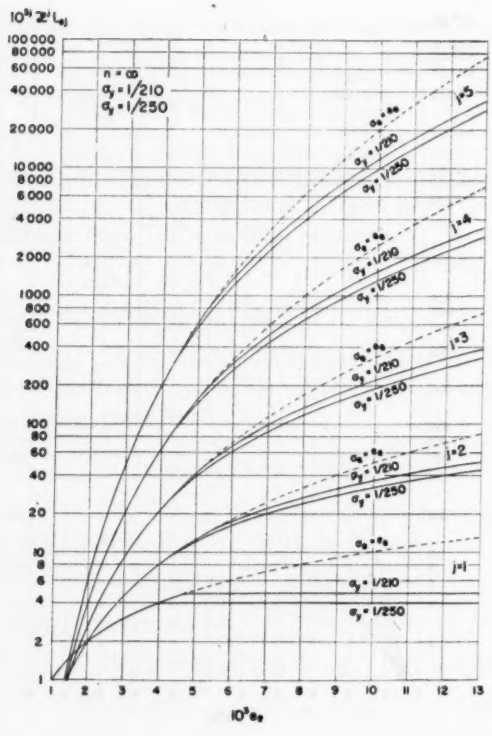

FIG. 4.

stress-strain curves, each graph showing $\kappa^j \iota_{ej}$ for $j = 1, 2, 3, 4, 5$. The graphs are representations of the first five of Eqs. (115) for the four stress-strain curves considered in reference 1, shown in Fig. 5, and defined by

$$n = 2, \quad K = 105 \tag{143}$$

$$n = 2, \quad K = 125 \tag{144}$$

$$n = \infty, \quad \sigma_y = 1/210 \tag{145}$$

$$n = \infty, \quad \sigma_y = 1/250 \tag{146}$$

where σ_y is the value of σ at the yield point (horizontal part of the stress-strain curve) of the material. The dotted curves in Fig. 4 are obtained by letting $\sigma_1 = e_1$ in Eqs. (115); they correspond to elastic behavior.

A group of beams will now be studied, the materials of which have the mechanical properties defined by Eqs. (143)–(146) and the cross sections of which have a variety of shapes. It will be convenient to distinguish three cases as before:[1]

Case I—The stress-strain relations of the material on both sides of the neutral axis are characterized by $1 < n < \infty$. In the numerical solutions that follow $n_1 = 2$, $K_1 = 105$, $n_2 = 2$, and $K_2 = 125$.

Case II—The stress-strain relations of the material on both sides of the neutral axis are characterized by $n = \infty$. In the numerical solutions that follow $\sigma_{y1} = 1/210$ and $\sigma_{y2} = 1/250$.

Case III—The stress-strain relations of the material on one side of the neutral axis are characterized by $1 < n < \infty$ and on the other side by $n = \infty$. In the numerical solutions that follow $n_1 = \infty$, $\sigma_{y1} = 1/210$, $n_2 = 2$, and $K_2 = 125$.

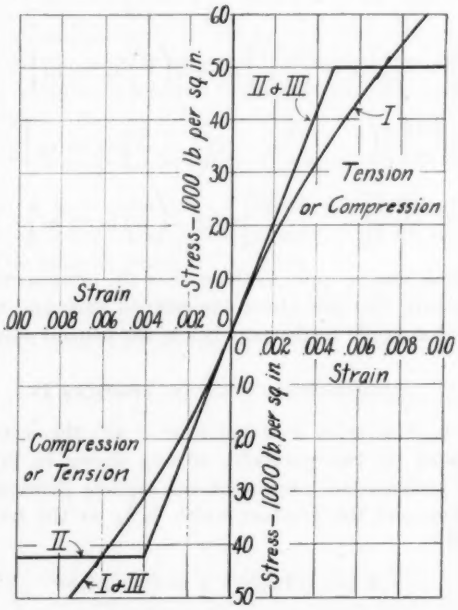

FIG. 5

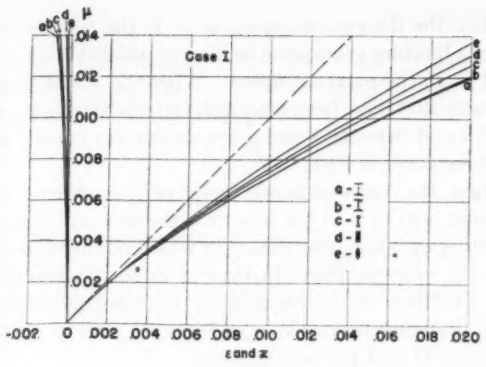

FIG. 6.

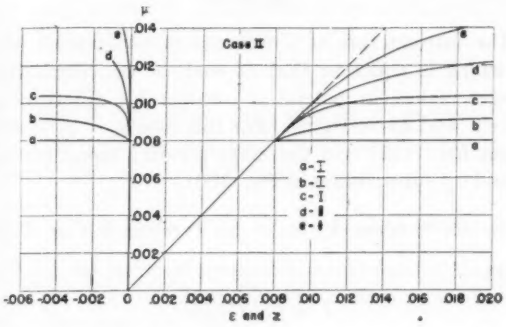

FIG. 7.

The curves marked I, II, and III in Fig. 5 correspond to Cases I, II, and III, respectively.

Most of the significant results can be shown by, or easily obtained from, curves of μ against κ and of μ against the strain-difference,

$$\epsilon = e_1 - e_2 \tag{147}$$

In the following sections the equations determining these curves are set up. The curves themselves are shown in Figs. 6–8 for symmetric cross sections and in Figs. 9–11 for unsymmetric cross sections. The curves at the right in each figure are the κ,μ-curves and those at the left the ϵ,μ-curves. The short crosslines in Figs. 7 and 10 indicate the values of κ and μ at which $e_2 = \sigma_{y2}$, and those in Figs. 8 and 11 indicate the values at which $e_1 = \sigma_{y1}$.

IDEALIZED I-SECTION

The simplest section to handle is the idealized I-section, consisting of two thin flanges and a negligible web $b_w = A_w = 0$. Eqs. (125) and (126) and the corresponding equations for ψ_2/κ and μ_2/κ apply. Substituting in Eq. (100) and multiplying through by $A\kappa$ gives

$$A_1\sigma_1 = A_2\sigma_2$$

or with

$$\alpha = A_1/A_2 \tag{39c}$$

$$\sigma_1/\sigma_2 = 1/\alpha$$

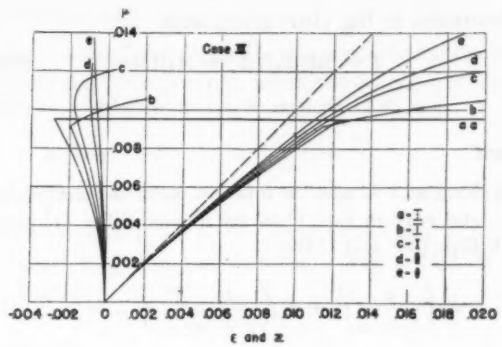

FIG. 8.

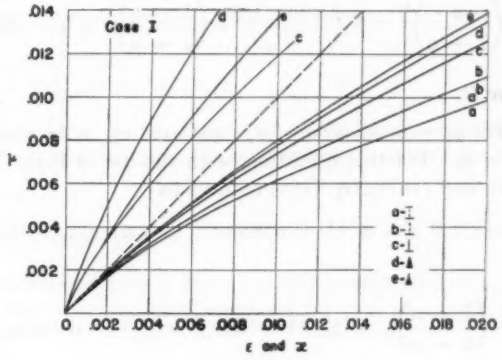

FIG. 9.

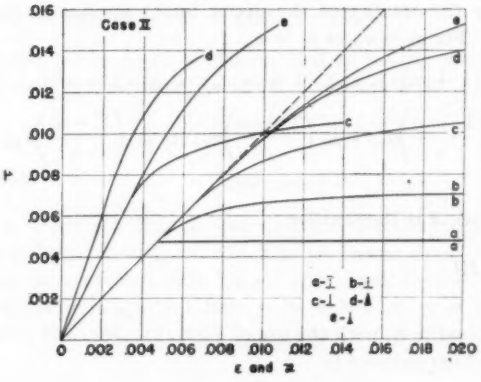

FIG. 10.

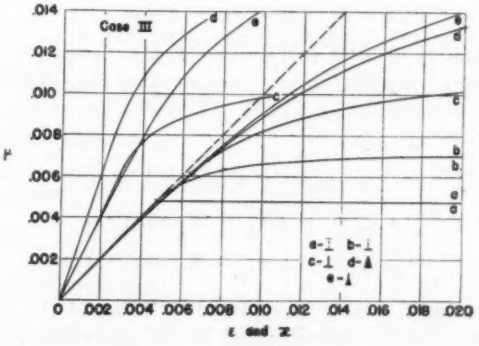

FIG. 11.

Substitution in Eq. (101) gives, with

$$I = [A_1A_2/(A_1 + A_2)]h^2 \qquad (39b)$$

$$\mu = (1 + \alpha)\sigma_1 = [(1 + \alpha)/\alpha]\sigma_2 \qquad (148)$$

Case I

So long as $1 < n_1 < \infty$ and $1 < n_2 < \infty$, elimination of σ_1 and σ_2 from Eqs. (148) by means of Eq. (1) gives, with Eqs. (38) and (147),

$$K_1\left(\frac{\mu}{1 + \alpha}\right)^{n_1} + K_2\left(\frac{\alpha\mu}{1 + \alpha}\right)^{n_2} + \mu = \kappa \qquad (41a)$$

and

$$K_1\left(\frac{\mu}{1 + \alpha}\right)^{n_1} - K_2\left(\frac{\alpha\mu}{1 + \alpha}\right)^{n_2} + \left(\frac{1 - \alpha}{1 + \alpha}\right)\mu = \epsilon \qquad (149)$$

Case II

For $n_1 = n_2 = \infty$, $\sigma_1 < \sigma_{y1}$, and $\sigma_2 < \sigma_{y2}$, $\sigma_1 = e_1$ and $\sigma_2 = e_2$. For this condition, with the use of Eqs. (1), (38), and (147), Eq. (148) reduces to

$$\mu = \kappa, \quad 0 \leqq \kappa \leqq (1 + \alpha)\sigma_{y1} \text{ or } [(1 + \alpha)/\alpha]\sigma_{y2} \qquad (43a)$$

or

$$\mu = \left(\frac{1 + \alpha}{1 - \alpha}\right)\epsilon, \quad |\epsilon| \leqq |(1 - \alpha)\sigma_{y1}| \text{ or } |[(1 - \alpha)/\alpha]\sigma_{y2}| \qquad (150)$$

where the smaller of the upper limits applies in each case. For $\sigma_1 = \sigma_{y1}$ or $\sigma_2 = \sigma_{y2}$

$$\left.\begin{aligned} \mu &= (1 + \alpha)\sigma_{y1},\ \kappa \geqq (1 + \alpha)\sigma_{y1},\ |\epsilon| \geqq |(1 - \alpha)\sigma_{y1}| \\ \mu &= \left(\frac{1 + \alpha}{\alpha}\right)\sigma_{y2},\ \kappa \geqq \left(\frac{1 + \alpha}{\alpha}\right)\sigma_{y2},\ |\epsilon| \geqq \left|\left(\frac{1 - \alpha}{\alpha}\right)\sigma_{y2}\right| \end{aligned}\right\} \qquad (46a)$$

whichever is the smaller.

Case III

For $n_1 = \infty$, $1 < n_2 < \infty$, and $\sigma_1 < \sigma_{y1}$, $\sigma_1 = e_1$. For this condition, with the use of Eqs. (1), (38), and (147), Eq. (148) reduces to

$$\left.\begin{aligned} K_2[\alpha\mu/(1 + \alpha)]^{n_2} + \mu &= \kappa \\ 0 \leqq \kappa &\leqq (1 + \alpha)\sigma_{y1} + K_2(\alpha\sigma_{y1})^{n_2} \end{aligned}\right\} \qquad (48a)$$

$$\left.\begin{aligned} -K_2[\alpha\mu/(1 + \alpha)]^{n_2} + [(1 - \alpha)/(1 + \alpha)]\mu &= \epsilon \\ |\epsilon| \leqq |(1 - \alpha)\sigma_{y1} - K_2(\alpha\sigma_{y1})^{n_2}| \end{aligned}\right\} \qquad (151)$$

For $\sigma_1 = \sigma_{y1}$

$$\left.\begin{aligned} \mu &= (1 + \alpha)\sigma_{y1} \\ \kappa &\geqq (1 + \alpha)\sigma_{y1} + K_2(\alpha\sigma_{y1})^{n_2} \\ |\epsilon| &\geqq |(1 - \alpha)\sigma_{y1} - K_2(\alpha\sigma_{y1})^{n_2}| \end{aligned}\right\} \qquad (50a)$$

Obviously, α may be replaced by $1/\alpha$ and the subscripts 1 and 2 interchanged in the preceding paragraphs.

When the flanges are equal, $\alpha = 1$, the section becomes a limiting symmetric section in which all the material is at the extreme fibers. With the stress-strain diagrams that have been assumed, the relations between κ and μ and between ϵ and μ are shown as curves *a* for the three cases in Figs. 6–8.

When the cross-sectional area of one flange approaches zero, $\alpha = 0$ (or $\alpha = \infty$), the section becomes a limiting unsymmetric section in which all the material is at the extreme fibers in tension or in compression. This condition is represented for the assumed stress-strain diagrams by curves *a* in Figs. 9–11. The curves for Cases II and III are the same.

I-Section

The introduction of a web the cross-sectional area of which is equal to that of each of two equal thin flanges makes, in general, a considerable difference in the ϵ,μ- and κ,μ-relations. For this case $\rho_1 = \rho_2 = 1/3$. From Eq. (125) and the corresponding equations for ψ_2 and by substitution in Eq. (100),

$$(e_1 + e_2)\kappa\iota_{11} + \kappa^2\iota_{12} = (e_1 + e_2)\kappa\iota_{21} + \kappa^2\iota_{22} \qquad (152)$$

With

$$I = (7/36)Ah^2$$

substitution in Eq. (101) from Eq. (126) and the corresponding equation for μ_2 gives

$$\mu = (12/7\kappa^2)[\kappa e_1(\kappa\iota_{11}) + \kappa^3\iota_{13} + \kappa e_2(\kappa\iota_{21}) + \kappa^3\iota_{23}] \qquad (153)$$

For a given value of e_2 (or e_1), Eq. (152) is solved by trial for e_1 (or e_2) most easily with the aid of such charts as Figs. 2–4. For example, suppose $n_1 = 2$, $K_1 = 105$, $n_2 = 2$, $K_2 = 125$, and let $e_2 = 0.00500$. From Fig. 3 is read off, corresponding to $e_e = e_2 = 0.00500$: $10^3\kappa\iota_{e1} = 10^3\kappa\iota_{21} = 3.48$ and $10^6\kappa^2\iota_{e2} = 10^6\kappa^2\iota_{22} = 9.59$. Eq. (152) now becomes, when multiplied by 10^6 for convenience,

$$(10^3e_1 + 5)10^3\kappa\iota_{11} + 10^6\kappa^2\iota_{12} = 3.48(10^3e_1 + 5) + 9.59 = 3.48\ (10^3e_1) + 27.0 \qquad (154)$$

By trying a few values of e_1 and reading the corresponding values of $10^3\kappa\iota_{11}$ and $10^6\kappa^2\iota_{12}$ from Fig. 2, it is found that Eq. (154) is satisfied by $e_1 = 0.00482$ for which $10^3\kappa\iota_{11} = 3.52$ and $10^6\kappa^2\iota_{12} = 9.26$. Then $\kappa = 0.00482 + 0.00500 = 0.00982$ and $\epsilon = 0.00482 - 0.00500 = -0.00018$. In order to evaluate μ from Eq. (153), $10^9\kappa^3\iota_{13}$ and $10^9\kappa^3\iota_{23}$ are read from Figs. 2 and 3, respectively, as 29.0 and 31.1, and μ becomes

$$\mu = \frac{12 \times 10^{-3}}{7 \times 96.4}[(9.82)(4.82)(3.52) + 29.0 + (9.82)(5.00)(3.48) + 31.1] = 0.00707 \qquad (155)$$

The preceding procedure was followed to obtain the curves *b* of Figs. 6–8.

Parabolic Section, Vertices In

A symmetric section that is somewhat less spread out than the I-section just treated is the parabolic section with the vertices in, Fig. 1g. For this section, Eqs. (133) and (134), the corresponding equations for ψ_2/κ and μ_2/κ, and Eqs. (100) and (101) give

$$(e_1 - e_2)^2\kappa^2\iota_{12} - 4(e_1 - e_2)\kappa^3\iota_{13} + 4\kappa^4\iota_{14} = (e_1 - e_2)^2\kappa^2\iota_{22} + 4(e_1 - e_2)\kappa^3\iota_{23} + 4\kappa^4\iota_{24} \tag{156}$$

$$\mu = (20/\kappa^4)[(e_1 - e_2)^2\kappa^3\iota_{13} - 4(e_1 - e_2)\kappa^4\iota_{14} + 4\kappa^5\iota_{15} + (e_1 - e_2)^2\kappa^3\iota_{23} + 4(e_1 - e_2)\kappa^4\iota_{24} + 4\kappa^5\iota_{25}] \tag{157}$$

With the aid of charts such as Figs. 2–4, Eq. (156) is solved by trial for e_1 (or e_2) for given values of e_2 (or e_1) in the same way as Eq. (152), and then μ [Eq. (157)] can be evaluated by direct substitution. The results for the assumed stress-strain diagrams are represented by curves *c* in Figs. 6–8.

Rectangular Section

A more compact symmetric section than those considered so far is the rectangular section. For this section $\rho_1 = \rho_2 = 0$ and $I = (1/12)Ah^2$. Eqs. (125) and (126) and the corresponding equations for ψ_2/κ and μ_2/κ, together with Eqs. (100) and (101) give

$$\kappa^2\iota_{12} = \kappa^2\iota_{22} \tag{158}$$

$$\mu = (12/\kappa^2)(\kappa^3\iota_{13} + \kappa^3\iota_{23}) \tag{159}$$

Eq. (158) is solved by trial for e_1 (or e_2) for given values of e_2 (or e_1) in the same way as Eq. (152), and then μ [Eq. (159)] can be evaluated by direct substitution. The results for the assumed stress-strain diagrams are represented by curves *d* in Figs. 6–8.

Parabolic Section, Vertices Out

The most compact symmetric cross-section that will be considered here is the parabolic section with the vertices out, Fig. 1f. For this section Eqs. (131) and (132), the corresponding equations for ψ_2/κ and μ_2/κ and Eqs. (100) and (101) give

$$e_1e_2\kappa^2\iota_{12} + (e_1 - e_2)\kappa^3\iota_{13} - \kappa^4\iota_{14} = e_1e_2\kappa^2\iota_{22} - (e_1 - e_2)\kappa^3\iota_{23} - \kappa^4\iota_{24} \tag{160}$$

$$\mu = (120/\kappa^4)[e_1e_2\kappa^3\iota_{13} + (e_1 - e_2)\kappa^4\iota_{14} - \kappa^5\iota_{15} + e_1e_2\kappa^3\iota_{23} - (e_1 - e_2)\kappa^4\iota_{24} - \kappa^5\iota_{25}] \tag{161}$$

From these equations the relation between κ and μ and between ϵ and μ can be determined as for the preceding sections. The results for the assumed stress-strain diagrams are represented by curves *e* in Figs. 6–8.

T-Section with Infinitesimal Web

Another limiting case of an unsymmetrical section is the T-section with thin flange and an infinitesimally narrow (thin) web. Here $\rho_1 = 0$ and $\rho_2 = 1$ or $\rho_1 = 1$ and $\rho_2 = 0$. For $\rho_1 = 0$ and $\rho_2 = 1$, Eqs. (125) and (100) give

$$\iota_{21} = \sigma_2 = e_2 = 0 \tag{162}$$

With $I = (1/12)\,(1 - \rho_2)\,(1 + 3\rho_2)Ah^2$, Eqs. (126) and (100) give, when $\rho_2 = 1$,

$$\mu = (3/\kappa^2)\kappa^3\iota_{13} \tag{163}$$

The relations between κ and μ and between $\epsilon(= e_1 = \kappa)$ and μ are shown as curves *b* in Figs. 9–11 for the assumed stress-strain diagrams. The curves for Cases II and III are the same.

T-Section

A T-section that is not extreme, like the one just considered, is one for which $\rho_1 = 0$ and $\rho_2 = {}^1/_2$*—that is, a section with flange area equal to web area. With

$$I = (5/48)Ah^2$$

Eqs. (125), (126), (100), and (101) give

$$\kappa^2\iota_{12} = (e_1 + e_2)\kappa\iota_{21} + \kappa^2\iota_{22} \tag{164}$$

$$\mu = [24/(5\kappa^2)]\,[\kappa^3\iota_{13} + (\kappa e_2)(\kappa\iota_{21}) + \kappa^3\iota_{23}] \tag{165}$$

The relations between κ and μ and between ϵ and μ are shown as curves *c* in Fig. 9–11 for the assumed stress-strain diagrams.

* ρ in this paper has a different significance from ρ in the previous paper.[1]

Semiparabolic Section, Vertices Out

For the unsymmetric section bounded by two half-parabolas with the vertices out, Fig. 1h, Eqs. (135)–(138), together with Eqs. (100) and (101), give

$$e_1(e_1 + 2e_2)\kappa^2\iota_{12} - 2e_2\kappa^3\iota_{13} - \kappa^4\iota_{14} = e_1(e_1 + 2e_2)\kappa^2\iota_{22} + 2e_2\kappa^3\iota_{23} - \kappa^4\iota_{24} \tag{166}$$

$$\mu = [480/(19\kappa^4)]\,[e_1(e_1 + 2e_2)\kappa^3\iota_{13} - 2e_2\kappa^4\iota_{14} - \kappa^5\iota_{15} + e_1(e_1 + 2e_2)\kappa^3\iota_{23} + 2e_2\kappa^4\iota_{24} - \kappa^5\iota_{25}] \tag{167}$$

The relation between κ and μ for the assumed stress-strain diagrams, within the range of κ's considered, differ so slightly from that for the triangular section, to be discussed next, that it is not shown in the figures; nor is the relation between ϵ and μ shown.

Triangular Section

For a triangular section, Fig. 1e, Eqs. (127)–(130), together with Eqs. (100) and (101), give

$$e_1\kappa^2\iota_{12} - \kappa^3\iota_{13} = e_1\kappa^2\iota_{22} + \kappa^3\iota_{23} \tag{168}$$

$$\mu = (36/\kappa^3)(e_1\kappa^3\iota_{13} - \kappa^4\iota_{14} + e_1\kappa^3\iota_{23} + \kappa^4\iota_{24}) \tag{169}$$

The relations between κ and μ and between ϵ and μ are shown as curves *d* in Figs. 8–10 for the assumed stress-strain diagrams.

Semiparabolic Section, Vertices In

An unsymmetric section for which the center of gravity lies at the same point as for the T-section treated above is a section bounded by two half-parabolas with the vertices in, Fig. 1i. For this section Eqs. (139)–(142), together with Eqs. (100) and (101), give

$$e_1^2\kappa^2\iota_{12} - 2e_1\kappa^3\iota_{13} + \kappa^4\iota_{14} = e_1^2\kappa^2\iota_{22} + 2e_1\kappa^3\iota_{23} + \kappa^4\iota_{24} \tag{170}$$

$$\mu = (80/\kappa^4)(e_1^2\kappa^3\iota_{13} - 2e_1\kappa^4\iota_{14} + \kappa^5\iota_{15} + e_1^2\kappa^3\iota_{23} + 2e_1\kappa^4\iota_{24} + \kappa^5\iota_{25}) \tag{171}$$

The relations between κ and μ and between ϵ and μ are shown as curves *e* in Figs. 9–11 for the assumed stress-strain diagrams.

Discussion

With charts such as Figs. 2–4 and curves similar to those of Figs. 6–11 available, all information relating extreme fiber strains and stresses with bending moments can be readily obtained. For example, for a given section and a given μ (that is, a given moment) ϵ and κ can be read off from such figures as Figs. 6–11; then the extreme fiber strains $e_1 = (1/2)(\kappa + \epsilon)$ and $e_2 = (1/2)(\kappa - \epsilon)$, and with e_1 and e_2 known, since $\sigma_1 = \kappa\iota_{11}$ and $\sigma_2 = \kappa\iota_{21}$, the extreme fiber stresses can be read off from such charts as Figs. 2–4. If, on the other hand, the value of μ is desired for a given value of e_2, an e_2-scale graduated to twice the scale of ϵ and κ can be slid parallel to the axis of ϵ and κ with the zero on the ϵ-curve until the given e_2-reading comes in coincidence with the κ-curve. The ordinate will be the desired value of μ. The value of μ for a given e_1 may be obtained in the same way from a plot of $-\epsilon$ and κ against μ. Alternatively, e_1 can be stepped off by trial with compasses or dividers. If σ_1 or σ_2 is given, e_1 or e_2 is first read from a chart similar to Figs. 2–4 and μ is then obtained as just outlined.

All this is not to say, of course, that the charts and curves mentioned are necessary for the solution of a problem in plastic bending. Any problem can always be solved for a given set of conditions by means of Eqs. (100) and (101). The charts and curves are a convenience when ψ_1, ψ_2, μ_1, and μ_2 are given by Eqs. (104a)–(107a).

The solid lines in Fig. 4 depart from the dotted lines at the strains 0.004762 and 0.004000 at which the materials cease to be elastic.

The dotted lines, $\mu = \kappa$, in Figs. 6–11 give the upper limits for μ. For example, a section consisting of an infinitely wide, infinitesimally thin (in the direction of the depth of the beam) web of finite area and of one or two infinitesimal flanges at finite distances from the web would be a section for which $\mu = \kappa$ for all possible stress-strain diagrams.

The ϵ,μ-curves illustrate the wanderings of the neutral axis as μ changes. Except for symmetric sections, Case I, Fig. 6, these peregrinations are considerable. That they are not greater in Fig. 6 is because of the fact that the tensile and compressive stress-strain curves do not differ widely from each other in the range of the strains entering in Fig. 6. When $d\epsilon/d\mu$ passes through zero, as in Fig. 8, there may be a slight error in the values of μ above the value at which $d\epsilon/d\mu = 0$, for when $d\epsilon/d\mu$ passes through zero the strains near the neutral axis reverse their signs, and the material locally may be in effect a different material—one that has been strain-hardened. But it is inconceivable that an error of detectable magnitude can result in a practical section.

It is unlikely that the exact solution of the general problem of plastic bending can be much simplified beyond the solution presented here. For symmetric

(*Continued on page 272*)

A Consideration of Calculated Versus Flight Test Take-Off Performance

M. H. KIEHLE* AND A. VANTINE†

Curtiss-Wright Corporation

ABSTRACT

Theoretic methods for calculating the ground run, transition, and steady climb distances during the take-off of an airplane are derived. The velocity for minimum take-off distance over a 50-ft. obstacle is clearly indicated.

A series of approximately 40 take-off tests were made on a C-46 airplane. The technique for measuring and recording the test results and the presentation of the final data are described.

The test data are compared with the theoretic calculations. It is shown that not only the actual minimum take-off distances but also the effect of flap deflection and velocity on the total take-off distance can be accurately predicted by the theoretic methods. The relative effects of C_L, C_D, thrust, ground proximity, ground friction, and other variables on take-off distance are discussed, and the pilot technique derived for minimum take-off is stated.

Finally, it is shown that the complete take-off characteristics of an airplane may be obtained from a short, well-planned test program, with the emphasis placed on determining the maximum accelerations acting on the airplane rather than on testing for minimum distances.

SYMBOLS

C_D = total drag coefficient
C_{Di} = induced drag coefficient
C_{DP} = parasite drag coefficient
C_H = rate of climb, ft. per sec.
C_L = lift coefficient
D = drag, lbs.
F = force, lbs.
K_1 = numerical constant, T/qS
K_2 = numerical constant, $(W/qS)V_{TO}$
KE = kinetic energy
L = lift, lbs.
M = mass, slugs per cu.ft.
P = power, b.hp.
PE = potential energy
R = ratio, test rate of climb to standard rate of climb
S = wing area, sq.ft.
T = thrust, lbs.
V = velocity, ft. per sec.
W = gross weight, lbs.
X = distance, ft.
a = acceleration, ft. per sec. per sec.
e = span efficiency factor
g = acceleration due to gravity, 32.2 ft. per sec. per sec.
q = dynamic pressure, lbs. per sq.ft.
t = time, sec.
α = angle of attack, rad.
θ = angle of climb, rad.
μ = ground friction coefficient
π = 3.1416
σ = density ratio; also, ground interference factor

Subscripts

a = refers to air distance conditions
c = corrected
f = friction
g = refers to ground run conditions
h = horizontal
m = inertia
n = normal
o = standard, specified
t = tangential
TO = refers to take-off point
v = vertical
w = wind
x = horizontal

Received December 29, 1944. To have been presented at the I.A.S. Thirteenth Annual Meeting, which was canceled to cooperate with a Government appeal (January, 1945) to refrain from holding conventions and meetings.

* Senior Flight Test Engineer, Airplane Division, Buffalo Plant.

† Flight Test Engineer, Airplane Division, Buffalo Plant.

INTRODUCTION

THE TAKE-OFF PERFORMANCE of an airplane is a problem that for a long time has defied an adequate, practical solution. Even though take-off has received considerable emphasis lately because of the trend toward high-wing loadings by both the armed services and the air cargo and transport industries, there still remains the necessity of developing an analytic method for calculating take-off distances which is reliable and simple.

This paper is not intended to present a perfect solution to the take-off problem. However, it is intended to develop a sound, practicable method that agrees well with flight-test data. Also, by application of the principles of the method, the complete take-off characteristics of any airplane may be derived from a suggested flight-test procedure.

The fundamentals of the analytic method and the flight test techniques as presented in this paper were developed by the St. Louis Plant of the Airplane Division of the Curtiss-Wright Corporation.[7]

TREATMENT OF THEORETIC METHOD

The take-off path of an airplane is considered as consisting of three parts: (a) the ground run is the horizontal distance covered by the airplane from a point of zero velocity to the point of take-off velocity, V_{TO}; (b) the transition distance is the horizontal distance covered from the point of take-off velocity, V_{TO}, to the point where a steady state of climb is attained; and

(c) the steady climb distance is the horizontal distance covered from the beginning of the steady climb until a 50-ft. obstacle is passed. It may be, as in the case of airline performance, that the transition phase extends well beyond the 50-ft. obstacle point.

It is apparent to those persons familiar with the take-off problem that, while equations can be evolved to satisfy the complete performance of the airplane, it is nearly impossible to find satisfactory solutions to these equations. The basic difficulty lies in the inability of the pilot to "sense" or accurately control the lift variation of the airplane during accelerated free flight in the transition phase of take-off. Hence, the method presented herein will be concerned only with the optimum or minimum take-off distance since it can be shown that this type of performance depends upon the maximum lift the pilot can obtain on the airplane.

Ground Run

The take-off point of the airplane is considered as the point where the aerodynamic lift becomes equal to the weight of the airplane. At this point the airplane is traveling with the forward velocity of V_{TO}, and has covered a distance of X_g from its start.

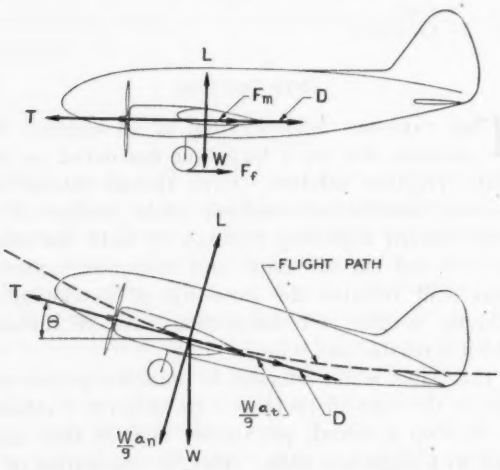

FIG. 1 (*top*). Forces acting on airplane during ground run.
FIG. 2 (*bottom*). Forces acting on airplane during transition.

From a force diagram of the airplane during the ground run, Fig. 1, the following equations may be derived:

The summation of forces in the horizontal direction are:

$$F_x = F_m - T + F_f + D = 0 \tag{1}$$

The total friction force:

$$F_f = \mu(W - C_L qS) \tag{2}$$

The total aerodynamic drag:

$$D = C_D qS \tag{3}$$

The inertia force:

$$F_m = Ma = (W/g)a_t \tag{4}$$

Substituting Eqs. (2), (3), and (4) in Eq. (1)

$$(W/g)a_t - T + \mu(W - C_L qS) + C_D qS = 0 \tag{5}$$

Now

$$a_t = dV/dt = V(dV/dx) \tag{6}$$

By substitution and rearrangement,

$$X_g = \int_0^{V_{TO}} \frac{WV\,dV}{g[\,T - \mu(W - C_L qS) - C_D qS]} \tag{7}$$

This equation includes only the important factors, the inconsequential factors neglected being the incidence of the thrust relative to the horizontal and the forces necessary to accelerate rotation of the wheels. Values of C_L and C_D include the effect of the proximity of the ground and power. The expression may be integrated in velocity increments since T, C_L, C_D, and q are unique for any instantaneous V and α. The values of these quantities can be obtained from wind-tunnel, flight-test, or theoretic data.

Transition Distance

The transition phase of take-off is characterized by a continuous change in the horizontal and vertical accelerations of the airplane. During any portion of the phase, the forces acting on the c.g. of the airplane are shown on Fig. 2.

Summation of the forces along the tangential and normal axes of the path result in the following equations:

$$F_{tangential} = T - D - (W/g)a_t - W\sin\theta = 0 \tag{8}$$

$$F_{normal} = L - (W/g)a_n - W\cos\theta = 0 \tag{9}$$

In order to simplify these expressions so that they are workable, two assumptions are made:

(a) $\cos\theta = 1.0$; $\sin\theta = \tan\theta$

This assumption is entirely within reason for all airplanes, since the angle of climb, θ, seldom reaches more than 10° before the 50-ft. obstacle is passed, even for high-performance pursuit airplanes.

(b) $a_t = 0$

Normally, the transition phase occurs in such a short time that the increase in tangential speed is only of the order of 3–5 m.p.h. Although most airplanes increase their air speed during transition, it will be demonstrated that this assumption does not nullify the accuracy of the results.

Contingent upon these two assumptions, the following now hold true:

$$V_{path} = V_{TO} \tag{10}$$

$$a_n = a_s \tag{11}$$

$$\sin \theta = C_H/V_{TO} \tag{12}$$

Employing these results, then, Eqs. (8) and (9) now read

$$T - C_D qS - W(C_H/V_{TO}) = 0 \tag{13}$$

and

$$L - (W/g)a_v - W = 0 \tag{14}$$

Eqs. (13) and (14) can be rearranged to give

$$C_D = (T/qS) - (W/qSV_{TO})C_H \tag{15}$$

and

$$a_v/g = (L/W) - 1 \tag{16}$$

The total lift of the airplane is a direct function of the actual lift coefficient, which, in accelerated flight, is not the lift coefficient for steady flight, but somewhat larger.

$$L = C_{La}\, qS$$

On the other hand, the weight of the airplane can always be expressed as a function of the lift coefficient required for level flight; hence,

$$W = C_{LTO}\, qS$$

Substituting in Eq. (16),

$$(a_v/g) = C_{La}/C_{LTO} - 1 \tag{17}$$

One more well-known relationship is needed to complete the analysis.

$$C_D = C_{D_p} + (C_{La}^2/\pi \mathrm{AR}_e) \tag{18}$$

Thus, Eqs. (15), (17), and (18) express the entire force relationships for the airplane in the transition flight path. The validity of Eq. (18) at high angles of attack will be discussed later in the paper.

By using Eqs. (15), (17), and (18), the transition distance may easily be calculated for any desired take-off velocity. By assuming that data are available to determine the thrust of the power unit, it is seen that Eq. (15) takes the form:

$$C_D = K_1 - K_2 C_H$$

where K_1 and K_2 are constant throughout transition.

Thus, the procedure is to calculate the values of C_D that correspond to preselected values of C_H, taken in even increments. With the use of Eqs. (18) and (17), the actual lift coefficients, C_{La}, and the vertical accelerations, a_v, may be obtained. Finally, the increments of time and vertical height can be calculated from the expressions

$$\Delta t = \Delta C_H/[(a_{v_1} + a_{v_2})/2] \tag{19}$$

and

$$\Delta H = [(C_{H_1} + C_{H_2})/2]\Delta t \tag{20}$$

The time increments multiplied by the forward velocity give the incremental horizontal distances.

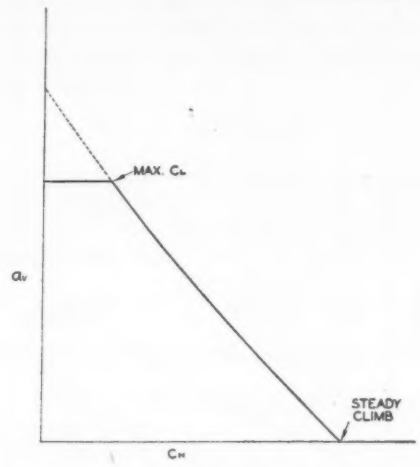

FIG. 3. Vertical acceleration versus rate of climb at constant velocity.

One point should be made clear. The variation of a_v with C_H is shown on Fig. 3. If the calculation is performed without restriction, lift coefficients well above the $C_{L_{max.}}$ of the airplane will result. Obviously, an upper limit to the vertical acceleration exists, determined by substituting $C_{L_{max.}}$ for C_{La} in Eq. (17), and values of a_v must be restricted accordingly. The calculation also will produce, quite naturally, the value of C_{H_1}, the steady rate of climb at a value of $a_v = 0$.

Here, then, lies the solution to the problem of short take-off air distance. The maximum vertical acceleration and, consequently, the shortest air distance possible to attain are direct functions of the maximum lift coefficient in the take-off configuration. This salient feature of the take-off will be discussed more thoroughly shortly.

Steady Climb

The value of the steady rate of climb, C_{H_1}, as determined above, supplies the final solution to the total distance over a 50-ft. obstacle provided that the transition is completed prior to that point.

If the preceding calculations are carried out for a series of take-off velocities, the results can be plotted on a curve of distance versus velocity, as shown on Fig. 4.

The velocity for minimum take-off distance is clearly indicated, since the air distance reaches a minimum at a speed approximately 10 per cent above stall speed. The feasibility of taking an airplane off the ground at this speed is considered shortly.

So that these analytic equations provide a correct prediction of take-off performance, it is necessary for the engineer to define accurately the various design data needed. While only a brief indication of the sources of these data is given now, the authors intend to emphasize strongly a practical application of these data.

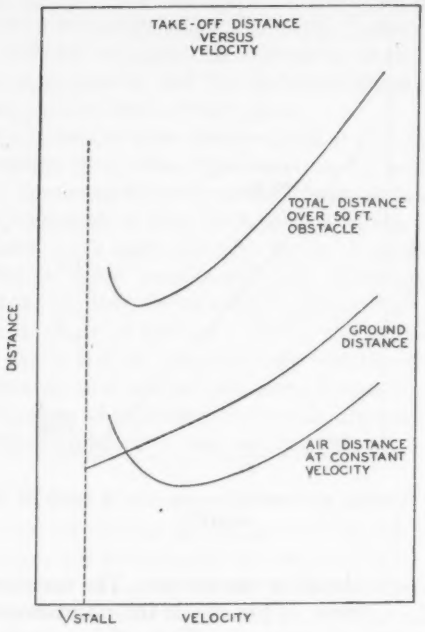

FIG. 4.

The variation of net propeller thrust with airplane speed can be calculated from adequate propeller performance information supplied by propeller manufacturers[4, 5] or by the N.A.C.A. Although much skepticism has been directed at thrust data during low-speed operation in the past, recent refinements of analytic methods and more accurate test data have provided the engineer with reliable thrust information.

The lift and drag coefficients during the ground run are easily obtained from wind-tunnel or flight-test data for an average angle of attack. The effect of the proximity of the ground can be estimated by the use of Wieselsberger's functions[1] or other suitable methods. As far as the air distance is concerned, the same procedure is employed to determine lift and drag. Ground effect on the air distance may be neglected to simplify the computations. The assumption that it is negligible is a conservative one and since it is a diminishing effect, the error is small. Values of ground friction coefficient, μ, are found in any standard aerodynamic reference for various types of surfaces.[2, 8]

FLIGHT TESTING FOR TAKE-OFF

Equipment and Procedure

A series of approximately 40 take-off tests at various wing flap settings and take-off velocities were carried out on a Curtiss-Wright C-46 type airplane, a low-wing twin-engined transport. Specialized equipment was employed which consisted of an electrically driven Bell and Howell Take-Off Performance Analysis Camera using 16-mm. film. The camera recorded eight double frames a second, each double frame consisting of a picture of the airplane during the take-off run, a run number configuration card, and a stop watch located integrally within the camera. The camera was located 1,650 ft. from the centerline of the runway on a normal to the approximate center of the take-off run. At 150 ft. from, and parallel to, the runway on which the tests were being made, successively numbered flags were spaced 100 ft. apart. Thus, as the airplane proceeded along the take-off path, a photographic record of its position and time from the start of the run was obtained. The airplane was painted with white stripes arranged to facilitate accurate recording of the position of the airplane from the film. See Fig. 5 for a typical picture.

The picture records obtained with the camera were transcribed to data form by the use of a special double-frame projector using a set of calibrated grid plates at the projection screen. The time, distances, and heights were read, frame by frame (depending on the path accuracy desired), by lining up the centerlines and bases, respectively, of the projected images of the flags with the lines on the calibrated grid plates. The heights of the airplane thus obtained were corrected for changes in elevations of the reference flags by use of the airfield survey chart. The vertical displacement of the airplane was measured from the bottom of the main wheels. The wheels were not retracted during the

FIG. 5. A typical film record of a take-off.

tests, since the air time over a 50-ft. obstacle averaged about 5 sec.

Having the increments of distances, heights, and time per frame, the forward velocity of the airplane was computed and then the curves of time, velocity, and height were plotted versus runway distance. These curves present a picture of the take-off of the airplane as it progresses through the test run and are not reduced to standard conditions.

Near the take-off point along the runway, there was located an instrument board from which the following readings were obtained by an observer during the take-off: wind direction and velocity, outside air temperature, and barometric pressure. In the airplane an engineer recorded both engine r.p.m.'s and manifold pressures, torque pressure on the left engine on which a torquemeter was installed, mixture setting, indicated air speed, wing and cowl flap position, and Bowser fuel recorder readings. It now appears, in the light of the experience obtained, that the following measurements should have been included in addition to those above on a photorecorder—outside air temperature, carburetor air temperature, carburetor ram, elevator position, elevator stick force, angle of attack, and horizontal and vertical acceleration. These data would have enabled the engineers to determine more accurately the power output of the engines and the control effectiveness at the take-off point.

In general, tests were run only when the wind velocity was less than 10 m.p.h. Tests were made at a series of take-off air speeds from stalling speed to 15 m.p.h. above stalling speed and at wing flap deflections of 0°, 11°, 15.5°, and 20°.

The procedure followed in each run consisted of running the engines to full power with brakes on, releasing the brakes, and raising the tail as soon as the air speed was sufficiently high. When a previously specified air speed was reached, the tail was lowered rapidly and the airplane was "pulled off" in a sharp attitude. While it was attempted to maintain constant air speed from the take-off point to the 50-ft. clearance point, it was seldom possible to do this.

Reduction Methods

The following method for reducing observed take-off ground and air-distance data to standard conditions of power, gross weight, air speed, and altitude is based on the assumption that the test conditions match the specified conditions within 8–10 per cent. These limits, of course, are not rigid and are subject to the amount of accuracy desired from the test results.

Obviously, the greater the divergence between specified conditions and test conditions, the larger the discrepancy in the correction method will be. Within the limits shown, the accuracy is greater than the normal testing technique.

In deriving a formula for correcting observed take-off ground distance to standard conditions of power, gross weight, wind velocity, and altitude, a general equation of work will be used.

$$\text{work} = \Delta KE + \Delta PE$$

Since the change in potential energy is zero during the ground run and the initial velocity at the start of the take-off is zero, the generalized work equation of ground motion becomes:

$$W = FX_g = {}^1/_2(W/g)(V_{TO}/\sqrt{\sigma})^2 \tag{21}$$

Under standard conditions, this formula becomes:

$$F_cX_{gc} = {}^1/_2(W_o/g)[(V_{TO})_o/\sqrt{\sigma_o}]^2 \tag{22}$$

In test work, Eq. (21) reads

$$FX_g = {}^1/_2(W/g)[(V_{TO}/\sqrt{\sigma}) - V_w]^2 \tag{23}$$

Solving for X_{gc} and X_g and transposing,

$$X_{gc} = X_g\left(\frac{W_o}{W}\right)\left(\frac{F}{F_o}\right)\frac{[(V_{TO})_o/\sqrt{\sigma_o}]^2}{[(V_{TO}/\sqrt{\sigma}) - V_w]^2} \tag{24}$$

The net force, F, is expressed as

$$F = T - D - \mu(W - L) \tag{25}$$

The value of thrust is the dominating factor in this equation. If the assumption is made that the aerodynamic drag and ground friction will be nearly alike for both the standard and test conditions, a small error will result by the use of the ratio

$$F/F_o = T/T_o \tag{26}$$

Furthermore, it may also be assumed that the difference between the test and standard values of velocity and propeller efficiency is small. Hence,

$$F/F_o = P/P_o \tag{27}$$

Thus, Eq. (24) now reads

$$X_{gc} = X_g\left(\frac{W_o}{W}\right)\left(\frac{P}{P_o}\right)\left[\frac{(V_{TO})_o/\sqrt{\sigma_o}}{(V_{TO}/\sqrt{\sigma}) - V_w}\right]^2 \tag{28}$$

Now $(V_{TO}/\sqrt{\sigma}) - V_w$ is the actual true ground speed of the airplane at the instant of take-off, which is determined directly from the film record, and it may be designated V_{g_1}. Also, if the specified indicated take-off velocity is taken to be the actual indicated velocity, then

$$(V_{TO})_o = (V_{g_1} + V_w)\sqrt{\sigma} \tag{29}$$

By making these two substitutions, Eq. (28) finally becomes:

$$X_{gc} = X_g\left(\frac{W_o}{W}\right)\left(\frac{P}{P_o}\right)\left[\frac{(V_{g_1} + V_w)^2}{V_{g_1}^2}\right]\left(\frac{\sigma}{\sigma_o}\right) \tag{30}$$

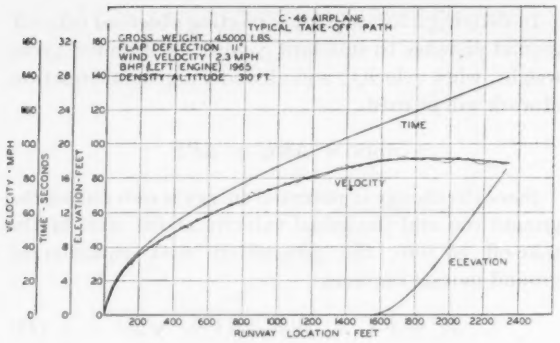

FIG. 6.

Eq. (30) is applied to each flight-test point separately, and the corrected test points are plotted at the corrected test values of $(V_{g_1} + V_w)\sqrt{\sigma}$.

The method of correcting the take-off air run to standard conditions is taken directly from the *Army Handbook for Airplane Designers*[9] as

$$X_{a_c} = (X_a + V_w t_a)\sqrt{\sigma}\, R \qquad (31)$$

The parameter, R, is the ratio of the test rate of climb to the standard rate of climb of the airplane. The values of R are calculated directly using the "*iw*" performance method or a suitable substitute.

Presentation of Test Results

The calibrated test data transcribed from the photo records are plotted to give a clear picture of the "space-time" history of the take-off run as in Fig. 6.

Then the desired test values of the above curves are reduced to standard conditions, as described in the above reduction method, and the final distances are plotted versus the corresponding velocity. Figs. 10 to 13 show the flight-test points for the various flap deflections tested.

CORRELATION OF THEORETIC AND FLIGHT-TEST DATA

Before any comparison of theoretic calculations and flight-test data is made, the quantities affecting take-off distance should be investigated to determine their relative effect on the final result. Accordingly, C_L, C_{D_p}, the ground interference factor σ, the ground friction coefficient μ, and the thrust were systematically varied in Eq. (7) for an average take-off velocity of the C-46. Typical values of these variables were chosen from flight-test, wind-tunnel, and design sources. The results are shown on Figs. 7 and 8.

The fact is immediately apparent that, for the C-46 airplane, large changes in the lift coefficient, parasite drag coefficient, and ground interference factor have a minor effect on ground run distance, Fig. 7, when compared to similar changes in the ground friction coefficient and thrust. Therefore, in calculating ground distance, emphasis must be placed on the thrust and

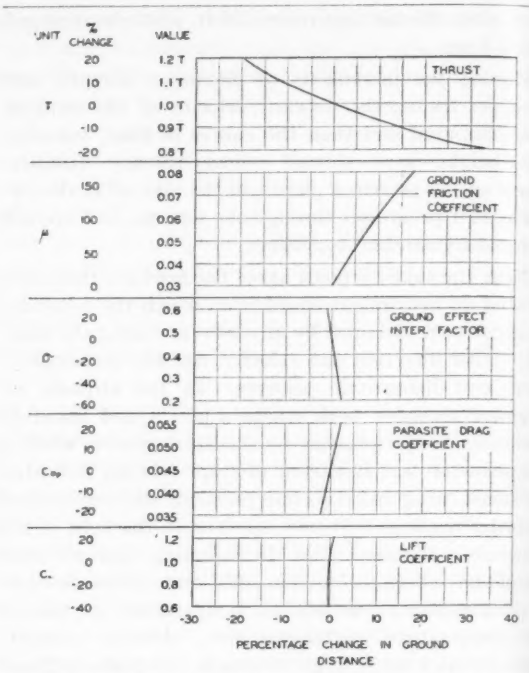

FIG. 7. Effect of variables on take-off ground run.

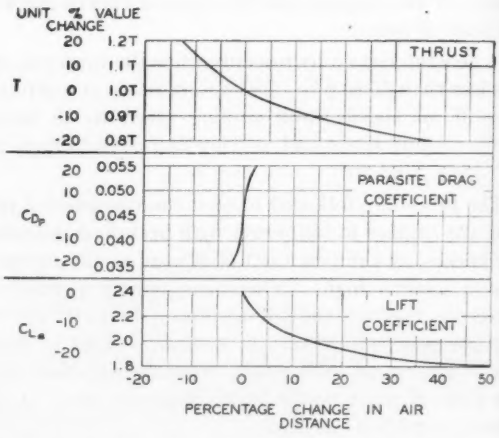

FIG. 8. Effect of variables on take-off air distance.

ground friction coefficient determination. For example, it appears rather unreasonable to find the ground effect on lift and drag in detail and yet perform a rough estimation of μ or thrust.

Of course, it should be kept in mind that the particular variations shown apply to the C-46. A high-performance, low-wing fighter plane might yield quite a different pattern of effects.

A similar procedure was followed for the air distance calculation and the results are shown on Fig. 8. The effect of thrust on air distance is of nearly equal importance as the effect of maximum lift coefficient. However, the effect of $C_{L_{max.}}$ is not clearly indicated by this

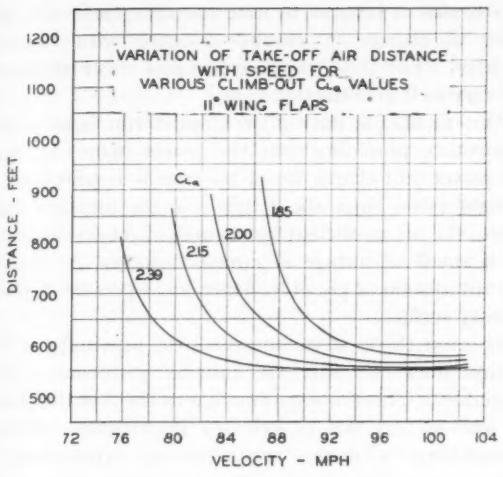

FIG. 9.

curve. Fig. 9 bears this out by showing the variation in air distance with take-off speed for various values of C_{L_a}. As the lift coefficient is decreased, the air distance is increased considerably, especially at the lower speeds. It is interesting to note that, at the higher take-off speeds, the air distance is little affected by changes in maximum lift.

A question referred to earlier in the paper arises in respect to the correctness of applying Eq. (18) to high angles of attack, such as are encountered during the transition. While it cannot be denied that the parabolic variation of drag with lift does not hold true at high angles of attack near the stall, nevertheless, the effect of aerodynamic drag on the air distance, Fig. 8, is so small that a large error will not appreciably affect the results. Because a drag determination is difficult in this region, the equation is considered as the best means available.

Having obtained the relative effect of the performance values on take-off distance, then, basic data, directly from flight-test, wind-tunnel or theoretic sources were derived. Take-off calculations carried out for flap deflections of 0°, 11°, 15.5°, and 20° show reasonable agreement with flight-test data. For each flap deflection, Figs. 10 to 13, the calculated distances represent the minimum performance obtainable in actual tests.

Ground Run

The accuracy of the basic data and the method in predicting the effect of flap deflection on take-off distance is apparent. The majority of the flight-test data are within 100 to 150 ft. of the calculated curve for all flap deflections. It is the opinion of the authors that the attempts to limit the allowable discrepancy to less than this amount are useless. Pilot technique and the multitude of small errors and deviations that enter into the analysis of flight data are responsible for this belief.

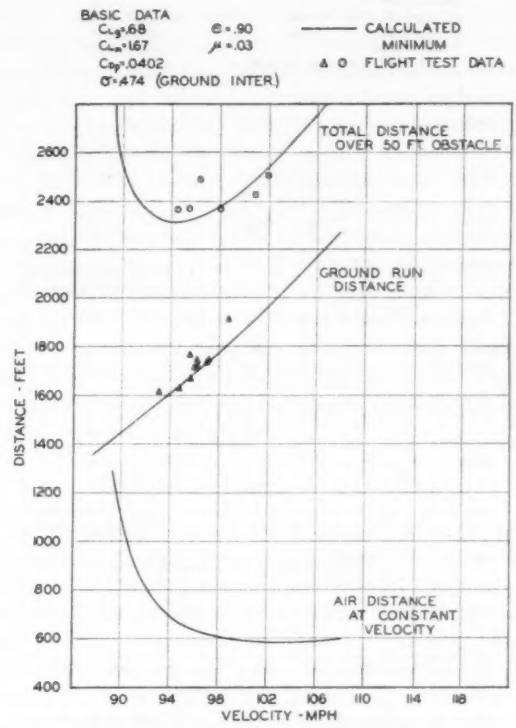

FIG. 10. Take-off distances for 0° flap deflection.

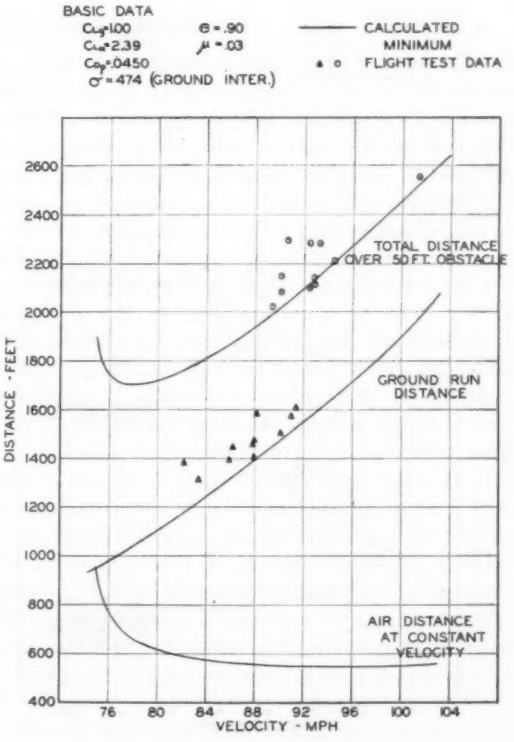

FIG. 11. Take-off distances for 11° flap deflection.

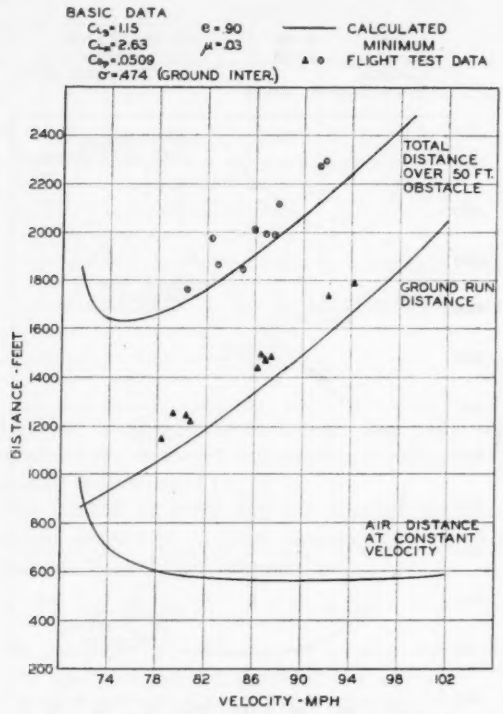

FIG. 12. Take-off distances for 15.5° flap deflection.

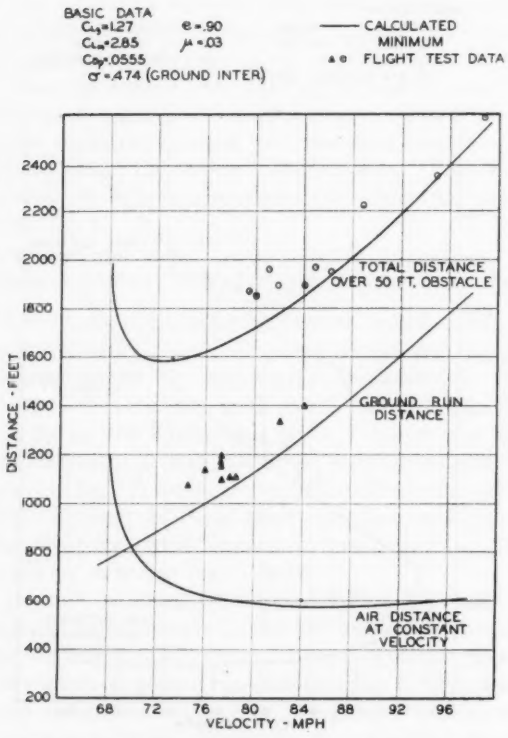

FIG. 13. Take-off distances for 20° flap deflection.

It is also of interest to note the agreement with respect to change in ground distance with take-off velocity. The slope of the calculated curve aligns itself very well with the test data.

Pilot technique during the ground run is of minor importance providing that the power plants develop full power and that little or no trim is required for a straight path, since the attitude of the airplane and, hence, the lift coefficient have small effect on distance. Some small advantage is gained, however, by raising the tail as soon as possible, depending upon the type of runway surface.

As far as the C-46 is concerned, the proximity of the ground does not alter the take-off performance appreciably. This is obvious in view of the fact that both C_L and C_D are not of primary importance. Hence, Wieselsberger's function[1] was considered satisfactory.

During the test program, the ground friction was not determined. However, fairly accurate information was secured from N.A.C.A. data.[2] A value of 0.03 for the ground friction coefficient was selected as representative of the combination of macadam runways, low-pressure tires, and roller bearings.

It can be shown[3] that, if μ exceeds a certain critical value, it is of definite advantage to take-off in the three-point attitude. This critical value of μ is obtained from the equation

$$\mu_{cr} = (C_D - C_{D_p})/C_L$$

As a matter of curiosity, this critical value was calculated for the C-46 for the 11° flap deflection and found to be 0.045. Thus, on soft turf or muddy fields, the three-point attitude will result in a shorter take-off distance. This critical value will obviously be different for other flap deflections.

Total Distance over a 50-Ft. Obstacle

The variation of total distance over a 50-ft. obstacle again is satisfactorily predicted by the theoretic method. Maximum lift coefficients obtained from flight tests in the take-off configuration with full take-off power applied were used. The scatter of test points, while slightly greater than that for the ground run, is nonetheless acceptable.

The calculated variation of total distance with velocity is also satisfactory. It is interesting to note that, while most airplanes show an increasing air distance with velocity after the minimum distance point is reached, the subject airplane indicates a nearly constant air distance for a spread of from 15 to 20 m.p.h. if constant speed is maintained throughout the air run. The fact that the theoretic method was able to reveal this feature, which apparently is borne out by the test data, is a strong point in favor of its accuracy.

There is a somewhat annoying aspect of the test data with respect to the increase in velocity throughout the transition. The theoretic method assumes a constant

air run velocity that results in a nearly constant air distance. However, the tests show an average increase in velocity of 4 to 6 m.p.h. from the take-off point to the 50-ft. obstacle. The actual test air distances, accounting for this increase in velocity, are not those shown by calculation. Attempts to derive a method that allowed for increasing velocity resulted in an apparently endless repetition of trial-and-error techniques.

For the moment, consider only the ground distance and *total* distance curves. The ground distance is plotted versus take-off velocity, while the total distance is plotted versus velocity over the 50-ft. obstacle. Both calculated curves agree well with test data. Hence, it is within reason to say that the air distance is the difference between the ground distance at V_{TO} and the total distance at V_{50}. That is, referring to Fig. 11, for example, if V_{TO} = 86 m.p.h. and V_{50} = 90 m.p.h. the air distance is 710 ft. Such a procedure would give different air distances for each speed, as well as for each speed increase throughout transition. To what extent the empiric system of determining air distances would hold is hard to say because of the relatively small range of test speeds. Certainly, however, it is valid for the subject airplane within the limit of data shown.

Fig. 14 indicates the effect of flap deflection on take-off. The use of flaps aids greatly in shortening the take-off of the airplane in that it lowers the allowable take-off velocity. However, in order to accelerate to a given air speed, the ground run is increased with the use of flaps because of the fact that the aerodynamic drag at the higher speeds is much greater in proportion to the ground friction drag.

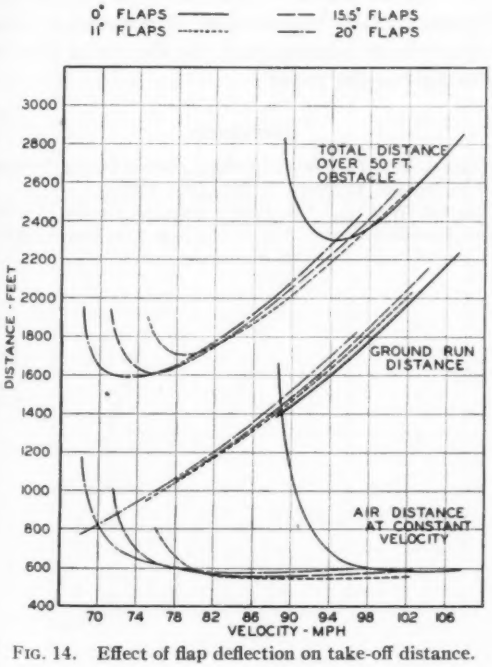

FIG. 14. Effect of flap deflection on take-off distance.

The curves of total distance over a 50-ft. obstacle show a velocity for minimum distance for each flap deflection. However, it is extremely doubtful that any airplane would perform satisfactorily at such a low speed. Not only are the control forces large in this low-velocity region, but the difficulty of maintaining a maximum C_L without actually stalling makes this type of take-off performance nearly impossible for even the best of test pilots. Several of these types were attempted by the pilots for C-46 airplanes. All resulted in an intermittent wing stall with the accompanying buffeting, and the airplane did not rise more than 3 ft. from the ground until more speed was attained. The actual best take-off then lies along the total distance curve somewhat above the velocity for the calculated minimum distance and is a function of pilot ability and the airplane's characteristics.

RESULTS OF TAKE-OFF ANALYSIS

The theoretic method for predicting take-off performance in combination with flight-test data has resulted in a fairly thorough knowledge of the take-off characteristics of the C-46 airplane. Although it is false reasoning to assume that every airplane will conform to the same pattern of effects, nevertheless, the system for investigating the take-off performance of any airplane is clearly indicated. Also, certain general statements may be made with regard to the procedure for obtaining minimum take-off distance.

Flight Testing for Take-Off

A flight-test program for take-off performance may be designed for an aircraft based on the knowledge provided by the theoretic method in this paper. Assuming that sufficient speed-power tests at various flap deflections are available to provide the basic lift and drag values, it remains to determine the maximum lift coefficients of the airplane with take-off power and configuration preliminary to the actual test program.

The determination of certain basic force variables throughout take-off should be the object of the program rather than direct attempts to find the shortest distance. These variables include the ground friction coefficient, the ground run acceleration, the maximum vertical acceleration during transition, accurate power information, and an indication of control forces at low take-off speeds. Equipped with these data, the engineer is in an excellent position to define quite precisely the practical minimum take-off distance and the best pilot technique using the theoretic method for analytic purposes. Then, with a few check flights, his predictions can be proved or disproved. It is not necessary or desirable to run exhaustive tests covering haphazardly, all combination of speeds, flap settings, pilot technique, etc.

Although the data presented in this report concern only an engine-propeller thrust unit, the authors feel

that the methods will equally well apply to partial or full jet thrust units. Regardless of the type of propulsion employed, the take-off performance is fundamentally a function of the maximum accelerations attainable, and the program should be designed accordingly.

Technique for Minimum Take-Off

Many previous writers have indicated in their respective papers the technique for minimum take-off distance. Since, in the last analysis, the object of this study is likewise the same, the authors feel justified in adding their conclusions to others.

To obtain the shortest take-off distance over a 50-ft. obstacle, the brakes should be held until full rated power is reached. Then they should be released, allowing the airplane to accelerate in the take-off configuration with tail high. At a take-off speed approximately 5 per cent above the power on stalling speed, the control stick should be pulled back sharply, within the limits of safety as permitted by the stall characteristics of the individual airplane. The pilot should keep the air speed as nearly constant as possible. Even though some may feel that this speed is on the low side, it should be remembered that, while the tail is being lowered and during the initial stage of transition, the speed will increase slightly, thereby increasing the margin of safety.

References

[1] Wieselsberger, C., *Wing Resistance Near the Ground*, N.A.C.A. T.M. No. 77, 1922.

[2] Wetmore, J. W., *The Rolling Friction of Several Airplane Wheels and Tires and the Effect of Rolling Friction on Take-Off*, N.A.C.A. T.R. No. 583, 1937.

[3] Williams, R. DeH., *Technique to Shorten Take-Offs and Landings*, Aviation, Part I, page 94, January, 1943.

[4] *Hamilton Standard Method of Propeller Performance Calculation*, Hamilton Standard Propellers, Division of United Aircraft Corporation, East Hartford, Conn., 1941.

[5] *Propeller Performance Analysis Procedure and Data*, Propeller Division, Curtiss-Wright Corporation, Report C-1400, 1943.

[6] *An Investigation of the Take-Off Flight Path of Airplanes*, Flight Branch Report 103, Aircraft Airworthiness Section, Bureau of Air Commerce, March, 1938.

[7] *Aerodynamics and Flight Test Manual*, St. Louis Plant, Airplane Division, Curtiss-Wright Corporation, Report N-1, 1943. (Not available for general distribution.)

[8] Diehl, Walter S., *Engineering Aerodynamics*, Revised Edition; The Ronald Press Company, New York, 1940.

[9] *Handbook of Instructions for Airplane Designers*, U.S. Army Air Forces, Vol. I, Section II, Part III, page 418.

Plastic Bending—Further Considerations

(*Continued from page 262*)

cross sections, together with material having the same stress-strain curves in tension and compression, the problem undoubtedly can be simplified somewhat; but the tensile and compressive stress-strain curves of so few materials today are alike that this special case is not of much value. It seems quite possible, however, that satisfactory approximate solutions may be invented, particularly for symmetric cross sections.

It may be noted that, as the ϵ,μ-curves in Figs. 7, 8, 10, and 11 show, the assumption sometimes made—that the neutral axis remains at the centroid—is likely to lead to large inaccuracies.

Acknowledgment

This paper forms part of a project being carried out at the National Bureau of Standards for the Bureau of Aeronautics, Navy Department. The author is pleased to acknowledge permission of the Bureau of Aeronautics to publish the paper.

References

[1] Osgood, Wm. R., *Plastic Bending*, Journal of the Aeronautical Sciences, Vol. 11, No. 3, p. 213, July, 1944.

[2] Osgood, Wm. R., *The Double-Modulus Theory of Column Action*, Civil Engineering, Vol. 5, No. 3, p. 173, March, 1935.

The Relation of Stress to Strain in Magnesium Base Alloys

E. J. EASTMAN,* J. C. McDONALD,† AND A. A. MOORE‡

The Dow Chemical Company

ABSTRACT

Stress-strain curves to the yield strength are given for most of the commercially available forms of magnesium base alloys. For the high-strength wrought alloys, typical curves based on tests of large numbers of different lots are presented. The curves for the other materials are the averages of a few tests on one lot.

The values obtained for the modulus of elasticity were found to be a sensitive function of the testing technique. With careful testing, the values were distributed quite closely around a mean of about 6,500,000 lbs. per sq.in. This figure should be used in normal design calculations.

The ratio of compressive yield strength to tensile yield strength is close to unity for the high-strength wrought alloys and for the casting alloys. It is substantially less than unity for the lower strength wrought alloys.

INTRODUCTION

THE PROBLEM OF THE DESIGNER of a structure is to predict the deformations that the structure will undergo as a function of the amount and type of loading. It is of particular importance to know the loading conditions at which the deformation will increase suddenly with small increases in load. If the structure will carry further load after this point is reached, it is desirable to ascertain the actual ultimate load-bearing ability of the structure.

The solution of this problem may vary greatly in difficulty, depending on the complexity of the structure. In all cases certain basic information must be available even to attempt its solution. For many problems the fundamental relation of stress to strain of the material is required; that is, the relationship of pure tensile or compressive strain to applied tensile or compressive stress. This information is obtained by testing specimens of a geometry such that the strains will be uniaxial in nature—e.g., buckling or bending is absent.

The purpose of this paper is to present such information on magnesium base alloys now in commercial use. In the case of a few of the alloys, enough tests have been made so that typical stress-strain curves can be presented. For the rest, curves are given which have been obtained from one lot of commercial material.

Received December 15, 1944. To have been presented at the I.A.S. Thirteenth Annual Meeting which was canceled to cooperate with a Government appeal (January, 1945) to refrain from holding conventions and meetings.

*, †, ‡ Metallurgical Department.

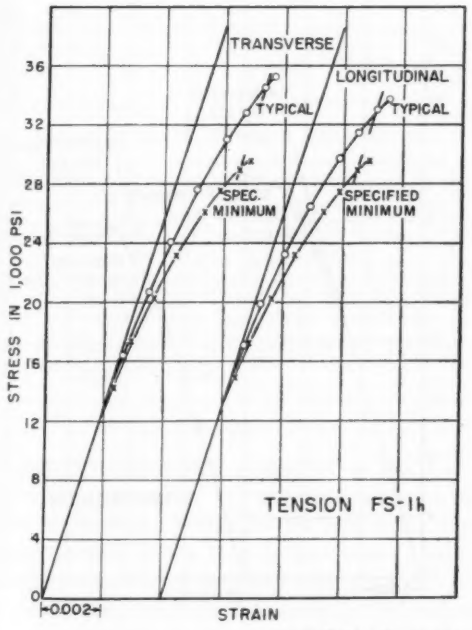

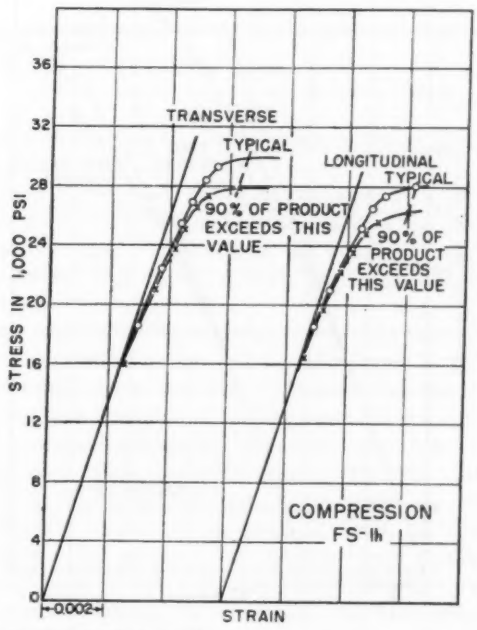

FIG. 1 (*left*). Typical tensile curves; Dowmetal FS-1h sheet.
FIG. 2 (*right*). Typical compressive curves; Dowmetal FS-1h sheet.

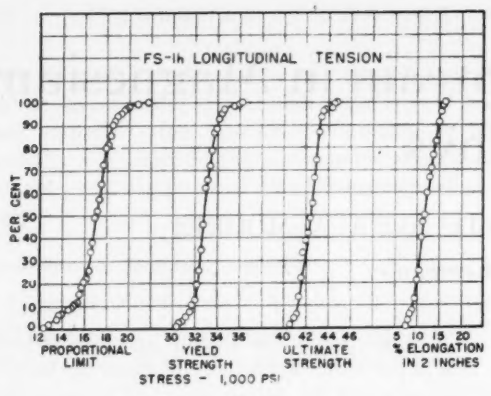

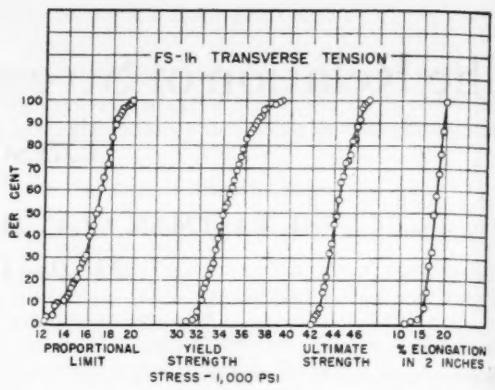

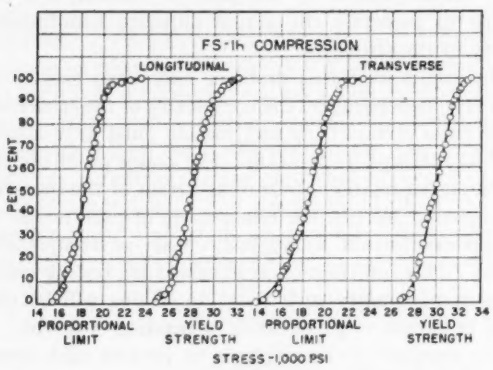

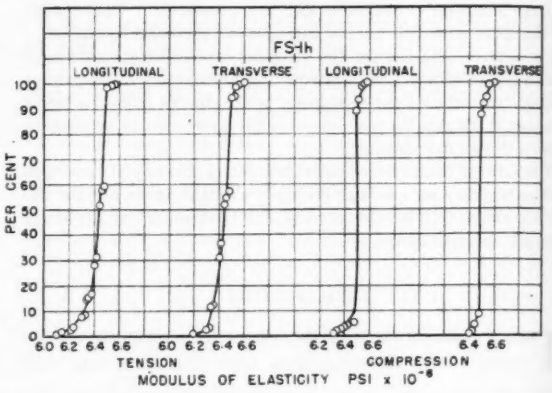

FIG. 3 (*upper left*). Distribution of tensile proportional limit, tensile yield, tensile strength, and per cent elongation for Dowmetal FS-1h sheet in the longitudinal direction.

FIG. 4 (*upper right*). Distribution of tensile proportional limit, tensile yield, tensile strength, and per cent elongation for Dowmetal FS-1h sheet in the transverse direction.

FIG. 5 (*lower left*). Distribution of compressive proportional limit, and compressive yield of Dowmetal FS-1h sheet in the longitudinal and transverse directions.

FIG. 6 (*lower right*). Distribution of modulus of elasticity of Dowmetal FS-1h sheet.

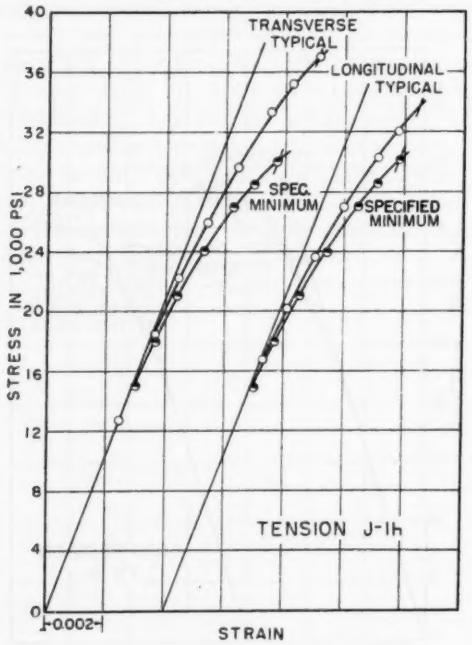

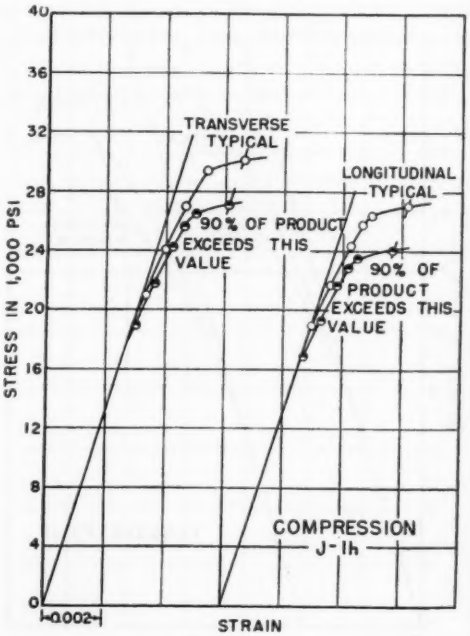

FIG. 7 (*left*). Typical tensile curves; Dowmetal J-1h sheet.
FIG. 8 (*right*). Typical compressive curves; Dowmetal J-1h sheet.

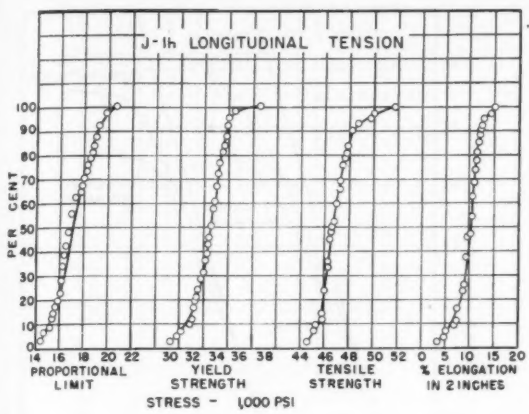

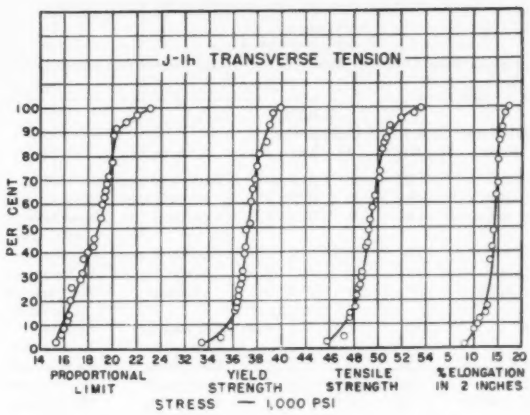

FIG. 9 (*left*). Distribution of tensile proportional limit, tensile yield, tensile strength, and per cent elongation for Dowmetal J-1h sheet in the longitudinal direction.

FIG. 10 (*right*). Distribution of tensile proportional limit, tensile yield, tensile strength, and per cent elongation for Dowmetal J-1h sheet in the transverse direction.

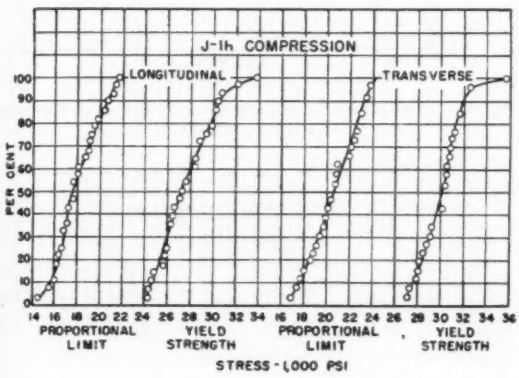

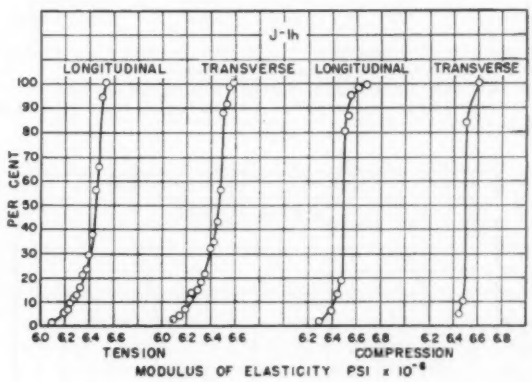

FIG. 11 (*left*). Distribution of compressive proportional limit, and compressive yield of Dowmetal J-1h sheet in the longitudinal and transverse directions.

FIG. 12 (*right*). Distribution of modulus of elasticity of Dowmetal J-1h sheet.

COMMERCIAL MAGNESIUM BASE ALLOYS

Magnesium alloys are sold in the form of sand castings, permanent mold castings, die castings, extrusions, forgings, and sheet. Table 1 lists the alloys for which data are presented in this paper. This list includes nearly all of the commercially available materials. For further information, the reader may refer to the various publications of the manufacturers, the Services, and the technical societies.

TESTING METHODS

In general, stress-strain curves of metals are distinguished by two parts: (1) Elastic—stress is a linear function of strain. (2) Plastic—the rate of increase of stress with strain is less than in the elastic portion in continuously decreasing measure until rupture occurs. The ratio of stress to strain in the first part of the curve is known as the modulus of elasticity. Its importance in design is well known. The form of the curve for a short distance into the plastic range is also of high importance.

Beyond this point the exact relationship is of less importance. The ultimate strength and the energy to rupture give a measure of the possibility of complete failure of a structure when the design limits are exceeded.

The form of the stress-strain curve may be defined by the stresses at which various percentages of plastic deformation have occurred.[1] Usually, the stress at 0.01 per cent deviation from the modulus line is defined as the proportional limit. The stress at 0.2 per cent deviation is called the yield strength. The three values required to define the stress-strain curve are then: modulus of elasticity, proportional limit, and yield strength. In addition, in tension tests, ultimate strength and strain over some specified gage length after rupture are usually measured. The last quantity is referred to as percentage of elongation and is usually measured over a gage length of 2 in.

TABLE 1

Magnesium Base Alloys for Which Stress-Strain Curves Are Given in This Paper

Dowmetal Alloy	A.S.T.M. No.	Nominal Composition, % Al	Mn	Zn	Use	Condition
H-AC	4	6	0.2	3	Sand and permanent mold castings	As-cast
H-HT	4	6	0.2	3		Heat-treated
H-HTA	4	6	0.2	3		Heat-treated and aged
C-AC	17	9	0.2	2	Sand and permanent mold castings	As-cast
C-HT	17	9	0.2	2		Heat-treated
C-HTA	17	9	0.2	2		Heat-treated and aged
R	13	9	0.2	0.7	Die castings	As-cast
M	11	...	1.5	...	Extrusions	As-extruded
FS-1	18X	3	0.3	1	Extrusions	As-extruded
J-1	8X	6	0.2	1	Extrusions	As-extruded
O-1 HTA	9X	8.5	0.2	0.5	Extrusions	Heat-treated and aged
J-1	8X	6	0.2	1	Forgings	As-forged
O-1A	9X	8.5	0.2	0.5	Forgings	Aged
Ma	13	...	1.5	...	Sheet	Annealed
Mh	13	...	1.5	...	Sheet	Hard-rolled
FS-1a	18X	3	0.3	1	Sheet	Annealed
FS-1h	18X	3	0.3	1	Sheet	Hard-rolled
J-1a	8X	6	0.2	1	Sheet	Annealed
J-1h	8X	6	0.2	1	Sheet	Hard-rolled

NOTES: (1) The designation -1, or X, refers to alloys of controlled impurity content, with improved resistance to corrosion.

(2) Curves for the casting alloys are on separately cast test bars.

(3) Curves for forgings are on bars cut from forgings in the direction of flow.

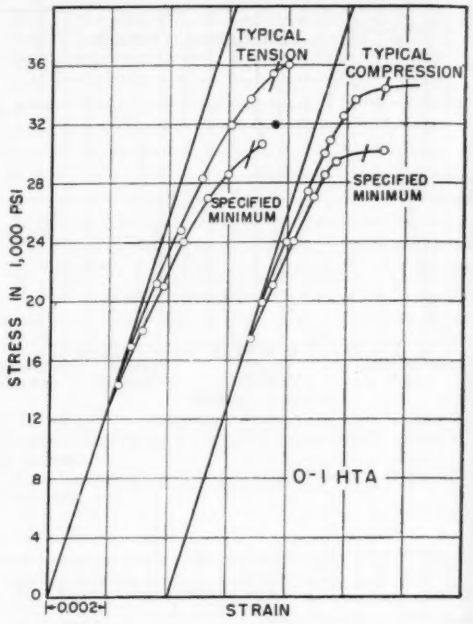

FIG. 13. Typical tensile and compressive curves of Dowmetal O-1 HTA extrusions.

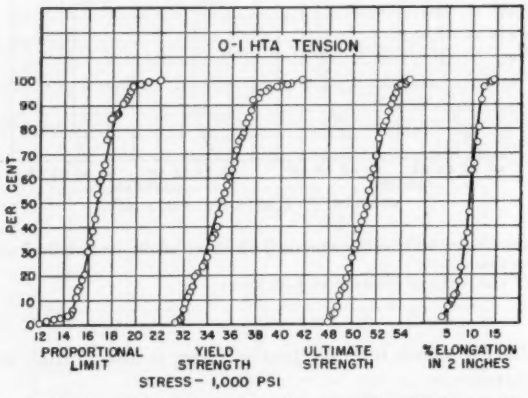

FIG. 14 (*left*). Distribution of tensile proportional limit, tensile yield, tensile strength, and per cent elongation of Dowmetal O-1 HTA extrusions.

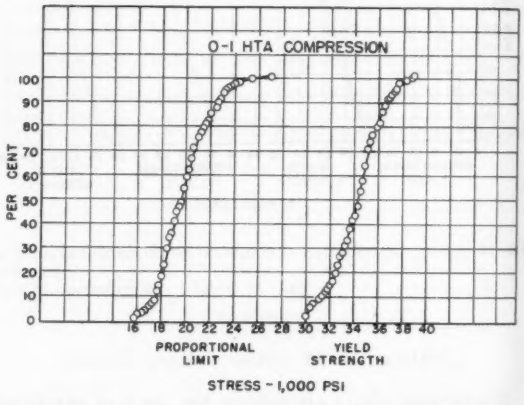

FIG. 15 (*right*). Distribution of compressive proportional limit and compressive yield of Dowmetal O-1 HTA extrusions.

The accurate determination of a stress-strain curve calls for observance of careful experimental technique. The modulus of elasticity, particularly, is sensitive to various factors in the test.[5, 6, 7] On none of the stress-strain curves presented here is the modulus considered to be exact but is rather what may be expected from careful testing. The errors found in normal testing account for the variation in the moduli obtained and are not due to inherent differences in the material.

The tensile tests were made on a Riehle universal testing machine with an accuracy of 0.5 per cent.[3] Strain was measured over a 1-in. gage length by two Tuckerman optical strain gages on opposite sides of the specimen. The Tuckerman gages were Class A gages

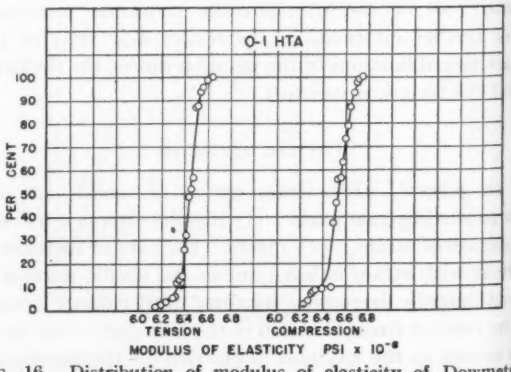

FIG. 16. Distribution of modulus of elasticity of Dowmetal O-1 HTA extrusions.

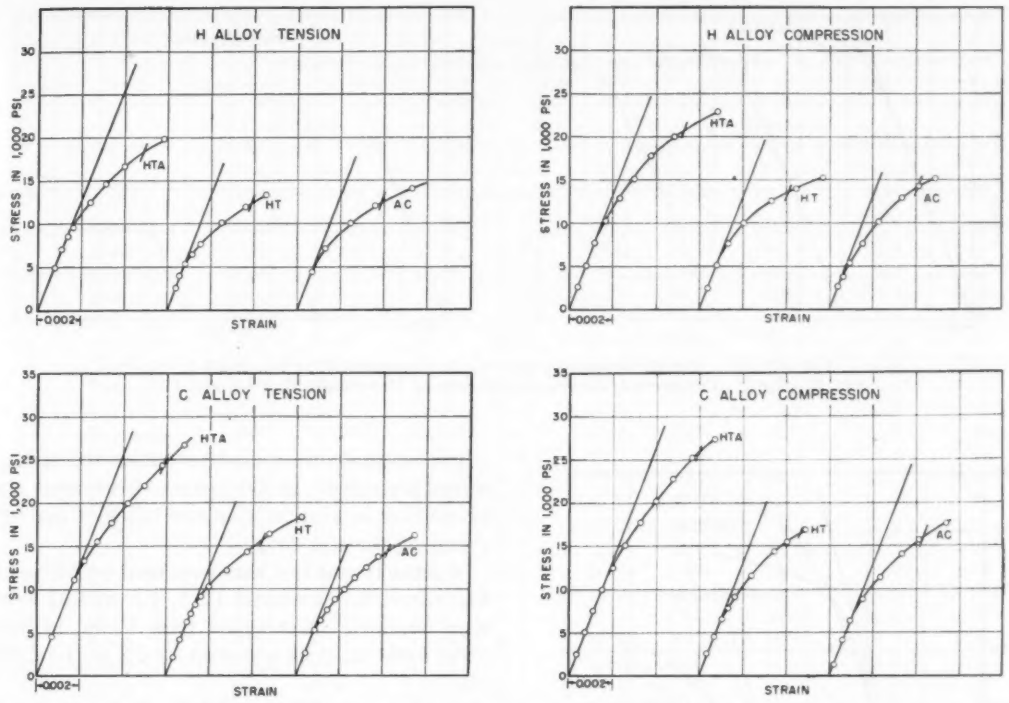

FIG. 17 (*upper left*). Tensile curves of Dowmetal H in the as-cast, heat-treated, and heat-treated and aged condition.
FIG. 18 (*upper right*). Compressive curves of Dowmetal H in the as-cast, heat-treated, and heat-treated and aged condition.
FIG. 19 (*lower left*). Tensile curves of Dowmetal C in the as-cast, heat-treated, and heat-treated and aged condition.
FIG. 20 (*lower right*). Compressive curves of Dowmetal C in the as-cast, heat-treated, and heat-treated and aged condition.

as defined in an A.S.T.M. Proposed Method of Verification and Classification of Strainometers.[4, 8] No calibration factors were used on either the testing machine or extensometers. No attempt was made to control temperature during testing, but normal room temperature variation during the course of a test was ±2°F.

The flat tensile specimens from sheet and extruded sections were milled with a standard 0.500-in. wide reduced section if possible, otherwise a 0.250-in. wide reduced section was used.[2] Templin grips were used to secure uniform gripping and special care was taken to obtain alignment.

The round tensile test bars were 0.505-in. diameter reduced section with threaded shoulders. The load was applied through shackles fitted with spherical seats.

The compression specimens used were either cylinders with the length three times the diameter or single-sheet specimens 0.750 in. wide by 2.660 in. long. The single-sheet specimens were supported in a Montgomery-Templin jig with roller supporting surfaces. All strain was measured with Tuckerman strain gages.

On alloys that have a low proportional limit, the testing technique must be good or even the yield strength will be in error. If a good initial modulus line is not obtained, a tangent modulus is used which may cause the yield strength to be in error by several thousand pounds per square inch if the stress-strain curve gradually changes slope until the yield strength is reached.

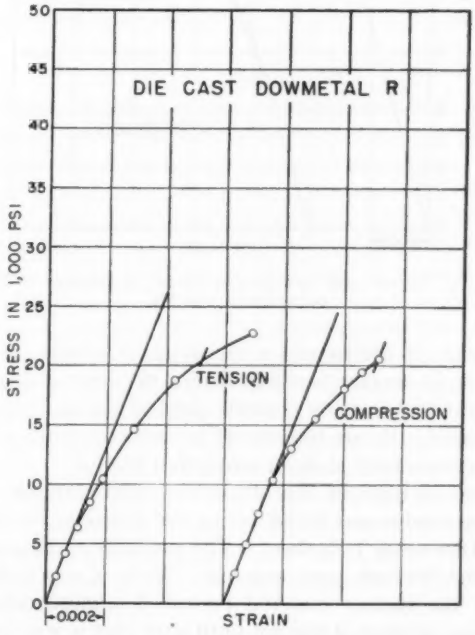

FIG. 21. Tensile and compressive curves of die cast Dowmetal R.

Such errors would be easy to obtain with the usual type of wedge grips used in conjunction with many extensometers that cannot average bending strain. While no

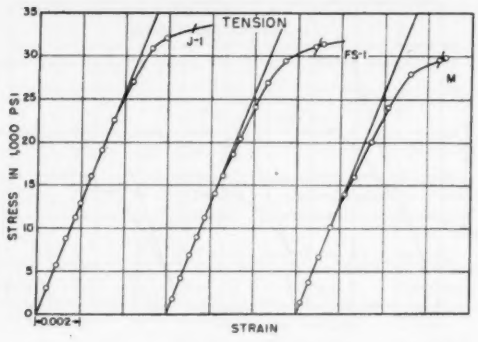

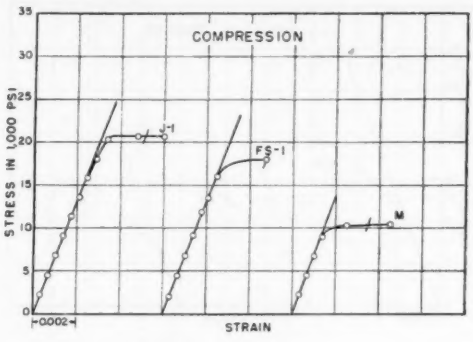

FIG. 22 (*left*). Tensile curves of extrusions of Dowmetals M, FS-1, and J-1.
FIG. 23 (*right*). Compressive curves of extrusions of Dowmetals M, FS-1, and J-1.

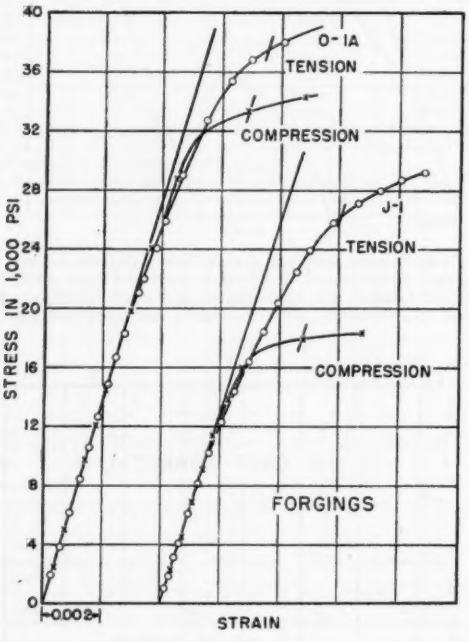

FIG. 24. Tensile and compressive curves of forgings of Dowmetals O-1A and J-1.

mechanical extensometer or group of extensometers will truly average bending strains, the error is small if separate readings on opposite sides of the test bar are averaged. Errors introduced by nonaxial loading account for a large share of erratic test results.

One example of how an unlooked-for variable can cause trouble was found during the course of the tests on Dowmetal J-1h sheet. The modulus as measured on the thinnest gages was low. While it was realized that the thinner material presented a more difficult testing problem, it was not until later that it was found that one of the back-lash eliminators was sticking so that a few pounds pressure was required to bring the cross head in contact with the loading side of the screw. This movement was sufficient to cause misalignment with a resulting bending moment.

Two methods were used to obtain the stress-strain curves presented. In most cases, curves were obtained by running several tests on one batch of material and averaging the test data.

Separately cast test bars were used for all cast alloys. The curves on Dowmetal FS-1, J-1, and M extrusions were obtained on extruded bars $^3/_4$ in. in diameter. Sheet 0.064-in. thick was used for FS-1a, J-1a, Ma, and Mh.

On Dowmetal FS-1h and J-1h sheet and on extruded Dowmetal O-1 HTA, data for typical curves were obtained from tests on a number of batches processed over a period of time. The typical stress-strain curves, as well as the ones for the specified minimum, were constructed by averaging the stress at a series of offsets between the proportional limit and the yield strength on all the measured stress-strain curves and then by using the same type of curve fitted to the selected yield strength value.[10]

The distribution curves on the properties measured are given for Dowmetal FS-1h, J-1h, and O-1 HTA. The modulus values for 0.025-in. thick J-1h are omitted from the distribution curve for both longitudinal and transverse directions for the reason given above. The data on J-1h were obtained from 41 batches of metal consisting of about an equal number of batches from 0.025-, 0.040-, 0.064-, 0.125-, and 0.250-in. thick sheet. Duplicate specimens were used on all tests. The FS-1h data were obtained from 61 batches of sheet in the same range of gages as used for the J-1h. The O-1 HTA extrusions were obtained from 48 batches of various angles, channels, I-beams, and other shapes.

RESULTS

The pertinent values obtained from the various stress-strain curves are listed in Table 2. The curves themselves are shown in the various figures. Figs. 3–6, 9–12, and 14–16 show the distribution curves for the properties measured in the cases of FS-1h, J-1h, and O-1 HTA, where the results of a considerable number of tests are available.

TABLE 2
Properties of the Materials from the Stress-Strain Curves

Dowmetal Alloy	Form	Modulus, 1,000,000 Lbs. per Sq.In. Tension	Modulus, 1,000,000 Lbs. per Sq.In. Compression	Proportional Limit, 1,000 Lbs. per Sq.In. Tension	Proportional Limit, 1,000 Lbs. per Sq.In. Compression	Yield Strength, 1,000 Lbs. per Sq.In. Tension	Yield Strength, 1,000 Lbs. per Sq.In. Compression	Tensile Strength, 1,000 Lbs. per Sq.In.	Per Cent Elongation	CYS / TYS	CPL / TPL
H-AC	Sand Cast	6.20	6.25	6.5	6.0	13.0	14.0	32.0	7.1	1.08	0.92
H-HT	Sand Cast	6.44	6.30	5.7	7.0	13.0	13.5	36.0	12.5	1.04	1.23
H-HTA	Sand Cast	6.47	6.40	10.0	9.5	18.5	21.0	42.0	9.0	1.13	0.95
C-AC	Sand Cast	6.20	6.55	6.5	6.0	15.0	16.2	26.0	3.5	1.08	0.92
C-HT	Sand Cast	6.44	6.20	8.7	6.0	16.0	16.2	42.0	8.5	1.01	0.69
C-HTA	Sand Cast	6.46	6.55	12.5	15.0	24.0	25.5	44.0	2.0	1.04	1.20
R	Die Cast	6.30	6.20	9.9	8.0	21.0	20.5	35.0	4.0	0.97	0.81
M	Extruded	6.50	6.65	14.8	9.2	29.3	10.2	39.1	6.0	0.35	0.62
FS-1	Extruded	6.42	6.61	18.3	16.2	31.0	17.9	41.4	12.0	0.58	0.89
J-1	Extruded	6.35	6.51	24.2	18.1	33.3	20.7	45.5	14.5	0.62	0.75
O-1 HTA*	Extruded	6.45	6.55	16.9	19.9	35.4	34.3	51.3	9.6	0.97	1.18
J-1	Forged	6.40	6.55	13.1	13.5	28.9	17.7	43.9	13.7	0.61	1.03
O-1A	Forged	6.47	6.66	21.4	25.0	37.8	33.8	52.7	4.0	0.89	1.17
Ma-L	Sheet	6.49	6.53	4.5	6.0	16.0	14.5	31.0	17.5	0.87	1.33
Ma-T	Sheet	6.50	6.43	4.6	6.5	15.1	13.0	29.0	14.5	0.86	1.41
Mh-L	Sheet	6.40	6.60	10.6	10.0	26.5	21.5	37.0	7.8	0.78	0.94
Mh-T	Sheet	6.45	6.42	9.2	9.6	24.8	19.5	35.0	15.2	0.79	1.04
FS-1a-L	Sheet	6.47	6.30	10.2	10.0	21.5	17.0	36.0	21.0	0.79	0.98
FS-1a-T	Sheet	6.27	6.40	11.0	14.2	23.0	18.0	36.0	18.0	0.78	0.98
FS-1h*-L	Sheet	6.44	6.50	17.0	18.4	33.0	28.0	42.6	12.5	0.85	1.08
FS-1h*-T	Sheet	6.45	6.50	16.4	18.5	34.5	29.9	44.3	17.8	0.87	1.13
J-1a-L	Sheet	6.21	6.50	10.4	13.0	24.0	14.0	42.5	12.0	0.58	1.25
J-1a-T	Sheet	6.3	6.50	12.8	13.2	25.6	14.0	43.8	17.0	0.55	1.03
J-1h*-L	Sheet	6.39	6.50	17.3	18.1	33.6	27.8	46.9	9.9	0.83	1.05
J-1h*-T	Sheet	6.37	6.51	18.6	20.7	37.6	30.2	49.5	13.9	0.81	1.11

* Typical curves.

NOTE: Suffixes L and T denote longitudinal and transverse directions, respectively, in sheet.

DISCUSSION

Particular attention is called to the relative constancy of the modulus of elasticity of the material as manufactured and shipped. The possible effect of subsequent fabrication and service on the modulus is discussed elsewhere.[11] It has been claimed that there is a considerable variation in the modulus of magnesium alloys.[9] While some of this variation may be due to stressing after shipment,[11] it should be recognized that the difficulty of making precise measurements of the modulus of any material can create quite a variation.

The ratio of compressive yield strength to tensile yield strength averages slightly more than unity for castings. In certain wrought metal alloys the ratio may be as low as 0.4–0.6, particularly for the low-strength extrusion alloys. High-strength sheet and extrusions have ratios ranging from 0.8 up to unity. Low ratios are considered to be due to the combined action of two factors: (1) the preferential orientation of the individual grains with respect to the direction in which the material is usually tested and (2) the lower yield strength in compression under these conditions of the grains. Various metallurgic conditions can decrease the effect of the second factor so that, despite the preferred orientation, the compression properties approach and can equal the tension properties.

In actual shape, the stress-strain curves of cast alloys in both tension and compression are quite similar. This would be expected because of the random orientation of the grains generally found in castings. In wrought metal the compression curves tend to break away faster from the modulus line than do the tension curves. In some cases it is quite feasible to determine the yield strength in compression by the "drop of the beam" method because of this fast break.

The ratio of proportional limit in compression to that in tension behaves somewhat similarly to the ratio of yield strengths. The average ratio for castings appears to be close to unity. For the lower strength extrusions it is considerably less than unity. For the higher strength extrusions and in sheet, it approaches or exceeds unity.

SUMMARY

(1) Typical stress-strain curves have been presented for the highest strength commercial wrought magnesium alloys.

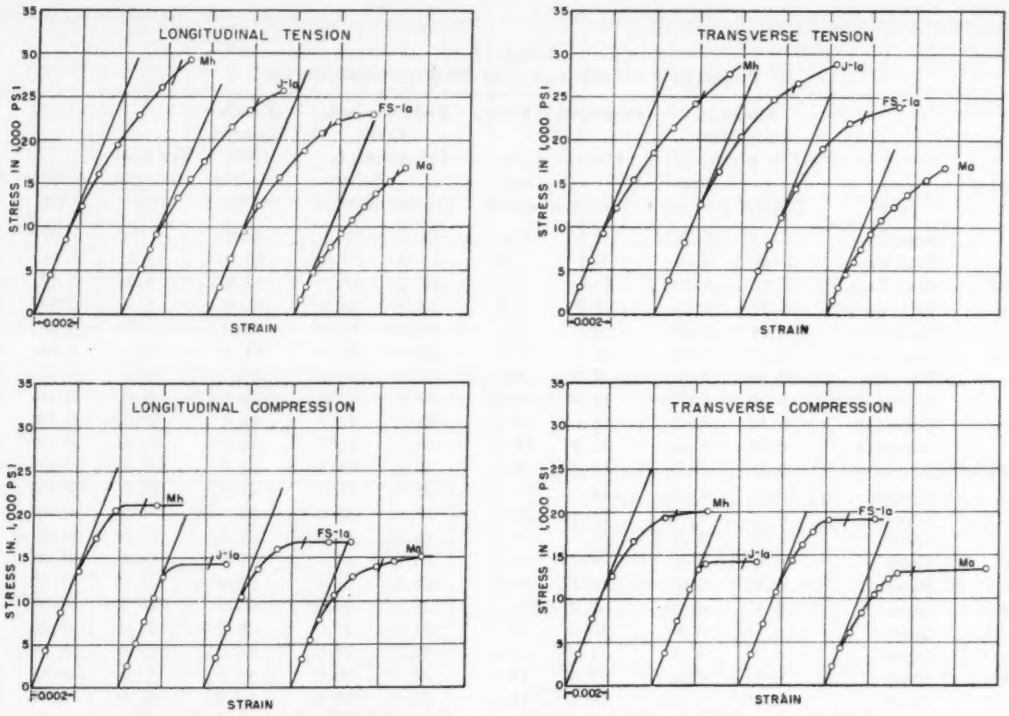

FIG. 25 (*upper left*). Longitudinal etnsile curves of Dowmetals Mh, J-1a, FS-1a, and Ma sheet.
FIG. 26 (*upper right*). Transverse tensile curves of Dowmetals Mh, J-1a, FS-1a, and Ma sheet.
FIG. 27 (*lower left*). Longitudinal compressive curves of Dowmetals Mh, J-1a, FS-1a, and Ma sheet.
FIG. 28 (*lower right*). Transverse compressive curves of Dowmetals Mh, J-1a, FS-1a, and Ma sheet.

(2) Individual curves from a few tests on material of typical properties have been presented on other commercial magnesium alloys.

(3) The modulus of elasticity has been found to be substantially constant in compression and tension. The best value to use in design is 6,500,000 lbs. per sq.in.

REFERENCES

[1] A.S.T.M. Designation: E-36, *Standard Definitions of Terms Relating to Methods of Testing.*

[2] A.S.T.M. Designation: E8-42, *Standard Methods of Tension Testing of Metallic Materials.*

[3] A.S.T.M. Designation: E4-36, *Verification of Testing Machines.*

[4] *Proposed Method of Verification and Classification of Strainometers,* A.S.T.M. Bulletin, August, 1942.

[5] Templin, R. L., *The Determination and Significance of the Proportional Limit in the Testing of Metals,* Proceedings, A.S.T.M., Vol. 29, p. 523, 1929.

[6] Templin, R. L., *Some Factors Affecting Strain Measurements in Tests of Metals,* Proceedings, A.S.T.M., Vol. 34, Part II, p. 182, 1934.

[7] Smith, C. S., *Proportional Limit Tests of Copper Alloys,* Proceedings, A.S.T.M., Vol. 40, p. 864, 1940.

[8] Wilson, Bruce L., *Characteristics of the Tuckerman Strain Gage,* Proceedings, A.S.T.M., Vol. 44, 1944.

[9] Britton, R. O., *Notes on Magnesium Alloys in Design,* Automotive Industries, Vol. 90, p. 26, June 15, 1944.

[10] Templin, Hartman, and Paul, *Typical Stress-Strain Curves of Aluminum Alloys,* Technical Paper No. 6, Aluminum Company of America.

[11] Rappleyea, F. A., Perry, R. E., and Ansel, G., *Influence of Pre-Stressing and Cyclic Stressing on Stress-Strain Characteristics of Magnesium Alloys,* Preprint, Thirteenth Annual Meeting, I.A.S., 1945.

Design and Application of High-Pressure Coefficient Axial-Flow Fans

J. G. SAWYER*

Buffalo Turbine Corporation

Introduction

Two fundamental characteristics have long been associated with the axial-flow fan: (1) its inability to develop high pressure; (2) its sharp loss of pressure with increasing flow. The popular concept has been that it is necessary to go to the radial-flow fan to obtain high pressures. However, in the past few years, great advancements in the art of axial-flow fan design have entirely changed this concept. We now have available design methods which have made possible axial-flow fans with pressure characteristics superior to all other types of fans.

The Conventional Axial-Flow Fan

Fan pressure characteristics may best be discussed in terms of the following pressure coefficient:

$$\psi = \Delta P/(\rho/2)U_{tip}^2 \qquad (1)$$

where

ψ = pressure coefficient
ΔP = fan pressure rise
ρ = air density
U_{tip} = fan tip peripheral speed

The conventional axial-flow fan utilizes runner blades made up of conventional airfoil sections. The design calculations assume the characteristics of the airfoil sections to be substantially the same on the fan runner as in an infinite air stream. This design method makes use of the theory developed by Ackeret[1] and is outlined by Keller.[2] The method arrives at the expression for the fan pressure rise in terms of the airfoil lift coefficient, C_L:

$$\Delta P = C_L w_\infty l \rho \omega z/4\pi \qquad (2)$$

where

w_∞ = mean relative velocity past the runner blade section
l = chord of blade section
ω = angular velocity, rad. per sec.
z = number of runner blades

This method yields good results up to chord/pitch ratios of the order of unity, pitch being defined as the peripheral distance between adjacent blades. Pressure coefficients as high as $\psi = 0.80$ have been obtained in this manner. Efforts to obtain higher pressure coefficients by this method have led to the use of chord/pitch ratios substantially greater than unity, but these fans have invariably failed. The cause of these failures may be found in an investigation of the basic flow problem.

The Basic Flow Problem

Neglecting frictional losses, Bernoulli's equation,

$$\Delta P = (\rho/2)(W_1^2 - W_2^2) \qquad (3)$$

is valid between any two points of a given streamline within an axial-flow fan passage, W_1 and W_2 being the upstream and downstream velocities relative to the passageway. Pressure is developed by so controlling the flow direction as to make W_2 less than W_1. In other words, the passageways between adjacent fan blades are simple curved diffusers. This may be seen in Fig. 1. By so investigating each stage of the fan, the total pressure rise of the fan may be determined.

The fan pressure rise may also be determined from the simplified form of Euler's turbine equation:

$$\Delta P_{fan} = \rho u \Delta C_u \qquad (4)$$

where u is the runner peripheral speed, and ΔC_u is the change in rotational component of the fluid velocity It is apparent, by inspection of Eq. (4), that for given values of ρ and u, the only means of increasing ΔP is to increase ΔC_u. From Fig. 2 it may be seen that to increase ΔC_u the angle ϑ through which the air is turned within the runner must be increased. Thus, higher pressures call for highly curved blades. This is the

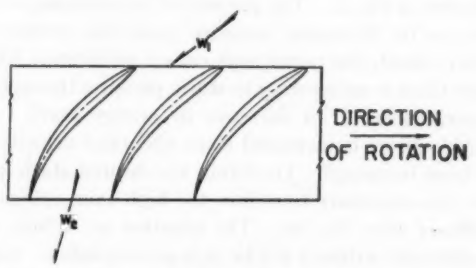

Fig. 1. Runner velocity vectors.

Received January 4, 1945. To have been presented at the I.A.S. Thirteenth Annual Meeting, which was canceled to cooperate with a Government appeal (January, 1945) to refrain from holding conventions and meetings.

* Vice-President and Chief Engineer.

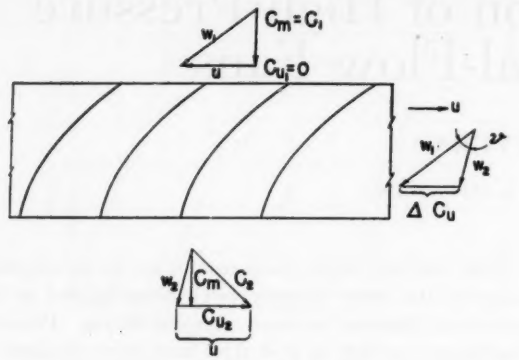

FIG. 2. Fan vectors.

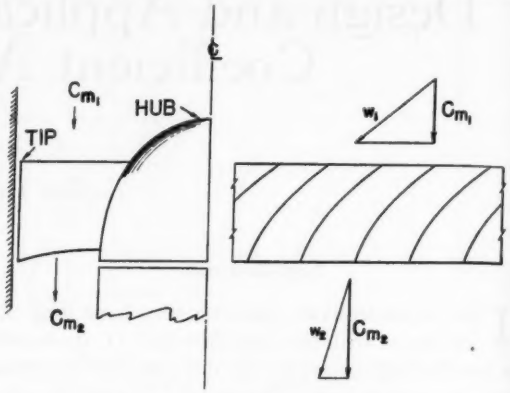

FIG. 3. Constant pressure fan.

reason the flat type of airfoil blades have failed to develop high pressures.

THE HIGH-PRESSURE COEFFICIENT FAN

The design approach to the high-pressure coefficient fan has been to abandon the conventional airfoil and employ blade sections developed specifically for the design problems. The net result is the use of highly curved, closely spaced blades that guide the fluid in the directions arrived at by a vector analysis. This method is relatively simple and is exactly the method used in turbine blade design.

The Schicht Fan

Apparently this concept of axial-flow fan design is not new but is revived, having been employed some years ago. The so-called Schicht fan was designed upon this principle in Germany and is described in an N.A.C.A. paper by Sörensen.[3] The paper, which is a discussion of the constant-pressure principle, refers to this method of design as the stream filament theory but does not speak of it as a new theory. Pictures are shown of fans designed on the stream filament theory, with chord/pitch ratios considerably greater than unity.

This constant-pressure principle is of some interest. It proposes, by reducing the fan annular area toward the runner outlet, to increase the axial velocity, and thus the relative velocity w, to the point where w is constant throughout the runner. This is done by increasing the hub diameter toward the runner discharge as shown in Fig. 3. The purpose of maintaining w constant is to eliminate pressure gradients within the runner, which the paper says causes prohibitive losses. While there is no increase in static pressure through the runner, there is an increase in energy level. The kinetic energy is increased since the axial velocity C_M has been increased. To obtain the desired static pressure, it is necessary to reduce the high axial velocity in a diffuser after the fan. The question is: Where may the diffusion within a fan be best accomplished—within the runner or after the runner in a straight diffuser?

The Wattendorf Fan Theory

Also of some interest is the fan work done by Dr. Frank Wattendorf. He points out in his patent[4] that the airfoil is unsuitable for high pressures because of its flatness. His design method is to bend the conventional airfoil so as to direct the fluid in the desired direction.

Some of his designs have employed chord/pitch ratios substantially greater than unity and have developed pressure coefficients also substantially greater than unity.

Aircraft Application

A great deal of research on the high-pressure coefficient axial-flow fan has been done in the aircraft industry in the past 3 years. The first designs were influenced by the Sörensen paper and the generally pessimistic point of view toward the development of high static pressures. The results of this work were sufficient to encourage the pursuit of further development programs.

Engine cooling fans were built using sheet-metal blades. These fans produced pressure coefficients considerably greater than unity, but the performance fell off badly at flow coefficients away from the design point. However, such fans might be used in applications where the range need not be great. Fans with theoretically calculated blade sections were also investigated. These blades have the appearance of highly cambered airfoils. Pressure coefficients as high as three were obtained with good efficiency over a comparatively large range of flow coefficient. Good performance was obtained without resorting to the Schicht principle, thus disproving the principle. From the foregoing, it may be seen that three types of fan are possible: (1) a Schicht fan in which the energy increase is 100 per cent kinetic energy; (2) a partially Schichted fan in which the energy increase is part kinetic energy and part pressure energy; (3) a 100 per cent static pressure fan in which no increase in kinetic energy occurs.

Theory of Blade Development

In designing a high-pressure fan, it is necessary to space the blades closely enough so that the flow direction is substantially parallel to the blade camber line. Then the relative velocity w is fixed by the interblade passage width. This passage width is defined by the local camber line slope and corresponding blade thickness according to the equation:

$$a = \text{pitch} \cos \theta - t \qquad (5)$$

where

a = local passage width
pitch = blade peripheral spacing
t = local blade thickness
θ = local angle camber line makes with fan axis

Fig. 4 represents the variables pictorially.

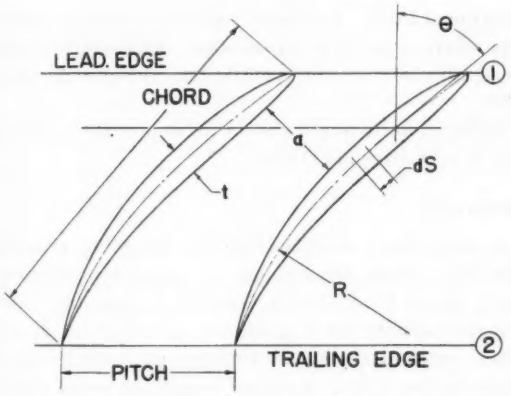

FIG. 4. Fan blade nomenclature.

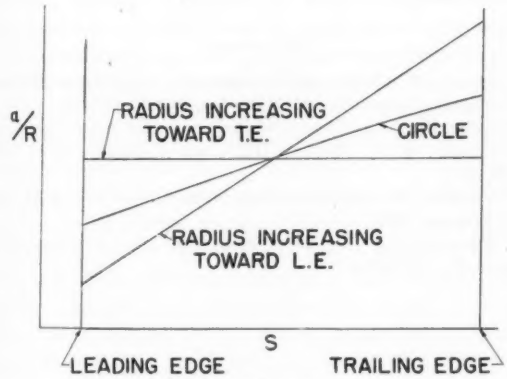

FIG. 5. Variation of a/R.

As in duct elbow design, the basic variable is the ratio of the channel width to the radius of curvature, a/R. This ratio may be controlled by the choice of pitch and also by varying the local radius along the camber line. A constant a/R may be obtained by properly reducing R toward the leading edge. However, the optimum variation of a/R with respect to distance along the camber line can be determined by experiment only. Fig. 5 represents typical variations of a/R along the blade. Similar to straight diffusers, the relationship of channel width to distance along the channel is important. The channel width variation may be controlled by the blade thickness distribution t. Fig. 6 represents a blade with no thickness and a blade with thickness distribution such that a linear variation of channel width takes place, the difference in the two curves representing the thickness t.

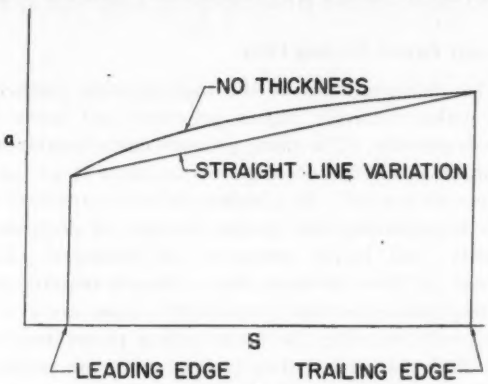

FIG. 6. Blade thickness distribution.

Lattice Wind Tunnel Tests

Properly executed, lattice tests are invaluable to the fan designer. However, the test setup and procedure must be developed to such degree that good correlation of lattice test data and fan test data is obtained. In this way, data are obtainable much more quickly and less expensively than by constructing and testing complete fans.

Pressure-Flow Characteristics

Conventional fans show a decrease in pressure with increased flow. However, high-pressure coefficient fans have rising pressure curves with increasing flow. Fig. 7 represents pressure-flow characteristics for several values of pressure coefficient. The importance of the rising pressure curve will be discussed in the next section.

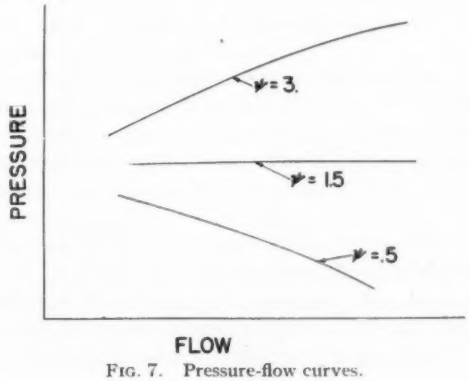

FIG. 7. Pressure-flow curves.

Application of the High-Pressure Coefficient Fan

Aircraft Engine Cooling Fans

The characteristics of the high-pressure coefficient fan make relatively higher pressures and lower fan speeds possible. The rising pressure curve is extremely desirable in aircraft cooling systems, since it acts as an automatic control. As a higher altitude is reached, the flow requirements are greater because of decrease in density, and higher pressures are produced. Conversely, at lower altitudes, less air flow is required with corresponding decrease in pressure. Fans are also effective in reducing the total cooling power required. Fig. 8 shows total cooling power versus fan power at sea level and at altitude. Note that the optimum value of fan power increases as altitude increases.

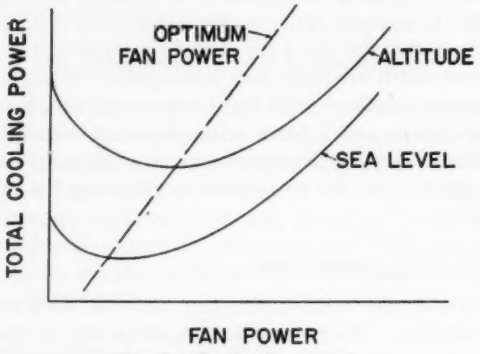

Fig. 8. Cooling fan curves.

The Schicht fan finds an application on pusher-type airplane (see Fig. 9). The air is discharged from the fan directly to the cooling system exit where relatively high desirable velocities are maintained. The conversion to static head, which is unnecessary in this case, would require both space and losses.

General Utility Fan

The fact that greater pressures may be secured with no increase in speed gives the high-pressure coefficient fan a distinct advantage over conventional types. There is no increase in the stress problem because of centrifugal loads. Increased capacity is also an advantage where space is at a premium. An example of such an application is the ventilating systems in naval craft.

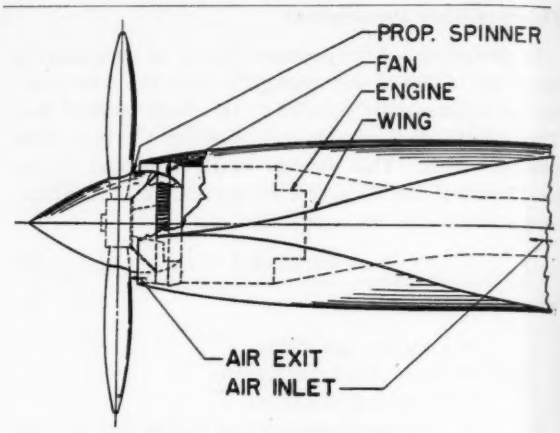

Fig. 9. Pusher-type installation.

Reduced noise might also be an important consideration in certain applications.

Compressor

A compressor designed on the foregoing principles also has certain advantages. A greater pressure rise for a given blade Mach Number is possible. Also, greater capacity for a given size is important in some cases, particularly in gas turbine, jet propulsion, and supercharger units. Reduced weight, of course, results from reduced size and is of great importance in aircraft installations.

References

[1] Ackeret, J., *Theorie und Berechnung von Tragflügelprofilen auf vereinfachter Grundlage*, AMIV.-Verlag, E.T.H., Zürich.

[2] Keller, Curt, *The Theory and Performance of Axial-Flow Fans*, 1st Edition, p. 3; McGraw-Hill Book Company, Inc., New York, 1937.

[3] Sörensen, E., *Constant Pressure Blower*, N.A.C.A. T.M. No. 927, January, 1940.

[4] Wattendorf, F. L., *Axial Flow Type Fan or Pump*, U.S. Patent No. 2,208,615.

The Buckling of Sandwich-Type Panels

N. J. HOFF* AND S. E. MAUTNER†

Polytechnic Institute of Brooklyn and *Skydyne, Inc.*

SUMMARY

Fifty-one flat rectangular sandwich-type panels were tested in edgewise compression with the unloaded edges of the panels restrained by V-grooves. The sandwich consisted of papreg faces and a cellular cellulose acetate core. The thickness of the faces varied from 0.00675 to 0.02025 in.; the core, from 0.066 to 0.741 in.; the width of the panel, from 4 to 11 in. The length of the panel was always 10.5 in. The buckled shape consisted of a ripple of short wave length across the panel. It was either symmetric, the two faces bulging out symmetrically according to sine curves, or skew, the two faces deflecting in the same sense according to sine curves having a phase angle of 90°.

A strain energy theory of buckling is presented for both the symmetric and the skew cases, and the buckling load in the symmetric case is also calculated by integration of the differential equation. The agreement between the theoretic and the experimental buckling stress is reasonable, that between the predicted and actual buckled shape good. A simple formula is developed which permits a choice of the most suitable core material when the mechanical properties of the face material are given.

INTRODUCTION

A SANDWICH PANEL, as well as the skin of a sandwich-type monocoque wing or fuselage, consists of two external layers of thin high-strength material and a thick internal layer of lightweight material. The former are denoted as the faces, the latter is known as the core. The basic advantage of the sandwich skin is its great bending rigidity. Because of this, in sandwich construction there is little need for stringers and rings such as are used in aluminum-alloy monocoque structures to stabilize the skin and prevent its buckling.

Although sandwich construction attracted general attention only after it was disclosed that the de Havilland Mosquito was built according to the sandwich principle, the sandwich skin is not of recent origin. According to a communication from C. J. McCarthy, Vice-President of United Aircraft Corporation, the pontoons of the Sundstedt airplane built in this country in 1919, had a sandwich skin. In 1924 a German patent was granted to Th. von Kármán and P. Stock[1] for sandwich-type fuselages. In France in 1938, S. E. Mautner designed and built for the private owner a small cabin plane that had wings of sandwich construction. It is believed that in this country the first sandwich-type wing surface was an aileron manufactured by Skydyne in 1939.

Additional material concerning the history, advantages, and manufacture of sandwich-type airplanes, as well as the mechanical properties of the sandwich skin, were presented in an earlier paper by the authors.[2] In the present paper an account is given of the theoretic and experimental investigations undertaken to clarify the most important mechanical property of the skin—namely, its behavior in compression.

The authors acknowledge their indebtedness to Matthew G. Forte and Julius Korsak, Jr., for their careful work in testing, computations, and drawing the diagrams.

BUCKLING TESTS

The test series included 51 flat rectangular sandwich-type panels. The face material was papreg, a high-strength laminated paper plastic developed by the Forest Products Laboratory of Madison, Wis.,[3] and manufactured by the Consolidated Water Power and Paper Company of Wisconsin Rapids, Wis. The designation of the material is CPS-WP 23; it is molded under a pressure of 100 lbs. per sq.in. at a temperature of 315°F. The specific gravity is 1.38, which corresponds to a density of 86.4 lbs. per cu.ft. The core material was a compression-molded cellular cellulose acetate manufactured by E. I. du Pont de Nemours & Company in Arlington, N.J. It was used in a fully expanded state and had a specific gravity of 0.069, which corresponds to a density of 4.35 lbs. per cu.ft. The faces were cemented to the core with Plaskon 250, a urea-formaldehyde glue manufactured by Libby-Owens-Ford Glass Company of Toledo, Ohio, Plaskon Division. The test specimens were glued under normal workshop conditions by Skydyne, Inc., at 120°F. under what is known as "contact pressure" (corresponding to 4–5 lbs. per sq.in.).

The length of the specimens in the direction of the applied compressive force was 10.5 in. The width of the specimens perpendicular to the direction of the force varied from 4 to 11 in. The thickness of the face material varied from 0.00675 to 0.02025 in.; that of the core, from 0.066 to 0.741 in.

The specimens were tested at the Polytechnic Institute of Brooklyn in a Riehle Bros. lever-type testing machine of 30,000 lbs. load capacity. The accuracy of the load measurement was ±20 lbs. The test rig used in all the buckling tests is shown in Figs. 1 and 2. It

Received January 16, 1945. To have been presented at the I.A.S. Thirteenth Annual Meeting, which was canceled to cooperate with a Government appeal (January, 1945) to refrain from holding conventions and meetings.

* Associate Professor of Aeronautical Engineering, Polytechnic Institute of Brooklyn, and Consultant, Skydyne, Inc.

† Vice-President and Chief Engineer, Skydyne, Inc.

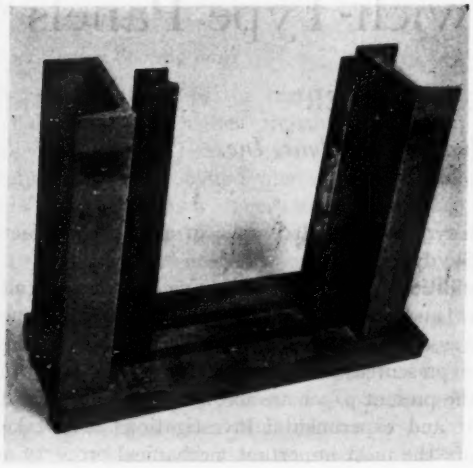

FIG. 1. Test rig.

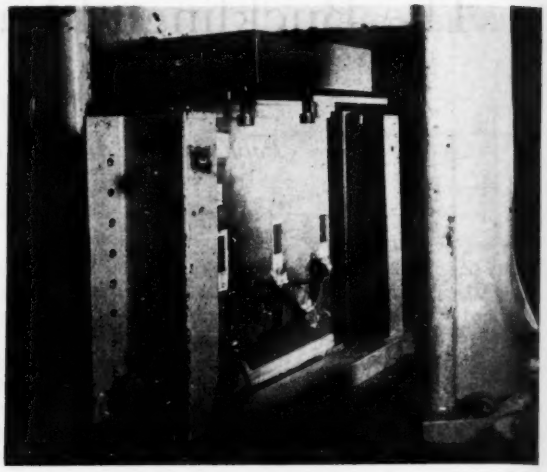

FIG. 3. Test set up in testing machine.

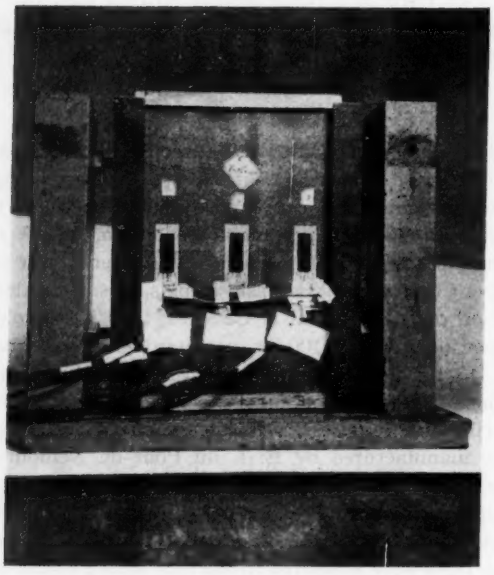

FIG. 2. Test rig with 7-in. wide test specimen.

consists of a base plate with two uprights that can be shifted so as to accommodate test specimens of different width. One V-groove bar is attached to each upright by two screws of adjustable length. This arrangement permits a fine adjustment of the position and the direction of the V-groove bars with the effect that the vertical edges of the test specimen can be uniformly supported even when they are not absolutely perpendicular to the edge resting on the base plate.

Fig. 3 shows the test rig in the testing machine. An adjusting plate is inserted between the test specimen and the movable head of the testing machine. With the aid of six screws the position of this plate can be adjusted so as to ensure contact along the entire width of the test specimen even when the upper edge of the specimen is not perfectly parallel to the lower edge. Wooden strips $^1/_2$ in. wide and $^1/_8$ in. thick were glued to the faces of each specimen at the upper and lower edge in order to prevent the crushing of these edges. Both the upper and lower edges were carefully sandpapered in a jig until no light could be seen between the specimen and base plate or adjusting plate, respectively.

The strain was measured in all five 11-in. wide specimens, in twelve of the 17 7-in. wide specimens, and in two of the 29 4-in. wide specimens. Measurements were made with the aid of Baldwin-Southwark SR-4 metalectric strain gages type A-1, which were attached to the faces with Duco household cement. Three pairs of gages were used with the 7- and 11-in. wide specimens and two pairs with the 4-in. wide specimens. The two gages of each pair were cemented to opposite faces of the specimen in the same position. The gages were connected with No. 19 insulated solid conductor copper wires to a Baldwin-Southwark SR-4 Portable Strain Indicator, which is capable of indicating strains of the order of 5×10^{-6}.

After each load increment the strain was measured at the six (or four) gage points. If the deviation from uniformity was considered excessive, the screws of the adjusting plate were adjusted and thus the plate was tilted and bent until a more satisfactory strain distribution was obtained. This procedure was not successful with the 11-in. wide specimens. In them the strain in the middle—that is, the average of the two middle gages on opposite faces—was about 40 per cent lower than the average in the specimen, and adjusting the screws did not correct the nonuniformity of the distribution. One of this group of specimens, No. 30, showed less deviation (20 per cent maximum) and carried a load materially higher than the average of the group.

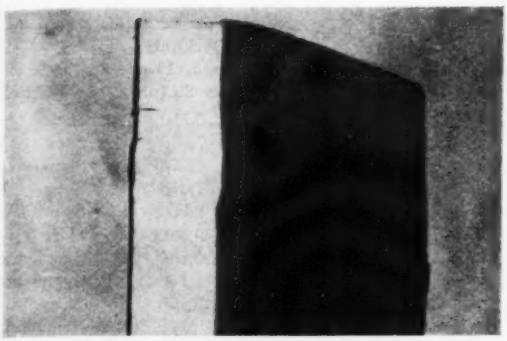

FIG. 4. Symmetric ripple 1. Core thickness 0.457 in., face thickness 0.01575 in.

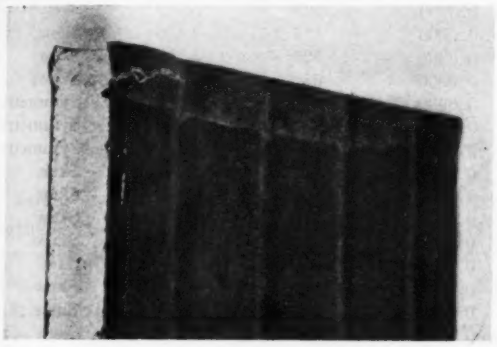

FIG. 5. Symmetric ripple 2. Core thickness 0.450 in., face thickness 0.00675 in.

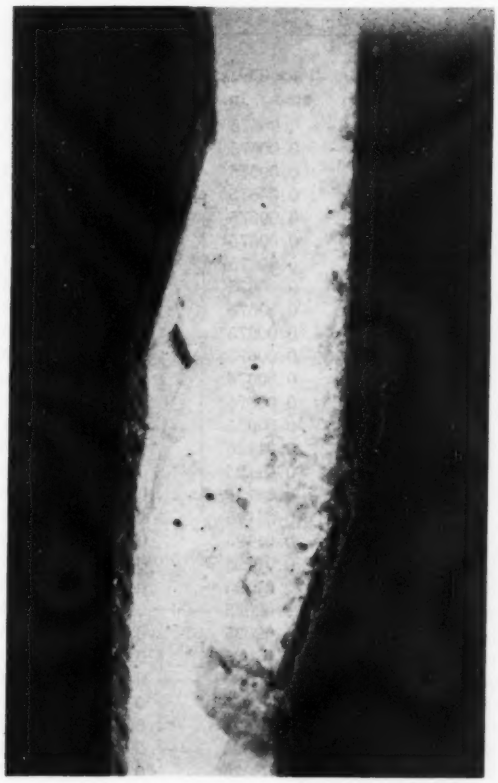

FIG. 6. Skew ripple. Edge view. Core thickness 0.233 in., face thickness 0.02025 in.

Strain Deviations

In most of the 7-in. wide specimens the maximum deviation of the average strain in any two opposite strain gages from the average of all the six strain gages was between 2 and 5 per cent. With the two 7-in. wide specimens of a nominal thickness of $^1/_8$ in. this was true only up to three-fourths of the final load. In the last readings before failure the deviation was 16 and 30 per cent, respectively, for the two specimens. The two 4-in. wide specimens took the load so uniformly that it was decided to test the rest of these narrow specimens without strain gages.

Differences in the readings of opposite strain gages indicate a bending of the specimen. The greatest deviation of this kind occurred in the middle of the two 7-in. wide, $^1/_8$-in. thick specimens. It amounted to 20 and 45 per cent, respectively, at three-fourths of the final load and 60 and 160 per cent, respectively, at the final load. The two 4-in. wide, $^1/_8$-in. thick specimens had maximum deviations of 22 and 32 per cent, respectively, under full load. The 4-in. wide and the 7-in. wide specimens of $^1/_4$-in. and $^1/_2$-in. thickness remained straight under load. In them the maximum deviations between the readings of opposite strain gages was, as a rule, between 2 and 7 per cent. The exceptions were specimens Nos. 23 and 26, which showed deviations of 12 per cent, and specimen No. 7, which showed a deviation of 27 per cent under full load. Some of the 11-in. wide specimens were considerably bent, the maximum deviation observed being 95 per cent.

Data concerning the specimens are collected in Table 1. All the specimens failed by buckling in the shape of a short wave length ripple which reached across the entire width of the specimen. Two distinct types of buckling were observed. One was symmetric as shown in Figs. 4 and 5, and the other skew as shown in Figs. 6 and 7. It was not possible to determine exactly the wave length of the incipient buckle, since buckling occurred suddenly and the material was permanently distorted.

EXPERIMENTAL DETERMINATION OF THE MODULI OF THE MATERIALS

Tensile Tests

Many layers of papreg, the face material of the sandwich panels, were glued together to form plates of total thicknesses of $^1/_8$ and $^1/_4$ in. Tensile test specimens of a total length of 14 in. and a central gage length of 2 in. were cut from the plates and tested in the same Riehle Bros. testing machine as was used for the buckling experiments. The strain was measured with

TABLE 1

Specimen No.	Width w, In.	Face Thickness t, In.	Core Thickness b, In.	b/t	Area of Faces $2wt$, Sq.In.	Buckling Load, Lbs.	Buckling Stress, Lbs. per Sq.In.	Type of Failure
1	7	0.00675	0.112	16.60	0.0945	540	5,710	Skew
2	7	0.00675	0.119	17.64	0.0945	750	7,930	Skew
3	7	0.00675	0.103	15.27	0.0945	574	6,070	Skew
4	7	0.00675	0.117	17.33	0.0945	695	7,350	Skew
5	4	0.00675	0.120	17.78	0.0540	478	8,860	Skew
6	4	0.00675	0.113	16.75	0.0540	504	9,320	Skew
7	7	0.00675	0.219	32.45	0.0945	1,030	10,800	Symmetric
8	7	0.00675	0.223	33.05	0.0945	1,100	11,630	Symmetric
9	7	0.00675	0.244	36.15	0.0945	1,240	13,100	Skew
10	7	0.00675	0.450	66.7	0.0945	960	10,160	Symmetric
11	7	0.00675	0.468	69.4	0.0945	830	8,770	Symmetric
12	7	0.00675	0.460	68.2	0.0945	710	7,510	Symmetric
13	7	0.00675	0.483	71.55	0.0945	705	7,450	Symmetric
14	7	0.00675	0.479	71.0	0.0945	810	8,560	Symmetric
15	4	0.01125	0.070	6.22	0.0900	520	5,780	Skew
16	4	0.01125	0.073	6.49	0.0900	415	4,620	Skew
17	4	0.01125	0.066	5.86	0.0900	520	5,780	Skew
18	4	0.01125	0.076	6.75	0.0900	350	3,890	Skew
19	4	0.01125	0.248	22.05	0.0900	1,000	11,110	Symmetric
20	4	0.01125	0.239	21.25	0.0900	1,100	12,230	Symmetric
21	4	0.01125	0.207	18.40	0.0900	410	4,560	Symmetric
22	7	0.02025	0.229	11.30	0.2835	2,430	8,560	Skew
23	7	0.02025	0.234	11.55	0.2835	2,700	9,520	Skew
24	7	0.02025	0.240	11.84	0.2835	2,695	9,500	Skew
25	7	0.02025	0.233	11.50	0.2835	2,040	7,200	Skew
26	7	0.02025	0.249	12.29	0.2835	2,570	9,060	Skew
27	11	0.02025	0.230	11.35	0.4455	1,600	3,590	Skew
28	11	0.02025	0.233	11.50	0.4455	1,860	4,180	Skew
29	11	0.02025	0.233	11.50	0.4455	2,280	5,120	Skew
30	11	0.02025	0.234	11.55	0.4455	2,900	6,510	Skew
31	11	0.02025	0.247	12.19	0.4455	2,300	5,160	Skew
32	4	0.00675	0.449	66.6	0.0540	580	10,730	Symmetric
33	4	0.00675	0.458	67.9	0.0540	750	13,880	Symmetric
34	4	0.00675	0.448	66.4	0.0540	700	12,970	Symmetric
35	4	0.00675	0.442	65.5	0.0540	600	11,110	Symmetric
36	4	0.01125	0.443	39.4	0.0900	800	8,890	Symmetric
37	4	0.01125	0.445	39.55	0.0900	820	9,110	Symmetric
38	4	0.01125	0.458	40.7	0.0900	680	7,560	Symmetric
39	4	0.01125	0.458	40.7	0.0900	935	10,390	Symmetric
40	4	0.01575	0.457	29.0	0.1260	1,250	9,930	Symmetric
41	4	0.01575	0.465	29.5	0.1260	1,425	11,310	Symmetric
42	4	0.01575	0.456	28.95	0.1260	1,320	10,480	Symmetric
43	4	0.01575	0.467	29.65	0.1260	1,295	10,290	Symmetric
44	4	0.02025	0.441	21.75	0.1620	2,240	13,830	Symmetric
45	4	0.02025	0.434	21.4	0.1620	2,220	13,700	Symmetric
46	4	0.02025	0.443	21.85	0.1620	2,040	12,590	Symmetric
47	4	0.02025	0.452	22.3	0.1620	2,060	12,710	Symmetric
48	4	0.01125	0.725	64.4	0.0900	1,455	16,160	Symmetric
49	4	0.01125	0.731	65.0	0.0900	1,075	11,940	Symmetric
50	4	0.01125	0.735	65.35	0.0900	750	8,340	Symmetric
51	4	0.01125	0.741	65.9	0.0900	960	10,670	Symmetric

Baldwin-Southwark metalectric strain gages cemented to both sides of the specimens.

A typical tensile stress-strain diagram is represented by the curve labeled "tension" in Fig. 8. The curve shows the average of the readings of the two strain gages. The individual readings were so close that they could not be distinguished in a diagram of this size.

Altogether four tensile specimens of $^1/_4$-in. thickness and four tensile specimens of $^1/_8$-in. thickness were tested. The average value of Young's modulus calculated from the initial slopes of the diagrams was 2.47×10^6 lbs. per sq.in. for the former group and 2.92×10^6 lbs. per sq.in. for the latter. Unfortunately, when the test specimens were manufactured, no attention was paid to the directional properties of papreg so that it is not known how many layers were oriented in the lengthwise and crosswise directions. The values obtained for Young's modulus fall between those given

FIG. 7. Skew ripple. Face view. Core thickness 0.119 in., face thickness 0.00675 in.

by Erickson and Boller[4] for parallel laminates tested lengthwise and cross laminates. The situation is the same with regard to the compression tests described below. The curves of Fig. 8 are similar to those given by Erickson and Boller.

Fig. 8 also contains a curve labeled "compression." It represents the data obtained with a parallelepipedon of glued papreg having a height of 2 in. and a cross section of $(1.5)(1.5) = 2.25$ sq.in.

Compression Tests

The compression tests were carried out with the same Riehle Bros. testing machine as was used in the tension tests. The strain was measured with the aid of Baldwin-Southwark metalectric strain gages cemented to four faces of the specimens. The average modulus computed from tests with three specimens was found to be 2.43×10^6 lbs. per sq.in.

Compression tests were also made with the core material. The cellulose acetate was glued and cut into cubes of 3-in. edge length. The cubes were then compressed in a Fairbanks lever-type testing machine of 2,000-lb. load capacity which can be read with an accuracy of ± 1 lb. In tests with six cubes the deflections of the loading head were measured with two Ames dial gages having $^1/_{1,000}$-in. subdivisions. A typical load-displacement diagram is shown in Fig. 9. Three specimens were subjected to a series of alternating load increases and decreases. Fig. 10 contains a load-displacement diagram obtained in this manner.

The average modulus calculated from the slope of the middle portion of the curves was found to be about 3,000 lbs. per sq.in. The initial slope was in the neighborhood of 1,500 lbs. per sq.in. The reason for the small initial value may be found in a nonuniform stress

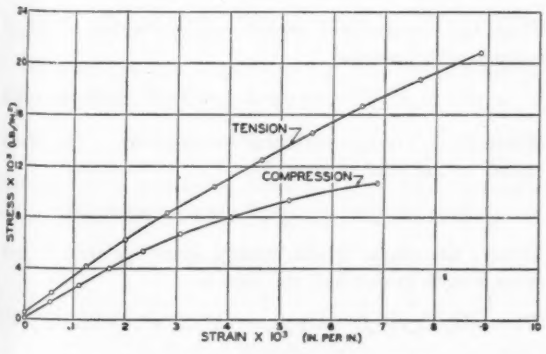

FIG. 8. Stress-strain diagram of papreg.

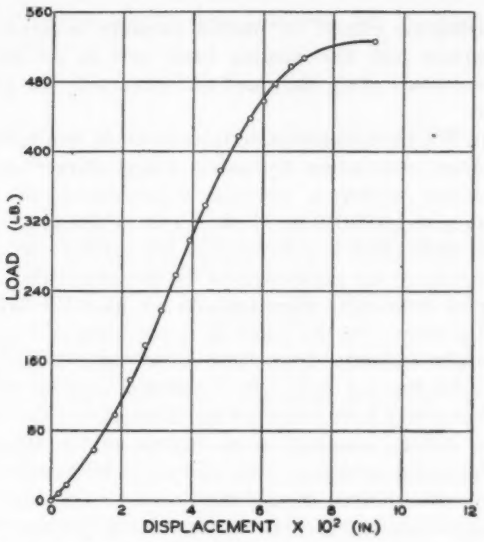

FIG. 9. Load-deflection diagram of core material in compression.

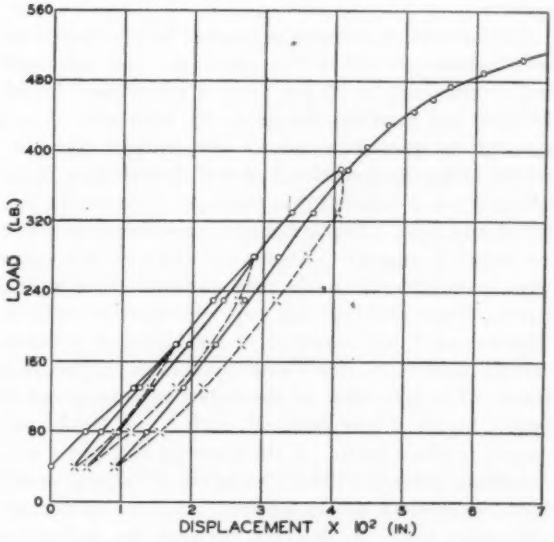

FIG. 10. Load-deflection diagram of core material in repeated compression.

distribution caused by uneven pressure between the specimen and the loading head and in an imperfect contact along the glued surfaces inside the specimen.

In five more compression tests an effort was made to measure the strain by using Huggenberger extensometers having a nominal magnification of 320. Papreg strips 0.010 in. thick, $^1/_8$ in. wide, and $^1/_2$ in. long were glued to four faces of the cubes to serve as supports for the knife edges of the extensometers. The curves obtained in these tests do not have the flat initial portion. On the other hand, the value of Young's modulus computed from these curves varies from 5,500 to 9,630 lbs. per sq.in. It is believed that the extensometer may have restricted the distortions of the cellulose acetate, resulting in an increase of the apparent value of the modulus. This appears to be a reasonable assumption, since the pressure necessary to hold the Huggenberger extensometers against the papreg strips was of considerable magnitude as compared to the ultimate compressive strength of the cellular cellulose acetate.

The maximum pressure supported by the specimens was between 50 and 60 lbs. per sq.in. One specimen was compressed to 60 per cent of its original length without any material change in the load after it had reached its maximum value. No changes were observed in the cross-sectional area of the specimen, from which it was concluded that Poisson's ratio for the material was zero. This conclusion was corroborated in an indirect manner. About one-third of the cubes were manufactured of the core material alone with a papreg layer glued to the top and bottom surfaces. The second third consisted of six layers of cellulose acetate, each $^1/_2$ in. thick, with layers of papreg between them. The last third of the cubes was composed of twelve layers of core material, each $^1/_4$ in. thick, with papreg between them. If the material had had a non-vanishing Poisson's ratio, the layers of papreg should have diminished the deflections; yet no systematic differences could be detected between the deflections of the three types of cubes tested.

Strain Energy Calculation of the Symmetric Ripple

Inspection of the specimens after failure led to the assumption of the deflected shape of the cross section of the sandwich panel as indicated by the dash-dotted line in Fig. 11. This shape involves the bending of the faces of thickness t, and the elongation or the compression of the horizontal fibers of the core which have the initial length b. Since, however, a short wave on the surface can hardly have any effect upon the material in the middle of the core when b is large, it is assumed that displacements occur only in marginal zones of depth w. The vertical displacement u at buckling is assumed to be negligibly small. The horizontal displacement v of the point originally at x, y in the right-hand side marginal zone is given by the equation

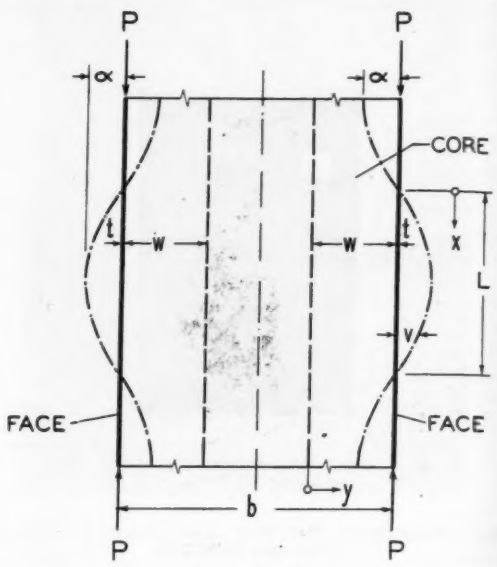

Fig. 11. Assumed shape of the symmetric ripple.

$$v = \alpha(y/w) \sin (\pi x/L) \quad (1)$$

The buckling load is now calculated from the requirement that the work done by the compressive force during the vertical displacement of its point of attack caused by the bending of the face layer be equal to the strain energy of bending stored in the face material plus the strain energy of extension and shear stored in the core.

The compressive load carried by the core is neglected and not shown in the figure. This is reasonable since the ratio of Young's moduli for face and core is about 2,000. Poisson's ratio for the core material is taken as zero. Because of the symmetry it is sufficient to calculate the work and the strain energy for one-half of the cross section. The width of the sandwich skin perpendicular to the plane of the drawing is taken as unity.

The normal strain in the core is

$$\epsilon_y = (\partial v/\partial y) = (\alpha/w) \sin (\pi x/L) \quad (2)$$

Thus the extensional strain energy within one-half wave length becomes

$$U_\epsilon = (E_c/2)\int_0^L \int_0^w \epsilon_y^2 dy\, dx = (\alpha^2/2)(E_c/2)(L/w) \quad (3)$$

where E_c is Young's modulus for the core. The shear strain in the core is given by

$$\gamma = (\partial v/\partial x) = \alpha(\pi/L)(y/w) \cos (\pi x/L) \quad (4)$$

Hence, the shear strain energy stored within a half wave length in one-half the core is

$$U_\gamma = (G_c/2)\int_0^L \int_0^w \gamma^2 dy\, dx = (\alpha^2/2)(\pi^2/6)G_c(w/L) \quad (5)$$

where G_c is the shear modulus of the core.

The strain energy of bending stored in one face is

$$U_f = (E_f I_f/2)\int_0^L (\partial^2 v_w/\partial x^2)^2\, dx = (\alpha^2/2)(\pi^4/24)E_f(t/L)^3 \quad (6)$$

where v_w is the horizontal displacement at $y = w$, E_f is Young's modulus for the face material, and the moment of inertia I_f of the cross section of the face is calculated from the formula

$$I_f = t^3/12 \quad (7)$$

Because of the smallness of t, the displacements at $y = w + (t/2)$ were taken to be equal to those at $y = w$. With this same assumption the shortening ΔL of the distance between the points that were originally at $x = 0$ and $x = L$ can be calculated as

$$\Delta L = (1/2)\int_0^L (\partial v_w/\partial x)^2\, dx = (\alpha^2/4)(\pi^2/L) \quad (8)$$

The work done by the constant force

$$P = \sigma_{cr} t \quad (9)$$

during the displacement of its point of application caused by the bending of the face is

$$W = P\Delta L = (\alpha^2/2)(\pi^2/2)(t/L)\sigma_{cr} \quad (10)$$

The equation

$$W = U_c + U_\gamma + U_f \quad (11)$$

can be solved for σ_{cr} after substitution of the expressions just developed:

$$\sigma_{cr} = (1/\pi^2)E_c(L^2/tw) + (1/3)G_c(w/t) + (\pi^2/12)E_f(t/L)^2 \quad (12)$$

The critical stress in this equation depends upon the parameters w and L. The actual values of these parameters are those which make the critical stress a minimum. Consequently, $\partial\sigma_{cr}/\partial w$ and $\partial\sigma_{cr}/\partial L$ must vanish:

$$\partial\sigma_{cr}/\partial w = -(1/\pi^2)E_c(L^2/tw^2) + (1/3)G_c(1/t) = 0 \quad (13)$$

$$\partial\sigma_{cr}/\partial L = (2/\pi^2)E_c(L/tw) - (\pi^2/6)E_f(t^2/L^3) = 0 \quad (14)$$

Solution of the two simultaneous equations gives

$$w/t = 0.91\sqrt[3]{E_f E_c/G_c^2} \quad (15)$$

$$L/t = 1.65\sqrt[4]{E_f^2/E_c G_c} \quad (16)$$

Substitution in the equation for the critical stress finally yields

$$\sigma_{cr} = 0.91\sqrt[3]{E_f E_c G_c} \quad (17)$$

This formula is correct only if w is smaller than or equal to $b/2$, as may be seen from Fig. 11. Thus,

$$w = 0.91t\sqrt[3]{E_f E_c/G_c^2} \leq (b/2)$$

that is,

$$(b/t) \geq 1.82\sqrt[3]{E_f E_c/G_c^2} \quad (18)$$

When this inequality does not hold, Eq. (1) may be replaced by

$$v = \alpha(2y/b)\sin(\pi x/L) \quad (19)$$

The expression for the critical stress then becomes

$$\sigma_{cr} = (2/\pi^2)E_c(L^2/tb) + (1/6)G_c(b/t) + (\pi^2/12)E_f(t/L)^2 \quad (20)$$

The differential coefficient of σ_{cr} with respect to L must again vanish. This condition yields

$$L/t = 1.42\sqrt[4]{E_f/E_c}\sqrt{b/t} \quad (21)$$

Substitution in Eq. (20) gives

$$\sigma_{cr} = 0.817\sqrt{E_f E_c}\sqrt{t/b} + 0.166G_c(b/t) \quad (22)$$

In Fig. 12 the critical stress is plotted against (b/t) for the case when $E_f = 3 \times 10^6$ lbs. per sq.in. and $E_c = 1{,}500$ lbs. per sq.in. Since Poisson's ratio μ is zero, the shear modulus

$$G_c = E_c/[2(1+\mu)]$$

has a value

$$G_c = (1/2)E_c \quad (23)$$

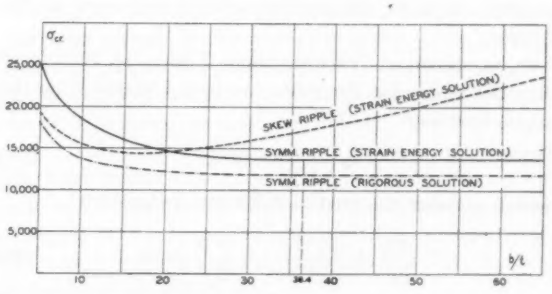

FIG. 12. Critical stress when $E_f = 3 \times 10^6$ lbs. per sq.in., $E_c = 1{,}500$ lbs. per sq.in., and $\mu_c = 0$.

Eq. (17) is represented by a horizontal straight line

$$\sigma_{cr} = 13{,}650 \text{ lbs. per sq.in.} \quad (24)$$

Eq. (22) becomes

$$\sigma_{cr} = 54{,}700\sqrt{t/b} + 125(b/t) \quad (25)$$

The latter is represented by the curved part of the full line in Fig. 12. When $b/t = 36.4$, the straight line is the tangent of the curve.

Solution of the Problem by Integration of the Differential Equation

The problem can also be solved by integrating the differential equation as was done by Gough, Elam, and de Bruyne[5] for other boundary conditions. The core is considered as a plate of unit thickness (Fig. 13) upon which given loads are acting parallel to the plane of the drawing. In the present case the loads are assumed to be distributed according to the sine law:

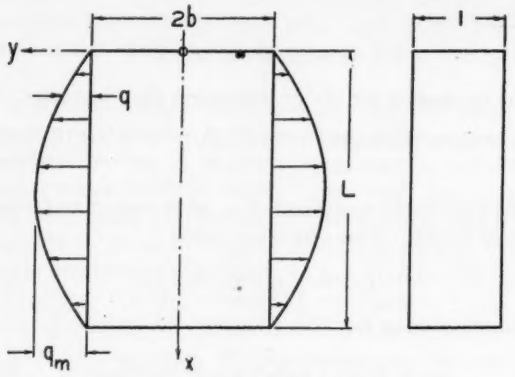

FIG. 13. Core considered as plate.

$$q = q_m \sin(\pi x/L) = q_m \sin \alpha x \tag{26}$$

where

$$\alpha = \pi/L \tag{27}$$

and where q_m is the maximum value of the load per unit area. The loads are applied symmetrically to the x axis along the boundaries $y = b$ and $y = -b$. The positive sense of the applied load is indicated in the figure.

It is shown in Timoshenko's *Theory of Elasticity*[6] that the stresses in the plate can be calculated from the stress function

$$\phi = f(y) \sin \alpha x \tag{28}$$

which satisfies the partial differential equation

$$\frac{\partial^4\phi}{\partial x^4} + \frac{2\partial^4\phi}{\partial x^2\,\partial y^2} + \frac{\partial^4\phi}{\partial y^4} = 0 \tag{29}$$

provided that

$$f^{IV}(y) - 2\alpha^2 f''(y) + \alpha^4 f(y) = 0 \tag{30}$$

The general integral of this ordinary differential equation can be written in the form

$$f(y) = C_1 \cosh \alpha y + C_2 \sinh \alpha y + C_3 y \cosh \alpha y + C_4 y \sinh \alpha y \tag{31}$$

The coefficients C_1, C_2, C_3, and C_4 must be determined from the boundary conditions.

One such condition can be derived for the strain in the x direction at $y = \pm b$. The face, which is cemented to the core, deflects according to a sine curve when buckling occurs, as will be derived later. The infinitesimal deflection in the y direction gives rise to a contraction in the x direction, which is infinitesimal of the second order. This contraction can be neglected in the calculation of the stresses prevailing in the core, particularly since the modulus of the core is about 2,000 times smaller than that of the face. Hence, it may be stated that

$$\epsilon_x = 0 \text{ when } y = \pm b \tag{32}$$

Because of $\mu = 0$, however, this condition is equivalent to

$$\sigma_x = 0 \text{ when } y = \pm b \tag{33}$$

On the other hand, the stress in the x direction can be calculated from the stress function:

$$\sigma_x = (\partial^2\phi/\partial y^2) \tag{34}$$

Differentiation of the right-hand side term of Eq. (28), in which $f(y)$ must be replaced by the expression given in Eq. (31), and substitution of the boundary conditions contained in Eq. (33) yield

$$C_1 = -C_4(\alpha b \sinh \alpha b + 2 \cosh \alpha b)/(\alpha \cosh \alpha b) \tag{35}$$

$$C_2 = -C_3(\alpha b \cosh \alpha b + 2 \sinh \alpha b)/(\alpha \sinh \alpha b) \tag{36}$$

The stress in the y direction is given by

$$\sigma_y = (\partial^2\phi/\partial x^2) \tag{37}$$

Its value must be equal to q as given by Eq. (26) when $y = \pm b$. This condition, in conjunction with Eqs. (35) and (36), suffices for the determination of the coefficients:

$$C_3 = 0 \tag{38}$$

$$C_4 = q_m/(2\alpha \cosh \alpha b) \tag{39}$$

Thus the stress function becomes

$$\phi = \frac{q_m b}{2\alpha b \cosh \alpha b} \times \left[y \sinh \alpha y - \left(\frac{\alpha b \sinh \alpha b + 2 \cosh \alpha b}{\alpha \cosh \alpha b} \right) \cosh \alpha y \right] \sin \alpha x \tag{40}$$

and the stress in the y direction is given by

$$\sigma_y = \frac{\alpha q_m}{2 \cosh \alpha b} \times \left[\frac{\alpha b \sinh \alpha b + 2 \cosh \alpha b}{\alpha \cosh \alpha b} \cosh \alpha y - y \sinh \alpha y \right] \sin \alpha x \tag{41}$$

The displacements in the y direction of the points originally situated along the line $y = b$ can now be calculated. The strain ϵ_y is equal to σ_y/E, since Poisson's ratio is zero. On the other hand, $\epsilon_y = \partial v/\partial y$. Consequently,

$$v_b = \int_0^b \epsilon_y dy \tag{42}$$

where v_b is the horizontal displacement at $y = b$. The displacement at $y = 0$ may be taken as zero because of the symmetry. Integration gives

$$v_b = (q_m/2E_c)[(b/\cosh^2 \alpha b) - (3/\alpha) \tanh \alpha b] \sin \alpha x \tag{43}$$

It may be seen that the displacement is proportional to the load at every point along the boundary $y = b$. The factor of proportionality is

$$\psi = (q/v_b) = (2E_c/b)(\alpha b \cosh^2 \alpha b)/ (3 \cosh \alpha b \sinh \alpha b - \alpha b) \quad (44)$$

The face may now be considered as a beam supported by an elastic foundation—namely, the core. The differential equation of such a beam is (see reference 7):

$$E_f I_f v^{IV} + P v'' + \psi v = 0 \quad (45)$$

where the subscript b is omitted for the sake of simplicity so that v designates the deflection of the face. Substitution proves that this differential equation is solved by

$$v = \sin \alpha x \quad (46)$$

provided that

$$E_f I_f \alpha^4 - P\alpha^2 + \psi = 0 \quad (47)$$

This equation can be solved for P:

$$P = E_f I_f \alpha^2 + (\psi/\alpha^2) \quad (48)$$

Division by t, substitution of I_f from Eq. (7) and ψ from Eq. (44), and use of the symbols

$$\Omega = (1/48)(E_f/E_c)(t/b)^2 \quad (49)$$

$$\sigma^* = (1/4)(\sigma_{cr}/E_c)(t/b) \quad (50)$$

leads to the equation

$$\sigma^* = (\alpha b)^2 \Omega + (1/\alpha b)(\cosh^2 \alpha b)/(3 \sinh 2\alpha b - 2\alpha b) \quad (51)$$

In this equation σ^*, which is the critical stress multiplied by a constant factor, is a function of $\alpha b = \pi(b/L)$. Buckling occurs with a wave length L that corresponds to the minimum of the critical stress. Consequently,

$$d\sigma^*/d(\alpha b) = 0 \quad (52)$$

After differentiation and solution for 2Ω,

$$2\Omega = (\cosh^2 \alpha b)/[(\alpha b)^3(3 \sinh 2\alpha b - 2\alpha b)] + (2 \cosh^2 \alpha b)(3 \cosh 2\alpha b - 1) \div [(\alpha b)^2(3 \sinh 2\alpha b - 2\alpha b)^2] - (\sinh 2\alpha b)/[(\alpha b)^2(3 \sinh 2\alpha b - 2\alpha b)] \quad (53)$$

For any arbitrary value of αb, 2Ω can be calculated from Eq. (53). Substitution of Ω and αb in Eq. (51) yields σ^*. Corresponding values of σ^* and (L/b) are plotted in Fig. 14 against Ω. The diagram permits the calculation of the critical stress and of the wave length when the mechanical and geometric properties of the sandwich skin are known.

For the example of the papreg face with $E_f = 3 \times 10^6$ lbs. per sq.in. and the cellulose acetate core with $E_c = 1{,}500$ lbs. per sq.in. and $\mu = 0$, Eq. (49) can be solved for (b/t):

$$(b/t) = 3.47/\sqrt[3]{\Omega} \quad (54)$$

Eq. (50) gives

$$\sigma_{cr} = 6{,}000(b/t)\sigma^* \quad (55)$$

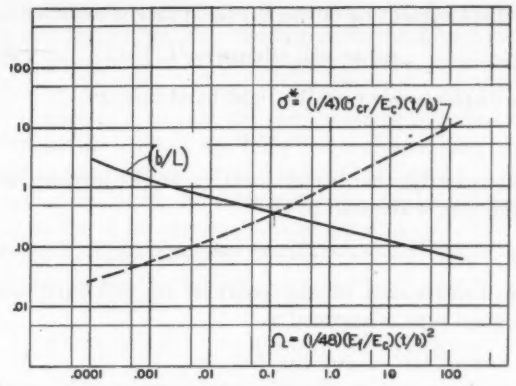

FIG. 14. Reduced critical stress σ^* and wave length ratio (L/b) plotted against parameter Ω.

Values of σ_{cr} plotted against (b/t) are shown in the dash-dotted curve of Fig. 12. It may be seen that the rigorous solution gives lower values for the buckling stress than does the strain energy calculation. The ratio is 0.873 for large values of (b/t).

STRAIN ENERGY CALCULATION OF THE SKEW RIPPLE

Many of the thinner specimens buckled according to the skew pattern shown in Figs. 6 and 7. The buckling stress corresponding to this type of instability is now calculated by the strain energy method. The deflected shape is assumed as indicated by the dash-dotted line in Fig. 15. The calculations are carried out in much the same manner as those of the buckling stress in the case of the symmetric ripple. Again a marginal zone of depth w is assumed to which all the extensions are restricted, but shearing deformations occur now throughout the entire core.

In the upper third of the figure—that is, where

$$0 \leq x \leq (L/2)$$

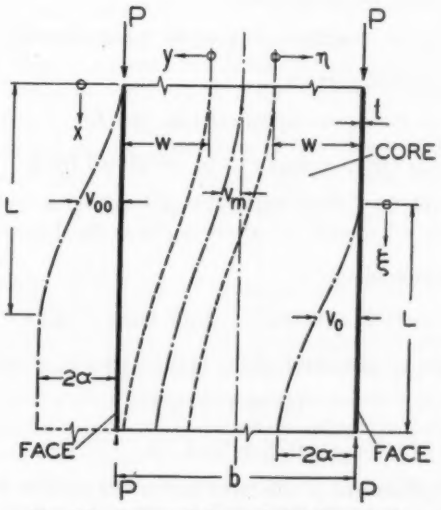

FIG. 15. Assumed shape of the skew ripple.

the displacement v_{00} of the left-hand face is assumed as

$$v_{00} = \alpha[1 - \cos(\pi x/L)] \quad (56)$$

The displacement v_0 of the right-hand face is

$$v_0 = 0 \quad (57)$$

Consequently, the displacement v_m of the median line of the core is assumed to be

$$v_m = (\alpha/2)[1 - \cos(\pi x/L)] \quad (58)$$

The displacement of any point in the left-hand side marginal zone is assumed as

$$v_L = (\alpha/2)[1 - \cos(\pi x/L)] + (\alpha/2)(y/w)[1 - \cos(\pi x/L)] \quad (59)$$

when $0 \leq y \leq w$.

In the right-hand side marginal zone

$$v_R = -(\alpha/2)[1 - \cos(\pi x/L)] + (\alpha/2)(\eta/w)[1 - \cos(\pi x/L)] \quad (60)$$

when $0 \leq \eta \leq w$.

In the middle portion

$$v_M = (\alpha/2)[1 - \cos(\pi x/L)] \quad (61)$$

The extensional strain in the left marginal zone is

$$\epsilon_L = (\partial v/\partial y) = (\alpha/2w)[1 - \cos(\pi x/L)] \quad (62)$$

In the right marginal zone

$$\epsilon_R = (\partial v/\partial \eta) = (\alpha/2w)[1 - \cos(\pi x/L)] \quad (63)$$

In the middle portion the extensional strain is zero. Consequently, the extensional strain energy is

$$U_\epsilon = 2(E_c/2)\int_0^{L/2}\int_0^w \epsilon_L^2 dy\, dx = (\alpha^2/2)[(3\pi - 8)/(8\pi)](L/w)E_c \quad (64)$$

The shear strain in the left marginal zone is

$$\gamma_L = (\alpha/2)[1 + (y/w)](\pi/L)\sin(\pi x/L) \quad (65)$$

In the right marginal zone

$$\gamma_R = -(\alpha/2)[1 - (\eta/w)](\pi/L)\sin(\pi x/L) \quad (66)$$

In the middle portion

$$\gamma_M = (\alpha/2)(\pi/L)\sin(\pi x/L) \quad (67)$$

The shear strain energy can be calculated from

$$U_\gamma = (G_c/2)\int_0^{L/2}[\int_0^w \gamma_L^2\, dy + \int_0^w \gamma_R^2\, d\eta + \gamma_M^2(b - 2w)]\, dx \quad (68)$$

Integration gives

$$U_\gamma = (\alpha^2/2)(\pi^2/48)[(3b + 2w)/L]G_c \quad (69)$$

In the middle third of the figure—that is, where

$$(L/2) \leq x \leq L$$

$$0 \leq \xi \leq (L/2)$$

the displacement of the faces and of the median line of the core, respectively, are assumed as

$$v_{00} = \alpha[1 + \sin(\pi\xi/L)] \quad (70)$$

$$v_0 = \alpha[1 - \cos(\pi\xi/L)] \quad (71)$$

$$v_m = \alpha[1 - (1/2)\cos(\pi\xi/L) + (1/2)\sin(\pi\xi/L)] \quad (72)$$

The displacement of a point in the left marginal zone, the middle portion, and the right marginal zone, respectively, is

$$v_L = \alpha[1 - (1/2)\cos(\pi\xi/L) + (1/2)\sin(\pi\xi/L)] + \alpha(y/w)[(1/2)\sin(\pi\xi/L) + (1/2)\cos(\pi\xi/L)] \quad (73)$$

$$v_M = \alpha[1 - (1/2)\cos(\pi\xi/L) + (1/2)\sin(\pi\xi/L)] \quad (74)$$

$$v_R = \alpha[-1 + (1/2)\cos(\pi\xi/L) - (1/2)\sin(\pi\xi/L)] + \alpha(\eta/w)[(1/2)\sin(\pi\xi/L) + (1/2)\cos(\pi\xi/L)] \quad (75)$$

The extensional strain is

$$\epsilon_L = \epsilon_R = (\alpha/2w)[\sin(\pi\xi/L) + \cos(\pi\xi/L)] \quad (76)$$

$$\epsilon_M = 0 \quad (77)$$

The shear strain is

$$\gamma_L = (\alpha/2)(\pi/L)[\sin(\pi\xi/L) + \cos(\pi\xi/L)] + (\alpha/2)(\pi/L)(y/w)[\cos(\pi\xi/L) - \sin(\pi\xi/L)] \quad (78)$$

$$\gamma_M = (\alpha/2)(\pi/L)[\sin(\pi\xi/L) + \cos(\pi\xi/L)] \quad (79)$$

$$\gamma_R = -(\alpha/2)(\pi/L)[\sin(\pi\xi/L) + \cos(\pi\xi/L)] + (\alpha/2)(\pi/L)(\eta/w)[\cos(\pi\xi/L) - \sin(\pi\xi/L)] \quad (80)$$

The strain energy can be calculated as before. Integration yields

$$U_\epsilon = (\alpha^2/2)[(2\pi + 4)/8\pi](L/w)E_c \quad (81)$$

$$U_\gamma = (\alpha^2/2)(\pi/16)[(2\pi + 4)b + (2/3)(2\pi - 4)w](G_c/L) \quad (82)$$

Because of the point symmetry of the distorted shape the strain energy in the lower third of the figure is the same as that in the upper third. The total strain energy U_c stored in the core is, therefore, the sum of the strain energy quantities given in Eqs. (81) and (82), plus twice those given in Eqs. (64) and (69):

$$U_c = (\alpha^2/2)[(2\pi - 3)/(2\pi)]E_c(L/w) + (\alpha^2/2)(\pi/12)G_c[3(\pi + 1)(b/L) + 2(\pi - 1)(w/L)] \quad (83)$$

The strain energy of bending U_f stored in the two faces is twice the amount given in Eq. (6) where only one face was considered:

$$U_f = (\alpha^2/2)(\pi^4/12)E_f(t/L)^3 \quad (84)$$

Similarly, the work W done by the external forces is twice the amount given by Eq. (10):

$$W = (\alpha^2/2)\pi^2(t/L)\sigma_{cr} \quad (85)$$

Substitution in the equation

$$W = U_f + U_c \quad (86)$$

and solution for σ_{cr} yields

$$\sigma_{cr} = \alpha(t/L)^2 + \beta(L^2/wt) + \gamma(b/t) + \delta(w/t) \quad (87)$$

where

$$\left.\begin{aligned} \alpha &= (\pi^2/12)E_f \\ \beta &= [(2\pi - 3)/(2\pi^3)]E_c \\ \gamma &= [(\pi + 1)/(4\pi)]G_c \\ \delta &= [(\pi - 1)/(6\pi)]G_c \end{aligned}\right\} \quad (88)$$

The critical stress can be minimized as follows:

$$\partial\sigma_{cr}/\partial L^2 = -\alpha(t^2/L^4) + (\beta/wt) = 0 \quad (89)$$

$$\partial\sigma_{cr}/\partial w = -\beta(L^2/w^2t) + (\delta/t) = 0 \quad (90)$$

Solution of the two equations yields

$$(L/t) = (\alpha^2/\beta\delta)^{1/6} = 2.15\sqrt[6]{E_f^2/E_cG_c} \quad (91)$$

$$(w/t) = (\alpha\beta/\delta^2)^{1/3} = 1.5\sqrt[3]{E_fE_c/G_c^2} \quad (92)$$

Substitution in Eq. (87) results in the expression

$$\sigma_{cr} = 3(\alpha\beta\delta)^{1/3} + \gamma(b/t) = 0.51\sqrt[3]{E_fE_cG_c} + 0.33G_c(b/t) \quad (93)$$

These formulas are valid only if w proves to be smaller than or equal to $b/2$; hence, if

$$(b/t) \leq 3\sqrt[3]{E_fE_c/G_c^2} \quad (94)$$

When this inequality is not satisfied, w must be replaced by $(b/2)$ in the expressions assumed for the deflected shape of the sandwich skin. If the calculations are carried out on the basis of this assumption, the following expression is obtained for the critical stress:

$$\sigma_{cr} = (\alpha/L^2) + \beta L^2 + \gamma \quad (95)$$

where

$$\left.\begin{aligned} \alpha &= (\pi^2/12)E_ft^2 \\ \beta &= [(2\pi - 3)/\pi^3](E_c/bt) \\ \gamma &= [(2\pi + 1)/(6\pi)]G_c(b/t) \end{aligned}\right\} \quad (96)$$

The critical stress is a minimum when

$$\partial\sigma_{cr}/\partial L^2 = -(\alpha/L^4) + \beta = 0 \quad (97)$$

Consequently,

$$L^4 = (\alpha/\beta) \quad (98)$$

and

$$(L/t) = 1.67\sqrt[4]{E_f/E_c}\sqrt[4]{b/t} \quad (99)$$

Substitution in Eq. (95) gives

$$\sigma_{cr} = 2\sqrt{\alpha\beta} + \gamma = 0.59\sqrt{E_fE_c}\sqrt{t/b} + 0.387(b/t)G_c \quad (100)$$

For the papreg-cellulose acetate sandwich skin referred to earlier, the numerical values of the critical stress are now calculated. They are also shown in Fig. 12. Eq. (93) becomes

$$\sigma_{cr} = 7{,}650 + 247.5(b/t) \quad (101)$$

Eq. (100) assumes the form

$$\sigma_{cr} = 39{,}600\sqrt{t/b} + 291(b/t) \quad (102)$$

The former equation is represented by the inclined dotted line in Fig. 12; the latter, by the dotted curve. The straight line is the tangent of the curve when $(b/t) = 60$.

It may be seen that the critical stress corresponding to the skew ripple is less than that corresponding to the symmetric ripple when (b/t) is smaller than 20.6. With such values of the b/t ratio, therefore, buckling according to the skew pattern is to be anticipated. The opposite situation prevails when b/t is greater than 20.6 so that symmetric buckling can then be expected.

Comparison of Theory and Experiment

Fig. 16 presents a comparison of the test results with the predictions of theory. Because of the uncertainties regarding the properties of the materials, six theoretic curves are shown. In test specimens 15–51 the papreg was parallel laminated and the load was applied lengthwise. In specimens 1–14 the number of crosswise layers was not known. According to Erickson and Boller,[4] the average value of Young's modulus in bending is 3×10^6 lbs. per sq.in. for parallel laminates loaded lengthwise and 2×10^6 lbs. per sq.in. for cross laminates. The former value was used in the calculation of curves A, B, and E, and the latter was used in the calculation of curves C, D, and F.

The highest values of Young's modulus for the core were obtained under loads corresponding to approximately one-half the ultimate load of the material. The average of these values was about 3,000 lbs. per sq.in. This was used when curves A and C were calculated. The initial modulus was found to be approximately 1,500 lbs. per sq.in. This value was assumed in the calculation of curves B and D. The value of E_c was taken as 750 lbs. per sq.in. for curves E and F.

Curves B and D are identical with those portions of the curves shown in Fig. 12, which correspond to the minimum value of the critical stress. The other four curves were calculated in the same manner as that described in the theoretic part of this paper in connection with Fig. 12, except for a different choice of the values of the moduli. The break in the tangent of each curve (around $b/t = 20$) indicates the transition from the symmetric to the skew type of buckling. The curve corresponding to the rigorous solution of the problem of the symmetric ripple is not shown, since a corresponding rigorous theory is not available at present for the skew ripple.

In Fig. 16 the critical stress of each of the 51 specimens is plotted against the b/t ratio. Three groups of specimens, however, should be disregarded when the experimental points are compared with the theory. The first of these groups contains specimens 1–3. These specimens were tested without an adequate support to prevent the crushing of the loaded edges. The second group is composed of specimens 15–18. The average thickness of the core of these specimens was 0.07 in.

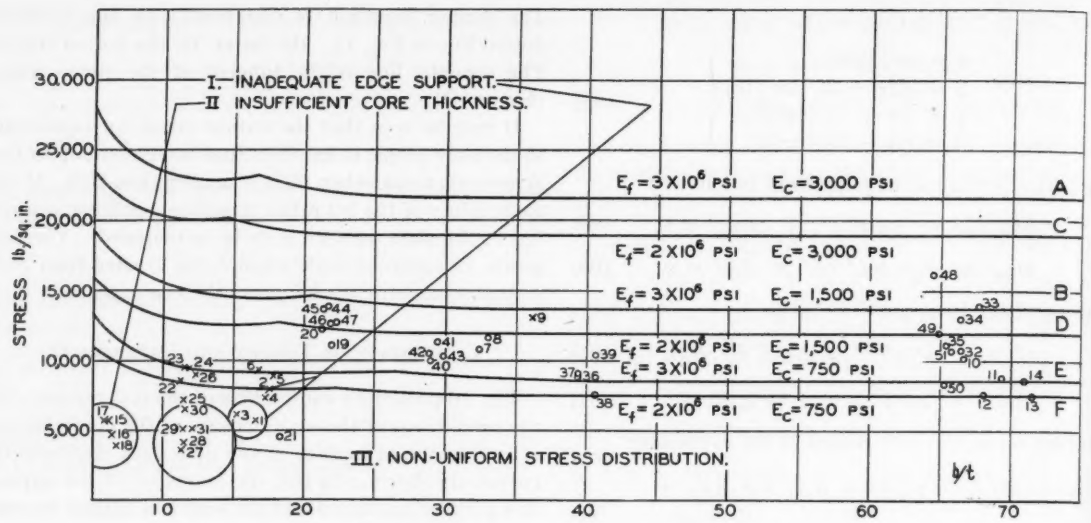

FIG. 16. Comparison of theoretical and experimental critical stress.

This value is equal to about twice the diameter of the larger air bubbles contained in the cellular cellulose acetate. Consequently, since the thickness of the core of specimens 15–18 was not sufficient to eliminate weak spots caused by an unfavorable location of the bubbles, the core of these specimens could not be considered as a homogeneous and isotropic element of the sandwich skin. The specimens failed under apparently too low loads because of local reductions in the elastic properties and strength of the core material. Finally, the apparently low failing stress of specimens 27–31 is amply explained by the nonuniformity of the stress distribution in these 11-in. wide specimens discussed in an earlier part of this paper. The actual buckling stress in these specimens was materially greater than the apparent stress obtained by dividing the total load by the cross-sectional area of the face material.

The remaining 39 test specimens show a considerable amount of scatter. Nevertheless, a definite trend can be clearly discerned: The buckling stress is practically constant throughout the range of the b/t values investigated and appears to be altogether independent of the geometric properties of the specimen. On the other hand, the curves of Fig. 16 demonstrate that this observation is in good agreement with the predictions of the theory.

As far as the actual value of the stress is concerned, the average experimental buckling stress does not differ much from the value of 11,900 lbs. per sq.in. predicted for high b/t ratios by the rigorous theory in the case when $E_f = 3 \times 10^6$ lbs. per sq.in. and $E_c = 1{,}500$ lbs. per sq.in.

It appears that reasonably safe values of the buckling stress can be obtained by using the simple approximate formula

$$\sigma_{cr} = (1/2)\sqrt[3]{E_f E_c G_c} \qquad (103)$$

On the basis of curves B and D the sandwich skin should buckle according to the symmetric pattern when b/t is greater than 18–20 and according to the skew pattern when b/t is smaller than 18–20. The buckled shape observed was in agreement with this prediction in 50 cases out of 51.

WORK DONE BY GOUGH, ELAM, AND DE BRUYNE

Gough, Elam, and de Bruyne showed in a thorough study[5] that the problem of the buckling of the sandwich skin can be solved by considering the face material as a beam supported by an elastic foundation—namely, the core. Although the present authors saw the British article at the time of its publication, they failed to recognize its significance until their own experiments and strain energy calculations, which are presented in the body of this paper, were completed.

The authors of the British publication made use of the results of Biot's[8] and Reissner's[9] theoretic work and determined the critical load of the face of the sandwich skin for several cases of different boundary conditions for the core. The buckled shapes of the sandwich skin observed in the tests described earlier in the present paper differ from the theoretic shapes presented by Gough, Elam, and de Bruyne.

In the experiments described in reference 5, steel and aluminum were used for the face and onazote, an expanded ebonite having a specific gravity of 0.04–0.13, was used for the supporting medium. A strip of thin face material about 5 in. long and $1/2$ in. wide was placed between layers of onazote, which, in turn, were clamped between steel plates in the first group of tests. In the second group the strip of face material was glued to a prism of onazote about $3/4$ in. thick, while in the last group of tests a strip of face material was glued to each face of the $3/4$-in. thick onazote prism.

In all these tests reasonable agreement was found between theoretic and experimental buckling stress.

Conclusions

In experiments with 51 flat sandwich panels, the faces of which had an elastic modulus approximately equal to 2,000 times that of the core material, it was observed that failure occurred according to either the symmetric ripple or the skew ripple pattern when the test specimens were compressed edgewise and the unloaded edges were supported by V-grooves. The buckled shape is shown in Figs. 4 and 5 for the symmetric case and in Figs. 6 and 7 for the skew case.

In the body of the paper a strain energy theory is presented for both types of buckling, and the buckling stress is also calculated by integration of the differential equation of the problem when the buckling is symmetric. The theory and the test results agree in establishing a buckling stress independent of the geometric properties of the panels and depending only upon the elastic moduli of the materials. It appears that a conservative estimate of the buckling stress may be had by using the approximate formula

$$\sigma_{cr} = (1/2)\sqrt[3]{E_f E_c G_c} \qquad (103)$$

where E_f is Young's modulus of the face, E_c is Young's modulus of the core, and G_c is the shear modulus of the core. In the specimens tested the values of the moduli were approximately

$$E_f = 3 \times 10^6 \text{ lbs. per sq.in.}$$
$$E_c = 1{,}500 \text{ lbs. per sq.in.}$$
$$G_c = 750 \text{ lbs. per sq.in.}$$

With these values Eq. (103) gives

$$\sigma_{cr} = 7{,}500 \text{ lbs. per sq.in.}$$

According to the predictions of the strain energy theory the test specimens should have failed by symmetric buckling when their b/t ratio was greater than 18–20 and by skew buckling when the ratio was less than 18–20. The symbol b denotes the thickness of the core; t, the thickness of one face. Fifty out of 51 specimens failed in agreement with these predictions.

Eq. (103) can be used for determining the desirable value of Young's modulus for the core when the properties of the face material are known. After $(1/2)E_c$ has been substituted for G_c and $\sigma_{max.}$ substituted for σ_{cr}, Eq. (103) can be solved for E_c:

$$E_c = 4\sqrt{\sigma_{max.}^3/E_f}$$

The value of $\sigma_{max.}$ should be chosen so as to be equal to the maximum value of the compressive stress that is considered practicable in the faces. For instance, 20,000 lbs. per sq.in., 40,000 lbs. per sq.in., and 60,000 lbs. per sq.in. might be taken for papreg, aluminum alloy, and steel, respectively. The value of Young's modulus for the core should then be 6,520 lbs. per sq.in., 10,120 lbs. per sq.in., and 10,720 lbs. per sq.in., respectively.

References

[1] Kármán, Th. von, and Stock, P., British Patent No. 235,884, July 21, 1924.

[2] Hoff, N. J., and Mautner, S. E., *Sandwich Construction*, Aeronautical Engineering Review, Vol. 3, No. 8, p. 29, August, 1944.

[3] Forest Products Laboratory, Madison, Wis., *High Strength Laminated Paper Plastics for Aircraft*, Mimeo. No. 1395; revised, April, 1943.

[4] Erickson, E. C. O., and Boller, K. H., *Strength and Related Properties of Forest Products Laboratory Laminated Paper Plastics (Papreg) at Normal Temperature*, Forest Products Laboratory Mimeo. No. 1319, March, 1943.

[5] Gough, G. S., Elam, C. F., and de Bruyne, N. A., *The Stabilization of a Thin Sheet by a Continuous Supporting Medium*, Journal of The Royal Aeronautical Society, Vol. XLIV, No. 349, p. 12, January, 1940.

[6] Timoshenko, S., *Theory of Elasticity*, 1st Edition, p. 44; McGraw-Hill Book Company, Inc., New York, 1934.

[7] Kármán, Th. von, and Biot, Maurice A., *Mathematical Methods in Engineering*, 1st Edition, p. 304; McGraw-Hill Book Company, Inc., New York, 1940.

[8] Biot, Maurice A., *Bending of an Infinite Beam on an Elastic Foundation*, Journal of Applied Mechanics, Vol. 4, No. 1, p. A-1, March, 1937.

[9] Reissner, Eric M., *On the Theory of Beams Resting on a Yielding Foundation*, Proceedings of the National Academy of Sciences, Vol. 23, No. 6, p. 328, June, 1937.

The Stress-Area Method of Designing Beams

GILBERT C. BEST*

Consolidated Vultee Aircraft Corporation

ABSTRACT

A method is developed to facilitate the design of structures having zero margins of safety in bending. It is intended primarily for use with sections composed of many elements, such as wing and fuselage sections, in which each trial computation is a long and tedious procedure. A method of computing the amount of area required at selected points to obtain preselected stresses is worked out. The method makes use of section properties already obtained, thereby reducing the amount of computation necessary and facilitating the development of zero margin of safety with attendant minimum weight. The method is general in principle and can be extended to cover any indeterminate structure—e.g., a frame or a truss. Only the case of a section in bending is discussed in this article, however. Two examples are given.

INTRODUCTION

IN FIG. 1 IS SHOWN a cross-sectional area with coordinate axes x, y (not necessarily principal axes) passing through the centroid of the section. The section is under stress from moments M_x and M_y producing compression on the positive sides of the x and y axes, respectively. A small area dA at point P_0 having coordinates x_0, y_0 works at stress f_0. If a small amount of area is added at P_0, it will cause a readjustment of the section properties and, hence, cause changes in the stresses throughout the section.

Received November 3, 1944.

* Stress Analyst.

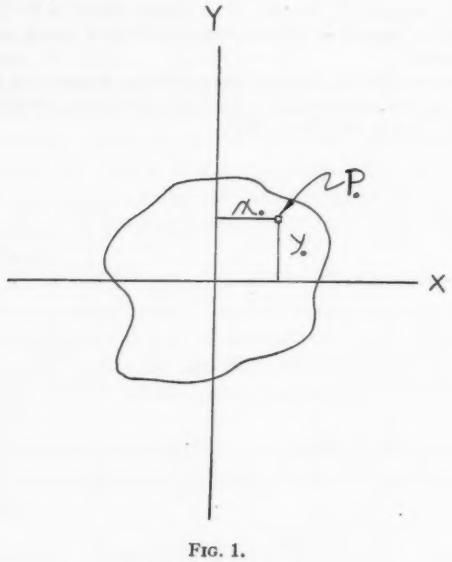

FIG. 1.

However, the problem can be looked at from another point of view. If it is known beforehand at what stress the area at P_0 will finally work—e.g., if it is desired to add a sufficient amount of area ($= a_0$) at P_0 to change the stress at that point from f_0 to F_0—it is possible to consider the area a_0 working at the stress F_0 replaced by a force ($= a_0F_0$) and that all changes in stress throughout the section are caused by this force acting upon the original section before a_0 was added. The advantage of this method of procedure is that a recomputation of the section properties is avoided, since the new stresses are computed from the original data. The moment of inertia of a_0 about its own c.g. is neglected and this causes a small error on the conservative side.

Moving the force a_0F_0 to the centroid of the original section gives:

$$\begin{aligned} M_x &= a_0F_0y_0 \\ M_y &= a_0F_0x_0 \\ P &= -a_0F_0 \end{aligned}$$

AREA AND STRESS AT SAME POINT

$$f = -(k_3M_y - k_1M_x)x - (k_2M_x - k_1M_y)y + (P/A) \tag{1}$$

where A = entire cross-sectional area of original section and

$$\left.\begin{aligned} k_1 &= I_{xy}/(I_xI_y - I_{xy}^2) \\ k_2 &= I_y/(I_xI_y - I_{xy}^2) \\ k_3 &= I_x/(I_xI_y - I_{xy}^2) \end{aligned}\right\} \tag{2}$$

$$\Delta f_{00} = -(k_3a_0F_0x_0 - k_1a_0F_0y_0)x_0 - (k_2a_0F_0y_0 - k_1a_0F_0x_0)y_0 - (a_0F_0/A) \tag{3}$$

where Δf_{00} is the change in stress at P_0 due to the addition of a_0 at P_0. Positive for a decrease in compressive stress, or

$$\Delta f_{00} = -\gamma_{00}F_0a_0 \tag{4}$$

where

$$\gamma_{00} = +(k_3x_0 - k_1y_0)x_0 + (k_2y_0 - k_1x_0)y_0 + (1/A) \tag{5}$$

γ_{00} will always be positive, since, if F_0 represents tension (i.e., is positive), the force a_0F_0 will produce compression at P_0. It should be noted that γ_{00} is exclusively a function of the geometric properties of the original section. From Eq. (4) it can be seen that $-\gamma_{00}F_0$ represents the change in stress due to a unit area at P_0.

Area and Stress at Different Points

In the above analysis an area was added at P_0 to reduce stress at P_0. Suppose it is desired to determine how much change in stress will occur at point P_1 having coordinates x_1, y_1 as a result of the addition of a_0 at P_0. In this case Eq. (4) becomes:

$$\Delta f_{10} = -\gamma_{10} F_0 a_0 \tag{6}$$

the subscripts indicating that the stress change at P_1 is due to the addition of a_0 at P_0, where

$$\gamma_{10} = +(k_3 x_0 - k_1 y_0)x_1 + (k_2 y_0 - k_1 x_0)y_1 + (1/A) \tag{7}$$

It should be noted that $\gamma_{10} = \gamma_{01}$.

Several Points Considered Simultaneously

Suppose now areas are to be altered (a deduction of area being equivalent to the addition of a negative area) at several points simultaneously and it is decided to add these areas in such a way as to make the stress changes at points P_0, P_1, P_2, equal Δf_0, Δf_1, Δf_2, respectively. The following simultaneous equations can be written.

$$\left.\begin{aligned} \Delta f_0 &= \Delta f_{00} + \Delta f_{01} + \Delta f_{02} \\ \Delta f_1 &= \Delta f_{10} + \Delta f_{11} + \Delta f_{12} \\ \Delta f_2 &= \Delta f_{20} + \Delta f_{21} + \Delta f_{22} \end{aligned}\right\} \tag{8}$$

Final Stresses Known

If the final stresses at each point are known (or can be assumed) for each loading for which each of the above equations is written—i.e., if the F's are known in each equation, Eqs. (8) become:

$$\left.\begin{aligned} \Delta f_0 &= -\gamma_{00} F_0 a_0 - \gamma_{01} F_1 a_1 - \gamma_{02} F_2 a_2 \\ \Delta f_1 &= -\gamma_{10} F_0 a_0 - \gamma_{11} F_1 a_1 - \gamma_{12} F_2 a_2 \\ \Delta f_2 &= -\gamma_{20} F_0 a_0 - \gamma_{21} F_1 a_1 - \gamma_{22} F_2 a_2 \end{aligned}\right\} \tag{9}$$

In this case the only unknowns are the areas, so Eqs. (9) are linear simultaneous equations and a solution presents no difficulty.

Several Points and Several Conditions

In most actual cases all the final stresses are not known. Usually it is desired to adjust a stress at one point in one loading condition and at some other point in some different condition. The problem and method of procedure can be best illustrated by a definite case. Suppose F_0 is known for Condition I and F_1 and F_2 for Condition II. Since $F_0 = f_0 + \Delta f_0$ or $\Delta f_0 = F_0 - f_0$ and $\Delta f_1 = F_1 - f_1$, etc., Eqs. (9) may be written, reversing signs,

$$\text{Cond. I.} \left\{\begin{aligned} +f_{0_I} - F_{0_I} &= +\gamma_{00} a_0 F_{0_I} + \gamma_{01} a_1 F_{1_I} + \gamma_{02} a_2 F_{2_I} \\ +f_{1_I} - F_{1_I} &= +\gamma_{10} a_0 F_{0_I} + \gamma_{11} a_1 F_{1_I} + \gamma_{12} a_2 F_{2_I} \\ +f_{2_I} - F_{2_I} &= +\gamma_{20} a_0 F_{0_I} + \gamma_{21} a_1 F_{1_I} + \gamma_{22} a_2 F_{2_I} \end{aligned}\right. \tag{10}$$

$$\text{Cond. II.} \left\{\begin{aligned} +f_{0_{II}} - F_{0_{II}} &= +\gamma_{00} a_0 F_{0_{II}} + \gamma_{01} a_1 F_{1_{II}} + \gamma_{02} a_2 F_{2_{II}} \\ +f_{1_{II}} - F_{1_{II}} &= +\gamma_{10} a_0 F_{0_{II}} + \gamma_{11} a_1 F_{1_{II}} + \gamma_{12} a_2 F_{2_{II}} \\ +f_{2_{II}} - F_{2_{II}} &= +\gamma_{20} a_0 F_{0_{II}} + \gamma_{21} a_1 F_{1_{II}} + \gamma_{22} a_2 F_{2_{II}} \end{aligned}\right. \tag{10}$$

The unknowns in the above are a_0, a_1, a_2, F_{1_I}, F_{2_I}, and $F_{0_{II}}$. Since there are six equations and six unknowns, a solution is possible, but the above equations are not linear.

Methods of Solution

Method (1)—Iteration

The most straightforward and also one of the quickest methods of solution is by iteration. This method revolves around the fact that, if approximate values for all but one of the unknowns are inserted in any one of the equations, the equation may then be solved for that unknown and an approximate value of that variable obtained. If the coefficient of the unknown being solved for is by far the largest in absolute value appearing in the equation, any errors that exist in the approximate values being used for the other variables will be reduced by successive applications of the process. The largest coefficients in this case will lie along the diagonal, since the addition of area at a point P_0 will always affect the stress at P_0 more than the stress at some other point, say P_1, so γ_{00} will be larger than γ_{01} and the product $\gamma_{00} F_0$—which is then the coefficient of a_0—will be larger than $\gamma_{01} F_0$. This method is illustrated by an example problem later in the article.

Method (2)

Another method[1] is as follows: In Eqs. (9) it should be noted that $F_0 a_0$, $F_1 a_1$, and $F_2 a_2$ always appear together on the right side of the equations. Hence, these equations may be solved for the (Fa)'s in terms of the Δf's by the usual process of solution of simultaneous linear equations. This yields:

$$\left.\begin{aligned} a_0 F_0 &= -A_{00}\Delta f_0 - A_{01}\Delta f_1 - A_{02}\Delta f_2 \\ a_1 F_1 &= -A_{10}\Delta f_0 - A_{11}\Delta f_1 - A_{12}\Delta f_2 \\ a_2 F_2 &= -A_{20}\Delta f_0 - A_{21}\Delta f_1 - A_{22}\Delta f_2 \end{aligned}\right\} \tag{11}$$

where A_{00} is the minor determinant of γ_{00} divided by the determinant of the system. An easy way to obtain these values is to solve the matrices:

$$\begin{vmatrix} \gamma_{00} & \gamma_{01} & \gamma_{02} & 1 \\ \gamma_{10} & \gamma_{11} & \gamma_{12} & 0 \\ \gamma_{20} & \gamma_{21} & \gamma_{22} & 0 \end{vmatrix} \quad \begin{vmatrix} \gamma_{00} & \gamma_{01} & \gamma_{02} & 0 \\ \gamma_{10} & \gamma_{11} & \gamma_{12} & 1 \\ \gamma_{20} & \gamma_{21} & \gamma_{22} & 0 \end{vmatrix} \quad \begin{vmatrix} \gamma_{00} & \gamma_{01} & \gamma_{02} & 0 \\ \gamma_{10} & \gamma_{11} & \gamma_{12} & 0 \\ \gamma_{20} & \gamma_{21} & \gamma_{22} & 1 \end{vmatrix} \tag{12}$$

Solution by the Crout method[1] is preferable, since the major part of the auxiliary matrix only need be computed once in this case. Also the fact that the matrix is symmetric simplifies the computations.

Since $\Delta f = F - f$, Eqs. (11) expand into

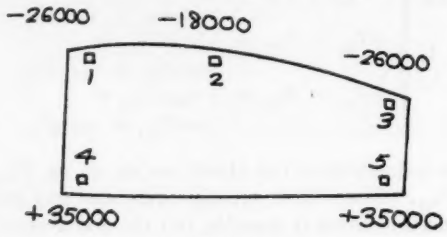

FIG. 2.

$$\left.\begin{aligned} a_0F_0 &= B_0 - A_{00}F_0 - A_{01}F_1 - A_{02}F_2 \\ a_1F_1 &= B_1 - A_{10}F_0 - A_{11}F_1 - A_{12}F_2 \\ a_2F_2 &= B_2 - A_{20}F_0 - A_{21}F_1 - A_{22}F_2 \end{aligned}\right\} \quad (13)$$

where $B_0 = A_{00}f_0 + A_{01}f_1 + A_{02}f_2$, etc.

The first of Eqs. (13) may now be divided by F_0, the second by F_1, and the third by F_2 leaving the areas alone on the left side. Eqs. (13) written for Condition I may then be equated to a similar set for Condition II, thus eliminating the areas from the computation. The resulting equations in the F's can then be solved by iteration.

Limits of Choice

When the stresses F are selected, they must be consistent with possible positions of the neutral axis. For example the stresses indicated in Fig. 2 could not actually occur, since no position of the neutral axis could simultaneously cause stresses in stringers ① and ③ of −26,000 and −18,000 lbs. per sq.in. in stringer ②. Similarly, the angle between the neutral axis in Condition I and the neutral axis in Condition II must not exceed possibilities.

Accuracy of Method

Inaccuracies are of course introduced by the use of point areas, which neglects the moment of each area about its own centroid. This is on the conservative side, however. Also, after the needed point areas have been computed, it is necessary to spread these areas over the neighboring portions of the section, which is strictly an exercise of judgment. Aside from these effects, the method is exact.

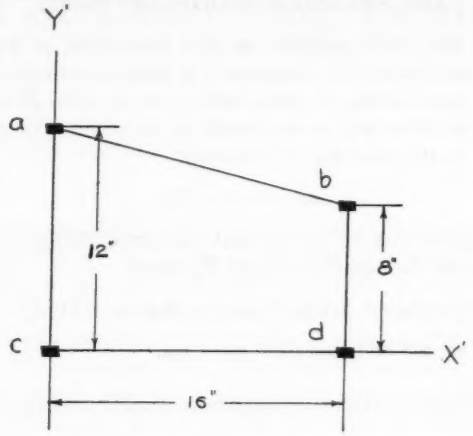

FIG. 3.

CONCLUSIONS

It should be noted that the formulas developed in this article only apply to structures that act as simple beams for which the stresses are given in the linear equation (Eq. (1)). Although the formulas are shown for three-point areas only, the method is general and can be extended to apply to any number of points. Also, the fundamental principle of the method can be extended to cover the analysis of frames by the column analogy method or, in fact, any redundant structure. Example problems follow illustrating its application.

EXAMPLE PROBLEM 1

Fig. 3 shows a cross section of an unsymmetric one-cell box beam with four corner flange members a, b, c, and d. Moments about the axes are: $M_x = 350{,}000$ in.lbs. and $M_y = -80{,}000$ in.lbs. Positive moments produce compression on the positive sides of the axes.

Calculation of Section Properties

Mem.	Area A	y'	x'	Ay'	Ax'	Ay'^2	Ax'^2	$Ax'y'$
"a"	1.0	12	0	12.0	0	144	0	0
"b"	0.5	8	16	4.0	8.0	32	128	64.0
"c"	0.8	0	0	0	0	0	0	0
"d"	0.3	0	16	0	4.8	0	76.8	0
Σ	2.6			16.0	12.8	176.0	204.8	64.0

$\bar{x} = \sum Ax'/\sum A = 12.8/2.6 = 4.93 \qquad \bar{y} = \sum Ay'/\sum A = 16.0/2.6 = 6.16$

$I_x = 176 - 6.16 \times 16 = 77.4$

$I_y = 204.8 - 4.93 \times 12.8 = 141.8$

$I_{xy} = 64 - 4.93 \times 6.16 \times 2.6 = -14.7$
$k_1 = I_{xy}/(I_x I_y - I_{xy}^2) = -14.7/[77.4 \times 141.8 - (14.7)^2] = -14.7/10{,}745 = -0.00137$
$k_2 = I_y/(I_x I_y - I_{xy}^2) = 141.8/10{,}745 = +0.01315$
$k_3 = I_x/(I_x I_y - I_{xy}^2) = 77.4/10{,}745 = +0.00720$

Computation of Stresses

$$f = -(k_3 M_y - k_1 M_x)x - (k_2 M_x - k_1 M_y)y$$

Stringer "a"

$$x = -4.93 \qquad y = +5.84$$

$f = -(-0.00720 \times 80{,}000 + 0.00137 \times 350{,}000)(-4.93) - (0.01315 \times 350{,}000 - 0.00137 \times 80{,}000)5.84 =$
$+95(-4.93) - 4491(5.84) = -26{,}670$ lbs. per sq.in.

Stringer "b"

$$x = +11.07 \qquad y = +1.84$$
$$f = +95 \times 11.07 - 4{,}491 \times 1.84 = -7{,}170 \text{ lbs. per sq.in.}$$

Stringer "c"

$$x = -4.93 \qquad y = -6.16$$
$$f = +95(-4.93) - 4{,}491(-6.16) = +27{,}133 \text{ lbs. per sq.in.}$$

Stringer "d"

$$x = +11.07 \qquad y = -6.16$$
$$f = +95(11.07) - 4{,}491(-6.16) = +28{,}450 \text{ lbs. per sq.in.}$$

Suppose the allowable stress for Stringer "a" is only $-22{,}100$ lbs. per sq.in. and it is desired to add sufficient area at this point to reduce the stress at "a" from $-26{,}670$ to $-22{,}100$ lbs. per sq.in. This represents a change ($= \Delta f$) of $+4{,}570$ lbs. per sq.in.

Calculation of Correction Area to Be Added at "a"

$$x_a = -4.93 \qquad y_a = +5.84$$

Eq. (5) gives:

$\gamma_{aa} = +(-0.00720 \times 4.93 + 0.00137 \times 5.84)(-4.93) + (0.01315 \times 5.84 - 0.00137 \times 4.93)5.84 + 1/$
$-0.0274(-4.93) + 0.06985(5.84) + 0.385 = +0.135 + 0.406 + 0.385 =$

Eq. (4) gives:

$$a_a = \frac{-\Delta f_{aa}}{\gamma_{aa} F_a} = \frac{-(+4{,}570)}{(0.926)(-22{,}100)} = 0.224 \text{ sq.in.}$$

Recalculation of Section Properties

Mem.	Area A	y'	x'	Ay'	Ax'	Ay'^2	Ax'^2	$Ax'y'$
"a"	1.224	12	0	14.7	0	176.2	0	0
"b"	0.5	8	16	4.0	8.0	32	128	64.0
"c"	0.8	0	0	0	0	0	0	0
"d"	0.3	0	16	0	4.8	0	76.8	0
Σ	2.824			18.7	12.8	208.2	204.8	64.0

$\bar{x} = \Sigma Ax/\Sigma A = 12.8/2.824 = 4.53 \qquad \bar{y} = \Sigma Ay/\Sigma A = 18.7/2.824 = 6.62$
$I_x = 208.2 - 6.62 \times 18.7 = +84.2$
$I_y = 204.8 - 4.53 \times 12.8 = +147.1$
$I_{xy} = 64.0 - 2.824 \times 4.53 \times 6.62 = -20.5$
$k_1 = I_{xy}/(I_x I_y - I_{xy}^2) = \dfrac{-20.5}{84.2 \times 147.1 - (20.5)^2} = \dfrac{-20.5}{11{,}980} = -0.00171$
$k_2 = I_y/(I_x I_y - I_{xy}^2) = +147.1/11{,}980 = +0.01225$
$k_3 = I_x/(I_x I_y - I_{xy}^2) = +84.2/11{,}980 = +0.00703$

Stress at Stringer "a"

$$x = -4.53 \qquad y = 5.38$$

$$f = -(-0.00703 \times 80{,}000 + 0.00171 \times 350{,}000)(-4.53) - (+0.01225 \times 350{,}000 - 0.00171 \times 80{,}000)(5.38)$$
$$= -35(-4.53) - 4{,}143(5.38) = -22{,}040 \text{ lbs. per sq.in.}$$

The slight difference between this value and $-22{,}100$ is due to slide rule errors.

EXAMPLE PROBLEM 2

In this problem two loading conditions will be applied to the section of problem 1.

Cond. I $\quad M_x = +350{,}000$ in.lbs.
$\qquad\qquad M_y = -80{,}000$ in.lbs.

Cond. II $\quad M_x = -180{,}000$ in.lbs.
$\qquad\qquad M_y = +36{,}000$ in.lbs.

The maximum allowable compressive stress is $-22{,}100$ lbs. per sq.in. and the maximum allowable tensile stress is $+50{,}000$ lbs. per sq.in. The stresses of the stringers in Condition II are:

Stringer "a"

$$f = -(0.0072 \times 36{,}000 - 0.00137 \times 180{,}000)(-4.93) - (-0.01315 \times 180{,}000 + 0.00137 \times 36{,}000)(+5.84)$$
$$= -13(-4.93) + 2{,}311(+5.84) = +13{,}564$$

Stringer "b"

$$f = -13(+11.07) + 2{,}311(+1.84) = +4{,}106$$

Stringer "c"

$$f = -13(-4.93) + 2{,}311(-6.16) = -14{,}136$$

Stringer "d"

$$f = -13(+11.07) + 2{,}311(-6.16) = -14{,}344$$

In Condition I the allowable compressive stress is exceeded at Stringer "a," hence area must be added there to bring the stress down. In both Conditions I and II stresses at "c" and "d" could be increased so area may be removed at these two stringers. Condition II shows the lowest margins for these stringers so the second system of equations will be written for Condition II. The γ's are dependent only upon the geometric properties of the section and are therefore the same for both conditions. However, if the section properties were different for $\pm M_x$, a set of γ's would be needed for each.

Computation of γ's (Eqs. (5) and (7))

$$\gamma_{aa} = +[+0.00720(-4.93) + 0.00137(+5.84)] \times (-4.93) + [+0.01315(+5.84) + 0.00137 \times (-4.93)] (+5.84) + 1/2.6 = -0.0274 \times (-4.93) + 0.0698(+5.84) + 0.385 = +0.926$$

$$\gamma_{ca} = -0.0274(-4.93) + 0.0698(-6.16) + 0.385 = +0.090$$

$$\gamma_{da} = -0.0274(+11.07) + 0.0698(-6.16) + 0.385 = -0.346$$

$$\gamma_{ac} = \gamma_{ca} = +0.090$$

$$\gamma_{cc} = +[0.00720(-4.93) + 0.00137(-6.16)] \times (-4.93) + [+0.01315(-6.16) + 0.00137 \times (-4.93)] (-6.16) + 1/2.6 = -0.0438 \times (-4.93) - 0.0878(-6.16) + 0.386 = 1.142$$

$$\gamma_{dc} = -0.0438(+11.07) - 0.0878(-6.16) + 0.385 = +0.441$$

$$\gamma_{ad} = \gamma_{da} = -0.346$$

$$\gamma_{cd} = \gamma_{dc} = +0.441$$

$$\gamma_{dd} = +[+0.00720(+11.07) + 0.00137(-6.16)] \times (+11.07) + [+0.01315(-6.16) + 0.00137 \times (+11.07)](-6.16) + 1/2.6 = +0.0710 \times (+11.07) - 0.0659(-6.16) + 0.385 = +1.575$$

The known stresses in Eqs. (10) become, for this problem:

$$f_{a_I} = -26{,}670 \quad f_{a_{II}} = +13{,}564 \quad F_{a_I} = -22{,}100$$
$$f_{c_I} = +27{,}133 \quad f_{c_{II}} = -14{,}136 \quad F_{c_{II}} = -22{,}100$$
$$f_{d_I} = +28{,}450 \quad f_{d_{II}} = -14{,}344 \quad F_{d_{II}} = -22{,}100$$

Rough Approximation of Area Changes

Assume that the load carried by the stringer is unchanged.

Stringer	Condition	Formula	a
"a"	I	$-26{,}670 \times 1.0 = -22{,}100(1.0 + a_a)$	$+0.21$
"c"	II	$-14{,}136 \times 0.8 = -22{,}100(0.8 + a_c)$	-0.287
"d"	II	$-14{,}344 \times 0.3 = -22{,}100(0.3 + a_d)$	-0.105

First Approximation of Unknown F's

From the first of Eqs. (10) Condition II:

$$F_{a_{II}} - 13{,}564 = -0.930(0.21)F_{a_{II}} - 0.089(-0.287) \times (-22{,}100) + 0.346(-0.105)(-22{,}100)$$
$$F_{a_{II}}(1 + 0.195) = 13{,}564 - 562 + 800 = +13{,}802$$
$$F_{a_{II}} = +11{,}500$$

From the last two Eqs. (10) Condition I:

$$F_{c_I} - 27{,}133 = -0.089(0.21)(-22{,}100) - 1.142 \times (-0.287)F_{c_I} - 0.441(-0.105)F_{d_I}$$
$$F_{d_I} - 28{,}450 = +0.346(0.21)(-22{,}100) - 0.441 \times (-0.287)F_{c_I} - 1.57(-0.105)F_{d_I}$$
$$0.673F_{c_I} - 0.046F_{d_I} = +27{,}545$$
$$-0.127F_{c_I} + 0.836F_{d_I} = +26{,}840$$
$$-0.673F_{c_I} + 4.42F_{d_I} = +142{,}000$$
$$+4.374F_{d_I} = +169{,}545$$
$$F_{d_I} = +38{,}700 \text{ lbs. per sq.in.}$$

$$F_{c_I} = (+0.046 \times 38{,}700 + 27{,}545)/0.673 = +43{,}500 \text{ lbs. per sq.in.}$$

TABLE 1

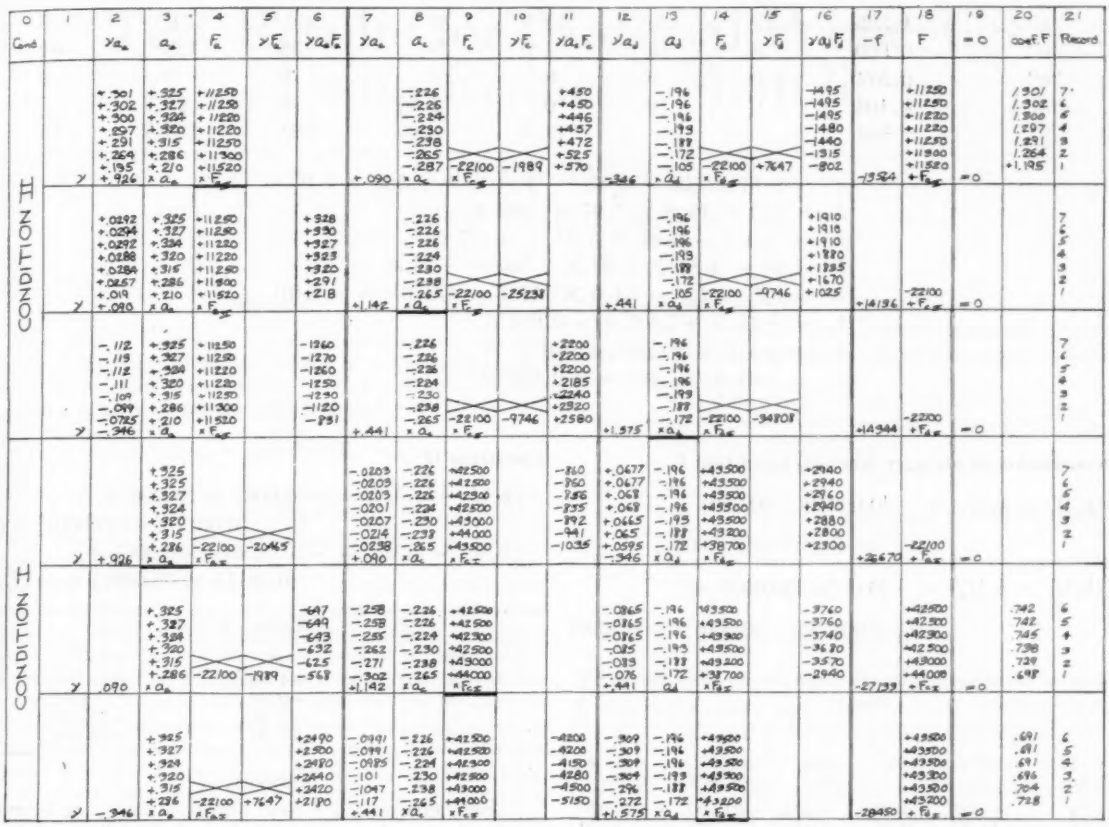

EXPLANATION OF TABLE 1

Table 1 shows the solution of Eqs. (10) by the method of iteration. The computation is started with the first of the equations for Condition II, since two stresses F_{cII} and F_{dII} are known exactly for this equation.

The formula itself is written in the lowest line of each group of figures, while first and subsequent approximations are written above the respective variables as they are obtained. Crosses are placed above exact values to indicate that no further computations are required.

Approximate and exact values (if they are known) are inserted for all unknowns except the one being solved for, which, in the table, is heavily underlined. The approximate values most recently obtained are, of course, used in each case. The unknown being solved for should have the largest coefficient in the equation and lies along the diagonal, as previously explained. In the six equations each one is solved for a different unknown, so in a single cycle of computations improvement is made in the approximate values of each variable. To assist computation of the terms of the form γaF the product γa, or γF is first written separately and combined later to obtain a complete term.

The values for γa are entered in the column above γ to save space (refer to Cols. $(2)_{II}$, $(7)_{I}$, $(12)_{I}$). Also, when a variable being solved for appears in two places in an equation, as does F_{aII} in the first of Eqs. (10), Condition II, rather than change the form of the equation by combining terms, the coefficient of the variable in question is shown in a separate column (refer to Col. (20)). Col. (21) shows a record of the successive cycles of approximation. The process is continued until a reasonable convergence is obtained. To check the results the section properties are recomputed.

Recalculation of Section Properties

Mem.	Area A	y'	x'	Ay'	Ax'	Ay'^2	Ax'^2	$Ax'y'$
"a"	1.325	12	0	15.9	0	191	0	0
"b"	0.500	8	16	4.0	8	32	128	64
"c"	0.574	0	0	0	0	0	0	0
"d"	0.104	0	16	0	1.67	0	26.7	0
Σ	2.503			19.9	9.67	223	154.7	64

$$\bar{x} = 9.67/2.503 = 3.85 \qquad \bar{y} = 19.9/2.503 = 7.97$$
$$I_x = 223 - 19.9 \times 7.97 = +64.6$$
$$I_y = 154.7 - 9.67 \times 3.85 = +117.5$$
$$I_{xy} = 64 - 3.85 \times 7.97 \times 2.503 = -13.0$$
$$D = I_x I_y - I_{xy}^2 = 64.6 \times 117.5 - (13.0)^2 = +7{,}401$$
$$k_1 = -13.0/+7{,}401 = -0.00175$$
$$k_2 = +117.5/+7{,}401 = +0.0158$$
$$k_3 = +64.6/+7{,}401 = +0.00870$$

Recalculation of Stringer Stresses, Condition I

$$-(k_3M_y - k_1M_x) = -[0.00870(-80{,}000) - (-0.00175)(350{,}000)] = +83$$
$$-(k_2M_x - k_1M_y) = -[0.0158(350{,}000) - (-0.00175)(-80{,}000)] = -5{,}380$$

TABLE 2

(1) Str.	(2) x	(3) y	(4) $83x$	(5) $-5{,}380y$	(6) $=(4)+(5)=f$
"a"	−3.85	+4.03	−320	−21,700	−22,020
"b"	+12.15	+0.03	+1,010	−161	+849
"c"	−3.85	−7.97	−320	+42,700	+42,380
"d"	+12.15	−7.97	+1,010	+42,700	+43,710

Condition II

$$-(k_3M_y - k_1M_x) = -[0.0087 \times 36{,}000 + 0.00175(-180{,}000)] = 0$$
$$-(k_2M_x - k_1M_y) = -[0.0158(-180{,}000) + (0.00175 \times 36{,}000)] = +2777$$

TABLE 3

Str.	y	$+2{,}777y$
"a"	+4.03	+11,200
"b"	+0.03	+83
"c"	−7.97	−22,100
"d"	−7.97	−22,100

REFERENCE

[1] Crout, Prescott D., *A Short Method of Evaluating Determinants and Solving Systems of Linear Equations with Real or Complex Coefficients;* Marchant Methods Paper MM-182, Marchant Calculating Machine Co., Oakland, Calif.

Correction of Aluminum-Alloy Compressive Test Results for Material Properties Using Reduced Moduli

JACOB KAROL*

Curtiss-Wright Corporation

SUMMARY

This paper presents a method of correcting compression test results of aluminum alloys for variation of test material properties from standard, similar to Fig. 1–4 of ANC-5.[1] Whereas the latter is based on the test column curve,[2]

$$f_c = 1.224f_{cy} - 0.0000497(f_{cy})^{3/2}(L/\rho)$$

the method herein uses column curves based on reduced moduli. Correction curves are given for 24S-T Alclad sheet and 75S-T Alclad sheet. A comparison of results using these curves with those obtained using Fig. 1–4 of ANC-5 is given which indicates differences less than ±2 per cent for test ultimate compressive stresses exceeding 70 per cent of the compressive yield stress of the test material, and maximum differences ranging from +8.7 to −4.1 per cent for test ultimate compressive stresses that are between 50 and 60 per cent of the compressive yield stress for the test material. The small differences shown for stresses above 60 per cent of the compressive yield stress are inherently caused by using different column formulas, while the rather large differences shown for stresses below 60 per cent of the compressive yield stress are primarily caused by the erroneous use, in reference 2, of the column formula given above for calculating stresses beyond its point of intersection with the Euler formula.

While the curves presented herein apply directly to sheet-stiffener combinations using formed sheet stiffeners, it is believed that they are sufficiently accurate for sheet-stiffener combinations using extruded stiffeners.

SYMBOLS

The symbols used throughout the paper are presented below.

For the Standard Material

E = compressive primary modulus of elasticity in lbs. per sq.in.
E_r = compressive reduced modulus of elasticity in lbs. per sq. in.
E_s = compressive secant modulus of elasticity in lbs. per sq.in.
E_t = compressive tangent modulus of elasticity in lbs. per sq.in.
E_2 = compressive secondary modulus of elasticity in lbs. per sq.in.
f_c = compressive stress in lbs. per sq.in.
f_c^* = compressive stress for an offset of $0.002/R_{cy}$
f_{cy} = compressive yield stress in lbs. per sq.in.
f_{cu} = compressive ultimate stress in lbs. per sq.in.

For the Test Material

E', E_r', E_s', E_t', E_2', f_c', f_{cy}', f_{cu}' are the corresponding designations of the terms defined above. Symbols generally applicable are:

R_{cy} = ratio of the compressive yield stresses = f_{cy}'/f_{cy}
R_{cu} = ratio of the compressive ultimate stresses = f_{cu}'/f_{cu}
L = column length of test specimen in in.
ρ = radius of gyration of test specimen in in.
ϵ = strain in in. per in.
K_r = correction factor for compressive test results based on reduced modulus = f_c/f_c'
K = correction factor for compressive test results from Fig. 1–4 of ANC-5

INTRODUCTION

FISCHEL[3] has shown that use of the reduced modulus in determining the effective width of sheet acting together with the stiffener in sheet-stiffener combinations in compression gives good agreement with the test data. An empiric method developed by the author[4] for calculating the crippling stresses of 24S-T Alclad bent-up sheet stiffeners and 24S-T extruded stiffeners acting alone or in combination with 24S-T Alclad sheet is also based on the reduced modulus. The calculated strengths using this method agree very well with the test data given by Crockett[5] and with test results on stiffened panels with hat stiffeners commonly used in Curtiss-Wright designs. Consequently, it is felt that in the interest of consistency, a method of correction of test data for material properties, as required by ANC-5, should be based on the reduced modulus.

The promising development of various new high-strength aluminum alloys presages their general use in the near future. It seems desirable, therefore, to present a material property correction curve for one of these materials, 75S-T Alclad sheet, for which stress-strain data were available, even though the information cannot be considered final.

The method of obtaining the standard stress-strain curves for 24S-T Alclad and 75S-T Alclad sheet is first discussed. The basic theory for correction of test results to standard is then presented, and the theory is used to develop material property correction curves for the materials mentioned. A comparison is finally made with results using these curves and Fig. 1–4 of ANC-5.

Received December 11, 1944, to have been presented at the I.A.S. Thirteenth Annual Meeting, which was canceled to cooperate with a Government appeal (January, 1945) to refrain from holding conventions and meetings.

* Head, Stress Analysis Unit, Airplane Division, St. Louis Plant.

Standard Stress-Strain Curves for 24S-T Alclad Sheet

A detailed description of the derivation of the standard stress-strain curve for 24S-T Alclad sheet in with-grain compression is given in reference 6. It will suffice here to outline the method used and present the final results.

The standard stress-strain curve is based on the minimum guaranteed mechanical properties given in reference 1 (Revised Edition, December, 1942). In order to determine the stress-strain curve, it is necessary to assume values for three items not given in reference 1—namely, the compressive proportional limit, the compressive ultimate strength, and the maximum strain. The first is taken equal to the ultimate strength in tension, the second is assumed to be 60 per cent of the compressive yield stress, and the third is assumed to be 0.15 in. per in. The main standard properties of the material in with-grain compression are as follows:

Proportional limit	24,000 lbs. per sq.in.
Yield stress	40,000 lbs. per sq.in.
Ultimate (block) stress	56,000 lbs. per sq.in.
Primary modulus of elasticity	10,500,000 lbs. per sq.in.
Secondary modulus of elasticity	9,500,000 lbs. per sq.in.
Maximum strain	0.15 in. per in.

For stresses below 6,000 lbs. per sq.in., the tangent modulus is equal to the primary modulus. For stresses between 13,000 lbs. per sq.in. and the proportional limit, the tangent modulus is equal to the secondary modulus. For stresses between 6,000 and 13,000 lbs. per sq.in. the tangent modulus follows a reverse curve as indicated in Fig. 10 of the Aluminum Research Laboratories Technical Paper No. 6.[7] Knowing the values of the tangent modulus, the values of the strain for the stress range 0 to 24,000 lbs. per sq.in. have been determined.

For the range of stress from 60 to 110 per cent of the yield stress, or 24,000 to 44,000 lbs. per sq.in., use has been made of the table of strain departures on p. 20, reference 7, in plotting the stress-strain curve. The tangent modulus has been computed from Eq. (1):

$$E_t = \Delta f_c / \Delta \epsilon \qquad (1)$$

where

Δf_c = increment of stress in lbs. per sq.in.
$\Delta \epsilon$ = increment of strain in in. per in.

It has been found that the value of E_t for a stress of 44,000 lbs. per sq.in. is 1,305,000 lbs. per sq.in. A formula for the stress-strain relationship above 44,000 lbs. per sq.in. has been developed which has a horizontal tangent for a stress of 56,000 lbs. per sq.in. and which is tangent to the stress-strain curve previously developed at a stress of 44,000 lbs. per sq.in. It is given by the expression

$$\epsilon = 0.1500 - \left[\frac{(56{,}000 - f_c)^{1/2}}{101 + 6.15\,(56{,}000 - f_c)^{1/2}}\right] \qquad (2)$$

where f_c = assumed stress in lbs. per sq.in. and ϵ = corresponding strain in in. per in.

Differentiating Eq. (2) and inverting, one obtains

$$E_t = df/d\epsilon = \frac{2(56{,}000 - f_c)^{1/2}[101 + 6.15\,(56{,}000 - f_c)^{1/2}]^2}{101} \qquad (3)$$

Having obtained the stress-strain curve and the stress-tangent modulus curve over the entire stress range, the secant modulus has been determined from the formula

$$E_s = f_c/\epsilon \qquad (4)$$

and the reduced modulus found from the formula

$$E_r = 4EE_t/(\sqrt{E} + \sqrt{E_t})^2 \qquad (5)$$

Table 1 presents the stress-strain and elastic moduli values for 24S-T Alclad sheet in with-grain compression, as well as values of f_c/E_r.

Table 1

Standard Stress-Strain and Elastic Moduli Values for 24S-T Alclad Sheet in With-Grain Compression

1 Stress in thousands of lbs. per sq.in. f_c	2 Strain in millionths of in. per in., ϵ	3 Moduli of elasticity in millions of lbs. per sq.in. Tangent, E_t	4 Secant, E_s	5 Reduced, E_r	6 f_c/E_r in millionths of in. per in.
2	190	10.50	10.50	10.50	190
4	381	10.50	10.50	10.50	381
6	571	10.50	10.50	10.50	571
7	666	10.48	10.50	10.49	667
8	762	10.40	10.50	10.45	766
9	859	10.20	10.48	10.35	869
10	959	9.80	10.43	10.15	985
11	1,062	9.60	10.36	10.04	1,096
12	1,167	9.52	10.28	10.00	1,200
13	1,272	9.50	10.22	9.99	1,302
14	1,377	9.50	10.17	9.99	1,402
16	1,588	9.50	10.08	9.99	1,602
18	1,798	9.50	10.01	9.99	1,803
20	2,009	9.50	9.96	9.99	2,003
22	2,219	9.50	9.92	9.99	2,203
24	2,435	9.50	9.86	9.99	2,404
26	2,650	9.00	9.81	9.72	2,674
28	2,880	8.35	9.73	9.33	3,000
30	3,130	7.12	9.58	8.56	3,506
32	3,450	5.45	9.28	7.36	4,348
34	3,880	4.08	8.76	6.19	5,493
36	4,450	3.15	8.09	5.26	6,844
38	5,170	2.46	7.35	4.47	8,501
40	6,110	1.99	6.55	3.86	10,360
42	7,190	1.66	5.84	3.40	12,356
44	8,550	1.305	5.12	2.86	15,380
46	10,300	1.013	4.46	2.36	19,490
48	12,600	0.750	3.81	1.87	25,670
50	16,000	0.513	3.125	1.376	36,340
52	20,800	0.301	2.500	0.883	58,890
54	31,100	0.1254	1.736	0.408	132,400
55	43,000	0.0547	1.280	0.209	263,200
56	150,000	0	0.373	0	∞

Standard Stress-Strain Curves for 75S-T Alclad Sheet

The method used to develop the stress-strain curves for 75S-T Alclad sheet in with-grain compression is similar to that used for 24S-T Alclad sheet. The standard stress-strain curve is based on the minimum guaranteed mechanical properties given in reference 8. The compressive ultimate strength is taken equal to the ultimate strength in tension, the compressive proportional limit is assumed to be 60 per cent of the compressive yield stress, and the maximum strain is assumed to be 0.08 in per in. The main standard properties of the material in with-grain compression are as follows:

Proportional limit	36,000 lbs. per sq. in.
Yield stress	60,000 lbs. per sq. in.
Ultimate (block) stress	72,000 lbs. per sq. in.
Primary modulus of elasticity	10,400,000 lbs. per sq. in.
Secondary modulus of elasticity	9,600,000 lbs. per sq. in.
Maximum strain	0.08 in. per in.

For stresses below the proportional limit, the stress-strain and tangent modulus curves have been constructed as previously described. For the range of stress from 60 to 105 per cent of the yield stress or 36,000 to 63,000 lbs. per sq.in., a study of typical stress-strain curves for 75S-T Alclad sheet indicates that the strain departures from the secondary modulus line agree closely with those given for Alclad 24S-RT sheet in with-grain compression on. p. 20, reference 7. These have been used to plot the stress-strain curve, and the tangent modulus has been calculated using Eq. (1).

The value of E_t for a stress of 62,000 lbs. per sq.in. is found to be 2,190,000 lbs. per sq.in. A formula for the stress-strain relationship above 62,000 lbs. per sq.in. has been developed having a horizontal tangent at a stress of 72,000 lbs. per sq.in. and tangent to the previously derived stress-strain curve at a stress of 62,000 lbs. per sq.in. It is given by the expression,

$$72{,}000 - f = 7.2235 \times 10^{21}(0.08 - \epsilon)^{15.545} \quad (6)$$

and by differentiation, one obtains

$$E_t = df/d\epsilon = 11.2244 \times 10^{22}(0.08 - \epsilon)^{14.545} \quad (7)$$

Having obtained the stress-strain and stress-tangent modulus curves over the entire stress range, the secant modulus and reduced modulus have been computed using Eqs. (4) and (5).

The stress-strain, elastic moduli and f_c/E_r values for 75S-T Alclad in with-grain compression are given in Table 2.

Table 2

Standard Stress-Strain and Elastic Moduli Values for 75S-T Alclad Sheet in with-Grain Compression

1 Stress in thousands of lbs. per sq.in. f_c	2 Strain in millionths of in. per in., ϵ	3 Moduli of elasticity in millions of lbs. per sq.in. Tangent, E_t	4 Secant, E_s	5 Reduced, E_r	6 f_c/E_r in millionths of in. per in.
2	192	10.40	10.40	10.40	192
4	385	10.40	10.40	10.40	385
6	577	10.40	10.40	10.40	577
7	673	10.37	10.40	10.38	674
8	770	10.27	10.39	10.33	774
9	868	10.12	10.37	10.26	878
10	968	9.88	10.33	10.14	987
11	1,070	9.73	10.28	10.06	1,094
12	1,173	9.63	10.23	10.01	1,199
13	1,277	9.60	10.18	9.99	1,302
14	1,381	9.60	10.14	9.99	1,402
16	1,590	9.60	10.06	9.99	1,602
18	1,798	9.60	10.01	9.99	1,802
20	2,006	9.60	9.97	9.99	2,002
22	2,215	9.60	9.93	9.99	2,203
24	2,423	9.60	9.90	9.99	2,403
26	2,631	9.60	9.88	9.99	2,603
28	2,840	9.60	9.86	9.99	2,803
30	3,048	9.60	9.84	9.99	3,004
32	3 256	9.60	9.83	9.99	3,204
34	3,465	9.60	9.81	9.99	3,404
36	3,673	9.60	9.80	9.99	3,604
38	3,886	9.16	9.78	9.75	3,897
40	4,110	8.75	9.73	9.52	4,201
42	4,343	8.32	9.67	9.27	4,529
44	4,591	7.75	9.53	8.93	4,928
46	4,860	7.25	9.47	8.61	5,341
48	5,143	6.58	9.33	8.17	5,879
50	5,471	5.59	9.14	7.44	6,717
52	5,865	4.73	8.87	6.75	7,705
54	6,323	4.08	8.54	6.17	8,752
56	6,851	3.55	8.17	5.66	9,897
58	7,455	3.05	7.78	5.13	11,300
60	8,173	2.63	7.34	4.66	12,880
62	9,021	2.19	6.87	4.12	15,060
64	10,030	1.777	6.38	3.56	17,980
66	11,310	1.358	5.84	2.93	22,510
68	13,080	0.929	5.20	2.203	30,870
70	16,010	0.486	4.37	1.314	53,270
71	61,210	0.254	3.78	0.750	94,690
72	80,000	0	0.90	0	∞

Properties of Families of Stress-Strain Curves for a Particular Material

Probably the chief cause of scatter in the test results on columns made of a particular material is the unavoidable variation in the properties of the material from specimen to specimen and along the length of the individual specimen. If the effect of variation in material properties along the length of the specimen is considered negligible, the variability in strength from specimen to specimen can be corrected for if the stress-strain curves for the materials in the specimens are interrelated.

In reference 2, it is assumed that the stress-strain curves are affinely related—i.e., if one is represented by the function $F(\epsilon, f_c) = 0$, any other curve in the family is represented by the function $F(p\epsilon, qf_c) = 0$, where p and q are constants. If p and q are unequal, the

initial slopes of the two curves, or the primary moduli, will be unequal. As indicated in reference 9, p. 6, the primary modulus of elasticity for aluminum alloys is sensibly constant regardless of variations in fabrication procedure. Therefore, p and q can be assumed equal; the stress-strain curves are consequently similar and can be obtained from one standard curve by simple magnification or reduction of the coordinates.

In reference 2 it is further assumed, as was done by Osgood,[10] that the compressive yield stress is defined for the entire family of curves as the intersection of the curves with a line passing through origin having a slope such that for the standard material the yield thus obtained would be the same as the yield for an offset of 0.002 in. per in. As is shown in Fig. 1, where the mag-

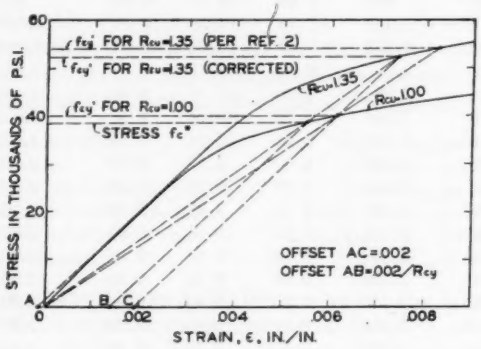

FIG. 1. Relation between R_{cy} and R_{cu}.

nification factor R_{cu} is 1.35, the yield stress obtained for the stronger material is somewhat higher than that for an offset of 0.002 in. per in. In the preparation of the material property correction curves, use is made of the ratios of the yield strength of the specimen material to that of the standard material, R_{cy}. The magnification factor or ratio of the ultimate strengths of the two materials is R_{cu}. From geometric considerations, it is evident that for a given value of R_{cy} the offset on the standard curve is $0.002/R_{cy}$. The stress on the standard curve at the point of intersection is f_c^*. Hence, the ratio $R_{cu} = f_{cy}'/f_c^*$. In order to obtain all the necessary data from the one standard curve, the expression may be written

$$R_{cu} = \left(\frac{f_{cy}'}{f_c^*}\right)\left(\frac{f_{cy}}{f_{cy}}\right) = \left(\frac{f_{cy}'}{f_{cy}}\right)\left(\frac{f_{cy}}{f_c^*}\right) = R_{cy}\left(\frac{f_{cy}}{f_c^*}\right) \quad (8)$$

For the entire range of stress, the column formula for the standard material is

$$f_c = \pi^2 E_r/(L/\rho)^2 \quad (9)$$

Rewriting Eq. (9) in nondimensional form

$$f_c/E_r = \pi^2/(L/\rho)^2 \quad (10)$$

Hence, for a given L/ρ, the value of f_c/E_r is found from Eq. (10), and from a plot of f_c/E_r vs. f_c, the value of f_c is obtained.

For the specimen material, the column formula in nondimensional form is

$$f_c'/E_r' = \pi^2/(L/\rho)^2 \quad (11)$$

To obviate the need of a plot of f_c'/E_r' vs. f_c' in finding f_c', Eqs. (10) and (11) will be considered more closely. For the same value of L/ρ,

$$f_c/E_r = f_c'/E_r' \quad (12)$$

Since the stress-strain curves are similar, the family of curves for f_c'/E_r vs. f_c' will also be similar. Therefore, dividing the abscissas and ordinates of each curve by R_{cu}, there is obtained the single curve $(f_c'/E_r')(1/R_{cu})$ vs. f_c'/R_{cu}. For the standard material, $R_{cu} = 1$, the primes are dropped, and the curve therefore is a plot of f_c/E_r vs. f_c. The value of f_c' may be found as follows: For the particular value of R_{cu}, determine $(f_c'/E_r') \times (1/R_{cu})$. Read value of f_c'/R_{cu} from the curve. Then f_c' is given by the expression

$$f_c' = R_{cu}(f_c'/R_{cu}) \quad (13)$$

Applying this procedure for various values of L/ρ and R_{cu}, one obtains values of f_c' for the specimen materials corresponding to the f_c for the standard material. These values may be plotted as a family of curves similar to Fig. 1–4 of ANC-5 where the abscissas represent $f_c' \div f_{cy}'$ and the ordinates represent f_c/f_c'. It is to be noted that the correction factor K_r, defined as the ratio f_c/f_c', is, from Eq. (12), also equal to E_r/E_r'.

Material Property Correction Curve for 24S-T Alclad Sheet

The data from Table 1 have been used to plot a large scale curve of f_c/E_r vs. f_c. Values of R_{cu} have been obtained for values of R_{cy} varying from 0.90 to 1.35 in increments of 0.05, using Eq. (8), and are given below.

R_{cy}	R_{cu}	R_{cy}	R_{cu}
0.90	0.8884	1.15	1.1699
0.95	0.9443	1.20	1.2264
1.00	1.0000	1.25	1.2830
1.05	1.0569	1.30	1.3402
1.10	1.1134	1.35	1.3982

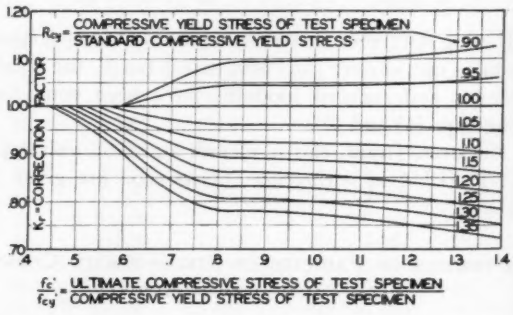

FIG. 2. Correction factors for compression tests on aluminum-alloy specimens (based on reduced modulus of 24S-T Alclad sheet).

For various values of L/ρ ranging from 0 to 65, the values of f_c and f_c' have been found for the values of R_{cu} given above using Eq. (13). The results, plotted as a correction graph similar to Fig. 1–4 of ANC-5, are shown in Fig. 2.

Material Property Correction Curve for 75S-T Alclad Sheet

The data from Table 2 have been used to plot a large scale curve of f_c/E_r vs. f_c. Values of R_{cu} have been obtained using Eq. (8) and are given below.

R_{cy}	R_{cu}	R_{cy}	R_{cu}
0.90	0.8893	1.15	1.1685
0.95	0.9452	1.20	1.2254
1.00	1.0000	1.25	1.2825
1.05	1.0553	1.30	1.3401
1.10	1.1110	1.35	1.3978

It is interesting to note that the corresponding values of R_{cu} for 24S-T Alclad sheet and 75S-T Alclad sheet are practically equal.

Values of f_c and f_c' have been found for the range of L/ρ and R_c as before, using Eq. (13). The results plotted as a correction graph are shown in Fig. 3.

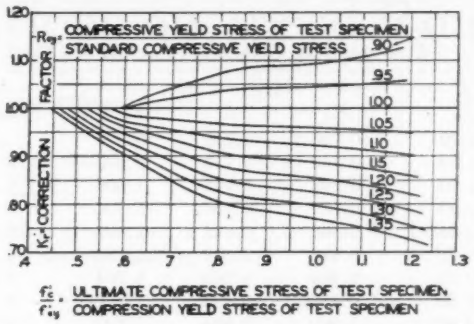

Fig. 3. Correction factors for compression tests on aluminum-alloy specimens (based on reduced modulus of 75S-T Alclad sheet).

Comparison of Results with Fig. 1–4 of ANC-5

Correction factors for 24S-T Alclad sheet for values of f_c'/f_{cy}' ranging from 0.40 to 1.20 in increments of 0.10 have been read from Fig. 2 and Fig. 1–4 of ANC-5 and are given in Table 3. The ratio of the correction factors is shown as K_r/K. Where the value of this ratio is greater than 1, the correction factor as given by

Table 3

Comparison of Correction Factors for 24S-T Alclad from Fig. 2 With Those from Fig. 1–4 of ANC-5

$\frac{f_c'}{f_{cy}'}$	R_{cy} = 1.35			R_{cy} = 1.30			R_{cy} = 1.25		
	K_r	K	K_r/K	K_r	K	K_r/K	K_r	K	K_r/K
1.20	0.757	0.743	1.019	0.780	0.770	1.013	0.808	0.800	1.010
1.10	0.764	0.753	1.015	0.792	0.779	1.017	0.819	0.809	1.012
1.00	0.773	0.765	1.010	0.800	0.790	1.013	0.827	0.818	1.011
0.90	0.779	0.780	0.999	0.805	0.803	1.002	0.831	0.830	1.001
0.80	0.782	0.796	0.982	0.807	0.818	0.987	0.832	0.845	0.985
0.70	0.821	0.819	1.002	0.845	0.839	1.007	0.869	0.863	1.007
0.60	0.898	0.849	1.057	0.917	0.866	1.059	0.934	0.887	1.053
0.50	0.970	0.892	1.087	0.980	0.904	1.084	0.990	0.923	1.073
0.40	1.000	0.955	1.047	1.000	0.964	1.037	1.000	0.975	1.026
$\frac{f_c'}{f_{cy}'}$	R_{cy} = 1.20			R_{cy} = 1.15			R_{cy} = 1.10		
	K_r	K	K_r/K	K_r	K	K_r/K	K_r	K	K_r/K
1.20	0.841	0.834	1.008	0.875	0.870	1.006	0.915	0.910	1.005
1.10	0.849	0.841	1.010	0.881	0.875	1.007	0.918	0.914	1.004
1.00	0.855	0.849	1.007	0.886	0.882	1.005	0.921	0.919	1.002
0.90	0.860	0.860	1.000	0.888	0.891	0.997	0.923	0.924	0.999
0.80	0.862	0.873	0.987	0.892	0.902	0.989	0.926	0.932	0.994
0.70	0.897	0.889	1.009	0.922	0.916	1.007	0.945	0.942	1.003
0.60	0.948	0.910	1.042	0.963	0.934	1.031	0.977	0.956	1.022
0.50	1.000	0.940	1.064	1.000	0.957	1.045	1.000	0.973	1.028
0.40	1.000	0.987	1.013	1.000	0.996	1.004	1.000	1.000	1.000
$\frac{f_c'}{f_{cy}'}$	R_{cy} = 1.05			R_{cy} = 0.95			R_{cy} = 0.90		
	K_r	K	K_r/K	K_r	K	K_r/K	K_r	K	K_r/K
1.20	0.955	0.952	1.003	1.048	1.050	0.998	1.106	1.110	0.996
1.10	0.957	0.954	1.003	1.045	1.047	0.998	1.100	1.103	0.997
1.00	0.959	0.958	1.001	1.044	1.043	1.001	1.097	1.096	1.001
0.90	0.960	0.961	0.999	1.044	1.039	1.005	1.095	1.088	1.006
0.80	0.961	0.966	0.995	1.043	1.035	1.008	1.090	1.077	1.012
0.70	0.971	0.971	1.000	1.027	1.029	0.998	1.052	1.064	0.989
0.60	0.992	0.978	1.014	1.002	1.021	0.981	1.003	1.046	0.959
0.50	1.000	0.986	1.014	1.000	1.010	0.990	1.000	1.023	0.978
0.40	1.000	0.997	1.003	1.000	1.000	1.000	1.000	1.000	1.000

Note: K_r is correction factor from Fig. 2 and K is correction factor from Fig. 1–4 of ANC-5.

TABLE 4

COMPARISON OF CORRECTION FACTORS FOR 75S-T ALCLAD FROM FIG. 3 WITH THOSE FROM FIG. 1–4 of ANC-5

f_c'/f_{cy}'	R_{cy} = 1.35			R_{cy} = 1.30			R_{cy} = 1.25		
	K_r	K	K_r/K	K_r	K	K_r/K	K_r	K	K_r/K
1.20	0.726	0.743	0.977	0.755	0.770	0.981	0.787	0.800	0.984
1.10	0.751	0.753	0.997	0.779	0.779	1.000	0.809	0.809	1.000
1.00	0.769	0.765	1.005	0.797	0.790	1.009	0.824	0.818	1.007
0.90	0.785	0.780	1.006	0.808	0.803	1.006	0.835	0.830	1.006
0.80	0.803	0.796	1.009	0.825	0.818	1.009	0.852	0.845	1.008
0.70	0.848	0.819	1.035	0.867	0.839	1.033	0.888	0.863	1.029
0.60	0.903	0.849	1.064	0.917	0.866	1.059	0.931	0.887	1.050
0.50	0.962	0.892	1.078	0.973	0.904	1.076	0.986	0.923	1.068
0.40	1.000	0.955	1.047	1.000	0.964	1.037	1.000	0.975	1.026
f_c'/f_{cy}'	R_{cy} = 1.20			R_{cy} = 1.15			R_{cy} = 1.10		
	K_r	K	K_r/K	K_r	K	K_r/K	K_r	K	K_r/K
1.20	0.822	0.834	0.986	0.859	0.870	0.987	0.902	0.910	0.991
1.10	0.840	0.841	0.999	0.875	0.875	1.000	0.913	0.914	0.999
1.00	0.853	0.849	1.005	0.887	0.882	1.006	0.922	0.919	1.003
0.90	0.863	0.860	1.003	0.895	0.891	1.004	0.928	0.924	1.004
0.80	0.879	0.873	1.007	0.907	0.902	1.006	0.937	0.932	1.005
0.70	0.911	0.889	1.025	0.933	0.916	1.019	0.954	0.942	1.013
0.60	0.947	0.910	1.041	0.962	0.934	1.030	0.973	0.956	1.018
0.50	1.000	0.940	1.064	1.000	0.957	1.045	1.000	0.973	1.028
0.40	1.000	0.987	1.013	1.000	0.996	1.004	1.000	1.000	1.000
f_c'/f_{cy}'	R_{cy} = 1.05			R_{cy} = 0.95			R_{cy} = 0.90		
	K_r	K	K_r/K	K_r	K	K_r/K	K_r	K	K_r/K
1.20	0.948	0.952	0.996	...	1.050	...	...	1.110	...
1.10	0.955	0.954	1.001	1.049	1.047	1.002	1.107	1.103	1.004
1.00	0.959	0.958	1.001	1.044	1.043	1.001	1.093	1.096	0.997
0.90	0.962	0.961	1.001	1.042	1.039	1.003	1.087	1.088	0.999
0.80	0.967	0.966	1.001	1.035	1.035	1.000	1.073	1.077	0.996
0.70	0.975	0.971	1.004	1.020	1.029	0.991	1.042	1.064	0.979
0.60	0.988	0.978	1.010	1.002	1.021	0.981	1.004	1.046	0.960
0.50	1.000	0.986	1.014	1.000	1.010	0.990	1.000	1.023	0.978
0.40	1.000	0.997	1.003	1.000	1.000	1.000	1.000	1.000	1.000

NOTE: K_r is correction factor from Fig. 3 and K is correction factor from Fig. 1–4 of ANC-5.

ANC-5 is conservative in comparison with that found from Fig. 2, and where it is less than 1, the correction factor is unconservative. From Table 3, it is seen that for a value of $f_c'/f_{cy}' = 0.50$ and $R_{cy} = 1.35$, the correction factor from ANC-5 is 8.7 per cent conservative. In the range of usual column design stresses, say 70 to 120 per cent of the specimen yield stress, it is seen that the ratio varies from 0.982 to 1.019, so that the correction factors from ANC-5 are within ±2 per cent of those from Fig. 2.

Correction factors for 75S-T Alclad sheet are compared with the corresponding values from Fig. 1–4 of ANC-5 in Table 4. From this table, it is seen that for a value of $f_c'/f_{cy}' = 0.50$ and $R_{cy} = 1.35$, the correction factor from ANC-5 is 7.8 per cent conservative. In the range of usual column design stresses, the ratio of the correction factors varies from 0.977 to 1.035, so that correction factors from ANC-5 are within ±3.5 per cent of the corresponding values from Fig. 3.

CONCLUDING REMARKS

It has been shown that for the usual range of design stresses, factors for correcting test column allowables for variation of test specimen material from standard based on the reduced modulus are not appreciably different from those obtained from ANC-5. Where the allowable stress is in the vicinity of the proportional limit, the correction factors obtained from ANC-5 are quite conservative.

From the data in Tables 1 and 2, it is possible to derive material property correction curves based on the tangent modulus, using the procedure outlined in the paper. The resulting curves would probably not differ greatly from Figs. 2 and 3.

Since the ratio f_{cu}/f_{cy} is 1.40 for 24S-T Alclad sheet and 1.20 for 75S-T Alclad sheet, it is believed that Figs. 2 and 3 can be used satisfactorily to correct test results for other aluminum alloys. Thus, for 24S-T extrusions, the ratio f_{cu}/f_{cy} is about 1.50; hence, Fig. 2 should be used.

For 14S-T extrusions, Fig. 3 should be used, since the ratio f_{cu}/f_{cy} is about 1.20.

(*Continued on page 328*)

Effect of Pressure Variations on Speed Runs

RICHARD M. HEAD*

Lockheed Aircraft Corporation

SUMMARY

Inaccuracies in flight-test data obtained from speed runs may arise from the fact that runs made at a constant pressure altitude, constant power, etc., are actually not at level flight conditions because of pressure fields and their movements in the atmosphere. This problem is analyzed and curves show the magnitude of the error involved for certain atmospheric conditions.

INTRODUCTION

IT HAS BEEN NOTED on numerous occasions that, in speed runs at constant power and constant pressure altitude, a different value of the velocity is obtained if the run is made in one direction than if it is in the opposite direction. In one particular instance, a variation of 6 m.p.h. at 300 m.p.h. was so obtained. An investigation has been made in order to determine how much of the discrepancy in these values can be attributed to pressure variations in the atmosphere—in the form of high- and low-pressure areas and their movements. If a speed run is made at constant-pressure altitude in the direction of the pressure gradient (toward the center of a low-pressure area), the ship will be flying "downhill," since the pressure in the direction of flight is continually decreasing and, hence, the airplane must lose altitude in order for the altimeter to read a constant value. Similarly, if the airplane is flying in the opposite direction (away from a low-pressure center or toward a high-pressure center), it will actually be climbing, even though the pressure altitude remains constant. Furthermore, a changing pressure field (resulting from the movement of the pressure centers) could possibly aggravate the situation. Both of these effects—that of pressure fields as well as their movements—will be considered in the following analysis.

ANALYSIS OF THE PROBLEM

In the following analysis, all pressure changes are assumed to be additive, and the maximum changes found in this vicinity (San Fernando Valley) over a 5-year period are used to obtain an extreme case to determine whether or not the magnitude of this effect is sufficient to account for the discrepancy in the aforementioned values.

The equation for the total rate of change of pressure for a body moving through the air is (assuming the direction of motion is along the positive x-axis and normal to the isobars):

$$Dp/Dt = (\partial p/\partial t) + u(\partial p/\partial x)$$

where u is the velocity in the direction of the pressure gradient and $\partial p/\partial x$ is the pressure gradient along the horizontal x-axis.

The partial change of pressure with respect to time is made up of two components: the diurnal (daily) change, and the change due to a moving pressure field.

The maximum rate of change of the diurnal is 1.5 MB. per 3 hours (at about 2:00 p.m.). (MB. = 1,000 dynes/cm.^{2})

The highest tendency (rate of change of pressure due to a moving pressure field) observed in this vicinity is 5.4 MB. per 3 hours (February 28, 1941), thus

$$\partial p/\partial t = 0.5 \text{ MB. per hour} + 1.8 \text{ MB. per hour} = 2.3 \text{ MB. per hour}$$

The greatest change of pressure with respect to distance is obtained when the gradient is in the direction of flight, the highest observed value being 0.2 MB. per mile (February 16, 1939).

Using these values, the total rate of change of pressure is:

$$Dp/Dt = 2.3 + U(0.2) \text{ MB. per hour} \qquad (1)$$

The total rate of change for different speeds can thus be determined, from which can be obtained the change in pressure and, hence, feet of altitude gained or lost for a given length run. Therefore, the actual flight angle versus speed for the given conditions is easily calculable (Fig. 1).

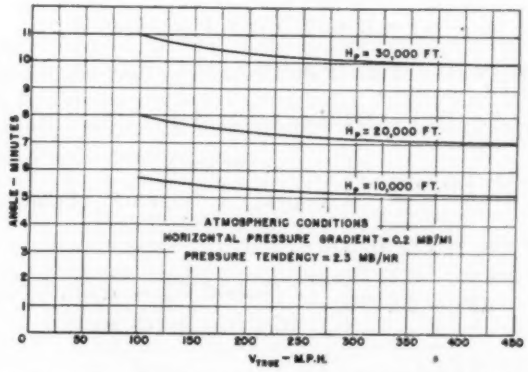

FIG. 1. Departure from level flight vs. velocity at altitude.

Received July 25, 1944.

* Engineering Flight Test Group. Now Ensign, U.S.N.R., Engineering Branch, Bureau of Aeronautics.

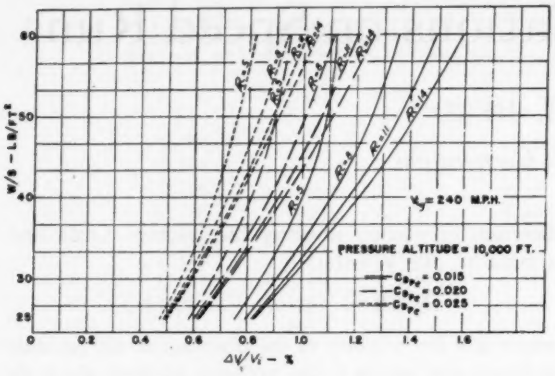

FIG. 2. Error in velocity during speed runs.

For an airplane traveling at 300 m.p.h., this corresponds to the following increases in elevation over 25 miles traversed (if the pressure is increasing in the line of flight):

Pressure Altitude, Ft.	Increase in Elevation per 25 Miles, Ft.
10,000	170
20,000	250
30,000	470

This assumes standard variation of barometric pressure with altitude.

The increase or decrease in velocity due to the angle of flight obtained from curve 1 may be determined from the following analysis:

The standard thrust equation assuming unaccelerated level flight is:

$$T = C_{D_{pe}} qS + (C_L^2/\pi \text{A.R.}_e) qS$$

The additional thrust due to flight at an angle θ to the horizontal is:

$$W \sin\theta = C_{D_{pe}} S(q_G - q_L) + C_L^2 S/\pi \text{A.R.}_e\,(q_G - q_L)$$

where $q_L = q$ for level flight, $q_G = q$ for gliding flight and

$$W \sin\theta = (q_G - q_L)[C_{D_p} S_e + (C_L^2 S/\pi \text{A.R.}_e)]$$

$$(q_G - q_L) = W \sin\theta/[C_{D_{pe}} S + (C_L^2 S/\pi \text{A.R.}_e)]$$

$$V_{i_G}^2 - V_{i_L}^2 = 391 W \sin\theta/[C_{D_{pe}} S + (C_L^2 S/\pi \text{A.R.}_e)]$$

$$V_{T_G}^2 - V_{T_L}^2 = 391 W \sin\theta/[C_{D_{pe}} S + (C_L^2 S/\pi \text{A.R.}_e)]\sigma$$

$$\Delta V^2 - 2\Delta V V_{T_G} = \left[\frac{-391 \sin\theta}{(C_{D_{pe}}/C_L) + (C_L/\pi \text{A.R.}_e)}\right]\left(\frac{W}{S\sigma C_L}\right)$$

for $V_{T_G} = V_{T_L} + \Delta V$

$$\Delta V^2 - 2\Delta V V_{T_G} = \frac{-\sin\theta (V_{T_G} - \Delta V)^2}{(C_{D_{pe}}/C_L) + (C_L/\pi \text{A.R.}_e)}$$

$$\frac{V_{T_G}^2}{(V_{T_G} - \Delta V)^2} = 1 + \frac{\sin\theta}{(C_L/\pi \text{A.R.}_e) + (C_{D_{pe}}/C_L)}$$

$$V_{T_G}^2\left[\frac{1}{V_{T_G}^2} + \frac{2\Delta V}{V_{T_G}^3} + \frac{3\Delta V^2}{V_{T_G}^4} + \cdots\right] = 1 + \frac{\sin\theta}{(C_L/\pi \text{A.R.}_e) + (C_{D_{pe}}/C_L)}$$

Neglecting $3\Delta V^2/V_{T_G}^2$ and higher order terms:

$$2\Delta V/V_{T_G} = \sin\theta/[(C_L/\pi \text{A.R.}_e) + (C_{D_{pe}}/C_L)]$$

therefore,

$$\Delta V = \frac{1}{2}\left[\frac{V_{T_G} \sin\theta}{(C_L/\pi \text{A.R.}_e) + (C_{D_{pe}}/C_L)}\right] \qquad (2)$$

This analysis is based on the following assumptions: (1) parabolic polar; (2) incompressible fluid; (3) engine thrust remains constant; and (4) $W = L(\theta$ small).

Using Eq. (2) in conjunction with Fig. 1 for the particular meteorologic conditions considered, Fig. 2 is developed showing the error in velocity ($\Delta V/V_{T_G}$) for different wing loadings at 10,000 ft. altitude and $V_i = 240$ with aspect ratio, A.R., and effective parasite drag coefficient, $C_{D_{pe}}$, as parameters.

The effect of altitude and velocity on the error is shown in Fig. 3. This variation with altitude assumes, of course, that the pressure field and its movement considered in Eq. (1) extends up through 30,000 ft. altitude.

This condition, in general, may not exist at a given location; however, the gradients used in Eq. (1) may still extend up to this altitude over different localities, and it is the purpose of this analysis to determine the magnitude of the error involved for this particular case in order to find out whether or not it is significant.

Conclusions and Recommendations

From the preceding analysis and curves, it is readily seen that pressure fields and their movements can have an effect on speed runs which cannot be neglected where accurate results are desired. This error will

(*Continued on page 319*)

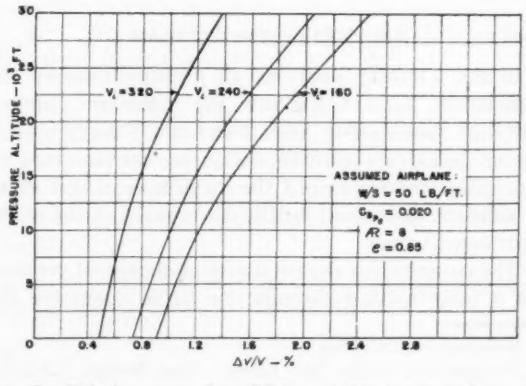

FIG. 3. Velocity error for different indicated velocities vs. pressure altitude.

Operational Methods in Servomechanism Design

WILLIAM E. RESTEMEYER*
University of Cincinnati

ABSTRACT

An important class of automatic control devices whose use is not restricted to any one field is that known as servomechanisms. Defined technically, a servomechanism is an automatic control system having a controlling element actuated by some function of the difference between the actual and desired response of the controlled element. By the use of operational methods in handling physical transients, the servo systems are readily analyzed and quantitative design characteristics obtained.

It is the purpose of this paper to show the use of the Laplace transformation in the analysis and design of servomechanisms. The treatment is divided into three main parts: (a) the fundamental theory of servomechanisms; (b) the Laplace transformation; and (c) application to a simple servomechanism.

Because of military secrecy, the most interesting applications are restricted and cannot be treated publicly. For this reason, the subject matter of this paper is based entirely on accessible literature, and the example chosen is typical of applications in various fields including the military.

THEORY OF SERVOMECHANISMS[1]

IN A BROAD SENSE, automatic control devices are used to replace human labor by supplying power of proper form and accurate amount to perform a given task with little or no direction. In fact, they are usually more reliable and accurate and economically cheaper than their human counterpart.

Automatic control mechanisms may be classified on the basis of the type of control requirements. In the open-cycle type the controlling quantity is independent of the controlled quantity—for example, a time-actuated traffic signal. When the controlling quantity is dependent upon the controlled quantity, the control is of the closed-cycle type. A simple example would be a thermostat. Combinations of both types are also used, such as in a clock-set thermostat.

The power requirements of the two types are quite different. Open-cycle devices are usually quite simple and rugged, since the controlling mechanism has sufficient power to operate the device directly. Closed-cycle devices are usually more complex, since the controlling mechanism is some form of measuring instrument and has insufficient power to operate the device. Hence, some sort of power or torque amplifier is required to give instrument indications at higher power levels. For example, in the automatic piloting of ships or aircraft, a measuring instrument sensitive to compass settings must eventually control the ship itself.

For purposes of technical definition, a servomechanism is an automatic control system having a controlling element actuated by some function of the difference between the actual and desired response of the controlled element. The power-amplifying device that tends to make this difference, or error, zero is called a servomotor or "servo." The component parts can be visualized better with the help of the block diagram in Fig. 1. If, in particular, it is desired to keep the corrected input constant, the servomechanism is called a "regulator."

The physical behavior of the servo and controlled system is always such as to affect the quantity under consideration and its successive rates of change with respect to time. The interrelation between the different quantities and the effects of the system components on them is expressed conveniently in the following manner. If $F(p)$ is the transfer polynomial operator for the servo and if $G(p)$ is the transfer polynomial operator for the system, where $p = d/dt$, then

$$\begin{aligned} e(t) &= i(t) - o(t) \\ c(t) &= F(p)e(t) \\ o(t) &= G(p)[c(t) + d(t)] \end{aligned}$$

Solving for the error as a function of the operators on the input

$$e(t) = [i(t) - G(p)d(t)]/[1 + F(p)G(p)]$$

and

$$o(t) = [F(p)G(p)i(t) + G(p)d(t)]/[1 + F(p)G(p)]$$

Since $G(p)$ is a function of the system and changes only with it, the basic problem of design in automatic control is to determine a servo having the required transfer operator such that the system is stable and the error lies within specified limits.

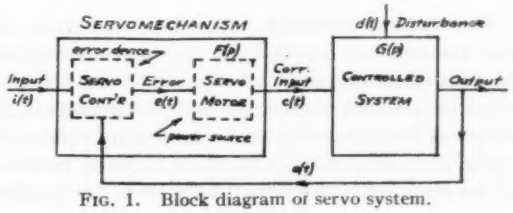

FIG. 1. Block diagram of servo system.

Presented at the National Fall Meeting, I.A.S., Dayton, Ohio, November 9–10, 1944.

* Assistant Professor of Mathematics and Mechanics, College of Engineering and Commerce. Now Ensign, Aircraft Electrical Division, Naval Research Laboratory.

Servo Errors

Servo errors are of two kinds: lag and oscillation. Lag is an average or unidirectional deviation, whereas oscillation is a periodic deviation of the output from the input (Fig. 2).

The amount and kind of error depends on the type of servo used:

Relay or "on-off" type. A correction is suddenly applied and then remains constant over interval of operation. Examples: gyrocompass repeaters, gyrostabilizers, automatic pilots. Both lag and oscillation are present; decreasing the lag increases overshoot.

Finite step or "impulse" type. The correction is made in finite steps at definite time intervals. Examples: recording instruments, controllers for slowly varying quantities. Persistent lag is present but no oscillation.

Continuous type. The correction is applied continuously. Examples: gyrocompass followers. Lag and steady-state error may be corrected by derivative or integral control. Arbitrary oscillation is present with any given decrement depending upon damping. Behavior is less violent than relay type and more rapid than impulse type.

For the continuous-type servo, three kinds of correction are used: proportional, derivative, and integral error control. This terminology refers to the mathematical form of the servo operator $F(p)$:

Proportional	$F(p) = k$	$c(t) = ke(t)$
Derivative	$F(p) = kp$	$c(t) = kpe(t)$
Integral	$F(p) = k/p$	$c(t) = (k/p)e(t)$

In practice, combinations of these types are usually found. Minorsky[2] in 1922 made use of these concepts in the problem of automatic steering of ships.

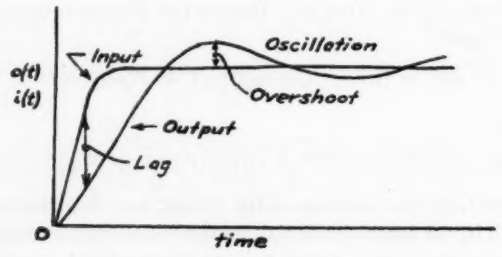

FIG. 2. Types of servo errors.

System Characteristics

Under normal operation, input functions which are quite random are applied to the servomechanism; hence, it becomes necessary to use certain test functions to determine the characteristics and performance of the system for both transient and steady-state conditions. Typical ones are the step function, impulse function, and the sinusoid. Mathematically, then, the problem is this: to solve the higher order differential equation of the physical system subjected to possibly discontinuous test functions with prescribed initial conditions, so as to obtain both steady-state and transient response. From these analytic solutions the relations of the physical quantities comprising the servomechanism are explicitly shown so that lag and oscillation errors may be minimized by proper selection and design and the system be made stable.

By the use of operational mathematics the problem becomes one of routine algebra for lumped constant systems and usually simple ordinary differential equations for distributed constant systems.

THE LAPLACE TRANSFORMATION[3, 4]

Heaviside's operational calculus has been popular with engineers and physicists for some time but is looked upon as a creature of ill repute by the more rigorous mathematician. Truthfully, the rules of procedure were not based on logic but on symbolism and therefore were not always reliable but sometimes meaningless and erratic. The Laplace transformation, however, is mathematically rigorous and has all of the advantages and less of the disadvantages of the Heaviside and other methods.

Mathematically speaking, a transformation expresses a correspondence between quantities. For example, $y = \log_e x$ denotes a transformation "$\log_e$" which establishes a correspondence between the numbers x and their transforms or "logarithms" y. The inverse transformation is given by $x = e^y$.

The Laplace transformation is defined by $\int_0^\infty e^{-st} \times f(t)\,dt = F(s)$, where $F(s)$ is called the Laplace transform of $f(t)$ and is denoted by $F(s) = L[f(t)]$. The quantity s is usually a variable that takes on complex values.

The inverse transformation can be shown to be $f(t) = (1/2\pi i)\int_{c-i\infty}^{c+i\infty} e^{st}F(s)\,ds$, where c is a real constant.

Simple examples of transform pairs are given in Fig. 3.

f(t)	Graph	F(s)
1(t)	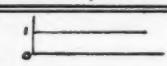	$\frac{1}{s}$
e^{-at}	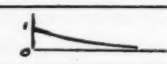	$\frac{1}{s+a}$
sin bt	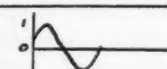	$\frac{b}{s^2+b^2}$
t	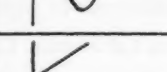	$\frac{1}{s^2}$

FIG. 3. Sample Laplace transforms.

Logarithms are used extensively in arithmetical computation, since problems involving multiplication and division are reduced to simpler problems in addition and subtraction. In an analogous manner, the Laplace transformation is used in the solution of differential and integral equations, since these problems reduce to algebraic relations.

Using the original definition of the Laplace transformation, simple integration by parts gives

$$L[f'(t)] = sF(s) - f(0)$$
$$L[\int f(t)\,dt] = F(s)/s + (1/s)\int f(t)\,dt\big|_{t=0}$$

These operation transforms show clearly the power of the Laplace method in simplifying operations: Differentiation is reduced to multiplication by s and integration corresponds to division by s. Most important of all, the initial conditions are automatically introduced into the problem from the very start. This property is not shared with other operational methods, since the initial values must be zero or else special tricks have to be used.

A third important property is known as the faltung or convolution and has to do with the product of transforms

$$L[\int_0^t f_1(t-x)f_2(x)\,dx] = F_1(s)F_2(s)$$

Its use permits considerable simplification in evaluating inverse transforms by the use of tables of functions and their transforms. This is analogous to the use of tables of logarithms or exponentials or, even better, the use of tables of integrals.

Two additional limiting relations that are extremely useful in the determination of initial and final values are

$$\lim_{s\to\infty} sF(s) = \lim_{t\to 0} f(t)$$
$$\lim_{s\to 0+} sF(s) = \lim_{t\to\infty} f(t)$$

provided $F(s)$ behaves properly. It is interesting to note that the behavior of $f(t)$ for both small and large values of t can be found without actually determining $f(t)$ analytically. The second relation may be used in the determination of steady state conditions.

Summarily, the scheme of solution of a general problem is this

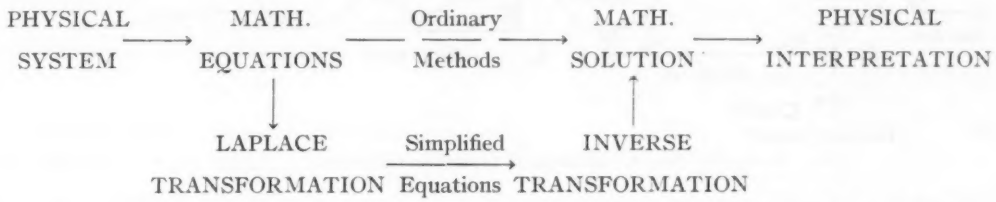

For ordinary differential equations of a certain order the simplified equations are algebraic in s to the same degree. Questions of stability of the physical system may be answered by consideration of the nature of the roots of this equation. Routh's stability criterion enables this to be done without actually finding the roots of the algebraic equation. For those with greater mathematical maturity, the location and order of the zeros and poles of the transform settle such matters.

The Laplace transformation, therefore, lends itself particularly well to the basic problems of the analysis and design of servomechanisms by its algebraizing effect and automatic introduction of arbitrary initial conditions. The procedures are straightforward and a working knowledge may be confined to three operation transforms. Extensive function transform tables like those in Gardner and Barnes[3] or Churchill[4] can be used as easily as integral tables. Mention should be made of the works of Carslaw and Jaeger[5] and McLachlan.[6] The treatment in both books is more advanced and contains many excellent applications in the various fields of physics and engineering.

Analysis of a Simple Servomechanism

Servomechanism systems in actual use are complex not because of the control problem itself but because of the refinements of the component equipment used in each engineering field. Since the methods of dynamic analogies are well known and it is common practice to reduce acoustic, hydraulic, or mechanical systems to equivalent electric circuits, an illustrative example employing electrical concepts and terminology will be used as a sort of common denominator. It is typical of a form of servomechanism which is in use in various fields, including the military.

In Fig. 4 the differential synchro system contains devices of the self-synchronizing type. The transmitter and receiver are similar to three-phase induction motors but have a single-phase rotor as primary and a three-winding stator as secondary. The induced voltages in the secondary are unequal and depend on the position of the rotor. When the two rotors are in corresponding positions, no current flows between the secondaries. If one rotor is not aligned with the other, the voltage unbalance causes secondary current to flow, which sets up sufficient torque to make the rotor positions correspond.

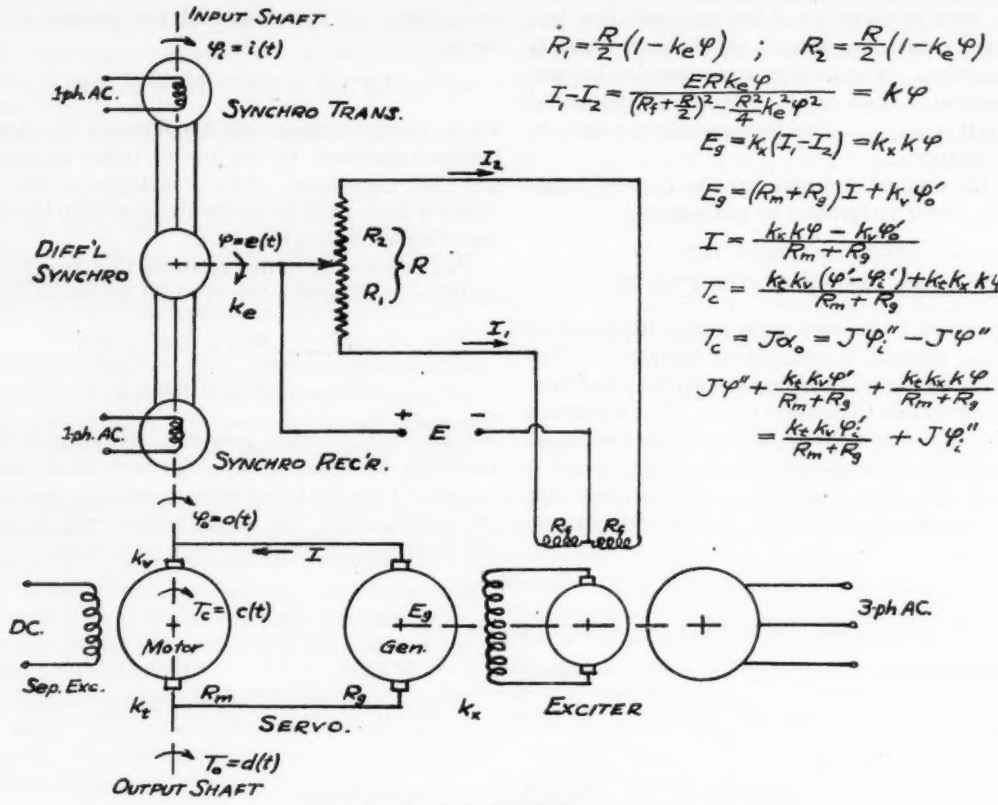

FIG. 4. Example of typical servo system.

If the two secondaries are connected through a differential synchro and each is turned through any angle, the differential synchro will indicate the difference between the rotor positions. Its function, therefore, is that of an error device or servo controller.

The error signal causes the potentiometer to control the net current in the exciter field. This in turn gives excitation to the servo generator coupled to the same constant-speed shaft. The current supplied to the servomotor or power source produces a correcting torque on the output shaft which tends to decrease the error between input and output. In this fashion, continuous follow-up is obtained between different power levels.

Assume that

$$\begin{aligned} R_1 &= (R/2)(1 - k_e\varphi) \\ R_2 &= (R/2)(1 + k_e\varphi) \end{aligned} \tag{1}$$

since $I_1 = E/(R_f + R_1)$ and $I_2 = E/(R_f + R_2)$,

$$I_1 - I_2 = \frac{ERk_e\varphi}{[R_f + (R/2)]^2 - (R^2/4)k_e^2\varphi^2} \doteq k\varphi \tag{2}$$

assuming the second term negligibly small. For linear saturation in both the exciter and servo generator

$$E_g = k_x(I_1 - I_2) = k_x k\varphi \tag{3}$$

But

$$E_g = (R_m + R_g)I + k_v\varphi_0' \tag{4}$$

where $k_v\varphi_0'$ is the counter-electromotive force of the servomotor for constant excitation. Eliminating E_g,

$$I = (k_x k\varphi - k_v\varphi_0')/(R_m + R_g) \tag{5}$$

For constant excitation $T_c = k_t I$; hence, the control is of the proportional type and

$$T_c = [k_t k_v(\varphi' - \varphi_i') + k_t k_x k\varphi]/(R_m + R_g) \tag{6}$$

since $\varphi_0 = \varphi_i - \varphi$.

Assuming no external disturbance, $T_0 = 0$, and the equation of motion for the output shaft is

$$T_c = J\alpha_0 = J\varphi_i'' - J\varphi'' \tag{7}$$

or explicitly,

$$J\varphi'' + \left(\frac{k_t k_v}{R_m + R_g}\right)\varphi' + \left(\frac{k_t k_x k}{R_m + R_g}\right)\varphi = \frac{k_t k_v\varphi_i'}{R_m + R_g} + J\varphi_i'' \tag{8}$$

It is convenient to nondimensionalize the coefficients of this equation by employing a notation used by Draper

and Bentley[7] and by Weiss:[8]

$$\varphi'' + 2\zeta\omega\varphi' + \omega^2\varphi = \varphi_i'' + 2\zeta\omega\varphi_i' \tag{9}$$

where

$$\left.\begin{aligned} \zeta &= (k_v/2)\sqrt{k_t/k_xkJ(R_m + R_g)} \\ \omega &= \sqrt{k_tk_xk/J(R_m + R_g)} \end{aligned}\right\} \tag{10}$$

The advantage of this notation becomes apparent later when ζ is interpreted as the ratio of damping present in the system compared with critical damping and when ω is the undamped natural frequency of the system. The effect of each of the system parameters upon the properties of the servomechanism can be observed regardless of its physical type or complexity.

As a specific case, assume that a constant speed n is suddenly applied to the input shaft when the output is stationary. Then

$$\left.\begin{aligned} &\varphi_i = \varphi_0 = \varphi = 0, t = 0 \\ &\varphi_i' = \varphi_0' = \varphi' = 0, t = 0 \\ &\varphi_i' = n1(t), t > 0 \end{aligned}\right\} \tag{11}$$

Taking Laplace transforms with $L[\varphi(t)] = \Phi(s)$,

$$\Phi(s) = 2\zeta\omega n/s(s^2 + 2\zeta\omega s + \omega^2) \tag{12}$$

The final or steady-state error $\varphi_s(t)$ may be obtained by taking the limit of $s\Phi(s)$ as s approaches zero; hence,

$$\varphi_s = 2\zeta n/\omega \tag{13}$$

The transient response is the inverse transformation, and by the use of transform tables,

$$\frac{\varphi}{\varphi_s} = 1 - \frac{e^{-\zeta\omega t}}{2\zeta\sqrt{1 - \zeta^2}} \sin\left(\sqrt{1 - \zeta^2}\omega t + \theta\right) \tag{14}$$

where

$$\tan\theta = (2\zeta\sqrt{1 - \zeta^2})/(2\zeta^2 - 1)$$

By inspection, the characteristic or delay time is $\tau = 1/\zeta\omega$ and the actual angular frequency for a given amount of damping is $\omega\sqrt{1 - \zeta^2}$. The transient error is expressed in terms of the steady-state error for convenience in plotting and is shown graphically in Fig. 5 for different amounts of damping.

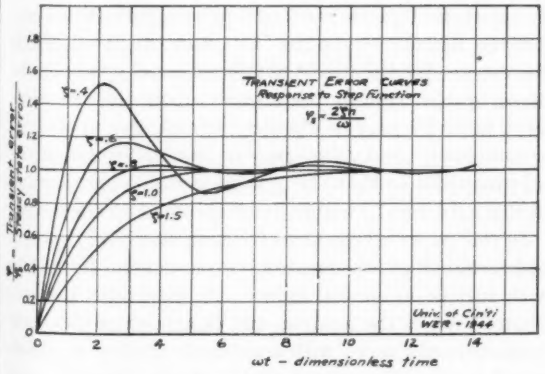

FIG. 5. Response curves of servo.

The steady-state lag error as given by Eq. (13) decreases with the amount of damping present and with the applied speed but is inversely proportional to the undamped angular velocity. The amount of overshoot and persistence of oscillation can be determined with the help of Fig. 5, where it is seen that a small ζ corresponds to a large overshoot and increased tendency to hunt. Hence, some sort of compromise must be made for a servo of this type. It is found[1] that ζ should lie between 0.5 and 1.0 for reasonable lag and overshoot errors. Specifically,

$$0.5 < \frac{k_v}{2}\sqrt{\frac{k_t}{k_xkJ(R_m + R_g)}} < 1.0 \tag{15}$$

Numerical Example

As a numerical example consider the following special case: a servomotor of 5 hp., 1800 r.p.m., 115 volts d.c., geared down to 120 r.p.m., $R_m = 0.1$ ohm, $R_g = 0.1$ ohm, total $J = 1$ slug-ft.^{2} Requirements: Steady-state lag error to be less than one-quarter revolution with no oscillation.

For rated conditions,

$$T = \frac{5(33{,}000)}{2\pi(1{,}800)} = 14.6 \text{ lb. ft.} = 218 \text{ lb. ft. at } 120 \text{ r.p.m.}$$

$$I = \frac{5(746)}{115(0.80)} = 40.5 \text{ amp. (assume efficiency = 80 per cent)}$$

$$k_t = 218/40.5 = 5.38 \text{ lb. ft./amp.}$$

Let the servogenerator produce $E_g = 100$ volts for $\varphi = 90°$ at the differential synchro. Then

$$k_xk = E_g/\varphi = 100/0.5\pi = 63.7 \text{ volts/rad.}$$

$$k_v = E_m/n = 115/(120/60)2\pi = 9.15 \text{ volt-sec./rad.}$$

$$\omega = \sqrt{\frac{k_tk_xk}{J(R_m + R_g)}} = \sqrt{\frac{5.38(63.7)}{1(0.2)}} = 41.4 \text{ rad. per sec.}$$

$$\zeta = \frac{k_v}{2}\sqrt{\frac{k_t}{k_xkJ(R_m + R_g)}} = \frac{9.15}{2}\sqrt{\frac{5.38}{63.7(1)0.2}} = 2.98 > 1 \text{ (no oscillation)}$$

Steady-state lag error

$$\varphi_s = 2\zeta n/\omega = k_vn/k_xk = 115/63.7 = 1.81 \text{ rad.} = 104° > 1/4 \text{ rev.}$$

For a stiffer system, let $E_g = 100$ volts for $\varphi = 15°$, then

$$\begin{aligned} k_xk &= 382 \text{ volts per rad.} \\ \omega &= 102 \text{ rad. per sec.} \\ \zeta &= 1.21 \\ \tau &= 0.051 \text{ sec.} \end{aligned}$$

and

$$\varphi_s = 0.301 \text{ rad.} = 17.3° < 1/4 \text{ rev.}$$

If the restriction of no overshoot and oscillation were removed, a more economical design could be made because of the smaller permissible value of damping ratio. This could be achieved by decreasing k_v and k_t, which means reduced power and torque requirements. For $\zeta = 0.75$ and all quantities kept at the above values except the torque constant, the new value becomes $k_t = 2.06$, since it is proportional to ζ^2, and thus the servomotor horsepower requirements are reduced to 1.91 or approximately 2 hp. The overshoot would be limited to less than 5 per cent of the steady-state error, or less than 1 degree, and the new time constant would be 0.0316 sec., or 62 per cent of its former value.

Effect of Time Delay

In the previous analysis, no account has been taken of the effect of time delay due to such energy storing devices as the generator field and motor and generator armatures. These effects are handled easily by using a concept from elementary circuit theory (Fig. 6).

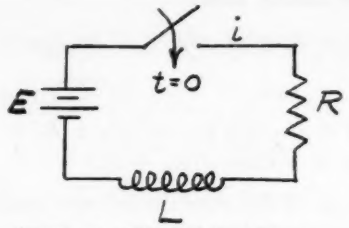

FIG. 6. Effect of time delay.

When a constant electromotive force E is suddenly applied to an RL circuit, $E1(t) = (R + Lp)i$, or taking transforms, $E/s = (R + Ls)I(s)$. The current transform is therefore

$$I(s) = \frac{E}{s}\left(\frac{1}{R + Ls}\right) = \frac{E}{Rs}\left(\frac{1}{1 + \tau s}\right)$$

where $\tau = L/R$ and is the time constant of the circuit. Thus, the factor $1/(1 + \tau s)$ prevents the current from suddenly becoming E/R.

In this example (see Fig. 4) τ_1 = delay time of generator field and τ_2 = delay time of generator and motor armatures; then

$$E_g = k_x k\varphi/(1 + \tau_1 p) = (R_m + R_g)(1 + \tau_2 p)I + k_v\varphi_0'$$

and the resulting transformed equation for $\Phi(s) = L[\varphi(t)]$ is

$$\Phi(s) = \frac{k_t k_v L[\varphi_i'] + J(R_m + R_g)L[\varphi_i'']}{J(R_m + R_g)(1 + \tau_1 s)(1 + \tau_2 s)s^2 + k_t k_v(1 + \tau_1 s)s + k_t k_x k}$$

The denominator is now a fourth degree expression in s, whose roots could be found in any specific numerical example by means of an approximation method such as that of Newton or Graeffe. The problem is then completed by finding the inverse transformation.

If the steady-state response of a linear servo system to an oscillatory input is desired, it can be obtained easily by using the rotating vector representation.[9] For either $\varphi_i(t) = \cos \beta t$ or $\sin \beta t$ let $\varphi_i = e^{i\beta t}$; then the steady-state behavior is found in complex number form by evaluating the expression $(s - i\beta)\Phi(s)$ for $s = i\beta$. The instantaneous response is written down in trigonometric form by mere inspection of the vector solution. The mathematical justification of this short-cut method employs the linearity of the Laplace transformation as well as that of the system itself.[3]

CONCLUSIONS

The foregoing treatment of a simple closed-cycle continuously controlled system is intended to show the applicability of operational methods in the formulation and solution of problems involving automatic control through transient feedback. Such problems are not restricted to any one field of application, typical examples being industrial recorders, calculating machines, telemetering devices, regulators, feedback amplifiers, governors, replica-cutting machines, gyrostabilizers, and automatic pilots. An extensive bibliography of the literature of automatic control may be found in reference 10.

The fundamental relations of the servo system components are expressed concisely in operational form. When the system is subjected to certain test inputs, the Laplace transformation simplifies the analysis by its algebraizing effect and automatically introduces arbitrary initial or boundary conditions. The transient and steady-state response are found by straightforward procedures usually involving no more than algebraic processes. By the use of nondimensional symbols, the effect of the system parameters upon the complete servo behavior may be observed irrespective of its type or complexity, and values may be assigned to the physical quantities so that the system is stable and lag and oscillation errors lie within limits specified for the design.

In this paper a typical servo using electrical concepts and terminology was treated both in general terms and with specific numerical values. It illustrates the procedure used in the analysis and design of an ideal proportional-error servo with a suddenly applied constant-speed input. By proper choice of the damping ratio

the response can be made aperiodic or oscillatory with any desired decrement. In nonideal cases where inertia effects are not negligible, the transformed equation is modified by factors involving the delay time of the element. A complete analysis of this problem or of one with a periodically applied input would require a discussion of the more general problem of stability criteria and is therefore beyond the scope of this paper.

References

[1] Hazen, H. L., *Theory of Servomechanisms,* Journal of The Franklin Institute, Vol. 218, No. 3, pp. 279–331, September, 1934.

[2] Minorsky, N., *Directional Stability of Automatically Steered Bodies,* Journal of the American Society of Naval Engineers, Vol. 34, No. 2, May, 1922.

[3] Gardner, M. F., and Barnes, J. L., *Transients in Linear Systems;* John Wiley and Sons, Inc., New York, 1942.

[4] Churchill, R. F., *Modern Operational Mathematics in Engineering;* McGraw-Hill Book Company, Inc., New York, 1944.

[5] Carslaw, H. S., and Jaeger, J. C., *Operational Methods in Applied Mathematics;* Clarendon Press, Oxford, 1941.

[6] McLachlan, N. W., *Complex Variable and Operational Calculus with Technical Applications;* The Macmillan Company, New York, 1942.

[7] Draper, C. S., and Bentley, G. P., *Design Factors Controlling the Dynamic Performance of Instruments,* A.S.M.E. Transactions, Vol. 62, pp. 421–432, July, 1940.

[8] Weiss, H. K., *Constant Speed Control Theory,* Journal of the Aeronautical Sciences, Vol. 6, No. 4, pp. 147–152, February, 1939.

[9] Johnson, W. C., *Mathematical and Physical Principles of Engineering Analysis;* McGraw-Hill Book Company, Inc., New York, 1944.

[10] Smith, E. S., *Automatic Control Engineering;* McGraw-Hill Book Company, Inc., New York, 1944.

Effect of Pressure Variations on Speed Runs

(*Continued from page 312*)

naturally be higher than indicated in the curves in regions where the pressure fields are more intense.

It would appear from Fig. 2 that the cleaner the airplane (smaller $C_{D_{pc}}$) the greater will be the error; however, the speed will in general be higher, with the result that the error will be about the same as for a ship with a higher $C_{D_{pc}}$ but lower speed. In any event, the error is not negligible around the cruising speed where range performance is important and should be taken into account.

Since meteorologic data at a given altitude and time will rarely be available to most companies, it will be necessary for identical speed runs to be made in exactly opposite directions within a small time interval and the mean of the two values taken in order to compensate for this effect. Another solution to the problem is to use a sonic altimeter over the ocean.

A Review of the Aerodynamics of Flight Load Factors in Relation to the Safety Regulations

HUGH B. FREEMAN*

Consolidated Vultee Aircraft Corporation

SUMMARY

This article reviews briefly the aerodynamics of flight load factors. An equation for the minimum maneuver load factor is proposed for planes in the transport category, based on the gust stalling speed and a "turbulent air maneuvering speed range" (V_π). For a value of (V_π) of 25 m.p.h., this equation yields load factors in good agreement with past experience. Suggested flight tests for the experimental determination of (V_π) would answer the question as to whether our load factors could safely be lowered. The equation applies to flapped, as well as unflapped, wings.

It is concluded that the existing formula for maneuver load factors, based on power loading and gross weight, should be abandoned for a more rational equation based on the dominant parameters of the airplane—i.e., wing loading and aspect ratio. A more reasonable lower limit for the maneuver load factor would be that imposed by a horizontal turn at an angle of bank of 60°—i.e., 2.00. This limit could be reached only by airplanes with wing loadings much higher than any now contemplated.

INTRODUCTION

THE RAPID GROWTH of the aircraft industry, especially with regard to the great increases in gross weight of aircraft in the past few years, makes it desirable to review the knowledge in certain fields and to examine our safety regulations in the light of that knowledge. The existing safety regulations are based largely on the experience obtained on airplanes with a gross weight of less than 25,000 lbs. Many airplanes now in service have four times that gross weight, and some that are contemplated for the near future have weights more than ten times that figure.

The purpose of this paper is to review the aerodynamics of flight load factors in relation to the safety regulations in the interest of stimulating further discussion on this subject, which seems to have received all too little attention considering its importance in relation to the economy of aircraft operation.

The problem of load factors is generally considered to be one for the structures engineer. This is true, of course, as far as the strength of the structure is concerned. It is, however, the problem of the aerodynamicist to tell the structures engineer what loads will be imposed on the structure in any flight operation. The failure to make this distinction, in the past, may be one reason for the surprising lack of understanding of this subject which prevails throughout the industry. Another reason may be that the extreme simplicity of the theory of load factors has deceived the aerodynamicists into accepting these equations as axiomatic. This is a dangerous procedure in any case and, especially so, where the whole theory revolves around the definition of the maximum lift coefficient.

Presented at the National Air Transport Meeting, I.A.S., Washington, D.C., October 20, 1944.

* Development Design Staff Engineer.

TERMINOLOGY

In the past, it has been the habit of technical men to talk about load factors in terms of accelerations. This comes from the fundamental equation:

$$f = ma$$

where f = the force in pounds, m = the mass of the body, and a = the acceleration. Since $m = W/g$, where W = the weight of the body in pounds and g = the gravitational constant we may write $f = (W/g)a$ or

$$\text{load factor} = f/W = a/g \qquad (1)$$

Now if we talk about the left side of this equation (f/W) instead of its equivalent (a/g) on the right, we obtain a much more understandable definition of a load factor. The load factor is simply the ratio of the force on a body to its weight in pounds for a given acceleration.

If a student pilot is told that he may place an acceleration of 6g on his airplane in a given maneuver, he may be impressed to the extent that he will try the maneuver on his next flight to see how it feels. If, however, he is told that in making the maneuver he will place a load on the airplane wing equal to six times the weight of the airplane, he will have some conception of the meaning of a load factor.

MAXIMUM MANEUVERING LOAD FACTORS

The maximum load that can be placed on an airplane wing at any speed or in any maneuver is that corresponding to the maximum angle of attack of the wing. If this angle is exceeded, the wing will stall and the load will decrease. Now if it is assumed that the control surfaces are nicely balanced and they are sufficiently large to overcome the inertia of the machine, an airplane can be stalled at any speed simply by pulling back sud-

denly on the control stick and placing the machine at its maximum angle of attack.

In such a maneuver the force or load on the wing is equal, for all practical purposes, to the lift on the wing L, so that f in Eq. (1) may be replaced by (L) and load factor $= L/W = a/g$, or placing

$$L = C_L(\rho/2)(V^2S)$$

and

$$W = C_{L_{max.}}(\rho/2)(V_S^2S)$$

the load factor becomes

$$L/W = a/g = (C_L/C_{L_{max.}})(V/V_S)^2 \qquad (2)$$

where V is the velocity at the time of the pull-up and V_S is the normal stalling speed of the wing—i.e., the minimum speed in level flight.

When $C_L = C_{L_{max.}}$

$$\text{maximum load factor} = (L/W)_{max.} = (V/V_S)^2 \qquad (3)$$

The maximum load factor that may be imposed on a wing at a given velocity is then equal to the square of the ratio of the velocity at which the maneuver is executed to the normal stalling speed of the wing.

The maximum velocity that an airplane may attain is its terminal velocity in a dive. The maximum possible load factor then would correspond to a sudden pull-up at this velocity. The terminal velocity may be approximated by equating the drag of the airplane to its weight

$$D = C_{D_0}(\rho/2)(V_t^2S) = W$$

The terminal velocity

$$V_t^2 = (2/\rho C_{D_0})(W/S)$$

since $W/S = (\rho/2)C_{L_{max.}}V_S^2$

$$(V_t/V_S)^2 = C_{L_{max.}}/C_{D_0} = (L/W)_t$$

equals maximum load factor at terminal velocity. Assuming a maximum lift coefficient ($C_{L_{max.}} = 1.5$) and a minimum drag coefficient ($C_{D_0} = 0.025$), then

$$(V_t/V_S)^2 = 1.5/0.025 = 60$$

The terminal velocity ratio corresponding to this load factor is

$$V_t/V_S = 7.75$$

This approximation illustrates at once the fact that it is impractical, if not impossible, to build a wing structure for a low drag airplane that will take the maximum loads that can be placed over its entire speed range.

It is interesting to compare the above load factor with an estimate of the maximum load factor for a very early type of airplane, such as the Wright or Curtiss biplanes.

Assuming

$$C_{L_{max.}} = 0.8 \qquad C_{D_0} = 0.08$$

then

$$(V_t/V_S)^2 = 0.8/0.08 = 10$$

and

$$V_t/V_S = 3.16$$

If these assumptions are correct, the terminal velocity of these planes was only a little more than three times the stalling speed, and the maximum load that could be placed on the wings was only ten times the weight of the plane. It is probably fortunate for the aircraft industry that this was the case. The "built-in head winds" of our early designs were probably responsible to a large extent for the survival of the aircraft industry during those early days when the knowledge of loads was even more limited than now.

The load factors computed from Eq. (2) for several values of the lift coefficient are shown in Fig. 1 plotted against the speed ratio V/V_S. The use of this ratio is convenient because it allows the maximum load factors for all airplanes to be represented by a single curve. The load factor for level flight is indicated by the horizontal line $(L/W = 1.0)$. The load factor in a dive at 60° to the horizontal is represented by the line $(L/W = \cos\theta = 0.5)$. The intersections of these lines with the various C_L curves give the lift coefficient at which the airplane is flying at any given speed.

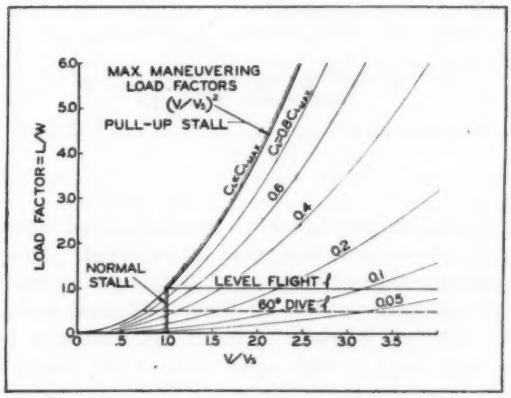

FIG. 1.

It is clear from this illustration that, in order to realize the maximum load factor at any given speed, the angle of attack must be changed instantaneously from the value at which the plane is flying to the maximum value, otherwise the great increase in drag at the higher angles of attack will slow the plane down and it will stall out at some lower speed. From this point of view, the curve of maximum load factors is conservative, since it is impossible to make this change in attitude instantaneously.

Another assumption made in deriving Eq. (3), however, is not conservative. This assumption is that the lift coefficient in a maneuver is equal to the "static" lift

coefficient. It is known that the lift coefficient with a rapidly changing angle of attack is higher than the static value. What meager experimental data there are, however (reference 1), seem to confirm Eq. (3). It may be that the two effects cancel one another.

Load Factors in a Turn

The load factors in a horizontal turn are given by the equation[2]

$$L/W = \sec \phi$$

where ϕ is the angle of bank.

This may be written

$$L/W = \sec \phi = (C_L/C_{L_{max.}})(V/V_S)^2 \qquad (4)$$

The load factors for various angles of bank are plotted in Fig. 2.

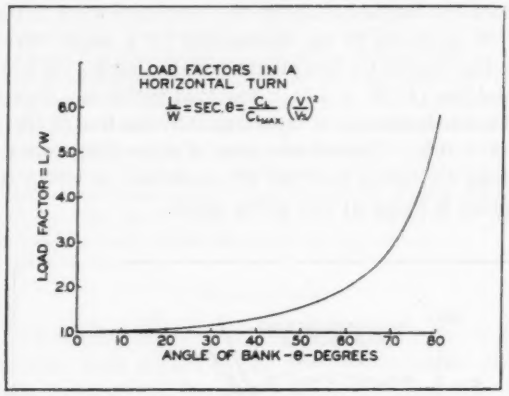

FIG. 2.

Note that the load factor in a turn for a given angle of bank is a constant independent of the speed. This is important in the consideration of an emergency maneuver at high speed to avoid a collision with another plane or to avoid an obstacle. This is one maneuver the pilot may make at high speed without the danger of overloading his wing, *within certain limits as to the angle of bank*. Note that at an angle of bank of 45° the load factor is only (1.41) and at 60° is equal to (2.0). At higher angles of bank the load factor increases rapidly. At an 80° bank the load factor is 5.75.

The load factors in a turn are compared to the maximum maneuvering load factors in Fig. 3. The load factors for a given angle of bank take the form of horizontal lines terminating in the curve of ($C_L = C_{L_{max.}}$) at the lower velocities. The intersections of these lines with the curve indicate the minimum speed at which a turn may be made without stalling. The pull-up curves for various lift coefficients are included to show the increase in lift coefficient required for a given angle of bank and indicate that the power required in a turn is higher than that required for level flight.

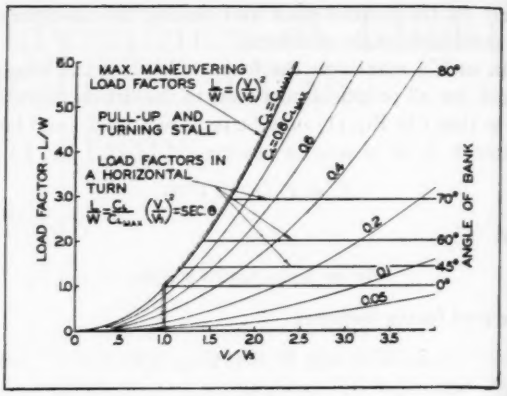

FIG. 3.

Load Factors in a Gust

In the past decade much has been learned about the loads imposed on an airplane by gusty or turbulent air, largely through the research of the N.A.C.A. under the direction of Mr. R. Rhode. A detailed review of this subject would be too lengthy for a paper of this kind; consequently, for the purposes of this discussion, the semiempiric equation for gust loads, developed by Mr. Rhode and adopted by the C.A.A., will be used here as though it were an exact equation. While this is not true and as the research on this subject continues this equation may be altered from time to time, much may be learned by assuming that it is true.

The gust load factor as adopted by the C.A.A. is

$$L/W = 1 + [aKUV/575(W/S)] \qquad (5)$$

where

a = the slope of the lift curve C_L per rad.
K = a constant depending on the wing loading
U = the gust velocity in ft. per sec.
V = the indicated velocity of the airplane, m.p.h.

This is equivalent to

$$L/W = 1 + (\rho_0/2)[aKUV/(W/S)] \qquad (6)$$

where ρ_0 is the sea-level density of the air and V, in this case, is expressed in ft. per sec.

In order to compare the gust load factors with the maneuver load factors, previously discussed, it is convenient to substitute for (W/S) its equivalent

$$W/S = (\rho_0/2)C_{L_{max.}}V_S^2$$

The gust load factor equation then becomes

$$L/W = 1 + (aK/C_{L_{max.}})(U/V_S)(V/V_S)$$

or

$$L/W = 1 + aK'(V/V_S) \qquad (7)$$

where $K' = (K/C_{L_{max.}})(U/V_S)$ = a function of (W/S) for a given value of the gust velocity U.

The gust load factors for three wing loadings and two aspect ratios are compared to the maneuver load factors in Fig. 4. These curves are based on a gust velocity of 30 ft. per sec. and a $C_{L_{max.}}$ of 1.5. Eq. (7) yields approximately the same values as Eq. (5) with this value of $(C_{L_{max.}})$.

The gust load factors thus vary directly as the speed where the maneuver load factors vary as the square of the speed. Note that the gust load factors fall off rapidly with increasing wing loadings. This is also true for the maneuver load factors.

Going back to Eq. (3)

$$L/W = (V/V_S)^2 \tag{3}$$

and substituting for the value of V_S^2 its equivalent $(2/\rho C_{L_{max.}})(W/S)$, we obtain

$$L/W = (\rho/2)(V^2/C_{L_{max.}})(W/S) \tag{8}$$

From Eqs. (5) and (8) it is seen that the load factors that may be placed on an airplane wing, either by a maneuver or by a gust, decrease with an increase in wing loading. It is reasonable to expect that this difference should be given consideration in our safety regulations as to requirements for the design load factors.

Design Load Factors

All the aerodynamic data required for the design of the structure of an aircraft in regard to flight loads are now available. It remains to be decided for what speed range the structure must be designed both for gust loads and maneuver loads in order to provide a safe airplane.

Since the gust loads are not under the control of the pilot and he cannot anticipate when he is going to encounter turbulent air conditions, it is obvious that the structure must be strong enough to withstand a 30 ft. per sec. gust at any speed within the normal flight range—i.e., up to maximum level flight speed. This is according to the existing requirements of the safety regulations, and there seems to be no other alternative in this regard.

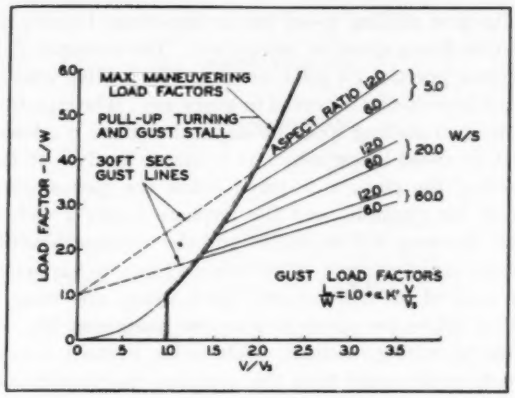

Fig. 4.

With respect to maneuvering loads, a safe design load factor will depend on the purpose for which the airplane is to be used. It has already been pointed out that it is impractical to design the structure for the maximum loads that can be placed on it over its entire speed range. The only alternative would seem to be to design for these loads at a given speed and placard the airplane so that the pilot will know the safe speed range in which he can make sudden maneuvers.

This discussion will deal only with airplanes of the transport category. By the transport category is meant any airplane that is designed solely for transportation of persons or goods from one place to another, whether private or public. For such planes, which are intended to be flown right side up and more or less in a level attitude, it should be sufficient to provide the pilot with a "safe maneuvering range" of speeds in which he can maneuver without fear of harming the airplane structure when coming in to land, in gusty air, and in avoiding obstacles under conditions of poor visibility. Pilots who fly such airplanes will have to learn that it is just as dangerous to make sudden pull-ups without slowing down as it is to try to make a sharp turn at the top speed of an automobile.

Gust Stalling Speeds

Before defining the "maneuvering speed range" we must consider the effect of a gust on the stalling speed of an airplane.

The gust stalling speed is determined by the intersection of the parabola (Eq. (3)) and the gust line (Eq. (5)). Equating these two values of the load factor and solving for V leads to a quadratic equation, the positive root of which is:

$$V \text{ gust stall} = \frac{\frac{aKU}{1.465} + \sqrt{\left(\frac{aKU}{1.465}\right)^2 + 1{,}572\, C_{L_{max.}}\,(W/S)}}{2C_{L_{max.}}} \text{ m.p.h.} \tag{9}$$

where

a = slope of the lift curve C_L per rad.
K = constant from *CAM 04*
U = gust speed, ft. per sec.

The gust stalling speed has an important bearing on the safe flying speed in bumpy air. For example, it is common practice for pilots to lower the landing gear as an aid in reducing air speed in gusty air. The equation of the gust stalling speed indicates that there is a lower limit in speed below which it is unsafe to fly. If the speed of the plane is reduced below the gust stalling speed, for example, and the airplane meets a violent gust, the wing will be stalled and the airplane possibly thrown out of control. This is most likely to happen in the case of an unsymmetric gust where one wing is stalled while the other is near the maximum lift. A powerful rolling moment would exist, in such a case, which could easily turn the airplane completely over with the pilot helpless to prevent it. One such accident is known to have occurred to an air liner when flying in turbulent air. This accident could well have been caused by an unsymmetric gust stall; in fact, it is difficult to explain it by any other consideration.

A safer method* of reducing speed when flying in bumpy air would be to lower the wing flaps, since this extends the safe speed range to lower speeds by reducing the gust stalling speeds. This is illustrated in Fig. 5. The lowest speed at which it is safe to fly this airplane, with the flaps neutral, is 133 m.p.h. With the flaps down, however, the plane may be safely flown at a speed 38 m.p.h. lower or at approximately 95 m.p.h. without fear of stalling because of gusts.

The foregoing remarks apply also in the case of the approach speed—i.e., to an airplane circling an airport for a landing—and to the landing speed. In any flight condition the minimum safe speed is determined by the gust stalling speed of the wing at the prevailing flap setting. Many of the unexplained accidents of airplanes getting out of control and crashing in the approach to a landing may have been caused by the gust stall where the pilot came in at too low a speed.

* Pilots take note: This is true only when the wing with flaps deflected is designed for a 30 ft. per sec. gust. The minimum requirements of the C.A.A. now specify only a 15-ft. gust with regard to flap design.

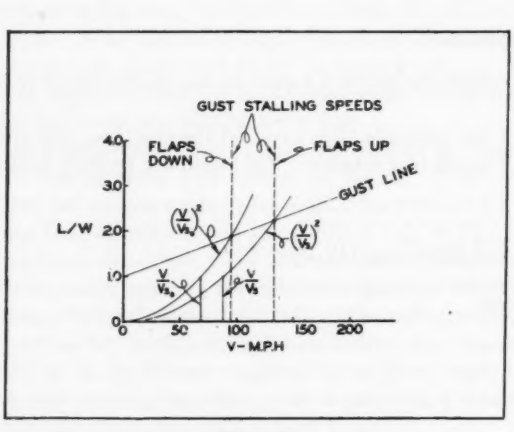

FIG. 5.

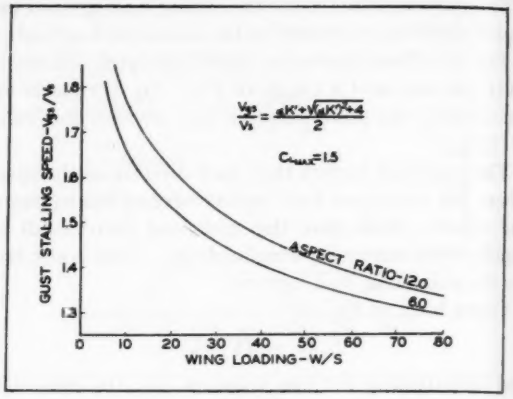

FIG. 6.

While the existing safety requirements recognize the importance of turbulent air conditions with regard to strength, this consideration is completely ignored in the performance and operational requirements. It would seem, from the point of view of safety, that this consideration was more fundamental than the design limitation as to stalling speeds.

Eq. (9) may be written in nondimensional form as follows (combining Eqs. (3) and (7)):

$$\frac{V_{gs}}{V_s} = \frac{aK' + \sqrt{(aK')^2 + 4}}{2} \qquad (9')$$

The gust stalling speed for a wide range of wing loadings and for two aspect ratios is shown in Fig. 6. This figure provides another illustration of the safety in flight of high wing loading relative to low wing loading. The minimum safe speed for a light plane in gusty air approaches a value twice its normal stalling speed. For some light planes this speed is equal to, or greater than, the cruising speed. At the other extreme of wing loading, the gust stall speed drops to 1.3 times the normal stalling speed.

It may be argued that planes of light wing loading should not be flying in turbulent air. This is true. On the other hand, as flying becomes more popular and cross-country flying, especially, becomes more common, there will be times when the pilot cannot avoid flying in gusty air whether he likes it or not.

MINIMUM-MANEUVER LOAD FACTOR

The maneuvering speed range of an airplane is illustrated in Fig. 7. For this example it is assumed that the strength of the structure is sufficient to withstand a limit maneuvering load factor of 2.60. This load factor could be placed on the structure by a sudden pull-up at a speed of about 202 m.p.h. The maneuvering speed range of this airplane in calm air is, then, the difference between this speed and the normal stalling speed or approximately 77 m.p.h. In this range of speeds, the pilot may maneuver as suddenly as he pleases and he cannot exceed the design load factor.

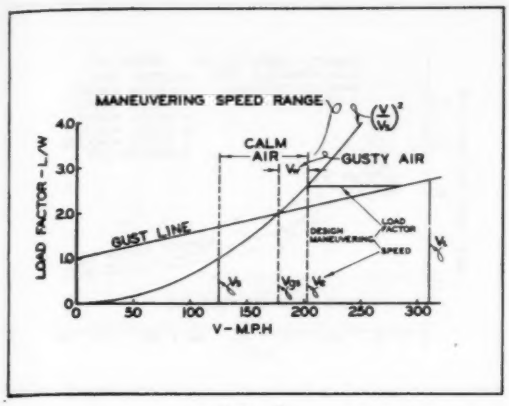

FIG. 7.

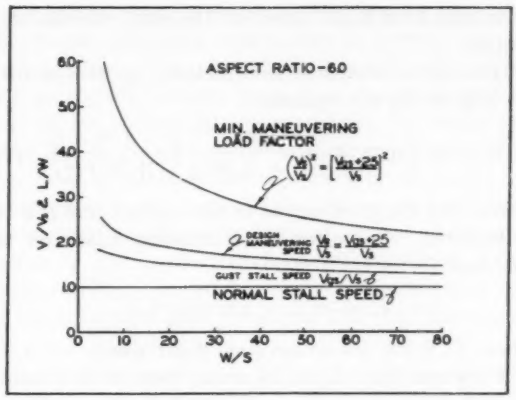

FIG. 8.

The gusty air maneuvering speed range (V_π) is the difference between the design speed and the gust stalling speed, or

$$V_\pi = V_e - V_{gs}$$

In this case it amounts to about one-third of the calm air speed range. The gust stall speed is the minimum speed at which it is safe to fly in turbulent air, and, since the pilot cannot hold his speed constant at any given value under these conditions, he should have a range of speeds above the gust stall in which he can make any sudden maneuvers that may be necessary in order to maintain control of the airplane. The magnitude of the speed range required will have to be determined by experiment.

Experimental data in this regard are meager; so much so, in fact, that only one flight test in turbulent air conditions could be found in which the fluctuations of the air speed were recorded in detail. These data consist of a photographic record of the speed indication over a period of about 48 sec. when flying in turbulent air with effective gust velocities ranging up to 28 ft. per sec.

The maximum short-period speed fluctuations of a duration of 1 sec. or less, over which the pilot would have little control, were of the order of plus or minus $12^1/_2$ m.p.h. This gives a value for V_π of 25 m.p.h.

An equation may now be written for the minimum maneuvering load factor that will provide any airplane with a turbulent air maneuvering speed range. Since $V_e = V_{gs} + V_\pi$ or

$$(V_e/V_S) = (V_{gs}/V_S) + (V_\pi/V_S) \qquad (10)$$

the minimum maneuvering load factor is

$$L/W = (V_e/V_S)^2 = [(V_{gs} + V_\pi)/V_S]^2 \qquad (11)$$

The equation for the minimum maneuvering load factor based on $V_\pi = 25$ m.p.h. then becomes

$$L/W = (V_e/V_S)^2 = [(V_{gs} + 25)/V_S]^2 \qquad (12)$$

The load factors computed from this equation are shown in Figs. 8 and 9 for aspect ratios of 6.0 and 12.0, respectively.

These curves clearly show the dominating influence of the wing loading with regard to load factors. The minimum load factor that is safe for a plane of high wing loading would not be safe for a plane of low wing loading. Figs. 8 and 9 illustrate the fallacy of the current trend of thought with regard to fixed strength classes of airplanes—i.e., arbitrarily assigning a constant minimum load factor to a category of airplanes in which a wide range of wing loadings exists. This could be accomplished safely only by making the load factor high enough to protect the plane of lowest wing loading and penalizing all of the rest of the planes of higher wing loading in the category.

Comparison with Existing Requirements

It is interesting to compare the maneuver load factors obtained by this method with those required by *CAR 04*. These requirements specify that the maneuver load factor used for design shall be equal to the maneuver load factor computed from an empirical equation or shall be equal to the gust load factor computed for the

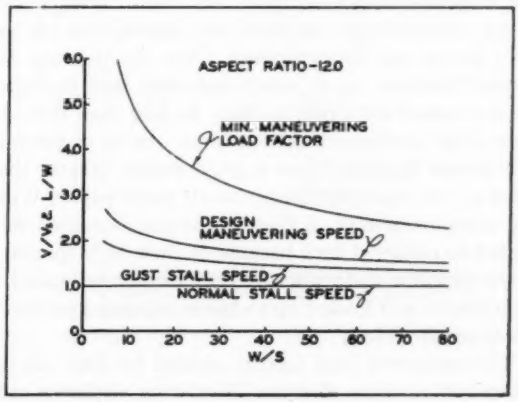

FIG. 9.

maximum level flight speed of the ship, whichever is greater.

The C.A.A. maneuver load factor (Fig. 04-3 of *CAR 04*) is given by the equation:

$$\frac{L}{W} = 1 + \left(0.77 + \frac{32{,}000}{W + 9{,}200}\right)\left(\frac{3.25}{(W/P)^{0.455}}\right) \quad (13)$$

where W is the gross weight of the airplane and P is the horsepower. The alternative equation based on the gust load factor is given by:

$$L/W = 1 + aK'(V_L/V_S) \quad (14)$$

where V_L is the maximum level flight speed.

A few remarks should be made here as to a fundamental difference between the C.A.A. Eqs. (13) and (14) and Eq. (12) derived in the previous pages. The C.A.A. equations for the maneuvering load factor are both functions of the power loading of the airplane, while the proposed Eq. (12) does not depend on this parameter.

In order to understand the reasons for not making the maneuver load factor dependent on power loading, it is necessary to go back to the original assumptions. It was pointed out previously that we cannot design a plane for the maximum loads a pilot can impose on the wing throughout its speed range. As an alternative, we design for the maximum gust at "high speed" and for a maneuvering load factor in the "low speed" range that will give the pilot a range of speeds in which he can safely maneuver as violently as is necessary. It is logical that the design load factor at the "high speed" should be a function of power loading. However, in the maneuvering ("low speed") range where the engine is throttled it is difficult to see why this should be so. It would be just as reasonable to require that the strength of an automobile in making a right angle turn be a function of the horsepower of the engine.

Another difference between Eqs. (12) and (13) is that the C.A.A. equation depends on the gross weight of the airplane. The reasons for this apparently were that it was thought that, with increasing weight and inertia, the control forces would tend to increase and thus reduce the maneuverability of these airplanes. With regard to the control forces, at least, this assumption has not been borne out by experience. The controls on our largest bombers are so nicely balanced that the stick force required for a pull-up may be less than those on some light airplanes of prewar days. Some of our pursuit planes of today have a gross weight greater than most of our transport planes of 10 years past. While the maneuverability of these ships has decreased with regard to radius of turn because of their high speeds, it is questionable as to whether they cannot be stalled at high speeds and loaded up to the maximum load factor predicted by theory.

The maneuver load factors yielded by Eq. (12) are compared to those of some 50 existing airplanes computed from the C.A.A. equations in Fig. 10. The values for the individual airplanes are only approximations, since the data on these ships had to be taken from current publications. It should be noted that these are not the actual design load factors for these ships but represent the load factors obtained by assuming that they were all designed to the minimum requirements of *CAR 04*.

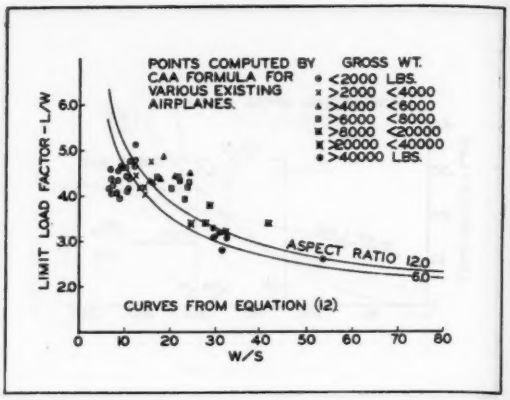

FIG. 10.

In considering Fig. 10 it should be remembered that Eq. (12) relates to planes of the transport category only, or planes that are to be used in cross-country flying where flying in turbulent air cannot always be avoided. It is seen that the curves agree well with the points for the larger planes of the transport category. It is interesting to note the rapid increase in load factors as the wing loading decreases. For extremely low wing loadings the load factors reach values that are usually associated with acrobatic planes. This has little significance, however, since these airplanes are not likely to be used extensively and possibly should not be used for this category.

The points for the light planes show no systematic variation with wing loading such as that of Eq. (12). This is not surprising, since this fundamental parameter does not even appear in the C.A.A. equation.

Eq. (12) assumes a constant turbulent air-speed range for all wing loadings. Whether this is correct or not is difficult to say, but it would certainly seem that this range for low wing loading should not be less than that for high wing loading. In turbulent air a plane with a wing loading of 60 would ride as steady as a battleship compared to a plane with a wing loading of 10, which would bounce around like a cork in a stormy sea.

Our existing regulations place a lower limit on the maneuvering load factor of 2.5. This limitation seems hard to justify, since the planes of high wing loading have the same turbulent air speed range as the lower wing loadings and are less subject to being upset in rough air. The only justification for a lower limit would seem to be the load factor in a turn at a limiting angle of bank which does not decrease with wing loading. For transport planes it is hard to conceive of the

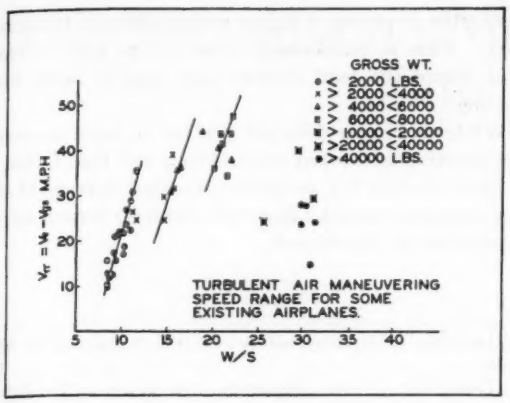
GROSS WT.
≤ 2000 LBS.
> 2000 <4000
> 4000 <6000
> 6000 <8000
> 10000 <20000
> 20000 <40000
> 40000 LBS.
$V_{\pi} = V_4 - V_{25}$ M.P.H
TURBULENT AIR MANEUVERING SPEED RANGE FOR SOME EXISTING AIRPLANES.
W/S

FIG. 11.

necessity of a turn at an angle of bank greater than 60°. This would place the lower limit at a load factor of 2.00.

Fig. 11 presents the turbulent air maneuvering speed ranges computed from the load factors of the airplanes shown in Fig. 10. This figure shows how completely irrational our present regulations are in this regard. Note, for example, the trend of this speed range for the light planes of less than 2,000 lbs. gross weight. For a wing loading of 7.0, V_{π} is 10 m.p.h. For a wing loading of 11, this value has increased to 35 m.p.h. These planes are all in the same category, which might be called "pleasure craft," and yet an airplane of wing loading of 11 is required to have 3.5 times the speed range of that of a plane with a wing loading of 7.0.

For pleasure craft such as these that are to be flown in the neighborhood of airports and that will dart for shelter at the first storm signal, the value of V_{π} might well be reduced to some lower value, resulting in lower load factors for this category.

In Fig. 12 are shown the maneuvering speed ranges, in m.p.h., corresponding to the load factors from Eq. (12). Included also is a curve of speeds corresponding to the ultimate design load factor. The ultimate load factor is 1.5 times the values given by Eq. (12). The difference between V_1 and V_u has been designated as an emergency speed range. If the pilot is forced to maneuver violently in this range, the worst he can do is to put a permanent set in his wing structure. It is interesting to note that the calm air maneuvering range and the total maneuvering range increase with the wing loading.

CONCLUSION

Further experimental data are needed for the accurate determination of $V\pi$, both with and without the use of flaps. The determination of this value would answer the question as to whether or not the load factors could safely be lowered. The value of 25 m.p.h., while it agrees with past experience, may be higher than necessary.

Eq. (11) offers a rational method for the determination of the maneuver load factors of a wing with and without flaps. The gust stalling speeds with the use of flaps are substantially lower than those without flaps, and the use of these devices in turbulent air might possibly lead to greater safety for these conditions, allowing lower speeds and better control of the speed. If future experiments indicate that the use of flaps allows better control of the speed in rough air and allows lower values of $V\pi$, a substantial reduction in load factors would result. This would encourage the design of flaps to the maximum gust instead of half that value, as is the present practice.

It should be noted that Eq. (11) yields conservative results for the load factors. The gust stalling speeds computed on the basis of the static lift coefficient are higher than they would be if the dynamic value were used. This error is squared in determining the final result.

While our existing regulations appear to be about as rational as our present knowledge will allow with regard to the gust loads, it seems that the "rule of thumb" with regard to maneuver load factors could well be replaced by a more rational method. There appears to be no justification for making this parameter depend on the gross weight or on the power loading. The fundamental parameter in determining the maneuver load factors appears to be the wing loading. This parameter is ignored completely by existing regulations. From the

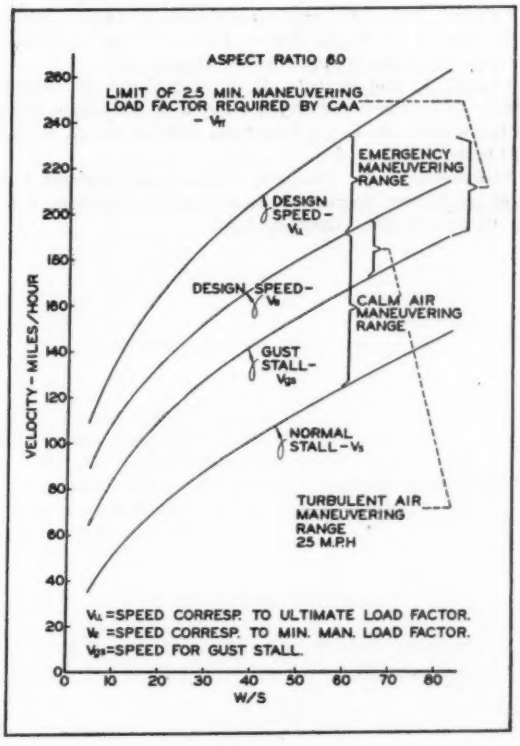
ASPECT RATIO 6.0
LIMIT OF 2.5 MIN. MANEUVERING LOAD FACTOR REQUIRED BY CAA - V_{π}
EMERGENCY MANEUVERING RANGE
DESIGN SPEED - V_1
DESIGN SPEED - V_u
CALM AIR MANEUVERING RANGE
GUST STALL - V_{25}
NORMAL STALL - V_s
TURBULENT AIR MANEUVERING RANGE 25 M.P.H
VELOCITY - MILES/HOUR
V_1 = SPEED CORRESP. TO ULTIMATE LOAD FACTOR.
V_u = SPEED CORRESP. TO MIN. MAN. LOAD FACTOR.
V_{25} = SPEED FOR GUST STALL.
W/S

FIG. 12.

aerodynamic standpoint, there appears to be no justification for the minimum limit of 2.5 imposed by present regulations. A more rational limitation would be that imposed by a horizontal turn at the angle of bank of 60°. This would place the minimum maneuver load factor at 2.0, and this value could only be reached by planes of wing loading much higher than any that are now contemplated.

This analysis shows the fallacy of the current trend of thought with regard to adopting fixed strength categories—i.e., a constant maneuver load factor for a whole category of airplanes with a wide range of wing loadings. This can be accomplished safely only by making the load factor correspond to that required for the airplane of lowest wing loading and penalizing all of the rest of the airplanes of higher wing loading in that category. This is particularly true in the light aircraft field where the load factors vary rapidly with wing loading.

While this paper does not pretend to have answered the question as to what constitutes a safe load factor, it is believed that the methods presented here point the way, at least, toward a more rational basis for our safety regulations in this regard.

References

[1] Doolittle, J. H., *Accelerations in Flight*, N.A.C.A. T.R. 203, 1924.

[2] Diehl, Walter Stuart, *Engineering Aerodynamics;* The Ronald Press Company, New York, 1936.

Correction of Aluminum-Alloy Compressive Test Results for Material Properties Using Reduced Moduli

(*Continued from page 310*)

References

[1] Army-Naval-Civil Committee on Aircraft Design Criteria, *ANC-5 Strength of Aircraft Elements*, Revised Ed., December, 1942.

[2] Epstein, A., *Correction of Compression Test Results of Aluminum Alloys for Material Properties*, A.C.T.R. No. 4519, March 22, 1940.

[3] Fischel, J. R., *The Compressive Strength of Thin Aluminum Alloy Sheet in the Plastic Region*, Journal of the Aeronautical Sciences, Vol. 8, No. 10, pp. 373–383, August, 1941.

[4] Karol, J., and Branahl, E. F., *Calculation of Crippling Stresses for Stiffeners and Stiffened Panels of Aluminum Alloys*, Curtiss-Wright (St. Louis) Structures Bulletin No. 27, April 10, 1944 (unpublished).

[5] Crockett, H. B., *Predicting Stiffener and Stiffened Panel Crippling Stresses*, Journal of the Aeronautical Sciences, Vol. 9, No. 13, pp. 501–509, November, 1942.

[6] Karol, J., and Branahl, E. F., *Standard Stress-Strain and Elastic Moduli Curves in With-Grain Compression*, Curtiss-Wright (St. Louis) Report R-134, December, 1943 (unpublished).

[7] Templin, R. L., Hartmann, E. C., and Paul, D. A., *Typical Tensile and Compressive Stress-Strain Curves for Aluminum Alloy 24S-T, Alclad 24S-T, 24S-RT, and Alclad 24S-RT Products*, Aluminum Research Laboratories Technical Paper No. 6, Aluminum Company of America, 1942.

[8] Thornton, K., *Alcoa Alloy 75S*, Memorandum, Aluminum Company of America, August 24, 1944.

[9] Templin, R. L., Sturm, R. G., Hartmann, E. C., and Holt, M., *Column Strength of Various Aluminum Alloys*, Aluminum Research Laboratories Technical Paper No. 1, Aluminum Company of America, 1938.

[10] Osgood, W. R., *Column Strength of Tubes Elastically Restrained Against Rotation at the Ends*, N.A.C.A. Report No. 615, 1938.

The Attenuation Method for Compressible Flow Systems

LEONARD MICHAEL GREENE*

Grumman Aircraft Engineering Corporation

ABSTRACT

The equation of Bernoulli and the condition of irrotationality of an inviscid fluid are combined to give the normal pressure gradient in terms of the local fluid density, velocity, and radius of curvature. In the attenuation plane the space coordinates are replaced by the radius of curvature and the equipotential spacing as the independent variables. When represented on the attenuation plane, the boundaries are the same for either compressible or incompressible flows. A point common to both flows on the attenuation plane will be at different distances from the body in the physical plane, but will be on an equipotential path which intersects the surface of the body at a point common to both flows on either plane.

For simplified flow systems, a relation between the rate of change of radius of curvature along the equipotential path and the local stream channel contraction is obtained. Using this relation, the adiabatic gas laws, and the condition of continuity, the ratio of the pressure gradients in the attenuation plane becomes a simultaneous first order differential equation which is readily integrated.

The critical condition beyond which a shock wave, flow separation, or both, must occur is the failure of a stream channel to contract from the free stream to a negative pressure peak. It coincides with the appearance of a singularity in the solution obtained by the attenuation method and not with the occurrence of the local speed of sound. A theory is presented on the behavior of flow systems having critical or supercritical regions.

Charts are included for the correction of incompressible pressure coefficients to the corresponding compressible pressure coefficients for values of the free stream Mach Number up to unity.

INTRODUCTION

STREAMLINE FLOW is a balance of forces and accelerations which enables a fluid to curve about a body shape in a steady equilibrium. Any elementary channel of this flow has a path determined by its surrounding medium and a width which expands or contracts in accordance with the mass flow requirements. The normal acceleration or centrifugal force required to divert this channel from a straight path is obtained from pressure gradients existing in the fluid.

For incompressible flow about a body, a pressure drop at the surface is accompanied by an increase in local flow velocity, the increase in local flow velocity causes a proportionate decrease in stream channel width, the contraction of the stream channels enables the flow at a large distance from the body to be essentially straight, and the curvature of the streamlines passing around the body causes the normal pressure gradient and the pressure drop at the surface through centrifugal force.

Compressibility is a flow problem involving flow continuity and centrifugal force. Continuity requires that the width of a stream channel expand as the enclosed gas expands with decreasing pressure. The centrifugal force effects are then magnified by the increased displacement of these dilated stream channels. The effects are cumulative, as the distorted streamlines produce greater pressure drops and hence greater expansion of the stream channels. Critical compressibility occurs when the process magnifies itself to the point where these cumulative effects augment themselves in a divergent manner.

This paper was originally issued by the Grumman Aircraft Engineering Corporation in March, 1943. Received October 30, 1944. To have been presented at the I.A.S. Thirteenth Annual Meeting, which was canceled to cooperate with a Government appeal (January, 1945) to refrain from holding conventions and meetings.

* Aerodynamicist.

NOTATION

ΔA = area of an elementary stream tube
C_p = pressure coefficient, $(P - P_1)/{}^1/_2\rho_1 v_1^2$
M = Mach Number of free stream
P = pressure
S = distance along an equipotential line from the body
ΔS = width of an elementary stream channel of flow, $\Delta\psi/\rho v$
R = radius of revolution
r = radius of curvature of streamline
t = local thickness of a symmetric body
v = fluid velocity
x = rectangular space coordinate parallel to free flow
y = rectangular space coordinate normal to free flow
λ = ratio of specific heats, 1.405 for air
ρ = fluid mass density
φ = flow potential
ψ = flow mass
ω = angle of revolution

Subscripts

M = compressible flow system
0 = incompressible flow system
s = point on the surface of the body
cr = critical value, not necessarily the local speed of sound
1 = point where free stream conditions exist
φ = relation for constant φ

ATTENUATION METHOD

It shall be assumed that the fluid is adiabatic and inviscid. For such a fluid the Bernoulli relation is

$$(dP/\rho) + v\,dv = 0 \qquad (1)$$

The rotation of a fluid element about its center is

$(dv/dS)_\varphi$ and its rotation about the streamline center of curvature is v/r. For irrotational motion

$$(dv/dS)_\varphi + (v/r) = 0 \tag{2}$$

Combining Eqs. (1) and (2) we have the normal pressure gradient required to balance the centrifugal force of the element

$$(dP/dS)_\varphi - (\rho v^2/r) = 0 \tag{3}$$

Introducing $dC_p = dP/(\rho_1/2)v_1^2$

$$(dC_p/dS)_\varphi - (2\rho v^2/r\rho_1 v_1^2) = 0 \tag{4}$$

For any given flow, a value of φ, S determines a point, and hence determines the value of r at that point. Conversely, there is a value of S which corresponds to the point, φ, r.

Eq. (4) is the relation of the pressure gradient with respect to distance along an equipotential line. If it is desired to evaluate the pressure gradient with respect to r, a change of independent variables is made

$$(dC_p/dr)_\varphi - (2\rho v^2/r\rho_1 v_1^2)(dS/dr)_\varphi = 0 \tag{5}$$

Consider two systems whose boundaries consist of the same body streamline and undisturbed flow at infinity. One system shall be composed of an incompressible fluid, the other, a compressible fluid. At the same point on the body streamline, (x_s, y_s), there will exist the potential lines, φ_0 = const. and φ_M = const. for the two systems, respectively, which pass through this point. It is desired to relate the pressure gradient with respect to the radius of curvature gradient existing at the points (φ_0, r) and (φ_M, r), where r is the same for both points.

$$\left(\frac{C_{pM}}{dr}\right)_\varphi \Big/ \left(\frac{dC_{p0}}{dr}\right)_\varphi = \left(\frac{\rho}{\rho_1}\right)_M \left(\frac{v}{v_1}\right)_M^2 \left(\frac{v_1}{v}\right)_0^2 \left(\frac{dS_M}{dr}\right)_\varphi \left(\frac{dr}{dS_0}\right)_\varphi \tag{6}$$

The physical space coordinates of the two points whose gradients are related by Eq. (6) are not necessarily the same. However, if Eq. (6) is integrated to a point, (φ, r_s), which is a point on the surface of the body, (x_s, y_s), this point will be common to both systems.

The representation of the two systems is shown in Fig. 1. In the attenuation plane the parametric use of r produces the representation of the points shown in the physical plane by points common to both systems.

In Eq. (6), the ratios of velocity and density are easily evaluated as functions of C_p and M. The exact evaluation of the curvature gradient would involve the determination of the specific streamline patterns for the systems. Solutions involving specific flow patterns obtained through successive approximations have so far proved to be unwieldy and impractical. This paper shall deal with an approximate solution for bodies of arbitrary shape by using assumed flow patterns which are not necessarily associated with any specific body. Several patterns are discussed in the following sections which achieve this purpose.

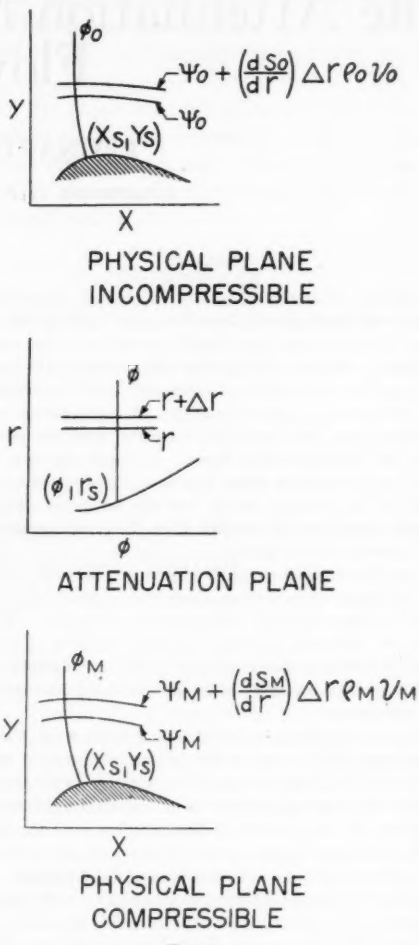

FIG. 1.

Circular Arc Pattern

The system, bound by lines on which free stream conditions exist, shall consist of streamlines of circular arc shape.

In the diagram shown for the system, Fig. 2, a right triangle is formed by drawing the perpendicular, b, to the radius vector. The distance from this intersection to the streamline is called h. The relation for the sides of this triangle is

$$r^2 = b^2 + (r - h)^2 \tag{7}$$

Similarly for the adjacent streamline

$$(r + dr)^2 = \left[b + \left(\frac{\Delta S_1}{\Delta S}\right) dS \sin\beta\right]^2 + \left\{(r + dr) - \left[h + dS - \left(\frac{\Delta S_1}{\Delta S}\right) dS \cos\beta\right]\right\}^2 \tag{8}$$

where β = angle of arc sector.

Solving Eqs. (7) and (8) for dr/dS produces (see Appendix I)

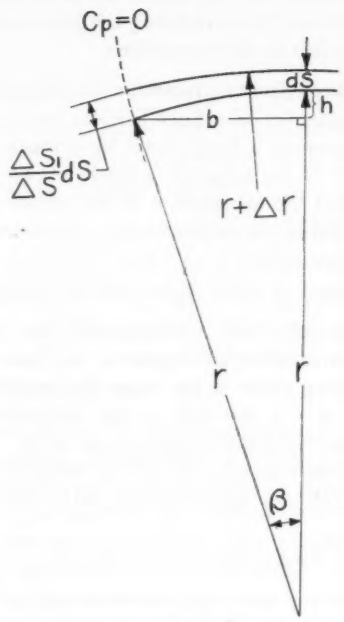

FIG. 2.

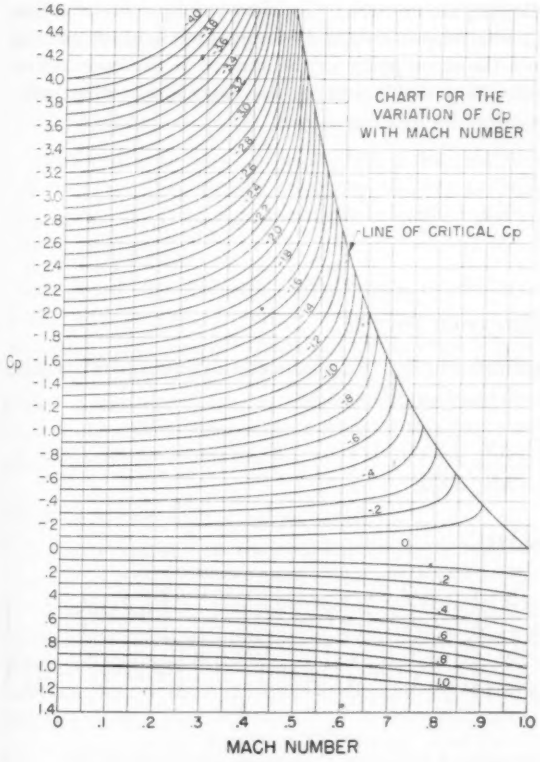

FIG. 3a.

$$dr/dS = [(\Delta S_1/\Delta S)\sec\beta - 1]/(\sec\beta - 1) \quad (9)$$

Using Eq. (9) to describe the ratio between compressible and incompressible flow

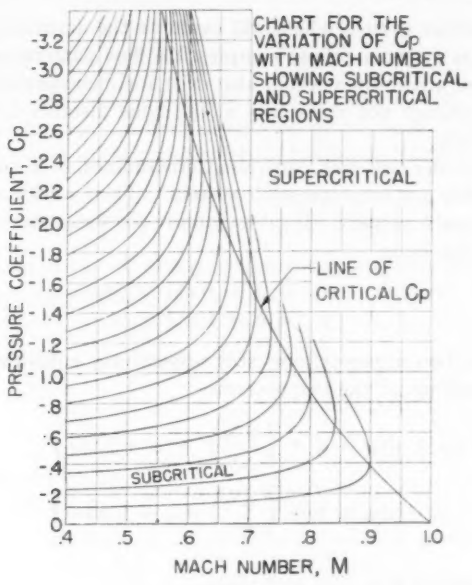
CHART FOR THE VARIATION OF Cp WITH MACH NUMBER SHOWING SUBCRITICAL AND SUPERCRITICAL REGIONS
SUPERCRITICAL
LINE OF CRITICAL Cp
SUBCRITICAL
PRESSURE COEFFICIENT, Cp
MACH NUMBER, M

FIG. 3b.

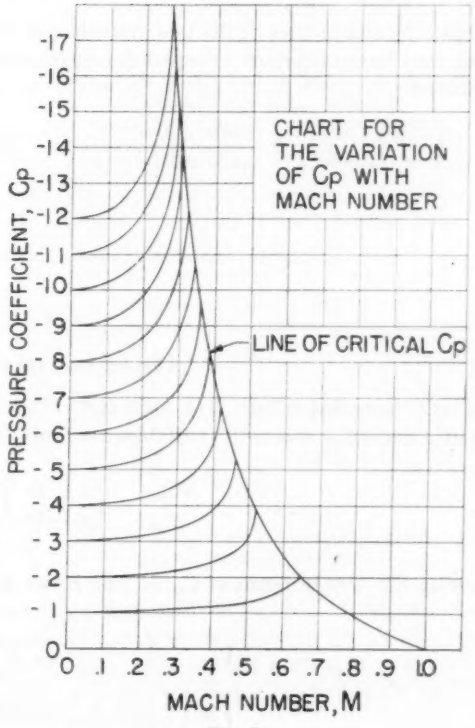

FIG. 3c.

$$\left(\frac{dS_M}{dr}\right)_\varphi \left(\frac{dr}{dS_0}\right)_\varphi \frac{(\Delta S_1/\Delta S)_0 \sec\beta - 1}{(\Delta S_1/\Delta S)_M \sec\beta - 1} \quad (10)$$

If β is small, Eq. (10) will become (see Appendix II)

$$\left(\frac{ds_M}{dr}\right)_\varphi \left(\frac{dr}{dS_0}\right)_\varphi = \frac{(\Delta S_1/\Delta S)_0 - 1}{(\Delta S_1/\Delta S)_M - 1} \quad (11)$$

Equivalent Streamline Pattern

Another system which will evaluate the attenuation ratio is a system whose compressible flow pattern consists of streamlines which also exist for incompressible flow, though not necessarily at the same distance from the body.

Consider two such equivalent streamlines in a compressible and incompressible system. Their y ordinates are a and b, respectively, at an infinite distance upstream from the body.

$$\left.\begin{aligned} y_M &= a + f(x) \\ y_0 &= b + f(x) \end{aligned}\right\} \tag{12}$$

For two adjacent, and still respectively equivalent, streamlines, of the two systems

$$\left.\begin{aligned} y_M + dy_M &= a + \left(\frac{\Delta S_1}{\Delta S}\right)_M dy_M + f_1(x) \\ y_0 + dy_0 &= b + \left(\frac{\Delta S_1}{\Delta S}\right)_0 dy_0 + f_1(x) \end{aligned}\right\} \tag{13}$$

Combining Eqs. (12) and (13)

$$dy_M/dy_0 = [(\Delta S_1/\Delta S)_0 - 1]/[(\Delta S_1/\Delta S)_M - 1] \tag{14}$$

Because the streamlines of the two systems still correspond, they have undergone an equal change in radius of curvature

$$\left(\frac{dS_M}{dr}\right)_\varphi \left(\frac{dr}{dS_0}\right)_\varphi = \frac{(\Delta S_1/\Delta S)_0 - 1}{(\Delta S_1/\Delta S)_M - 1} \tag{15}$$

In the above treatment there will be a small error introduced caused by considering the increment, dy, as measured normal to the streamlines.

Compressibility Effect on Streamline Displacement

The displacement of a fluid particle from a straight path when passing a body could be expressed by the displacement of an adjacent particle on an adjacent streamline less the contraction of the enclosed stream channel. Calling the displacement $t/2$, measured normal to the streamline,

$$(t/2)_{\psi + \Delta\psi} = (t/2)_\psi - (\Delta S_1 - \Delta S)_{\Delta\psi} \tag{16}$$

For compressible and incompressible flow about the same body streamline, each point of one flow will have a corresponding point in the other flow which has the same value of $t/2$ and lies on the equipotential line which intersects the same point on the body. To select such corresponding points it will be necessary, according to Eq. (16), to select normal path increments so that

$$\Delta S_M/\Delta S_0 = [(\Delta S_1/\Delta S)_0 - 1]/[(\Delta S_1/\Delta S)_M - 1] \tag{17}$$

Eq. (17) is the same ratio as developed in Eqs. (11) and (15). It is seen that the streamline patterns used in developing Eqs. (11) and (15) are equivalent to the following assumption: Consider the equipotential lines in a noncompressible and compressible fluid, originating from the same point on the surface of the body. Corresponding displacements are associated with corresponding radii of curvature.

Application of the Attenuation Factor

The ratio expressed in Eqs. (11), (15), and (17), when substituted in Eq. (6), produces a differential relation between dC_{p0} and dC_{pM} where the variables are functions only of C_{p0}, C_{pM}, M, and λ:

$$\frac{dC_{pM}}{dC_{p0}} = \left(\frac{\rho}{\rho_1}\right)_M \left(\frac{v}{v_1}\right)^2_M \left(\frac{v_1}{v}\right)^2_0 \left[\frac{(\Delta S_1/\Delta S)_0 - 1}{(\Delta S_1/\Delta S)_M - 1}\right] \tag{18}$$

Expressing Eq. (18) in terms of C_p, M, and λ (see Appendix III),

$$\frac{dC_{pM}}{dC_{p0}} = \left[\frac{(1 - C_{p0})^{1/2} - 1}{1 - C_{p0}}\right] \left\{ \frac{\left(1 + \frac{\lambda}{2} C_{pM} M^2\right)^{1/\lambda} \left\{ \frac{2}{\lambda - 1}\left[1 - \left(1 + \frac{\lambda}{2} C_{pM} M^2\right)^{(\lambda-1)/\lambda}\right] + M^2 \right\}}{M^2\left[\left(\frac{1}{M}\left(1 + \frac{\lambda}{2} C_{pM} M^2\right)^{1/\lambda} \left\{ \frac{2}{\lambda - 1}\left[1 - \left(1 + \frac{\lambda}{2} C_{pM} M^2\right)^{(\lambda-1)/\lambda}\right] + M^2 \right\}^{1/2} - 1\right)\right]} \right\} \tag{19}$$

Eq. (19) may be integrated analytically or, if a step by step method is chosen, it is necessary to obtain the initial slope at the origin, $C_p = 0$. Substituting $C_p = 0$ in Eq. (19) produces the indeterminate form, 0/0. Therefore, the expression is evaluated by differentiating the numerator and denominator with respect to C_{p0} (see Appendix IV).

$$\lim_{C_p \to 0} \quad dC_{pM}/dC_{p0} = 1/[(1 - M^2)(dC_{pM}/dC_{p0})] \tag{20}$$

or

$$\lim_{C_p \to 0} \quad dC_{pM}/dC_{p0} = 1/\sqrt{1 - M^2} \tag{21}$$

The integration of Eq. (19) is shown in Figs. 3a, 3b, and 3c, which show the attenuation correction for two-dimensional compressible flow. The positive pressure coefficient range has been integrated up to the stagnation point value, $C_{p0} = +1$. The compressible impact pressure coefficient is a function solely of the Mach Number and can be found by the exact relation.

$$C_{pM} = (2/\lambda M^2)(\{1 + [(\lambda - 1)/2]M^2\}^{\lambda/(\lambda-1)} - 1) \tag{22}$$

That Eq. (19) agrees with the exact solution, Eq. (22), is shown in Fig. 5. This agreement can also be proved analytically for arbitrary values of λ by integrating Eq. (19) (see Appendix V).

Critical Flow

Definition of Critical Flow

The occurrence of the local speed of sound is a sharply defined condition, but whether it describes any sudden change in aerodynamic properties is seriously open to question. Quoting from the conclusions of reference 1: "In flow over curved surfaces, the velocity of sound constitutes, in general, no critical state." Local shock waves will appear coincident with the occurrence of the local speed of sound if, and only if, the body surface is rough. These are to be distinguished from critical compressibility phenomena, since their existence and intensity are solvely dependent upon the roughness of the local surface.

The definition of critical flow used in this paper shall be as follows:

> The first appearance of a violation of the condition of irrotationality caused solely by the compressible nature of the fluid shall constitute a critical state of flow.

Associated with the critical flow are the conditions of shock, compressibility burble, compressibility stall, separation, drag and lift changes, infinite local flow acceleration, etc. These phenomena have not been included in the definition, as they are not well-defined conditions. The subsequent analysis of this paper will aid in describing critical flow.

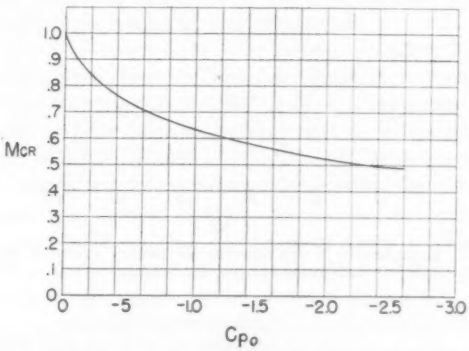

Fig. 4a. Variation of the critical Mach Number with the noncompressible pressure coefficient.

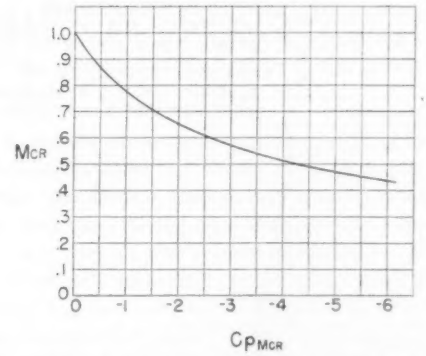

Fig. 4b. Variation of the critical Mach Number with the compressible pressure coefficient.

One-Dimensional Flow

In sharp contrast to the complexity of the solution of multidimensional flow systems, the properties of one-dimensional flow are easily evaluated by the relations of Bernoulli and continuity. Without going into the simple derivations involved, it is suffice to say that there are two points of interest in one-dimensional compressible flow: The occurrence of a minimum cross-sectional area at the local speed of sound; and the occurrence of an infinite local Mach Number, an absolute vacuum, and a maximum velocity on subsequent expansion to an infinite cross-sectional area.

At the point of minimum cross-sectional area it is found that any change of area with length (expressed as the derivative, $dS/dx \neq 0$) is accompanied by an infinite pressure gradient ($dP/dx = \infty$). However, for the condition of a smooth stream tube, the significance of a minimum area is that there is no change of area with length at this point. The solution for the lengthwise pressure gradient is

$$dP/dx = (dP/dS)(dS/dx) = (\infty)(0)$$

This indeterminate form will only have an infinite value if the walls of the channel have an infinite curvature (a sharp corner) at the minimum point. The one-dimensional flow of a compressible fluid expanding from rest to a vacuum in a smooth convergent-divergent channel contains no condition of infinite acceleration.

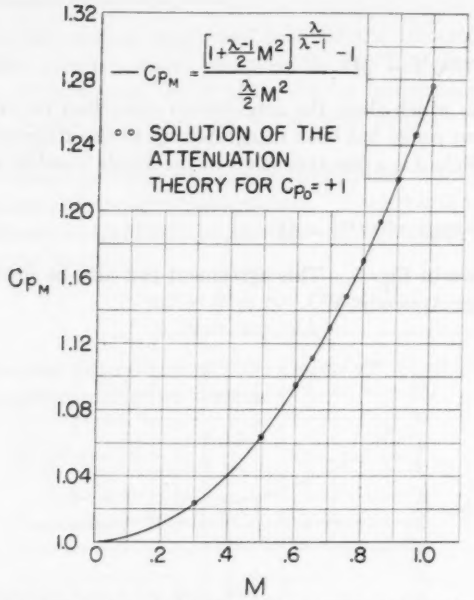

FIG. 5. Comparison of the attenuation theory with the known solution for the impact pressure.

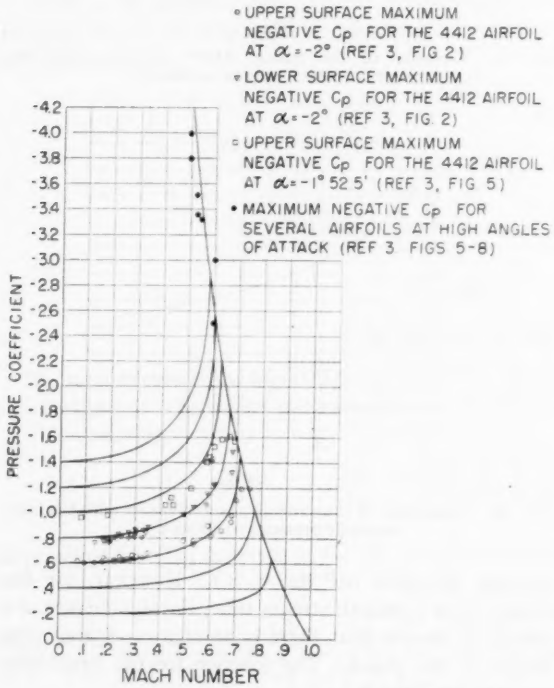
° UPPER SURFACE MAXIMUM NEGATIVE Cp FOR THE 4412 AIRFOIL AT α=-2° (REF 3, FIG 2)
▿ LOWER SURFACE MAXIMUM NEGATIVE Cp FOR THE 4412 AIRFOIL AT α=-2° (REF 3, FIG 2)
▫ UPPER SURFACE MAXIMUM NEGATIVE Cp FOR THE 4412 AIRFOIL AT α=-1° 52.5' (REF 3, FIG 5)
• MAXIMUM NEGATIVE Cp FOR SEVERAL AIRFOILS AT HIGH ANGLES OF ATTACK (REF 3 FIGS 5-8)
PRESSURE COEFFICIENT
MACH NUMBER

FIG. 6. Comparison of theory with experiments.

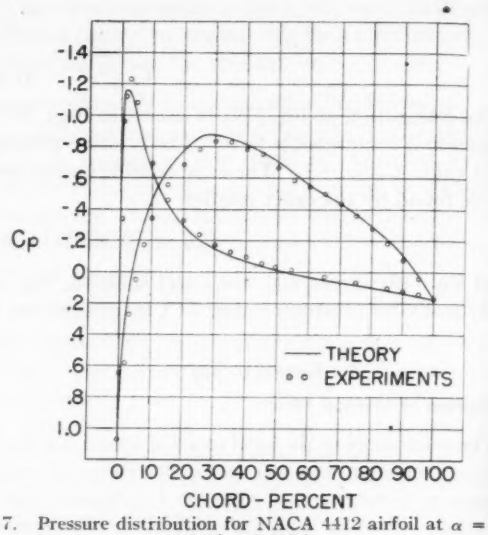

FIG. 7. Pressure distribution for NACA 4412 airfoil at $\alpha = 2°$ and $M = 0.603$.[2]

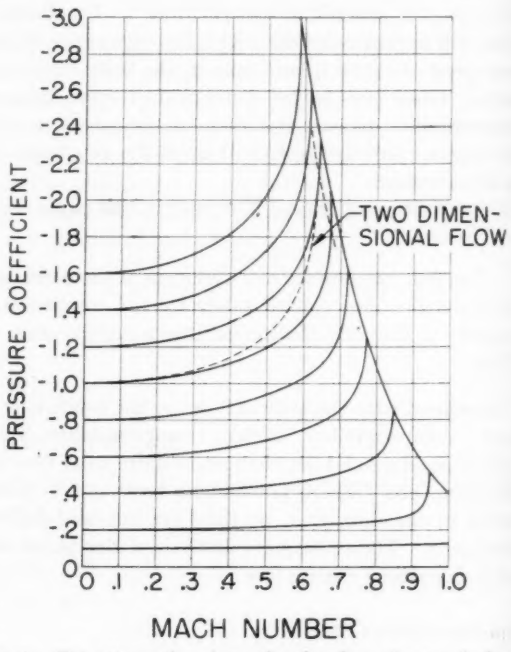

FIG. 8. The attenuation correction for flow about a body of revolution, $R/R_1 = 1.1$ (Eq. (27)).

Two-Dimensional Flow

For two-dimensional flow, there will exist some point between the minimum stream channel width and an infinite stream channel width where the consideration of the stream tube size becomes critical. This point may be determined in the following manner. It is important to note that the derivation is general and does not depend upon the streamline pattern involved. For bodies that differ only in thickness ratio, it can be proved that:

$$\lim_{t_b \to t_a} \frac{v_b - v_a}{t_b - t_a} = \frac{1}{t_a}\left[\left(\frac{v}{v_1}\right)_a - 1\right]$$

Consider the flow about a symmetric body, a, whose surface streamline is $\psi = 0$ and those adjacent streamlines are $\psi = \Delta\psi$ and $\psi = -\Delta\psi$. If the streamline $\Delta\psi$ were translated downward a distance, ΔS_1 and the

streamline $-\Delta\psi$ were translated upward a distance, ΔS_1, these two streamlines would form a body, b, similar in shape to the body, a. The flow external to the streamlines, $\Delta\psi$ and $-\Delta\psi$, will not be affected by the translation. The thickness, t_b, of the body, b, formed by these translated streamlines is found to be:

$$t_b = t_a + 2\Delta S - 2\Delta S_1$$

which, when substituted in the preceding equation, produces

$$\frac{v_b - v_a}{2\Delta S - 2\Delta S_1} = \frac{1}{t_a}\left[\left(\frac{v}{v_1}\right)_a - 1\right]$$

The right-hand side of this equation is positive for values of $(v/v_1)_a$ corresponding to a negative pressure coefficient. Therefore, v_b will be greater than v_a if ΔS exceeds ΔS_1. This would be in violation of the condition of irrotationality expressed in Eq. (2), where the direction of the velocity gradient is established by direction of the radius of curvature. The boundary of this critical condition is

$$\Delta S_1/\Delta S_{cr} = 1 \tag{23}$$

Substituting for $\Delta S_1/\Delta S$ as shown in Appendix III for an adiabatic compressible flow,

$$\frac{1}{M_{cr}}\left(1 + \frac{\lambda}{2} C_{p_{cr}} M_{cr}^2\right)^{1/\lambda} \left\{\frac{2}{\lambda - 1}\left[1 - \left(1 + \frac{\lambda}{2} C_{p_{cr}} M_{cr}^2\right)^{(\lambda-1)/\lambda}\right] + M_{cr}^2\right\}^{1/2} = 1 \tag{24}$$

Since $[1 + (\lambda/2)C_{p_{cr}}M_{cr}^2]^{1/\lambda} = (\rho/\rho_1)_{cr}$, Eq. (24) can be arranged to provide a relation between $C_{p_{cr}}$ and M_{cr} with the density ratio as a parameter.

$$\left.\begin{aligned} M_{cr} &= \left[\left(\frac{2}{\lambda - 1}\right)\frac{(\rho/\rho_1)_{cr}^2 - (\rho/\rho_1)_{cr}^{\lambda+1}}{1 - (\rho/\rho_1)_{cr}^2}\right]^{1/2} \\ C_{p_{cr}} &= 2[(\rho/\rho_1)_{cr}^{\lambda} - 1]/\lambda M_{cr}^2 \end{aligned}\right\} \tag{25}$$

The condition defined by Eq. (25) coincides with the boundary of Eq. (19) beyond which solutions contain singularities. The first attainment of a critical pressure point coincides with the appearance of a double-valued solution for the pressures on the downstream side of this point. Solutions are obtained having either returning subcritical pressures or continuing supersonic expansion, returning to the subcritical realm through a compression shock wave.

Supercritical Flow

A finite pressure gradient for an incompressible fluid approaches an infinite gradient as the critical pressure is approached with a compressible fluid. The viscosity of the fluid, neglected in the treatment of the problem, now becomes of importance in causing a boundary layer that fails to overcome this high adverse pressure gradient and results in flow separation.

The attenuation method does not give any solution for flow which is supercritical at some point on the body. However, there is an hypothesis that shows good agreement with experimental results. If the supercritical flow about a body is divided into two regions by the boundary of critical flow, the pressure coefficient at this boundary will be $C_{p_{cr}}$. Because of the low velocities existing in the region of separation, the pressure gradient across this region can be expected to be low. Thus, the pressure existing at the surface of the body will be approximated by the pressure existing at the boundary of the separated flow, $C_{p_{cr}}$.

As the separated stream channel is supersonic, there will be a shock wave formed when it impacts against the body surface aft of the region of separation. At this point the pressure on the surface of the airfoil will rise suddenly.

A departure from the above treatment of supercritical flow exists when the critical pressure region has low pressure gradients. Under this condition separation does not occur and the fluid continues to expand past $C_{p_{cr}}$ along the upper branch solutions of Eq. (19). This solution containing the second, lower pressure, values of C_{pM} as a function of C_{p0} is found to exist when the critical pressure occurs on the rear portion of an airfoil where the pressure gradients are low. After the continued expansion past the critical pressure, a compression shock wave occurs increasing the pressure to the subcritical range.

Flow About Bodies of Revolution

Eq. (19) can be modified to include the flow about a body of revolution whose axis is in line with the direction of flow. The two-dimensional analysis is unchanged, with the exception that the stream tube has a variable width in the plane of revolution which is proportional to the distance from the axis of revolution at that point. The area of an elementary tube will be

$$\Delta A = \Delta S R \Delta\omega \tag{26}$$

Substituting Eq. (26) in Eq. (19),

$$\frac{dC_{pM}}{dC_{p0}} = \frac{\left[(1 - C_{p0})^{1/2} - \frac{R_1}{R}\right]\left(1 + \frac{\lambda}{2} C_{pM}M^2\right)^{1/\lambda}\left\{\frac{2}{\lambda - 1}\left[1 - \left(1 + \frac{\lambda}{2} C_{pM}M^2\right)^{(\lambda-1)/\lambda}\right] + M^2\right\}}{(1-C_{p0})M^2\left[\left(\frac{1}{M}\left(1 + \frac{\lambda}{2} C_{pM}M^2\right)^{1/\lambda}\left\{\frac{2}{\lambda - 1}\left[1 - \left(1 + \frac{\lambda}{2} C_{pM}M^2\right)^{(\lambda-1)/\lambda}\right] + M^2\right\}^{1/2} - \frac{R_1}{R}\right)\right]} \quad (27)$$

The compressibility correction for bodies of revolution obtained from Eq. (27) for values of R_1/R less than unity is of lower slope and becomes critical at a higher Mach Number. Thus, the use of the two-dimensional correction for bodies of revolution will overestimate the effects of compressibility at subcritical Mach Numbers and will underestimate the critical Mach Number and the limiting negative pressure coefficient.

Wind-Tunnel Effects

As the Mach Number of a flow increases, its ability to contract becomes greatly reduced. As is shown by the attenuation factor, the effect of compressibility is to increase the normal distance away from the body required to reduce the distortion of the body streamline.

In order for wind-tunnel tests to duplicate free flight conditions, it is necessary that the streamlines replaced by the wind-tunnel walls be essentially straight. While a given model-tunnel area ratio may produce results within the desired accuracy for low speed testing, this ratio will have to be considerably reduced in order to produce the same accuracy at high speeds. In addition to the one-dimensional effects of model constriction of the tunnel are the following factors:

(a) The model may divide the tunnel flow into more critical and less critical regions, particularly when the model is set at an incidence to the tunnel flow direction.

(b) The stagnation point will be shifted by a difference in resistance of the flow on either side of the body.

(c) The induced velocities caused by the model will be more than linearly affected by the constriction of the flow caused by the tunnel walls.

References

[1] Ringleb, F., *Exact Solutions of the Differential Equations of an Adiabatic Gas Flow*, Zeit. Angen, Math u. Mech., August, 1940.

[2] Hayes, W. D., *Analytical Investigation of the Greene Theory*, Report No. 4529, Lockheed Aircraft Corporation, January 4, 1944.

[3] Stack, John, and Lindsey, W. F., and Littell, Robert E., *The Compressibility Burble and the Effect of Compressibility on Pressures and Forces Acting on an Airfoil*, N.A.C.A. T.R. No. 646, 1939.

Appendix I

Rearranging Eqs. (7) and (8)

$$r = b^2/2h + (h/2)$$

$$r + dr = \frac{[b + (\Delta S_1/\Delta S)\, dS \sin\beta]^2}{2[h + dS - (\Delta S_1/\Delta S)\, dS \cos\beta]} + (h + dS - \frac{\Delta S_1}{\Delta S} dS \cos\beta)/2$$

Subtracting

$$dr = \frac{(b + (\Delta S_1/\Delta S)\, dS \sin\beta)^2}{2[h + dS - (\Delta S_1/\Delta S)\, dS \cos\beta]} - \frac{b^2}{2h} + {}^1/_2 dS - \frac{1}{2}\left(\frac{\Delta S_1}{\Delta S}\right) dS \cos\beta$$

$$\lim_{dS \to 0} \frac{[b + (\Delta S_1/\Delta S)\, dS \sin\beta]^2}{2[h + dS - (\Delta S_1/\Delta S)\, dS \cos\beta]} = \frac{b^2}{2h} - \left(\frac{b^2}{2h^2}\right) dS + \left(\frac{b^2}{2h^2}\right)\left(\frac{\Delta S_1}{\Delta S}\right) dS \cos\beta + \left(\frac{b}{h}\right)\left(\frac{\Delta S_1}{\Delta S}\right) dS \sin\beta$$

$$\frac{dr}{dS} = \left\{\frac{\Delta S_1}{\Delta S}\left[-(h^2/2)\cos\beta + (b^2/2)\cos\beta + hb\sin\beta\right] + (h^2/2) - (b^2/2)\right\}/h^2$$

Substituting $b = r\sin\beta$; $h = r(1 - \cos\beta)$

$$dr/dS = [(\Delta S_1/\Delta S)(1 - \cos\beta) + \cos\beta\,(\cos\beta - 1)]/(1 - \cos\beta)^2$$

$$dr/dS = [(\Delta S_1/\Delta S)\sec\beta - 1]/(\sec\beta - 1)$$

Appendix II

As the relation given in Eq. (10) is restricted to an equipotential path, β can only approach zero when r is made to approach infinity. For this condition the distance from the body approaches infinity and $\Delta S_1/\Delta S$ approaches unity.

Substituting $\beta = 0$ in Eq. (10) produces the indeterminate form, 0/0. This indeterminate form can be evaluated by differentiating both numerator and denominator with respect to β:

$$\lim_{\beta \to 0} \frac{(\Delta S_1/\Delta S)_0 \sec \beta - 1}{(\Delta S_1/\Delta S)_M \sec \beta - 1} = \lim_{\beta \to 0} \frac{[d(\Delta S_1/\Delta S)_0/d\beta]_\varphi \sec \beta + (\Delta S_1/\Delta S)_0 \sec \beta \tan \beta}{[d(\Delta S_1/\Delta S)_M/d\beta]_\varphi \sec \beta + (\Delta S_1/\Delta S)_M \sec \beta \tan \beta}$$

$$= \lim_{\beta \to 0} \frac{[d(\Delta S_1/\Delta S)_0/d\beta]_\varphi}{[d(\Delta S_1/\Delta S)_M/d\beta]_\varphi}$$

This form is, in general, no longer indeterminate (i.e.—$\lim \beta \to 0 \quad [d(\Delta S_1/\Delta S)/d\beta]_\varphi = \sqrt{2}/2$ at the vertical axis of symmetry of an incompressible flow about a cylinder).

$$\lim_{\beta \to 0} \frac{[d(\Delta S_1/\Delta S)_0/d\beta]_\varphi}{[d(\Delta S_1/\Delta S)_M/d\beta]_\varphi} = \frac{(\Delta S_1/\Delta S)_{0,\ \beta=\Delta} - (\Delta S_1/\Delta S)_{0,\ \beta=0}}{(\Delta S_1/\Delta S)_{M,\ \beta=\Delta} - (\Delta S_1/\Delta S)_{M,\ \beta=0}}$$

$$\varphi = \text{const.} = \frac{(\Delta S_1/\Delta S)_0 - 1}{(\Delta S_1/\Delta S)_M - 1}$$

Appendix III

For an adiabatic gas

$$\rho/\rho_1 = (P/P_1)^{1/\lambda} \tag{a}$$

Expressing the pressure ratio in terms of the pressure coefficient

$$C_p = (P - P_1)/{}^1/_2\rho_1 v_1^2, \qquad P/P_1 = (\rho_1 v_1^2/2P_1)\ C_p + 1 \tag{b}$$

Substituting $v_1^2 = (\lambda P_1/\rho_1)M^2$

$$P/P_1 = 1 + (\lambda/2)C_{pM}M^2 \tag{c}$$

$$(\rho/\rho_1)_M = [1 + (\lambda/2)C_{pM}M^2]^{1/\lambda} \tag{d}$$

Writing Bernoulli's relation

$$P/P_1 = \{1 - [(\lambda - 1)/2]M^2[(v^2/v_1^2) - 1]\}^{\lambda/(\lambda-1)} \tag{e}$$

Substituting Eq. (c) and rearranging

$$(v/v_1)_M{}^2 = (1/M^2)(2/(\lambda - 1)\{1 - [1 + (\lambda/2)C_{pM}M^2]^{(\lambda-1)/\lambda}\} + M^2) \tag{f}$$

From the relation of continuity

$$\Delta S_1/\Delta S = \rho v/\rho_1 v_1 \tag{g}$$

Substituting Eqs. (d) and (f)

$$\left(\frac{\Delta S_1}{\Delta S}\right)_M = \frac{1}{M}\left(1 + \frac{\lambda}{2}\,C_{pM}M^2\right)^{1/\lambda}\left\{\frac{2}{\lambda - 1}\left[1 - \left(1 + \frac{\lambda}{2}\,C_{pM}M^2\right)^{(\lambda-1)/\lambda}\right] + M^2\right\}^{1/2} \tag{h}$$

For an incompressible flow

$$P_1 + {}^1/_2\rho v_1^2 = P + {}^1/_2\rho v^2 \tag{i}$$

which, when rearranged, produces

$$(v_1/v)_0{}^2 = 1/(1 - C_{p0}) \tag{j}$$

and

$$(\Delta S_1/\Delta S)_0 = (1 - C_{p0})^{1/2} \tag{k}$$

By substituting the ratios (d), (f), (h), (j), and (k) in Eq. (18), Eq. (19) will be obtained.

Appendix IV

Before differentiating Eq. (19), it is reduced by finding the limit of the finite portion:

$$\lim_{C_p \to 0} \frac{\left(1 + \frac{\lambda}{2}\,C_{pM}M^2\right)^{1/\lambda}\left\{\frac{2}{\lambda - 1}\left[1 - \left(1 + \frac{\lambda}{2}\,C_{pM}M^2\right)^{(\lambda-1)/\lambda}\right] + M^2\right\}}{M^2(1 - C_{p0})} = 1$$

$$\lim_{C_p \to 0} \frac{dC_{pM}}{dC_{p0}} = \frac{(1 - C_{p0})^{1/2} - 1}{\frac{1}{M}\left(1 + \frac{\lambda}{2} C_{pM} M^2\right)^{1/\lambda} \left\{\frac{2}{\lambda - 1}\left[1 - \left(1 + \frac{\lambda}{2} C_{pM} M^2\right)^{(\lambda-1)/\lambda}\right] + M^2\right\}^{1/2} - 1}$$

Differentiating numerator and denominator with respect to C_{p0}

$$\lim_{C_p \to 0} \frac{dC_{pM}}{dC_{p0}} = \frac{-1/2}{\frac{1}{M}\left[-\frac{1}{2M}\left(\frac{dC_{pM}}{dC_{p0}}\right) M^2 + \left(\frac{M}{2}\right)\frac{dC_{pM}}{dC_{p0}} M^2\right]} = \frac{1}{(dC_{pM}/dC_{p0})\,(1 - M^2)}$$

Appendix V

The curves of Figs. 3a, 3b, and 3c were obtained by numerical integration of Eq. (19) for $\lambda = 1.405$. As shown in reference 2, analytic integration produces:

$$\log (1 - C_{p0}) - 2(1 - C_{p0})^{1/2} + 2 = \log \frac{1}{M^2}\left\{\frac{2}{\lambda - 1}\left[1 - \left(1 + \frac{\lambda}{2} C_{pM} M^2\right)^{(\lambda-1)/\lambda}\right] + M^2\right\} + \ldots. +$$
$$\left(\frac{2}{(\lambda - 1)M^2}\right)^{1/2}\left(1 + \frac{\lambda - 1}{2} M^2\right)^{(\lambda+1)/2\lambda - 2}\left[B\left(1/2, \frac{\lambda}{\lambda - 1}, w_0\right) - B\left(1/2, \frac{\lambda}{\lambda - 1}, w\right)\right] \quad (19a)$$

where B is the incomplete Beta function

$$w = \left(\frac{\lambda - 1}{2}\left\{\frac{2}{\lambda - 1}\left[1 - \left(1 + \frac{\lambda}{2} C_{pM} M^2\right)^{(\lambda-1)/\lambda}\right] + M^2\right\}\right) \Big/ \left[1 + \left(\frac{\lambda - 1}{2}\right) M^2\right]$$

$$w_0 = [(\lambda - 1)/2]M^2/\{1 + [(\lambda - 1)/2]M^2\}$$

Examination of Eq. (19a) shows that the point $C_{p0} = 1$ produces a singularity which requires that

$$[2/(\lambda - 1)]\{1 - [1 + (\lambda/2)C_{pM}M^2]^{(\lambda-1)/2}\} + M^2 = 0$$

which is the same relation as Eq. (22) and is an exact solution for the stagnation point.

If a value of 1.4 is assigned to λ, Eq. (19a) can be expressed without the use of the incomplete Beta function.

$$\log_e (1 - C_{p0}) - 2(1 - C_{p0})^{1/2} + 2 = \log_e M^{-2}\{5[1 - (1 + 0.7C_{pM}M^2)^{0.28571}] + M^2\} + \ldots. +$$
$$\frac{(1 + 0.2M^2)^3}{0.44721M}\{1/3 w_0^{1/2}(1 - w_0)^{1/2}[1.875 + 1.25\,(1 - w_0) + (1 - w_0)^2] + \ldots. +$$
$$0.3125 \sin^{-1}(2w_0 - 1) - 1/3 w^{1/2}(1 - w)^{1/2}[1.875 + 1.25(1 - w) + (1 - w)^2] - \ldots.$$
$$-0.3125 \sin^{-1}(2w - 1) \quad (19b)$$

where $\sin^{-1}(2w - 1)$ is restricted to a principle value between $\pm\pi/2$. Eq. (19b) can be evaluated by the following procedure. Plot

$\log_e (1 - C_{p0}) - 2\,(1 - C_{p0})^{1/2} + 2$ vs. C_{p0} — Step (1)

$M^{-2}\{5[1 - (1 + 0.7C_{pM}M^2)^{0.28571}] + M^2\}$ vs. C_{pM} and M — Step (2)

$0.44721M\,(1 + 0.2M)^{-3}$ and w_0 vs. M — Step (3)

$1/3 w^{1/2}(1 - w)^{1/2}[1.875 + 1.25\,(1 - w) + (1 - w)^2] + 0.3125 \sin^{-1}(2w - 1)$ vs. w — Step (4)

The right-hand side of Eq. (19b) is obtained from Steps (2), (3), and (4) for any value of C_{pM} and M and, from Step (1), the corresponding value of C_{p0}.

Strength of Magnesium-Alloy Columns

F. A. RAPPLEYEA*

The Dow Chemical Company

ABSTRACT

In order to present data for designing magnesium-alloy columns, tests on round bars of various commercial magnesium alloys were made. Two sets of end conditions were used—pin-ended and flat-ended. The pin-ended tests were conducted using carefully machined semispheric ends, a modified version of a jig proposed by J. A. Van den Broek. The flat-ended tests were made between two closely ground platens.

Various types of formulas were studied as to applicability for design use. It was found that Van den Broek's limit stress formula or a straight line formula in the form

$$P/A = B - D(Kl/i)$$

where the constants depend upon the alloy used (the formula is conservative), may be used to predict the column strengths of magnesium alloys if secondary failure does not occur. At l/i values $>3E/B$, the Euler formula is used rather than the straight line formula. Values of the various constants used for different commercial magnesium alloys are given.

INTRODUCTION

COLUMN TESTING is over 200 years old. Many papers have been published both on testing procedure and theory. Since the early days in the history of columns and since Musschenbroek, Euler, Coulomb, Bauschinger, Engesser, Considère, and Tetmajer worked on the problem,[3] column curves for various materials have been determined. The published data on magnesium columns, however, are rather incomplete, and for this reason this study was made.

SCOPE

In order to determine the column characteristics of any material, it is necessary to determine the load at primary failure of columns having various slenderness ratio values. This type of failure has been quite completely discussed by other investigators[1–9] and needs no further explanation. Any form of secondary failure—e.g., local or crippling failure—should not be considered in a column curve. For these reasons round bars were selected as the simplest sections to use.

TEST PROCEDURE

There are two general methods of testing columns in order to obtain column curves. One is to test by means of pin-ended loading, and the other is to test by means of flat-ended loading. Both methods were used in this study. Whereas the latter method gives a coefficient of fixity, c, at the ends of from 3.0 to nearly 4.0, the former gives a degree of fixity of approximately 1.0. There are some frictional forces when testing pin-ended columns, but these are negligible.[9] For all practical purposes 1.0 may be used in the pin-ended tests. In order to obtain pin-ended conditions, a modified version of Van den Broek's testing semispheres was used.[1] The flat-ended tests required no special equipment.

Pin-Ended Column Tests

The jig for testing under pin-ended conditions consisted of two partial spheres each seated in a ring. The complete assembly is so designed that a load can be transmitted through the spheres to the centroid of the cross section of the specimens. These spherical ends, therefore, provide as nearly as possible the fixity of theoretic pin-ended columns. This general type of jig has been described by J. A. Van den Broek,[1] who cooperated in designing the modified version that was used for these tests. The value of the partial spheres used in these tests lies not only in the ability to approach an end fixity of 1.0 but also in the ability to have complete freedom of movement in all directions.

The component parts and the assembly of the loading spheres are shown in Figs. 1 and 2. Fig. 1 gives the dimensions of the assembly. The ring shown in the upper part of Fig. 2 is a retaining ring and serves the purpose of holding the partial sphere, a hardened plate, and a centering plate in line. These latter two items are shown in Fig. 2 just below the retaining ring, the centering plate having a hole in it to fit a $^1/_2$-in. round extrusion. The round plate to the left is a loading plate. To assemble the jig, the centering plate is dropped into the retaining ring, and the hardened surface plate is then placed in the ring on top of the centering plate. The partial sphere is then placed in the ring. The loading plate is placed between the head of the machine and the rounded portion of the partial sphere. The specimen is placed through the centering ring contacting the hardened plate so that the center of the partial sphere lies in the plane of the loading end and at the centroid of the cross section of the test specimen. This point corresponds to the end of the 2-in. radius shown in Fig. 1.

The sphere and the plates were ground to tolerances of ± 0.0005 in. in order to fit the hole as perfectly as

Received December 4, 1944. To have been presented at the I.A.S. Thirteenth Annual Meeting, which was canceled to cooperate with a Government appeal (January, 1945) to refrain from holding conventions and meetings.

* Development Engineering, Magnesium Division.

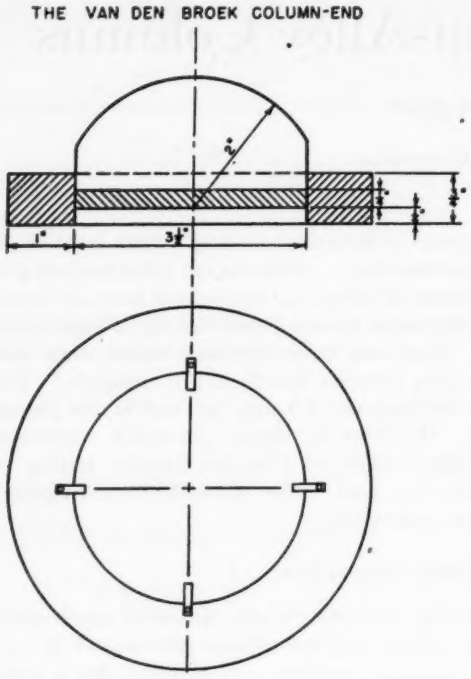

FIG. 1.

FIG. 2. Assembly of Van den Broek column end.

possible, so that nearly perfect alignment resulted automatically. The function of the hardened plate directly under the sphere is twofold. First, it protects the flat surface on the bottom of the partial sphere, and, second, the plate with the retaining ring allows for flexibility in choice of size and shape of specimens. Protection of the surface is important because, if this surface becomes damaged, it is necessary to remachine the whole sphere. This is a difficult job, since the sphere must be checked to 0.0005 in. by physical means. As it is, damage to the flat surface means only a remachining of the flat plate.

The testing machines used were two hydraulic loading machines; one was a Tate-Emery 60,000-lb. Compression Machine, which was used for testing columns less than 12 in. long; the other was a 300,000-lb. Riehle Tension and Compression Machine. Of the two, the Tate-Emery was somewhat more satisfactory and accurate, since it was primarily designed for compression tests only. Both machines had accuracies within less than $1/2$ per cent as determined by actual test with Moore proving rings. The sensitivity was 5 lbs. for the Riehle machine and 2 lbs. for the Tate-Emery machine.

The specimens used were commercially extruded $1/2$-in. diameter magnesium-alloy rods, carefully checked for straightness. The plot of the initial crookedness of a specimen chosen at random from those measured is shown on Fig. 3. All of the specimens were round. No ovality was observed. The

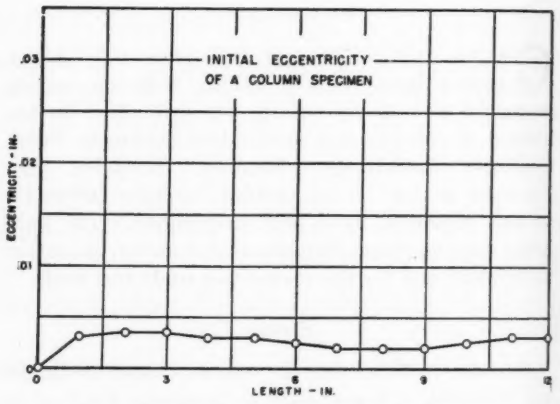

FIG. 3. Initial eccentricity of a column specimen.

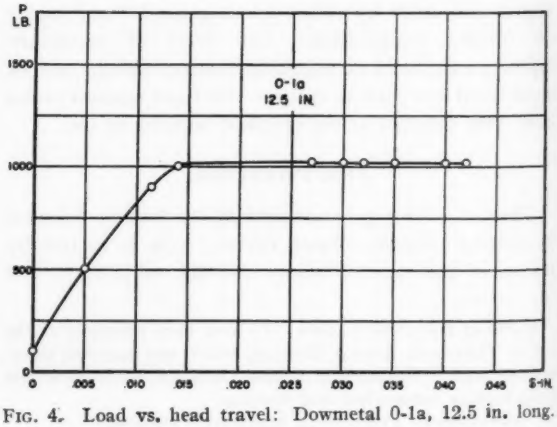

FIG. 4. Load vs. head travel: Dowmetal 0-1a, 12.5 in. long.

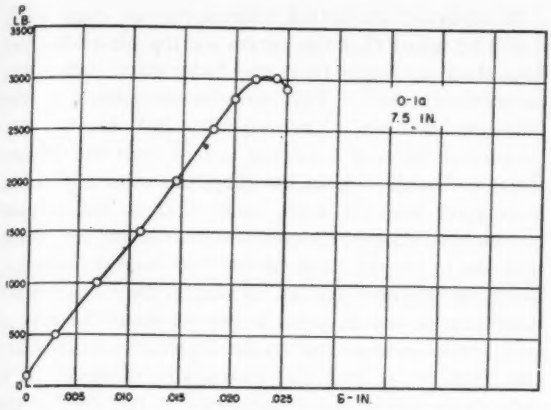

FIG. 5. Load vs. head travel: Dowmetal 0-1a, 7.5 in. long.

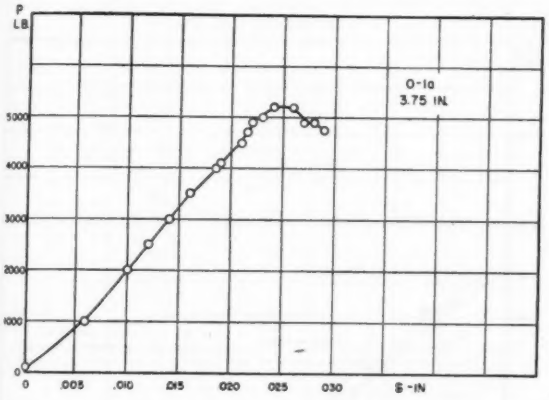

FIG. 6. Load vs. head travel: Dowmetal 0-1a, 3.75 in. long.

specimens were machined to length, and the ends were made as flat, parallel, and perpendicular to the stress axis as possible.

The specimens were centered in the machine by applying a small load and tapping one of the spheres until it was in alignment with the other sphere, as evidenced by a spirit level. Loads were applied slowly at a head travel rate of 0.05 in. per min. up to the point of complete failure of the column, at which time the load dropped suddenly. For three of the specimens axial deformation readings were taken simultaneously with applied loads, and the readings are shown plotted on Figs. 4, 5, and 6.

Flat Ended Column Tests

In running the flat-ended tests of the columns, the spherical ends were removed and the columns placed between the two flat plates of the testing machine. The specimens were aligned collinear with the loading axis of the machine by means of concentric rings marked on the base plates. Duplication of ultimate loads on identical specimens gives an indication of the accuracy of testing.

RESULTS

Data from the compressive and tensile stress-strain curves are given in Table 1, listing the properties of the materials studied. All the column data were reduced to a basis of stress versus slenderness ratio and plotted on Figs. 7–11. Both the results of the pin-ended tests and flat-ended tests were plotted on these figures.

The method used in obtaining the effective slenderness ratios for the specimens tested as flat-end columns

TABLE 1

Properties of Materials Used for Column Tests

		Tension*			Compression†	
Dowmetal Alloy	Specimen Number	Yield strength, lbs. per sq. in.	Ultimate strength, lbs. per sq. in.	% Elongation in 2 in.	Proportional limit 0.01% offset, lbs. per sq. in.	Yield strength, lbs. per sq. in.
M	31098-17	18,700	35,300	18.7	9,400	17,200
	31098-18	22,800	36,600	16.7	9,800	19,000
	31098-19	21,600	35,500	16.6	7,400	16,200
	31098-20	20,000	34,000	16.6	8,000	16,700
J-1	31100-11	35,500	46,900	15.3	18,400	23,300
	31100-12	35,600	47,600	13.3	18,600	25,200
	31100-13	35,800	48,400	13.3	20,200	25,300
	31100-14	32,400	46,200	16.0	14,000	24,600
FS-1	31099-17	34,200	40,900	14.0	15,400	18,200
	31099-18	30,400	41,000	14.0	15,200	18,500
	31099-19	28,800	39,800	12.7	14,300	17,600
	31099-20	31,200	41,100	14.0	14,400	18,000
	31099-21	30,100	40,800	15.3	15,600	21,700
O-1A	31092-8	37,600	53,400	8.0	16,600	28,000
	31092-9	42,500	57,200	8.0	18,200	30,100
	31092-10	41,300	56,600	6.0	22,800	31,500
O-1HTA	31089-3	44,100	59,000	4.0	24,200	40,600

* Tests by autographic strain recorder. Yield strengths by 0.2 per cent offset method.

† Tests by Tuckerman Extensometer. Yield strengths by 0.2 per cent offset method. Modulus of elasticity in tension and in compression was 6,500,000 ± 100,000 lbs. per sq.in.

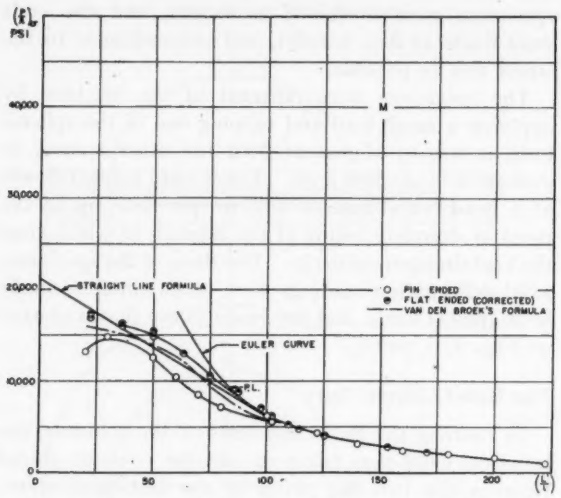

FIG. 7. Column curves for Dowmetal M alloy, round bars, $^1/_2$ in. nominal diameter.

cannot be described here because of wartime restrictions.

THEORY AND DISCUSSION OF TEST RESULTS

In order to understand the phenomenon of column failure, it is first necessary to realize that two aspects of testing technique influence the test results; eccentricity of loading and end conditions of loading. Another factor in the test which must be considered is initial crookedness of the specimen. Ideally, if a straight column could be loaded absolutely concentrically and if perfect end conditions could be obtained, the test points should fall on the Euler curve as long as the specimens fail elastically.[3, 4, 5] As soon as the average stress reaches the limit of proportionality, deviations from the Euler curve should be noted.[7, 8, 9]

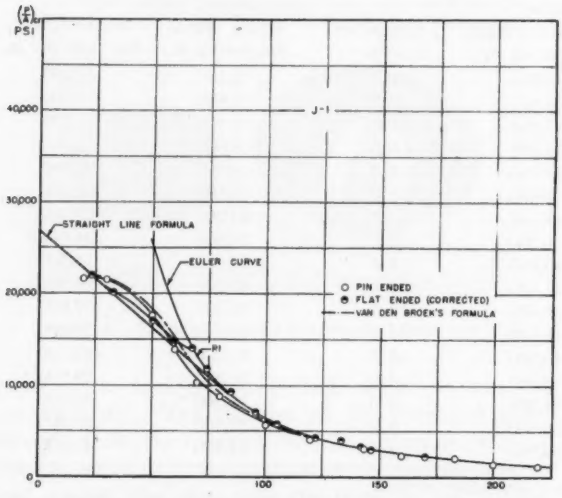

FIG. 8. Column curves for Dowmetal J-1 alloy, round bars, $^1/_2$ in. nominal diameter.

In studying the actual column curves, Figs. 7–11, it will be noted that the curves for the pin-ended test data start deviating from the Euler curve below the proportional limit. This can be explained in the following manner. Theoretically and ideally, the lateral deflection of a column is zero until the column starts to buckle. After buckling, the column sustains a constant load for some time—that is, the column continues to support the constant load during the period that the increasing eccentricity from lateral deflection builds up the fiber stresses, as long as the rate of strain hardening of the material is greater than the rate of such stress increase due to the increasing eccentricity (see Figs. 4, 5, and 6). Practically, however, it is difficult to obtain zero eccentricity at the start of the test, and, consequently, lateral deflection starts at a low load level. Deflection then continues until an ultimate load is reached. This ultimate load may or

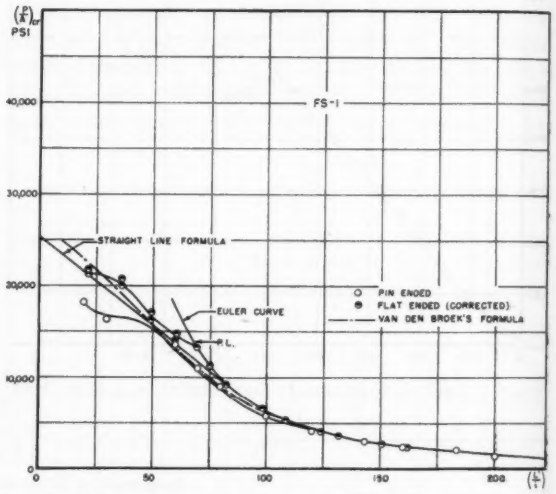

FIG. 9. Column curves for Dowmetal FS-1 alloy, round bars, $^1/_2$ in. nominal diameter.

may not reach the Euler value, depending upon the degree of eccentricity of loading and straightness of the specimen. For this reason deviations from the Euler curve at stress levels below the proportional limit can be and are noted. Necessarily, a formula involving limit stress and a known eccentricity must be used for evaluating data obtained from pin-ended column tests. Van den Broek[1] gives the following formula.

$$\frac{P}{A} = \frac{1}{2}\left\{ + \sigma\left(1 + \frac{ec}{i^2}\right) - \sqrt{\left[S_1 + S_{cr}\left(1 + \frac{ec}{i^2}\right)\right]^2 - 4S_1S_{cr}}\right\} \quad (1)$$

where

e = the initial eccentricity
c = distance from neutral axis to outermost fiber

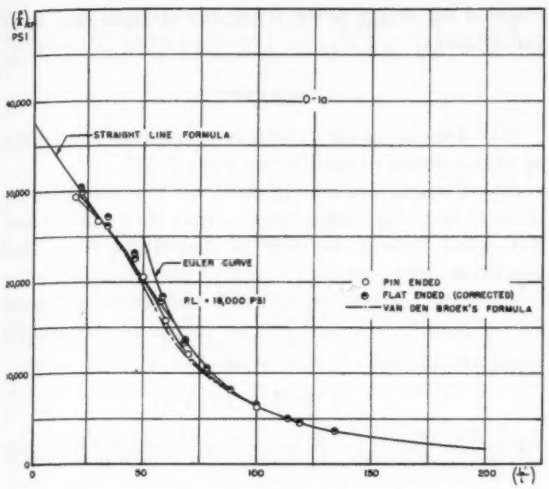

FIG. 10. Column curves for Dowmetal 0-1a alloy, round bars, $^1/_2$ in. nominal diameter.

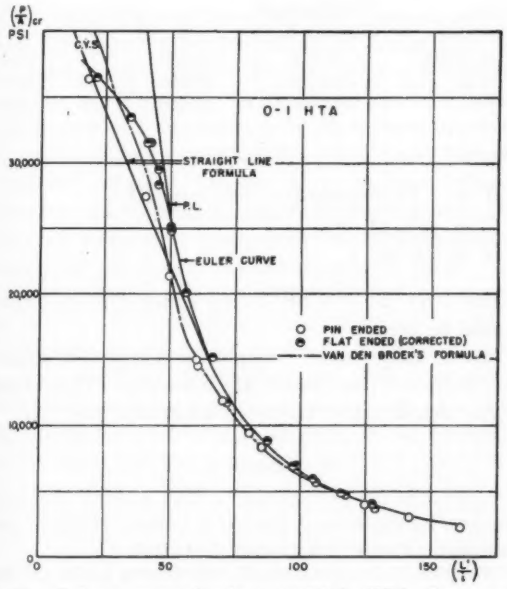

FIG. 11. Column curves for Dowmetal 0-1a HTA alloy, round bars, $^1/_2$ in. nominal diameter.

S_1 = elastic limit stress
$S_{cr} = \pi^2 E/(1/i)^2$
i = least radius of gyration

As is easily shown, the above formula reduces to the well-known Euler column equation when the eccentricity becomes zero. The test results in this paper were fitted by a value ec/i^2 equal to 0.10. In this capacity the formula serves only as an explanation of the results and includes any effect of initial crookedness. As can be readily determined, small amounts of eccentricity affect the test results. The formula may be used in design when the eccentricity is known, for usually, if the eccentricity is known, it is of a large enough value so that minor inaccuracies are negligible.

In studying the flat-ended column test curves on Figs. 7–12, it is noted that the corrected test data fall on the Euler curve, with but few minor deviations, up to the proportional limit stress marked on the graphs. It is felt that these curves of corrected test points represent the ideal behavior of magnesium alloy columns. If, in a certain application, absolute concentricity could be obtained, these curves could be used for design curves. However, to become slightly conservative, it is suggested that the values given by a straight line drawn tangent to the Euler curve and falling below any test point be used. It is observed that the straight-line curves drawn tangent to the Euler curve have a point of tangency below the proportional limit in all cases. Beyond the point of tangency the Euler formula should be used. These curves are plotted for columns reduced to an effective length. The designer must decide what end condition coefficient applies for the actual structure under consideration. When that factor has been decided, the actual length can be reduced to an effective length by dividing the length by the square root of the coefficient of end fixity.

On the figures in which the straight line was drawn tangent to the Euler curve, the point of tangency was selected so that the straight line was just below all the test points. The intercept of this straight line was then recorded and the other values of constants calculated in the formula

$$P/A = B - D(Kl/i)$$

where

P = ultimate column load, lbs.
A = cross-sectional area of the member, in.^{2}

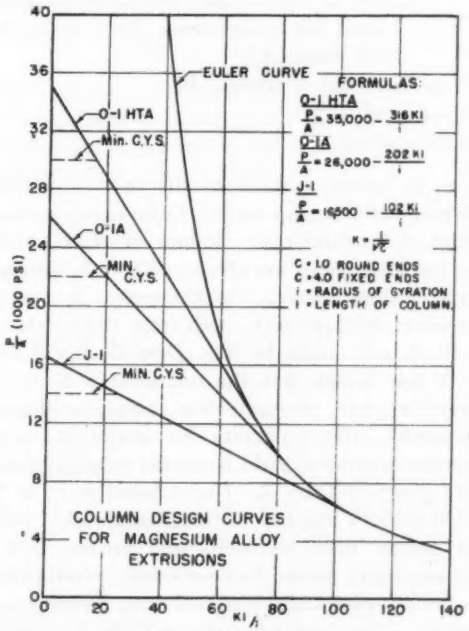

FIG. 12

TABLE 2

Compressive Yield Strengths and Corresponding Constants for Straight Line Column Curves of Wrought Magnesium Alloys as Tested*

All Values Except C Are in Lbs. per Sq. In.

Dowmetal Alloy	Compressive Yield Strength†	B	C	D
O-1HTA	40,600	47,500	65	490
O-1A	31,500	37,750	72	350
J-1	24,600	27,000	85	210
FS-1	21,700	25,000	87	200
M	16,700	21,200	95	150

* Use for $l/i < \pi\sqrt{3E/B}$; for $l/i > \pi\sqrt{3E/B}$ use Euler formula.

† Compressive yield strengths selected from bars tested as short columns—i.e., from specimen numbers 31089-3, 31092-10, 31099-21, 31100-14, and 31098-20.

TABLE 3

Minimum Compressive Yield Strengths and Corresponding Constants for Straight Line Design Column Curves of Commercial Magnesium Alloys*

All Values Except C Are in Lbs. per Sq. In.

Dowmetal Alloy	Minimum Compressive Yield Strength	B	C	D
O-1HTA	30,000	35,000	74	316
O-1A	22,000	26,000	86	202
J-1	14,000	16,500	108	102

B = 1.18 compressive yield strength.

* Use for $l/i < \pi\sqrt{3E/B}$; for $l/i > \pi\sqrt{3E/B}$ use Euler formula

Kl/i = effective slenderness ratio of the column. (B, C, and D are constants depending upon the compressive yield strength of the material.)

B = intercept of straight line

$C = \pi\sqrt{3E/B}$

$D = 2B/3C$

It can be proved mathematically that the ordinate at the point of tangency to the Euler curve is always one-third of the intercept.[2] Values of B, C, and D for the material tested are given in Table 2. Studying the relationship between the intercept, B, and the compressive yield strength, both from these data and from other tests made by The Dow Chemical Company, it was found that the relationship B = 1.18 compressive yield strength was quite satisfactory. Consequently, the constants for materials at the minimum compressive yield strengths were determined and are given in Table 3. Unpublished work at The Dow Chemical Company on magnesium-alloy shapes checks closely these constants and proves that so long as secondary failure does not occur, column curves on shapes are essentially identical with column curves on rounds. The constants given in Table 3 are recommended for design when using the straight line curve for columns.

CONCLUSIONS

(1) Dowmetal alloys behave as columns in a fashion similar to other materials (see Figs. 7–11).

(2) Column curves obtained by pin-ended testing deviate from the Euler curve earlier than curves from flat-ended testing, because of departures from ideal conditions of testing.

(3) The column strengths of magnesium alloys can be predicted conservatively by means of the straight line formula for $(l/i) < \pi\sqrt{3E/B}$

$$P/A = B - D(Kl/i)$$

where the values for B and D recommended for design are as follows.

Alloy	Minimum Compressive Yield Strength, Lbs. per Sq.In.	B	C	D
O-1HTA	30,000	35,000	74	316
O-1A	22,000	26,000	86	202
J-1	14,000	16,500	108	102

where

B = 1.18 compressive yield strength

$C = \pi\sqrt{3E/B}$

$D = 2B/3C$

For $(l/i) > \pi\sqrt{3E/B}$, the Euler column formula should be used.

(4) A more exact formula for pin-ended columns may be used if the eccentricity is known. This formula is Van den Broek's crookedness formula, Eq. (1).

REFERENCES

[1] Van den Broek, J. A., *Rational Column Analysis*, Engineering Journal of the Engineering Institute of Canada, December, 1941; discussion in Engineering Journal, June, 1942.

[2] Templin, R. L., Sturm, R. G., Hartmann, E. C., and Holt, M., *Column Strength of Various Aluminum Alloys*, Aluminum Research Laboratories Technical Paper No. 1, Aluminum Company of America, Pittsburgh, Pa.

[3] Timoshenko, S., *Theory of Elastic Stability;* McGraw-Hill Book Company, Inc., New York, 1936.

[4] Roark, R. J., *Formulas for Stress and Strain;* McGraw-Hill Book Company, Inc., New York, 1938.

[5] Nadai, A., *Plasticity;* McGraw-Hill Book Company, Inc., New York, 1931.

[6] Hartmann, E. C., *Structural Application of Aluminum Alloys*, Civil Engineering, Vol. 102, p. 1369, 1937.

[7] Westergaard, H. M., and Osgood, W. R., *Strength of Steel Columns*, A.S.M.E. Transactions (Applied Mechanics), Vol. 50, No. 17, May–August, 1928.

[8] Osgood, W. R., *Column Curves and Stress-Strain Diagrams*, National Bureau of Standards Journal of Research, Vol. 9, pp. 571–582, October, 1932.

[9] Barlow, H. W., *The Column Strength of Closed, Thin-Walled Sections of 18-8 Stainless Steel*, Journal of the Aeronautical Sciences, Vol. 4, No. 8, pp. 151–161, February, 1941.

Performance Methods for High-Speed Aircraft

WALLACE D. HAYES*
Lockheed Aircraft Corporation

SUMMARY

This paper presents methods for the calculation of the performance of an airplane when the influence of compressibility must be taken into account. The availability of correct high-speed wind-tunnel data and of engine characteristics in terms of thrust or thrust horsepower is assumed. The problems of rate of climb, maximum velocity, range, and dive histories are considered.

The methods are based on the principle of separating dimensional quantities into a dimensionless parameter times a dimensional quantity that is a function only of altitude.

INTRODUCTION

CLASSIC METHODS for the calculation of airplane performance were devised on the assumption that the basic compressibility parameter, Mach Number, need not be considered. With the advent of airplanes with higher speeds, the use of these methods often entails troublesome modification to account for compressibility effects. The use of jet engines indicates extremely high operating velocities at extremely high altitudes, a fact that brings even the problems of range and rate of climb into the compressibility range.

Compressibility effects must be included by considering in all cases the airplane Mach Number, M, which is the ratio between the airplane air speed and the speed of sound in undisturbed air. The necessity of considering this additional parameter causes much extra work but is helpful in allowing an advantageous reformulation of the equations defining dimensionless parameters. Since, at a given altitude, the velocity is proportional to the Mach Number, the introduction of the proper power of M into a conventional dimensionless parameter yields a dimensionless quantity whose relation with the corresponding dimensional quantity is independent of the velocity and dependent only upon the altitude. Such dimensionless quantities will be called velocity-reduced parameters and are useful for stability, control, and structural load calculations, as well as for performance.

The following development describes these quantities and their use in aerodynamic computations. Methods are outlined for the calculation of rate of climb, maximum velocity, range, and histories of steep or shallow dives. The engine characteristics are assumed to be known in terms of the thrust or thrust horsepower. A later section describes the way in which propeller characteristics may be investigated by these methods for airplanes with conventional power plants.

Received October 3, 1944.

* Aerodynamicist.

VELOCITY-REDUCED PARAMETERS

In addition to standard symbols the following notation is used:

q^*	=	dynamic pressure at speed of sound
π	=	dimensionless power available
τ	=	dimensionless thrust available
H	=	dimensionless altitude
L	=	scale length in Reynolds Number
λ	=	aerodynamic mean free path
a_i	=	indicated speed of sound
c	=	mean aerodynamic chord
l_t	=	effective tail length
S_e, c_e	=	area and chord of elevator
l_e	=	elevator mechanical advantage
θ	=	angle of dive from vertical

The quantity q^* is defined by the equation,

$$q^* = (\rho/2)a^2 \tag{1}$$

This equation, together with the relation,

$$V = Ma \tag{2}$$

gives an expression for the dynamic pressure,

$$q = M^2 q^* \tag{3}$$

This quantity q^* may be called the dynamic pressure of the speed of sound. It is actually a pressure that is proportional to the absolute static pressure,

$$q^* = (\rho/2)a^2 = (\rho/2)(\gamma p/\rho) = (\gamma/2)p \tag{1a}$$

With the use of Eqs. (1), (2), and (3) above, the following quantities may be expressed as a product of a dimensionless parameter and a dimensional quantity dependent only upon altitude.

True air speed	V	= M	× a		
Dynamic pressure	q	= M^2	× q^*		
Gross weight—level flight	W	= $C_L M^2$	× $q^* S$		
Acceleration in g	n	= $C_L M^2$	×	$\frac{q^* S}{W}$	
Drag	D	= $C_D M^2$	× $q^* S$		
Thrust available	T	= τ	× $q^* S$		
Power required	P_r	= $C_D M^3$	× $q^* a S$		(4)
Power available	P	= π	× $q^* a S$		
Tail load	P_T	= $C_M M^2$	×	$\frac{q^* S_e}{l_t}$	
Stick force—elevator	F	= $C_H M^2$	×	$\frac{q^* S_e c_e}{l_e}$	
Reynolds Number	R	= M	× L/λ		
Pressure difference	Δp	= $C_p M^2$	× q^*		

In the above quantities, the left-hand factors of the right-hand terms are the so-called velocity-reduced parameters. All the expressions are easily verified except for the equations that define π, τ, and λ. Of these, π and τ are dimensionless expressions for power and thrust, respectively, and λ is expressed:

$$\lambda = L(M/R) = L(V/a)(\nu/VL) = \nu/a \qquad (5)$$

This quantity equals 0.672 times Maxwell's mean free path of the kinetic theory of gases and may be called the aerodynamic mean free path. In considering the scale effect in the compressible range, the combined parameter,

$$R/M = L/\lambda \qquad (5a)$$

is often found to be more valuable than the parameter R.

An expression that arises in considerations of the kinetic energy correction to rate of climb and of vertical dive histories is $(V/g)(dV/dh)$. This may be transformed:

$$\frac{V}{g}\left(\frac{dV}{dh}\right) = \frac{1}{2g}\left[\frac{d(M^2a^2)}{dh}\right] = \frac{M^2}{2g}\left(\frac{da^2}{dh}\right) + \frac{a^2}{2g}\left(\frac{dM^2}{dh}\right)$$

The derivative in the first term is proportional to the temperature gradient, assumed constant (and negative) in standard atmosphere. The second term is simplified by using a dimensionless altitude defined by:

$$H = \int_0^h (2g/a^2)dh \qquad (6)$$

Then

$$(V/g)(dV/dh) = (dM^2/dH) - KM^2 \qquad (7)$$

where $K = 0.133$ in troposphere and 0 in stratosphere.

When the indicated air speed is desired, it may be obtained from the equation

$$V_i = Ma_i \qquad (8)$$

where $a_i = \sigma^{1/2}a$.

The quantities a, a_i, q^*, q^*a, λ, $a^2/2g$, and H are functions of the altitude and are tabulated for the N.A.C.A. standard atmosphere in Table 1.

The use of these velocity-reduced parameters in calculating buffet-limit accelerations, tail loads, stick forces, etc., from high-speed wind-tunnel results may be easily understood. The problems of rate of climb, range, etc., are investigated below.

Rate of Climb

The basic power (or thrust) required curves for rate of climb, high speed, and range are set up in dimensionless form by plotting C_DM^3 (or C_DM^2) vs. M with the parameter C_LM^2, thus obtaining a one-parameter family of curves. The classic method would require a two-parameter family of curves, the parameters being the gross weight and altitude. The rate of climb comes from the following equations, where P is thrust power available:

$$P - DV = WC + \left(\frac{W}{g}\right)V\left(\frac{dV}{dt}\right) = WC\left[1 + \frac{V}{g}\left(\frac{dV}{dh}\right)\right]\times$$

$$\pi - C_DM^3 = \frac{W}{q^*S}\left(\frac{C}{a}\right)\left(1 - KM^2 + \frac{dM^2}{dH}\right)$$

Then

$$C = a\left(\frac{q^*S}{W}\right)\frac{\pi - C_DM^3}{1 - KM^2 + (dM^2/dH)} \qquad (9)$$

With the assumption that the cosine of the climb angle equals 1, the procedure is as follows:

Maximum Rate of Climb

(1) Plot C_DM^3 vs. M with parameter C_LM^2 (thrust horsepower required).

(2) Plot $\pi = P/q^*aS$ vs. M with parameter h.

(3) Calculate $C_LM^2 = W/q^*S$ for various h.

Table 1

Properties of N.A.C.A. Standard Atmosphere

h, Ft.	a, M.P.H.	a, Ft. per Sec.	a_i, M.P.H.	q^*, Lbs. per Ft.^{2}	q^*a, Hp. per Ft.^{2}	$a^2/2g$, Ft.	H	λ, Ft. $\times 10^6$	h, Ft.
0	760.5	1,115.6	760.5	1,480.1	3,002	19,340	0	0.1402	0
5,000	747.3	1,096.3	693.7	1,231.4	2,455	18,680	0.2622	0.1610	5,000
10,000	733.8	1,076.6	630.6	1,017.7	1,992	18,010	0.5346	0.1859	10,000
15,000	720.2	1,056.5	571.2	835.1	1,604	17,350	0.8175	0.2158	15,000
20,000	706.2	1,036.1	515.4	680.0	1,281	16,680	1.1115	0.2518	20,000
25,000	692.0	1,015.2	463.2	549.1	1,014	16,020	1.4176	0.2955	25,000
30,000	677.5	993.9	414.3	439.3	794	15,350	1.7367	0.349	30,000
35,000	662.6	972.1	368.8	348.2	615	14,690	2.0700	0.415	35,000
35,332	661.6	970.7	365.9	342.7	605	14,640	2.0915	0.420	35,332
40,000	661.6	970.7	327.3	274.2	484	14,640	2.4102	0.525	40,000
45,000	661.6	970.7	290.4	215.8	380.9	14,640	2.7517	0.667	45,000
50,000	661.6	970.7	257.7	170.0	300.0	14,640	3.0931	0.847	50,000
55,000	661.6	970.7	228.7	133.9	236.3	14,640	3.4345	1.075	55,000
60,000	661.6	970.7	203.0	105.4	186.1	14,640	3.7760	1.365	60,000

(4) Find for each h the maximum $\Delta\pi$ and the Mach Number M_C at which that occurs.

(5) Plot M_C^2 vs. H; calculate for each h the kinetic energy correction factor,

$$1 - KM_C^2 + (dM_C^2/dH)$$

(6) $V_C = M_C a$, speed for best climb.

(7) $C = a(q^*S/W)\{\Delta\pi/[1-KM_C^2 + (dM_C^2/dH)]\}$, best rate of climb.

If the effect of the climb angle on the lift must be considered, the analysis above, with the omission of Step 5 and the kinetic energy correction factor, may be used to estimate the rate of climb. Then the analysis above should be repeated with the equation in Step 3 replaced by:

$$C_L M^2 = (W/q^*S)\sqrt{1 - (C^2/V_C^2)} \qquad (10)$$

using the estimated C and V_C from the first approximate analysis and with Step 5 and the kinetic energy correction factor included.

The calculation may be carried out in terms of thrust instead of thrust horsepower, but this involves finding maximums to $\Delta\pi = M\Delta\tau$ to find the optimum conditions.

Range and High Speed

In the standard Breguet method for range at constant altitude, $(L/D)(\eta/c)$ is plotted versus log W and integrated. Normally, this method is advantageous because the integrand remains fairly constant in the integration. At high speeds, and with jet power plants in particular, this is not true, and the integration may best be carried out versus the gross weight W or its equivalent. The term η is here dropped, and c is understood to be the specific fuel consumption with respect to thrust horsepower.

If the fuel consumption is given for the engine in different terms, the equations are slightly modified and may sometimes be simplified.

$$dR = \frac{L}{D}\left(\frac{1}{c}\right)\left(\frac{dW}{W}\right) = \frac{1}{c}\left(\frac{dW}{D}\right)(\text{constant altitude})$$
$$W = C_L M^2 q^* S$$
$$D = C_D M^2 q^* S$$
$$dR = d(C_L M^2)/cC_D M^2 \qquad (11)$$

The fuel consumption of the engine as a function of r.p.m. and velocity must be known at the altitude in question. The procedure is as follows, expressed for illustration in terms of thrust rather than thrust horsepower:

Level Flight Optimum Range

(1) Plot $C_D M^2$ vs. M with parameter $C_L M^2$ (thrust required).

(2) Plot $\tau = T/q^*S$ vs. M with parameter r.p.m.

(3) Plot level flight speed V or Mach Number M vs. r.p.m. with parameter $C_L M^2$ (at maximum r.p.m., M vs. $C_L M^2$ gives $V_{max.}$ vs. W).

(4) Plot c vs. M from Step 3 with parameter $C_L M^2$.

(5) Plot $1/cC_D M^2$ vs. $C_L M^2$ with parameter M.

(6) Integrate under envelope for range between final and original values of $C_L M^2 = W/q^*S$.

The procedure for maximum endurance is the same except that in Step 5 above $1/cC_D M^3$ is plotted and in Step 6 the integral is divided by the quantity a at the altitude in question. The effect of head wind on range may be included by a factor $[1 - (M_h/M)]$ in the integrand, where $M_h = V_h/a$ and V_h is the head wind. If there are other variables in the engine characteristics besides the r.p.m., maximums to the specific range with respect to each must be found.

Dive at Constant Angle

Let θ be the angle of the dive as measured from the vertical; then equating forces perpendicular and parallel to the airplane axis gives:

$$\left.\begin{aligned} W\sin\theta &= L \\ W\cos\theta + T &= D + (W/g)(dV/dt) \end{aligned}\right\} \qquad (12)$$

But

$$dh/dt = -V\cos\theta$$

Whence

$$\left(\frac{1}{g}\right)V\left(\frac{dV}{d(-h)}\right) = 1 + \sec\theta\left(\frac{T}{W} - \frac{D}{W}\right)$$

Then

$$\left.\begin{aligned} \frac{dM^2}{d(-H)} &= 1 - KM^2 + \sec\theta\left[\frac{T}{W} - \left(\frac{q^*S}{W}\right)C_D M^2\right] \\ C_L M^2 &= (W/q^*S)\sin\theta \end{aligned}\right\} \qquad (13)$$

The second equation of Eq. (13) gives $C_L M^2$ as a function of altitude, which gives $C_D M^2$ as a function of M or M^2 with the parameter altitude. T/W is a function of h and V at a given r.p.m., or of H and M^2, and q^* is a function of H. The first equation is a first-order differential equation in M^2 and H which must be solved with the appropriate initial conditions. It should be solved by one of the standard methods for the numerical solution of differential equations.[1]

For an almost vertical dive, the equations are slightly simplified. $C_L M^2$ may be set equal to zero, making $C_D M^2$ independent of H, and sec θ may be set equal to 1.

Terminal velocities, defined by zero acceleration, are obtained by setting

$$(V/g)[dV/d(-h)] = [dM^2/d(-H)] + KM^2 = 0$$

in the differential equation, whence

$$\left.\begin{aligned} C_D M^2 &= (T/q^*S) + (W/q^*S)\cos\theta \\ C_L M^2 &= (W/q^*S)\sin\theta \end{aligned}\right\} \qquad (14)$$

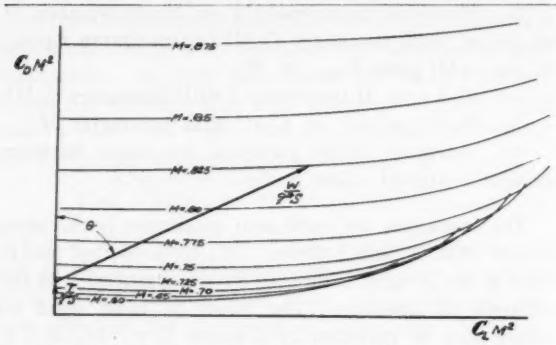

FIG. 1. Mach Number at terminal velocity for a constant angle dive.

These equations may be expressed geometrically on a plot of C_DM^2 vs. C_LM^2 with parameter M, as shown by Fig. 1. This plot may be used to find the angle for maximum terminal velocity at any altitude, since for that condition the W/q^*S vector above will be normal to the corresponding C_DM^2 curve. The Mach Numbers at terminal velocity for given altitudes and dive angles may be easily found by this graphic method.

PROPELLER CHARACTERISTICS FOR CONVENTIONAL POWER PLANTS

Propeller characteristics at low speed depend upon two parameters, generally chosen as J and C_P or, for range calculations, as J and T_c. At high speed, the parameter M enters, making the characteristics depend upon three parameters. An important parameter obtained from J and M is $(M/J) = nd/a$, which equals 1/3.1416 times the Mach Number of the circumferential tip speed. As for the airplane parameters, the additional parameter allows the formulation of dimensionless parameters whose relation with the corresponding dimensional quantities depends only upon altitude, not on velocity or r.p.m. These are:

$$\left.\begin{array}{lll} \text{Thrust} & T = C_T(M/J)^2 & \times q^*(2d^2) \\ \text{Thrust power} & TV = C_T(M/J)^2M & \times q^*a(2d^2) \\ \text{Brake power} & P = C_P(M/J)^3 & \times q^*a(2d^2) \end{array}\right\} \quad (15)$$

The dimensionless quantities above times the ratio $(2d^2m/S)$, where m is the number of propellers, give the airplane dimensionless thrust and power, τ and π, defined earlier.

The application of these quantities to rate of climb and high speed is simpler than that for range; therefore, only the latter will be here outlined, for thrust instead of power. It is assumed that the fuel consumption is known as $c(P, N)$ and that the propeller efficiency is known as $\eta[(M/J), M, C_T(M/J)^2]$. For an analysis in terms of power, the last parameter might more conveniently be $C_T(M/J)^2M$. The procedure is as follows:

(1) For various C_LM^2 and M, calculate C_DM^2.

(2) For various C_LM^2 and M, calculate $C_T(M/J)^2 = (S/2d^2m)C_DM^2$.

(3) For various C_LM^2, M, and (M/J), obtain η.

At the given altitude:

(4) For various C_LM^2, M, (M/J), calculate $P = C_DM^2q^*aS/\eta$ and $N = (60/k)(M/J)(a/d)$, where k is the gear ratio.

(5) Obtain $c = c(P, N)$ for above.

(6) Plot $(\eta/c)(1/C_DM^2)$ against C_LM^2 with M and (M/J) as parameters.

Obtain the envelopes with one parameter fixed; integrate under the envelope of these envelopes between the desired values of C_LM^2.

NOTE: The quantity $L/D = C_LM^2/C_DM^2$ may be calculated and $(\eta/c)(L/D)$ plotted against log (C_LM^2) in Step 6 above if desired.

DISCUSSION

There is no essential limitation of accuracy in the previous methods themselves. The limitations lie entirely in the accuracy of available data and of numerical calculations.

The methods represent no saving in work as compared with methods employable when compressibility effects may be neglected. For an isolated single performance problem on a given airplane with compressibility, classic methods would be about as rapid. The methods here presented will yield a large saving in calculation time in cases for which an appreciable amount of performance information is desired for a given airplane.

The curves of dimensionless power and thrust versus M used in the rate of climb and range methods have exactly the same shape as the usual curves of true power and thrust versus velocity; therefore, these dimensionless curves will not be unfamiliar to the aerodynamicist using them for the first time.

The essential feature of the methods is that by carrying out calculations of the classic type in the proper dimensionless form, attention is focused upon fundamental parametric quantities. This leads, for example, to a decrease in the number of parameters from two to one in the power-required curves for a given configuration and to the tabulation of the dimensional part of a dimensional quantity as a function of altitude alone.

REFERENCE

[1] *See*, for example, Ford, *Differential Equations*, Chapter VII. McGraw-Hill Book Company, Inc., New York, 1933.

A Vibration Theory Combining the Dynamic Stiffness and Mobility Methods

HUGH B. STEWART*

General Motors Corporation

ABSTRACT

Two new methods for calculating vibration problems—the dynamic stiffness method and the mobility method—have been introduced in recent years. Each of these methods offers certain advantages over the older vibration theory. This article is an attempt to unify these two methods so that the best features of each are included in one theory. By means of this theory it is possible to determine the resonance and antiresonance frequencies and the relative amplitudes of vibration of a mechanical system. The effect of the position of torque application on the vibration characteristics of a system are discussed. The application of the theory is demonstrated by a few examples including the problem of the pendulum damper.

INTRODUCTION

With the advent of higher power aircraft and automobile engines, the study of vibrations has become, and will continue to be, increasingly important. Undesirable torsional vibration in the crankshaft system and linear vibration of the engine can lead to excessive wear or failure of engine parts. Often it is necessary to adjust certain inertias or rigidities in the engine system in order to remove harmful resonances from the speed range of the engine.

The solution of the differential equations encountered in the analysis of complex mechanical systems is not only difficult but also obscure in its physical interpretation. The introduction of two new methods for solving vibration problems, known as the mobility method[1] and the dynamic modulus or dynamic stiffness[2, 3] method, has contributed much toward the simplification of vibration theory. Although these theories have, in general, been developed independently of each other, certain advantages of each method can be incorporated in a unified theory as will be demonstrated.

THE MOBILITY METHOD

The mobility method possesses the advantage of clarity of mechanical circuit representation, particularly for complex mechanical circuits. The importance of the position of the torque input, a fact that is often overlooked in vibration theory, is also quite apparent in the mobility theory. The theory has the disadvantage that it is based on electrical alternating current theory, which is not familiar to most mechanical engineers. The mobility theory provides a convenient method of including friction forces in the calculation when these forces are proportional to velocity. However, friction forces in mechanical systems are usually difficult to evaluate and are often not proportional to velocity, thus they are usually omitted in vibration problems. This omission does not seriously limit the theory, however, since it is the resonance frequencies and relative amplitudes that are most important and these factors are not critically affected by friction in most practical cases.

DYNAMIC STIFFNESS METHOD

The dynamic stiffness method has the advantage that it expresses the relation between force and displacement rather than force and velocity as in the mobility theory. Effective stiffness seems to be a more important concept in mechanical vibrations than mobility. The biggest disadvantage to the dynamic stiffness method is the confusion that arises in representing a mechanical circuit analytically.

By adopting the best features of each of these theories it is possible to develop a vibration theory that is easily applied and provides a clear picture of the analytic procedure. Anyone familiar with electrical theory will recognize the similarity between the mechanical circuits and certain electrical circuits; however, the circuit representation of mechanical systems is a concept that can easily be learned independently of electrical theory.

COMBINATION METHOD

The theory will be developed for torsional vibration systems although it applies equally well to linear vibration systems. Consider an inertialess shaft with torsional rigidity, K, one end of which is clamped. Suppose a torque $T = T_0 \sin \omega t$ is applied to the other end. The angular displacement, θ, of the free end of the shaft obeys the relation

$$T = K\theta \tag{1}$$

which requires that $\theta = \theta_0 \sin \omega t$.

Suppose an inertia has a torque $T = T_0 \sin \omega t$ applied to it. Assuming that the angular displacement, θ, of the inertia is sinusoidal with the same frequency as the torque—i.e., $\theta = \theta_0 \sin \omega t$—then

Received January 5, 1945.

* Research Engineer, Allison Division.

$$T = I(d^2\theta/dt^2) = -I\omega^2\theta \tag{2}$$

The negative sign indicates that T is out of phase with θ. The quantity

$$S = -I\omega^2 \tag{3}$$

is defined as the effective rigidity or dynamic stiffness of the inertia since

$$T/\theta = S = -I\omega^2$$

From Eq. (1) it is seen that the dynamic stiffness of a shaft is

$$S = K \tag{4}$$

or is equal to the static rigidity.

Now consider a shaft clamped at one end and having an inertia at the other end, and suppose a torque $T = T_0 \sin \omega t$ is applied to the inertia. The differential equation for the system is

$$I(d^2\theta/dt^2) + K\theta = T_0 \sin \omega t \tag{5}$$

and the steady state solution is

$$\theta = \theta_0 \sin \omega t \tag{6}$$

Substituting Eq. (6) in Eq. (5):

$$-I\omega^2\theta_0 \sin \omega t + K\theta_0 \sin \omega t = T_0 \sin \omega t$$

or

$$(-I\omega^2 + K)\theta = T \tag{7}$$

This solution is for the steady state vibration only, but in practical problems all transient effects die out in a small time; hence, this is usually the important part of the solution. Now

$$T/\theta = (-I\omega^2 + K) = S \tag{8}$$

is defined as the dynamic stiffness of the combination of shaft and inertia when the torque is applied to the inertia. When $K > I\omega^2$, T is in phase with θ and S is positive; when $I\omega^2 > K$, T is out of phase with θ and S is negative. Hence, a negative dynamic stiffness for such a system will mean that the inertia component of S is greater than the rigidity component.

When $K = I\omega^2$ in the above problem, then $T/\theta = 0$ or $S = 0$. This means that a finite T produces an infinite θ, which is the condition for resonance. In general, any mechanical system will be said to be in resonance when its dynamic stiffness is zero.

The dynamic flexibility of a system is defined as

$$F = 1/S = \theta/T \tag{9}$$

For example $F = 1/K$ and $F = -1/I\omega^2$ are the dynamic flexibilities of a shaft and inertia, respectively. Whenever the dynamic flexibility, F, of a mechanical system is zero, an infinite torque is necessary to produce a finite displacement. This is known as a condition of antiresonance.

Concepts of the Mobility Theory

It is convenient to introduce at this point some concepts of the mobility theory. This theory is based on the fact that displacement is a relative measurement, while torque is an absolute quantity. Consider, for example, a torque applied to the free end of a clamped shaft. The angular displacement of the shaft is the displacement of the free end relative to the fixed end. The displacement relative to the fixed end of the shaft will be different at consecutive points along the shaft. However, if the shaft is cut at any place, the same torque must be applied at this position to maintain the previous displacement of this point. For this reason the expressions torque *through* the shaft and displacement *across* the shaft are used. In the case of inertia elements the displacement is always measured relative to ground, or across the inertia itself to ground. To conform with the case of the shaft the torque is said to be measured through the inertia to ground.

From considerations of the mobility theory a set of rules is adopted which simplifies the solution of vibration problems.

Rule 1. Elements have two terminals. In the case of an inertia, one terminal is the inertia itself and the other terminal is ground, since the displacement of an inertia is always measured relative to ground. (This is also usually true for torque.)

Rule 2. Elements will be connected in parallel when their terminals are connected to common points.

Rule 3. Elements will be connected in series when their terminals are connected end to end with no more than two terminals to any junction point.

The following rules will be illustrated by means of two simple examples. By similar reasoning it will be seen that the rules will hold in general for any mechanical system.

Example 1

A circuit diagram of the mechanical system such as the one illustrated should always be drawn before analyzing the problem.

If the torque is applied to the inertia in the example, Fig. 1, the system is a parallel circuit—i.e., one end of the rigidity element is common with the inertia itself, while the other terminal of both the rigidity element and the inertia element is ground. It is seen that the displacement across each element is the same since they

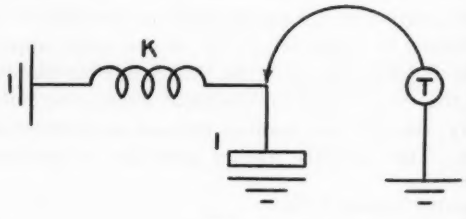

Fig. 1.

have common terminals. Furthermore, part of the torque is used to wind up the shaft and part to accelerate the inertia, thus

$$\theta_K = \theta_I = \theta$$

$$T = T_K + T_I$$

where θ is the displacement across the torque generator to ground and T is the torque through the generator to the system. Thus:

Rule 4. In parallel circuits the torques through the elements add, and the displacements across the elements are equal.

Then

$$T = S\theta = K\theta_K - I\omega^2\theta_I = (K - I\omega^2)\theta$$

or

$$S = (K - I\omega^2) \tag{10}$$

and when

$$T/\theta = S = 0$$

a displacement resonance exists.

This analysis yields the more useful rule:

Rule 4(a). In parallel circuits the dynamic stiffnesses of the separate elements add.

Example 2

Consider now the case of the simple series circuit, illustrated in Fig. 2, where the torque is applied between ground and the end of the shaft opposite the inertia.

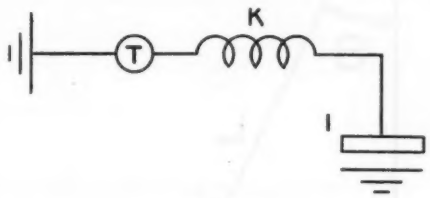

Fig. 2.

In order to have dynamic equilibrium, the torque through each of the elements must be the same. Also the angular displacements along the system must add. Thus

$$T_K = T_I = T$$

and

$$\theta = \theta_K + \theta_I$$

Rule 5. In series circuits the torques through the different elements must be equal and the displacements across the elements add.

Then

$$\theta = FT = \left(\frac{1}{K}\right) T_K - \left(\frac{1}{I\omega^2}\right) T_I = \left(\frac{1}{K} - \frac{1}{I\omega^2}\right) T$$

or

$$F = 1/S = (1/K) - (1/I\omega^2) \tag{11}$$

and when

$$\theta/T = F = 0$$

a displacement antiresonance exists. This is the principle of the tuned vibration absorber. Hence:

Rule 5 (a). In series circuits the dynamic flexibilities of the separate elements add.

By the use of Rules 4(a) and 5(a) the resonance and antiresonance frequencies of any mechanical systems can be determined without referring to the torque or the displacement—i.e., by considering only the rigidities and inertias of the system. The following example will illustrate the method of solution.

Example 3

Referring to Fig. 3, the elements K and I_2 are in series and this branch is in parallel with I_1. A useful rule for solving vibration problems by the outlined method is

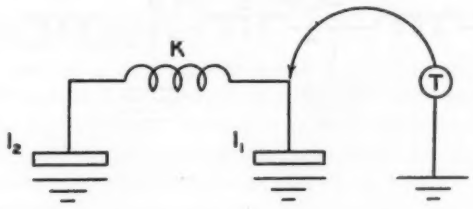

Fig. 3.

to begin with the elements that are the most remote to the point of torque application and work back to the torque. Thus, to determine the dynamic stiffness of the branch containing K and I_2:

$$F_2 = \frac{1}{S_2} = \frac{1}{K} - \frac{1}{I_2\omega^2} = \frac{I_2\omega^2 - K}{KI_2\omega^2}$$

and

$$S_2 = KI_2\omega^2/(I_2\omega^2 - K)$$

For the parallel circuit:

$$\begin{aligned} S &= S_2 - I_1\omega^2 \\ &= [KI_2\omega^2/(I_2\omega^2 - K)] - I_1\omega^2 \\ &= \frac{-\omega^2(I_1I_2\omega^2 - KI_1 - KI_2)}{I_2\omega^2 - K} \end{aligned}$$

Resonance occurs when $S = 0$—i.e., when

$$\omega^2 = K(I_1 + I_2)/I_1I_2$$

Antiresonance exists when $F = 0$ or $\omega^2 = K/I_2$. This system has one resonance and one antiresonance frequency.

By applying the torque to I_2 and solving, it can be found that the resonance frequency remains the same,

while the condition for antiresonance changes to $\omega^2 = K/I_1$. In general the resonance frequencies of a mechanical system are independent of the position of torque application, while the antiresonance frequencies change for different torque positions. This can be seen to be true for any system by means of the following reasoning:

Consider the case where the torque is applied at point A of the system shown in Fig. 4. The dynamic stiffness to the right of B is S_B, and the dynamic stiffness S_{-A} to the right of A is given by

$$1/S_{-A} = (1/S + 1/S_B)$$

or

$$S_{-A} = SS_B/(S + S_B)$$

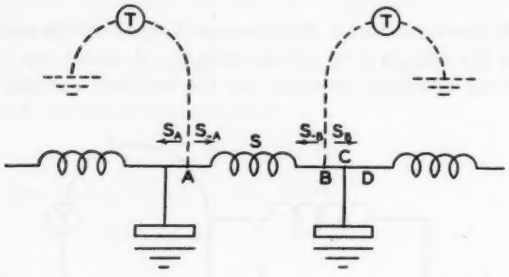

FIG. 4.

The total dynamic stiffness for this case is

$$(S)_A = S_A + S_{-A} = \frac{S_AS + S_AS_B + SS_B}{S + S_B} \quad (12)$$

Now suppose the torque is applied to the point B. If the dynamic stiffness to the left of A is S_A, then the dynamic stiffness S_{-B} to the left of B is

$$S_{-B} = SS_A/(S + S_A)$$

and the total dynamic stiffness for this case is

$$(S)_B = S_B + S_{-B} = \frac{S_BS + S_BS_A + SS_A}{S + S_A} \quad (13)$$

It is seen that the numerators of Eqs. (12) and (13) are the same; hence, if $(S)_A = 0$, it follows that $(S)_B = 0$. This means that if resonance occurs when the torque is applied at point A, resonance must also occur when the torque is applied at point B. Since the points B, C and D are actually identical points in the mechanical system, it is obvious that the resonance condition is not altered by moving the torque from B to D in the circuit. This can be shown analytically by summing the dynamic stiffnesses of the separate branches when the torque is applied to each of the three points and showing that the total dynamic stiffness is the same in each case. By continued application of the theorem it is apparent that the resonance is independent of the position of torque application.

If $(S)_A = \infty$ or $S = -S_B$ in Eq. (12), then a state of antiresonance is said to exist when the torque is applied at the point A. In general, this is not the condition for antiresonance at the point B, since $(S)_B = \infty$ requires that $S = -S_A$.

Theory of Pendulum Dampers

The application of the dynamic stiffness method to the pendulum damper provides a convenient solution to this problem. The theory will first be applied to a gravity pendulum to illustrate the principle, and later it will be extended to the centrifugally tuned pendulum damper.

The case of linear motion will be considered in the solution of the gravity pendulum damper. Referring to Fig. 5, let L be the length of the pendulum, m the mass of the bob, and x the horizontal displacement of the bob from the equilibrium position. The restoring force of the bob is

$$f_r = -mg \sin \theta = -mg(x/L) \quad (14)$$

and the acceleration is approximately

$$d^2x/dt^2 = L(d^2\theta/dt^2) \quad (15)$$

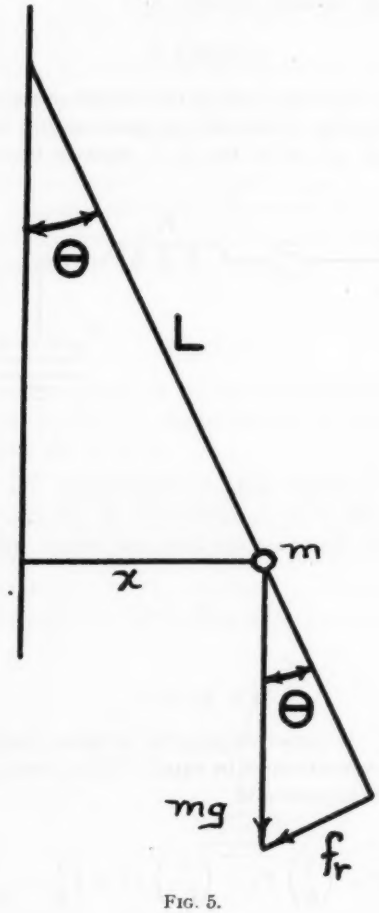

FIG. 5.

for small angles of swing. Applying Newton's second law

$$f = m(d^2x/dt^2)$$

or

$$m(d^2x/dt^2) + (mg/L)x = 0 \qquad (16)$$

This equation has the solution

$$x = x_0 \sin pt$$

if

$$p^2 = g/L \qquad (17)$$

Suppose an external force of magnitude

$$f = f_0 \sin \omega t$$

is applied to the pendulum bob in the x-direction. Then Eq. (16) becomes

$$m(d^2x/dt^2) + (mg/L)x = f_0 \sin \omega t \qquad (18)$$

The dynamic stiffness theory can be applied to the simple pendulum if the approximations previously mentioned are made. The dynamic stiffness of the mass element for linear motion is

$$S = -m\omega^2$$

and that of the rigidity is

$$S = K = mg/L$$

Fig. 6 shows the circuit diagram of the pendulum when the external force is applied to the pendulum bob. Since the elements are in parallel, their dynamic stiffnesses add and the dynamic stiffness of the combination is

$$S = -m\omega^2 + (mg/L) \qquad (19)$$

and when $S = 0$,

$$\omega^2 = g/L$$

which is the condition for resonance.

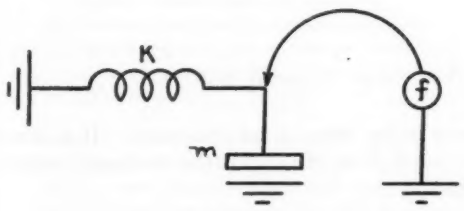

FIG. 6.

If the force is applied to the end of the pendulum opposite the mass, the elements are in series as is shown in Fig. 7. The dynamic flexibilities of the elements add; hence,

$$F = 1/S = (L/mg) - (1/m\omega^2) = (L\omega^2 - g)/mg\omega^2 \qquad (20)$$

and when $F = 0$—i.e.,

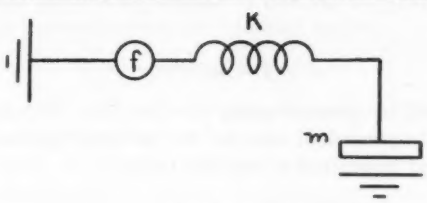

FIG. 7.

$$\omega^2 = g/L$$

a condition of antiresonance exists—i.e., a finite force produces zero displacement. This is the principle of the pendulum damper.

The centrifugally tuned pendulum damper is similar in principle to the gravity pendulum except that the restoring force on the bob is the result of centripetal acceleration. The procedure used for this derivation is to calculate the reaction of the pendulum on the hub which is consequently used to evaluate the restoring torque of the pendulum. By knowing the restoring torque and inertia of the pendulum bob, it is possible to express the characteristics of the damper by the dynamic stiffness method.

Consider a pendulum of length L attached to a disc with inertia I_1 as shown in Fig. 8. It will be assumed that the pendulum bob has a point mass m—i.e., the bob itself has no appreciable inertia about its center of gravity. Neglecting the Coriolis force, which is small for small bob angles, the force acting on the bob will be that due to centripetal acceleration. If Ω is the angu-

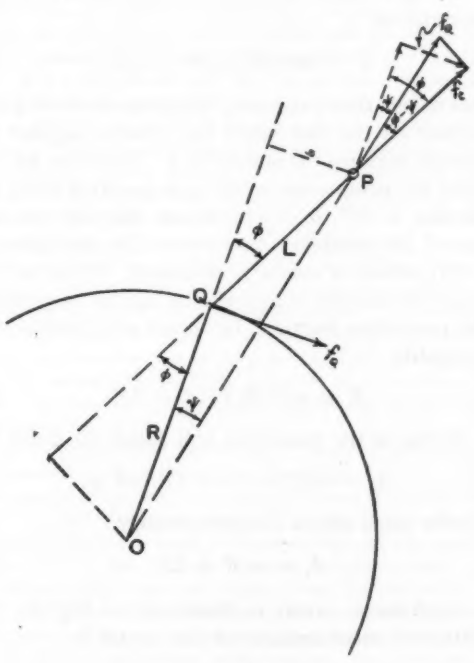

FIG. 8.

lar velocity of the hub in radians per second, this force is

$$f = mOP\Omega^2$$

and will be directed along the line PO. The tension, f_t, in the pendulum arm due to the centrifugal reaction is found from similar triangles to be

$$mOP\Omega^2/OP = f_t/(R\cos\phi + L)$$

or

$$f_t = m\Omega^2(R\cos\phi + L)$$

The reaction of the tension on the disc will produce a force perpendicular to OQ of amount

$$f_Q = f_t \sin\phi = m\Omega^2(R\cos\phi + L)\sin\phi$$

The torque on the disc is

$$T = Rf_Q = m\Omega^2R(R\cos\phi + L)\sin\phi \qquad (21)$$

The problem could be solved in terms of the angular displacement ϕ; however, the solution is more useful in terms of the angle ψ at the center of the disc. From the diagram it is seen that

$$L\sin\phi = s = (R + L\cos\phi)\tan\psi$$

or

$$\sin\phi = [(R + L\cos\phi)/L]\tan\psi \qquad (22)$$

Substituting Eq. (22) in Eq. (21), the torque on the disc due to the pendulum is

$$T = m\Omega^2(R/L)(R\cos\phi + L)(R + L\cos\phi)\tan\psi$$

and for small angles of swing this becomes, to a good approximation,

$$T = m\Omega^2(R/L)(R + L)^2\psi \qquad (23)$$

This means that a restoring torque given by Eq. (23) is exerted on the disc when the relative angular displacement between OQ and OP is ψ. Likewise, by considering the component of the bob restoring force perpendicular to OP, it can be shown that the restoring torque of the pendulum bob about O is also given by Eq. (23), which of course is necessary. Thus the system can be thought of as a disc of inertia I_1 connected to the pendulum inertia I_2 by means of a flexible shaft with rigidity

$$K = m\Omega^2(R/L)(R + L)^2 \qquad (24)$$

The inertia of the pendulum bob about the point O is

$$I_2 = m(R + L\cos\phi)^2/\cos^2\psi$$

which for small angles is approximately

$$I_2 = m(R + L)^2 \qquad (25)$$

The mechanical circuit is illustrated in Fig. 9. The condition of antiresonance for this circuit is

$$\omega^2 = K/I_2 = m\Omega^2R(R + L)^2/mL(R + L)^2 = \Omega^2(R/L)$$

or

$$\omega^2/\Omega^2 = n^2 = R/L \qquad (26)$$

where n is the order of vibration to be removed. Thus if the damper is tuned to antiresonance for a particular order of vibration, it w ll remain tuned to this condition for any engine speed.

It will be observed that this system will have a resonance somewhat above the antiresonance frequency. The resonance frequency can be determined by equating the dynamic stiffness of the system to zero. Thus the addition of the centrifugally tuned pendulum damper to a single inertia produces a system that has an antiresonance frequency and a resonance frequency. It can be seen that, if the pendulum damper is added to one of the inertias in a system consisting of two inertias connected by a flexible shaft, the new system will have two antiresonance frequencies and two resonance frequencies. In general, the addition of the pendulum damper to a mechanical system increases by one the number of resonance and antiresonance frequencies in the system. When the pendulum damper is used to remove torsional vibrations from a system, care should be taken to avoid any new resonances that might be introduced in the critical range of the system.

The dynamic stiffness of the single inertia (damper hub) and the pendulum damper for any exciting frequency is

$$S = -I_1\omega^2 + S_2$$

where S_2 is the dynamic stiffness of the series branch, and

$$S = -I_1\omega^2 + [KI_2\omega^2/(I_2\omega^2 - K)]$$

or rewriting,

$$S = -I_1\omega^2 + \{K\omega^2/[\omega^2 - (K/I_2)]\}$$

Substituting for K and I_2 from Eqs. (24) and (25):

$$S = -I_1\omega^2 + m\Omega^2\left(\frac{R}{L}\right)(R + L)^2\left[\frac{\omega^2}{\omega^2 - \Omega^2(R/L)}\right]$$

or

$$S = -I_1\omega^2 + m\omega^2(R + L)^2\left[\frac{1}{n^2(L/R) - 1}\right] \qquad (27)$$

where n is the order of the excitation. It is seen that if $n^2 = R/L$ in Eq. (27) the dynamic stiffness is infinite.

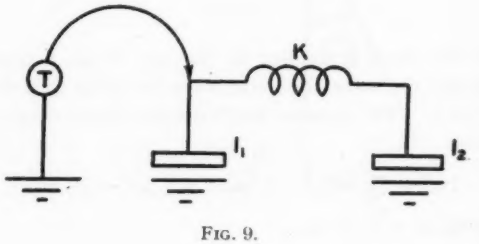

FIG. 9.

The effectiveness of the pendulum damper is usually expressed in terms of effective inertia instead of dynamic stiffness. The relation between dynamic stiffness and effective inertia is

$$S = -I_{\text{eff.}}\omega^2$$

or

$$I_{\text{eff.}} = -S/\omega^2$$

and therefore

$$I_{\text{eff.}} = I_1 + m(R + L)^2\left[\frac{1}{1 - n^2(L/R)}\right] \quad (28)$$

In order to find the amplitude of bob swing in the pendulum damper at antiresonance, the displacement across I_2 is calculated. Since the displacement across I_1 is zero, all of the torque must pass through K and I_2, and, since K and I_2 are in series, all of the torque that passes through K must also pass through I_2. Thus to determine the displacement across I_2, the torque through I_2 is divided by the dynamic stiffness of I_2—i.e.,

$$\psi = T/S_{I_2} = T/-m(R + L)^2\omega^2$$

or expressing the amplitude in terms of ϕ using Eq. (22), with the approximation due to small angles,

$$\phi = -T/mL(R + L)\omega^2$$

The derivation here is for the relatively simple case of one inertia plus the pendulum. However, by using the methods of dynamic stiffness it is possible to solve more complicated systems involving the pendulum damper. Not only can the resonance and antiresonance frequencies be calculated, but also the pendulum swing can be calculated when the magnitude and the position of the applied torque are known.

References

[1] Firestone, F. A., *The Mobility Method of Computing the Vibration of Linear Mechanical and Acoustical Systems: Mechanical-Electrical Analogies*, Journal of Applied Physics, Vol. 9, No. 6, pp. 373–387, June, 1938.

[2] Biot, M. A., *Coupled Oscillations of Aircraft Engine-Propeller Systems*, Journal of the Aeronautical Sciences, Vol. 7, No. 9, pp. 376–382, July, 1940.

[3] Manley, R. G., *Dynamic Stiffness and Effective Inertia Methods in Modern Torsional Vibration Theory*, Journal of The Royal Aeronautical Society, Vol. 47, pp. 5–21, January, 1943.

Letter to the Editor

Dear Sir:

The paper by M. Yachter, "A Note on Bending Beyond the Proportional Limit" (JOURNAL OF THE AERONAUTICAL SCIENCES, Vol. 12, No. 1, p. 21, January, 1945), calls for the following observations:

(1) Independently of the stress-strain properties of a material, simple considerations of symmetry prove the well-known fact that, in pure bending, strains are proportional to the distance to the neutral axis. This can be shown:

(a) from elementary considerations of geometry

(b) from the fundamental conditions of compatibility.

These relations reduce to one for plane stress problems:

$$\frac{\partial^2\epsilon_x}{\partial y^2} + \frac{\partial^2\epsilon_y}{\partial x^2} = \frac{\partial^2\gamma_{xy}}{\partial x\,\partial y}$$

(see Timoshenko, S., *Theory of Elasticity*, Eq. 21, p. 22).

The span of a beam submitted to a pure bending couple being directed along the x axis, it can be established that, far from the ends, the stress distribution σ_x remains the same in all sections ($\sigma_x = \sigma(y)$) which shows that $\sigma_y = \tau_{xy} = 0$ (assumption implicitly made by the author); then:

$$\epsilon_x = \epsilon_x(y); \quad \epsilon_y = \epsilon_y(y); \quad \gamma_{xy} = 0$$

and the above equation becomes:

$$\partial^2\epsilon_x/\partial y^2 = 0$$

Thus, ϵ_x is a linear function of y, which proves that the linear strain distribution is the correct distribution. This fact has been verified by numerous tests and is the basis of the theory of plastic bending which can be found in *Plasticity* by A. Nadai (Chap. 22, pp. 160–163). It is rather disconcerting to see that Mr. Yachter discards these theories and results without a word of explanation as to the reasons that led him to the research of a new theory.

(2) It is a well-known fact that the minimum strain energy theorem cannot be used in the case of nonproportional deformations, so that all the theory developed from this basis is entirely erroneous; this explains why nonlinear deformations are found.

This fact can be substantiated by simple application of results developed by S. Timoshenko in his *Theory of Elasticity*, paragraph 42, "Principle of Least Work."

The argument can be reduced to the following: from the definition of strain energy (integral of force × differential displacement), the derivative of the strain energy in respect to the displacement is equal to the corresponding force. The derivative of the strain energy in respect to the force is equal to the corresponding displacement only in the case when forces and displacements are proportional, and the principle of least work, Castigliano's theorem, and other similar relations can be established in this special case only.

It has been previously shown by F. Engesser (Architekten- und Ingenieur-Vereins, Hanover, *Zeitschrift*, Vol. 35, 1889), and subsequently by H. M. Westergaard (*Transactions*, American Society of Civil Engineers, Vol. 107, p. 765, 1942) that the principle of least work must be replaced, beyond the range of Hooke's law, by the principle of least complementary work. When stresses and strains are proportional, the two works are equal. This conclusively proves the incorrectness of Mr. Yachter's developments, since he mistakenly used strain energy instead of the complementary strain energy. An excellent example of incorrect application of the minimum strain energy

theorem is given by S. Timoshenko (*Strength of Materials*, Vol. 1, 2nd Ed., p. 339), who shows an error of 67 per cent in a special case. Still greater errors may occur in other types of structures.

It is interesting to find the physical significance of the incorrect and unduly complicated developments of the author. The latter has not realized that his quantity $\bar{S}$ has a simple significance and that the introduction of the modified strain curve is superfluous. Simple substitutions in the expression of $\bar{S}$ lead to the relation $\bar{S} = E_0 S/E_t$, in which E_t is the tangent modulus of the actual stress strain curve. This shows that the author's linear relation for $\bar{S}$ reduces to:

$$SE_0/E_t = Ky \tag{E}$$

In this form, it appears that the relation is valid for heterogeneous solids (reinforced concrete, etc.) that have *several constant moduli*, so that reduced stresses are used to define equivalent strains (E_t/E_0 would be the constant n for steel/concrete). The above relation can be established in a straightforward manner, instead of using the author's lengthy analysis. With the notation

$$M(y) = \int_a^y Sy\, da$$

the total applied moment M is equal to $M(b)$, a and b representing the extreme fibers.

The condition of minimum strain energy is, according to the author:

$$\delta \int_a^b \psi dA = 0 \tag{1}$$

with

$$\psi = \int_0^s Sd\epsilon \quad \text{or} \quad d\psi/d\epsilon = S$$

This condition, by application of the rules of calculus of variation, can be replaced by [A is the variable; $M(y)$ is the unknown function that fulfills condition (1) and $M(b) = M$]:

$$\partial\psi/\partial M' = \text{constant} = c \tag{2}$$

with:

$$M' = \partial M/\partial A = Sy$$

Condition (2) can be written (noting that S is not yet a function of y):

$$c = \frac{\partial\psi}{\partial S} \Big/ \frac{\partial(Sy)}{\partial S} = \left(\frac{d\psi}{d\epsilon}\right)\left(\frac{d\epsilon}{dS}\right)\left(\frac{1}{y}\right) = \left(\frac{S}{y}\right)\left(\frac{d\epsilon}{dS}\right)$$

Replacing c by K/E_0, in which K is an arbitrary constant, the previous equation becomes equivalent to relation (E). As indicated, however, both relations are meaningless in the case examined by the author since they are derived from incorrect assumptions.

As a conclusion, it can be stated that Mr. Yachter has tried to replace reliable and well-established formulas by an expression derived from an incorrect application of the minimum strain energy theorem, leading to incorrect and unconservative values, as proved by his numerical examples.

LEON BESKIN
Consolidated Vultee Aircraft Corporation

Library Facilities of the
Institute of the Aeronautical Sciences

To serve Institute members and others in the aeronautical industry, the Institute of the Aeronautical Sciences offers the facilities of:

The W. A. M. Burden Library
1505 RCA Building West
30 Rockefeller Plaza
New York 20, N. Y.

The facilities of this library are available for reference study at the offices of the Institute.

The Paul Kollsman Library
1505 RCA Building West
30 Rockefeller Plaza
New York 20, N. Y.

This library loans books without charge to members and others in the United States over eighteen years of age. Full information will be sent on request.

The Pacific Aeronautical Library
6715 Hollywood Boulevard
Hollywood, Calif.

This is a service and reference library for West Coast organizations. Full information as to its facilities will be sent on request.

Curved Aluminum-Alloy Sheets in Compression for Monocoque Constructions

GEORGES WELTER*

École Polytechnique de Montreal

Introduction

This study† is intended to throw some light on the mechanical behavior of thin light-alloy sheets under compression and to give some explanation about the minimum load that thin-walled structures can support under axial thrust. For the development of modern aircraft, it is important to possess a correct picture of the behavior and the failing process of stressed-skin constructions. It is well known to the designer of aircraft structures that the efficiency of compression members centers around the problem of making curved plates that can support a maximum load under compression.

The general idea of this investigation was to explore the field of rather unusual and delicate compression tests of panels up to the buckling load. Simple and timesaving tests were planned, and it was hoped to connect the results found during this investigation with the experimental and theoretic work of other authors (Cox, von Kármán, Redshaw) and to find a common basis for the interpretation of the results.

The execution of buckling tests in their present state may be compared with tensile tests of a century ago. To make a single tensile test was at that time rather a tedious and lengthy task. It was, in effect, an investigation rather than a test, because the numerous factors that have an influence on the test results were not yet known. For buckling tests, the situation is at present similar to that of the early tensile tests.

A proved and reliable testing technique is not yet known. Stiffened and curved panels have received, in relation to their importance in aircraft, comparatively little attention. Also, carefully controlled test results on curved thin plates under axial thrust are scarce and the uncertainty about theoretic behavior is great. Furthermore, the best devices for gripping the specimen for buckling tests have not yet been evolved. The loading conditions, clamping of the free edges of the sheets, as well as numerous other factors and their influence on the buckling and ultimate loads of the light-alloy sheets, have not been sufficiently investigated. Also, the influence of the properties of the sheet material itself on the maximum buckling values is insufficiently known.

Under these conditions it may be desirable to throw some light on this unexplored field. This cannot be done efficiently and in a short time by investigating only single points using slow and tedious methods. It seemed useful to direct the investigation in a practical manner toward a large number of specimens, using a carefully designed equipment giving a high accuracy of the test results. In view of the large number of tests, the equipment must permit a rapid setting up of the specimens, and the method of measurement should be as simple as possible. The equipment used in the laboratory of the École Polytechnique, which is considered to meet these requirements, has been especially developed for this purpose—that is, for an investigation of panels that have to be treated in a large number and in a minimum of time. It can be said that satisfactory results have been attained with the apparatus designed for this investigation. The equipment permits the making of complete buckling tests, including the determination of the ultimate load, with stress-strain records as well as an observation of the deflection of the loading tables at a load of 1,000 lbs: in a minimum time of less than a quarter of an hour, depending on the maximum load and the time required for the adjustment of the plates between the loading faces of the machine. With the present test equipment and a well-trained crew, about 100 panels a day can easily be tested in two shifts.

Description of Apparatus and Testing Technique

Testing Machine

The tests were conducted on a 60,000-lb. capacity Baldwin-Southwark Tate Emery Universal Testing machine, with a guaranteed accuracy of less than $^1/_2$ per cent of the load. The range used for most of these tests with the light metal alloy was of 2,400-lb. capacity with 2-lb. dial division. The accuracy of the machine was verified before the beginning of the main test series, and the degree of the stiffness of this type of testing machine was recorded.

Recorder and Compressometer

A load-strain recorder for recording the displacement of the loading faces of the machine was developed in

Received September 18, 1944.

* Professor.

† This investigation was executed in the Research Laboratory of the École Polytechnique, Montreal. The author appreciates the assistance of J. Hurtubise, R. Frigon, and other members of the staff of the Research Laboratory in the execution of this work.

order to obtain accurate load-deformation diagrams for the buckling of plates under axial thrust.

The translational movement of the crosshead (*a*, Fig. 1) of the machine is communicated through a flexible thin steel strip *b* to a segment *c* and is reduced by the segment *d* in the relation of one to five. The horizontal cylindric bolt *e*, with a spiral spring and a silvered top, is contacting a microscrew *f*, coupled by means of the axis *g*, to the Selsyn motor *n*, communicating the vertical movement of the crosshead to the recorder. A lever *i*, which frees the contact between the horizontal cylinder and the micrometric screw *f*, protects this screw from accidental damage when the device is not in use. By changing the ratio of the segments of the compressometer from one to five into five to one, for instance, a high magnification of the displacement of the crossheads of the machine was possible. Besides this, another method of recording load-strain diagrams has been used; the Templin extensometer has been adjusted, with some slight modifications, between the crossheads right in the axis of the machine. Some characteristic load-deflection diagrams on buckling tests, as recorded with thin aluminum-alloy sheets, are represented in Fig. 12. (About 400 diagrams of this kind have been made for the investigation of this problem.)

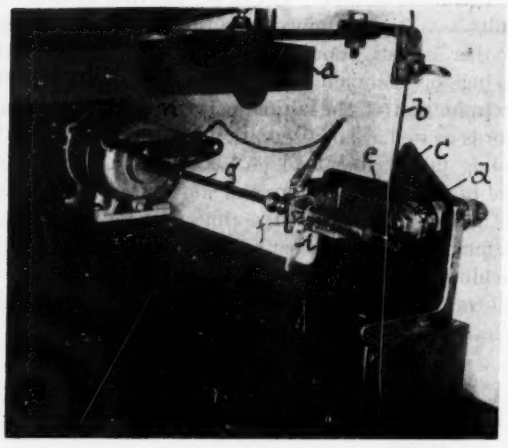

FIG. 1.

Curved Clamping Bars

A few preliminary compression tests with curved plates about 18 in. long showed that, in spite of an accurate preparation and fixation of these test specimens in casting boxes by means of Woods metal (Fig. 2), the results were not uniform. Inexplicable variations of about 20 to 25 per cent of the compression load were measured. After a more accurate measurement of the solidification temperature of the low fusible alloy (Woods metal), of the pouring temperature of the liquid metal, and of the temperature of the plates and casting boxes (conditions that are rather difficult to control), it was found that by this technique it is hardly possible to prevent the sheets from changing their original shape because of the thermal effect of the Woods metal. It was therefore decided to fix the plates mechanically between curved solid steel grips.

FIG. 2.

The solid steel grips, which fitted the curved plates on both ends by five screws, thus introducing the compression load regularly and equally into the sheets, are represented in Fig. 3. The radius of curvature used in the tests described was 24 in. After several tentative tests showing more equal buckling results than those obtained with panels fastened in boxes with Woods

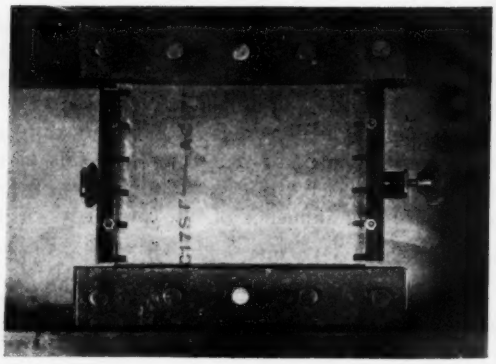

FIG. 3.

metal, these steel grips were later adopted for the testing technique of this investigation. The method of fixing the plates mechanically on the loading tables of the machine has many advantages; for instance: no release of stresses and no deflection of the plates due to the pouring temperature of the low-melting alloy, and no uncertainty in introducing the loads at the ends of the plates, as well as an incomparably rapid setting up of the plates.

The curved sheets were clamped mechanically in the divided-steel grips of the same radius of curvature as the panels. In order to assure identical loading conditions for all panels, one-half of the divided grips were fixed to the upper and lower compression tables of the testing machine. The center of gravity of the curved plates was located, as exactly as possible, right at the geometric center of the machine. By loosening the bolts of the grips and by removing the sheet specimen after the tests and adjusting another sheet in its place, there was no possibility of an error in eccentric loading of the panels, provided the grips were fixed right in the loading center of the machine. It was thought that in this way the parallelism of the loading faces of the tables, which is normally hard to obtain in practice, would be without marked influence on the loading conditions of the panels and that comparable test results could be obtained.

At the beginning of these tests, the panels were fixed by five bolts that clamped the sheets in the grips by friction. However, to prevent even a small amount of slipping which could eventually take place at higher loads (it was difficult to determine whether sliding in the grips or microplastic deformation occurred in the stringers), the panels were, in the second part of this investigation, adjusted in such a manner between the loading faces of the machine that they touched, through the grips, both the lower and upper loading tables of the machine. For each plate a certain adjustment was necessary, so that the sheet touched equally both end plates on its whole width. By these means, a prevention of any sliding of the sheets between the grips was secured.

Stringers

As the buckling is without doubt influenced by the stiffness of the longitudinal edges of the plates, different models of stringers were developed. Small flat stringers, as well as larger plain angle stringers, and stringers with a free space representing rivet pitch, as well as larger and stiffer ones, were tried. Also, a series of stringers of variable length (between 1 and 16 in. for the investigation of plates of different lengths) were designed and tried (see Fig. 4). The stringers were fastened on the edges of the plates to prevent any lateral movement.

According to preliminary results, these rather simplified stringers seemed to have a fairly big influence on the resistance of the panels. To prevent any influence of this kind on the test results, a completely different shape—that is, a far stiffer stringer—was chosen as shown in Fig. 5. The teeth of these stringers have been machined in rigid flat rods that are clamped together with screws; a shim sandwiched between keeps the flats separated at exactly the distance equal to the thickness of the sheet to be tested.

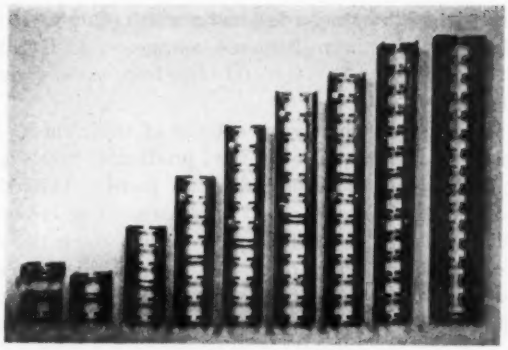

FIG. 4.

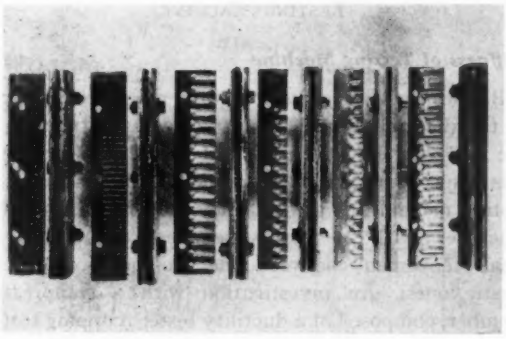

FIG. 5.

For most of the main tests, the free length of the sheets between the steel grips was 9 in., and the distance between the stringers and the grips was about $^1/_{16}$ in. at each end. The free length of the panels seems to have an influence on the buckling load only when its length is less than about three-fourths of the width, as will be shown later. For most of the test series, a length somewhat greater (about 50 per cent) than the width of the panels was chosen.

MATERIAL USED

Most of the sheets tested, commercial products of the Aluminum Company of Canada, designated by A-N, had a thickness of 0.032 in. The panels had a radius of 24 in. A few sheets of the 17ST alloy, having a thickness of 0.036 in., were also used. For the greater part of these tests, the 24ST alloy, with a somewhat higher yield strength than 17ST, was employed. Some of the sheets had an original width of 24 in. and

a length of 72 in., and a few had a width of up to 48 in. All sheets have been delivered commercially flat, but not all of them were completely free from small surface defects.

The test specimens were cut out of these sheets by means of an automatic jig saw, producing only slight local deformations at the ends of the panels. The light-alloy plates were cold-rolled between steel plates on a rolling machine with three rolls to give them the desired radius of curvature. To get reliable average results, most of the buckling tests were repeated, with different specimens, twice, frequently four times and more.

Determination of the Characteristics of the Testing Machine

Stiffness of Testing Machine

Besides the load indication of the machine, the strain or the deformation of the test piece as a function of the load is of equal interest. It is well known that in this respect the variation of the so-called stiffness of testing machines is great. They may range from stiff machines, with an impressive drop of the load for small movement between the crossheads, to fairly elastic ones. An investigation with a compression member, composed of a ductility tester (cupping tester) for sheet metal mounted in the testing machine, as represented in Fig. 6, showed that the Baldwin machine

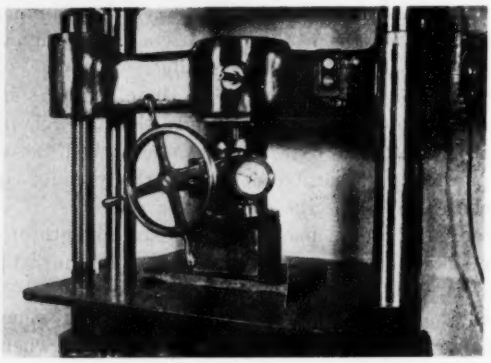

Fig. 6.

is sensitive in this respect. As illustrated in Fig. 7, by a movement of 0.01 in. between the crossheads of the machine and under a load of 2,400 lbs., this load drops to 0 lb.; for 0.005 in., the load drops from 2,000 to about 500 lbs. As will be seen later, the least local deformation of the panels under load will release the panel immediately by the dropping of the load to a fairly small amount. It would, however, not be without interest to investigate more closely this phenomenon and its influence on the results of light-alloy panels, because this kind of loading, with an immediate release of the specimen, is not in full accordance with

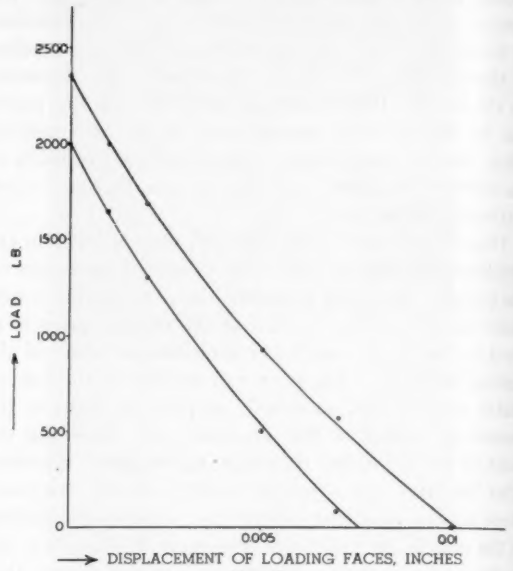

Fig. 7.

the applications of the load in service. In practice, the applied load may remain on the element, independent of its straining.*

The testing machine should provide, as generally admitted, a "true translational strain," so that the loading table with the grips remain parallel during the test. As this condition seems to be of great importance on the results on buckling, a series of check tests was made with an accurately adjusted light-alloy plate in the machine. The relative displacement of the loading faces of the machine during the compression test was measured up to the neighborhood of the maximum load under which the first buckling generally takes place. Four dial gages reading to 0.0001 in. were placed under the four corners of the loading tables, as shown in Fig. 8, and the displacement of these points were recorded for every 200 lbs. The distance between points A and B was about $7^1/_2$ in. and between A and C about 5 in. After a series of preliminary tests to obtain a better agreement between these four instruments, by placing thin shims between the steel grips and the loading tables, the results given in Table 1 were found.

* An investigation about this point has been completed recently and is entitled: "The Yielding Phenomenon of Metals; Influence of Speed and Loading Conditions." The results of this investigation will be published soon.

Table 1

Load, Lbs.	Right Front, Point A	Left Front, Point B	Right Back, Point C	Left Back, Point D
0	0	0	0	0
500	0.0037	0.0034	0.00355	0.0033
1,000	0.0072	0.0063	0.0067	0.00625
1,190	0.0094	0.00875	0.0088	0.0083

According to these results, the translational strain of the machine with this equipment is not at all assured. The displacement of the loading faces is, in this case, largest at point A (right front) and point C (right back). Under a load of 500 lbs. a difference of 0.0004 in., and under a 1,000-lb. load about 0.00095 in. could be noticed between points D and A. After buckling took place at 1,190 lbs., this difference was about 0.0011 in. In order to investigate how much these displacements might be influenced by a certain eccentricity of the test piece in relation to the loading center of the machine, a rigid steel bar of about the length of a panel—that is, about 9 in.—was placed between the tables and loaded up to 2,000 lbs., in different positions relative to the central loading axis of the machine. According to Table 2, an eccentricity of the steel bar of about $^1/_4$ in. caused, at points A and B (compared to points C and D) at a load of 1,000 lbs., an advance of about 0.0036 and 0.0043 in., respectively; at 2,000 lbs., an advance as high as 0.0064 and 0.0073 in. On the other hand, for an eccentricity of $^1/_4$ in. in the opposite direction, points C and D showed a maximum displacement, and their differences between points A and B were somewhat less at the load of 2,000 lbs. (about 0.0041 and 0.0029 in.).

For each buckling test, the displacement of the tables at a load of 1,000 lbs. was measured at the four points A to D. The numerous buckling results on about 330 plates showed that point C (right back) was generally in advance of a few 0.0001 in. over the other instruments; point B showed generally the least deflection. By these tests, which constituted an appreciable part of the preliminary investigations, it becomes clear that under those conditions the ultimate buckling-load results cannot be guaranteed as representing the maximum load that these sheets can support. It is quite evident that a great deal of the scattering of the buckling load, sometimes as high as 32 to 50 per cent, can be attributed to the nontranslational displacement of the loading tables of the testing machine.

If further tests of this kind are planned, it is suggested that it would be preferable to separate the true translational strain from the testing machine itself, using the latter only as a loading device. A device, as roughly sketched in Fig. 9, using a cylinder of a greater diameter than the panels, which are fixed rigidly on ground clamps and are provided with a true translational displacement by a piston sliding with a minimum of clearance in the cylinder, might give the desired results. By fixing the grips so that the center of gravity corresponds exactly with the geometric center of the cylinder and the piston, a maximum of true translational strain may be obtained. The plates are adjustable in the grips from the outside of the cylinder through two windows provided on the front and back of this cylinder. By introducing the compression load through steel balls placed in the centerline at the ends of the cylinder and the piston, there might be expected regular and reliable results concerning the buckling load of the plates.

TABLE 2

Load, Lbs.	Right Front, Point A	Left Front, Point B	Right Back, Point C	Left Back, Point D	Steel Bar
0	0	0	0	0	In center of machine
1,000	0.0051	0.0051	0.0058	0.0054	
2,000	0.0086	0.0085	0.00104	0.0094	
0	0	0	0	0	$+^1/_4$ in. out of center
1,000	0.0062	0.0057	0.0026	0.0014	
2,000	0.0098	0.0094	0.0034	0.0021	
0	0	0	0	0	$-^1/_4$ in. out of center
1,000	0.0034	0.0044	0.0055	0.0055	
2,000	0.0053	0.0065	0.0094	0.0094	

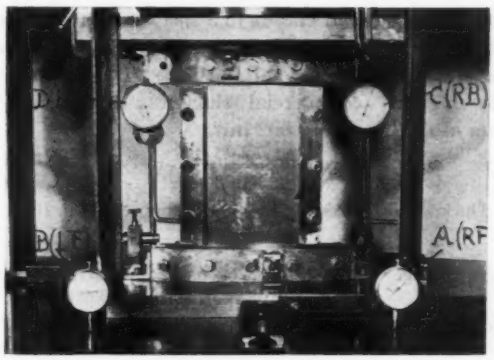

FIG. 8.

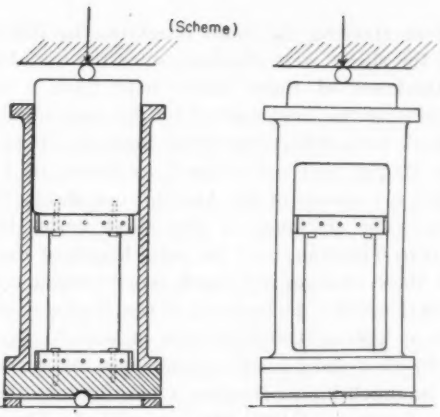

FIG. 9. Equipment for testing panels in compression.

RESULTS OF TESTS AND THEIR DISCUSSION

Measurement of Test Specimens

As it is desirable to determine the thickness of the light-alloy panels from at least six readings symmetrically distributed over the plates, a special device was set up for this purpose. Table 3 gives a series of results, measured with this device on 15 different spots

of one plate that was chosen in a sheet with a maximum of regularity in thickness. As may be seen, these results, varying between 0.0316 and 0.0324 in., are fairly regular (commercial thickness tolerances for sheets of 0.032 are ±0.002 in.).

TABLE 3
Thickness of Plates in 15 Equal Distant Spots in Inch

	1	2	3	4	5
Near right edge	0.0317	0.0320	0.0321	0.0321	0.0318
	0.0316	0.0318	0.0319	0.0320	0.0317
Middle of plate	0.0320	0.0321	0.0321	0.0322	0.0320
	0.0318	0.0319	0.0320	0.0321	0.0320
Near left edge	0.0319	0.0321	0.0323	0.0323	0.0321
	0.0318	0.0320	0.0323	0.0324	0.0321

Before starting the main program, the dimensions of all the sheets were checked, since the variability of the thickness of these sheets may have a marked influence on the load carried by the individual plate. By check tests, differences of the thickness of the sheets up to 10 per cent were found, as shown in Fig 10, where a few results of this kind for one sheet, "G," are shown. The thickness of this sheet varies between 0.0310 to 0.0338 in. over the total length of the sheet, while these changes are much more pronounced over the total width. Differences of the thickness of these sheets as high as 0.0025 in. were measured. According to light-alloy sheet specification, these differences may even be much higher because a tolerance in thickness of plus or minus 0.0025 in. is possible.* This means that sheets of this kind may vary from 0.0295 to 0.0345 in.

If these maximum tolerances are used, which is quite admissible for a commercial product, the load that such sheets may carry on a section of 1 in., at the yield point, for instance, can vary from 45,000 to about 52,500 lbs.

* See "Aluminum in Aircraft," Aluminum Company of America, 1941, (a) Table 20, p. 86.

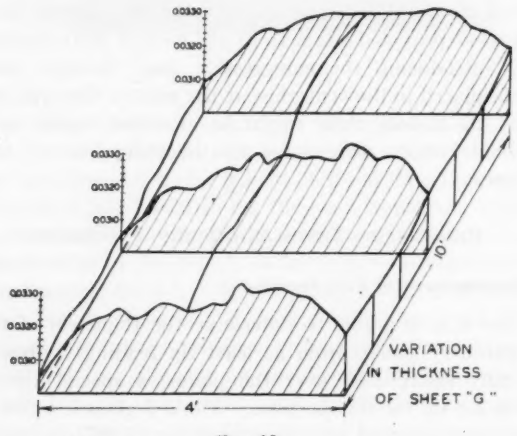

FIG. 10.

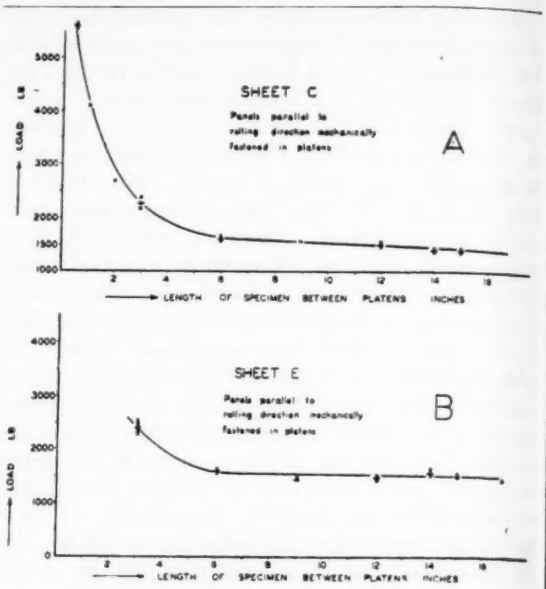
SHEET C
Panels parallel to rolling direction mechanically fastened in platens
A
LOAD LB
LENGTH OF SPECIMEN BETWEEN PLATENS INCHES
SHEET E
Panels parallel to rolling direction mechanically fastened in platens
B
LOAD LB
LENGTH OF SPECIMEN BETWEEN PLATENS INCHES

FIGS. 11A (*top*) and 11B (*bottom*).

Influence of Length of Plates on Buckling Load

Tests were made to determine the influence of the free length of the panels between the grips on the maximum buckling load. For this purpose two test series with two different sheets ("C" and "E") of 24 in. in width were planned and executed under identical conditions.

The results from plates with lengths from $^1/_2$ to 15 in. are given for sheet "C" in Fig. 11, while the results for sheet "E" with 3 to $16^3/_4$ in. in free length between the platens are shown in Fig. 11A. All these tests were executed with light stringers clamped at the longitudinal edges of the plates. For these results, as well as for all other tests of this kind, the highest load that the machine indicates, independent of the shape of the stress-strain diagram, was considered as the maximum load supported by the panel. These results show that the collapse load for short plates drops rapidly from about 5,500 lbs. (22,000 lbs. per sq.in.) to about 2,250 lbs. for a length of 3 in. Plates of 6 in. in length support only 1,600 lbs., and this load falls only a relatively small amount for plates with much greater length; for instance, for 15-in. length the load supported by the plate is only 200 lbs. lower than for plates of 6-in. length.

A second series of analogous tests was made with another sheet, "E," in order to check these results. These tests, reported in Fig. 11A, confirm the above results for plates of 3 to 16 in. in length. It can be seen that the results of the collapse loads of the plates are astonishingly regular. A difference of less than ±5 per cent from the average values of both plates "C" and "E" has been found. Based on the above results,

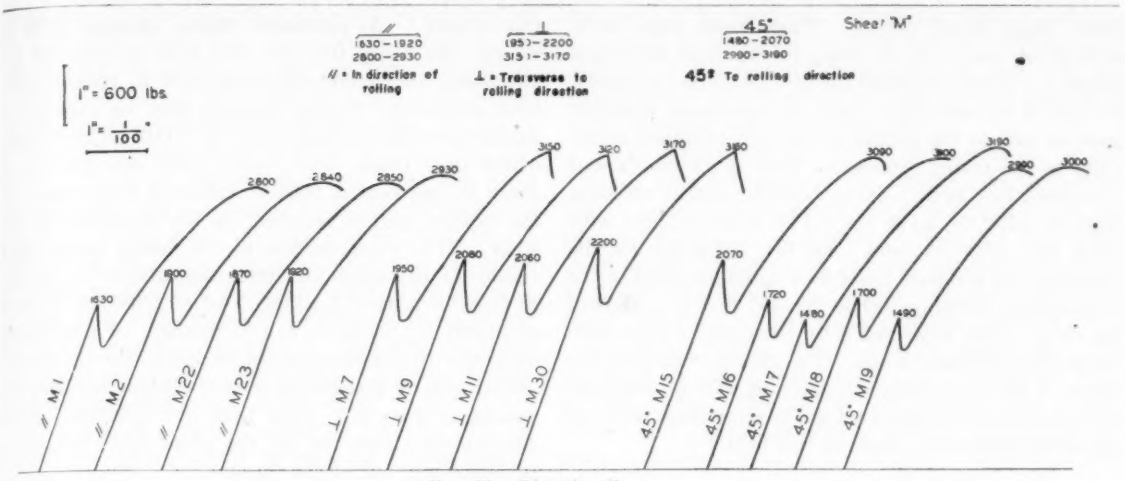

FIG. 12. Directionality.

it seems that the length of a panel becomes of importance if it is less than about three-quarters of its width.

Buckling Loads Measured on Plates Taken Parallel, Transverse and at 45° to the Rolling Direction

These tests were made on sheets of two different alloys. One sheet, "I" (24ST alloy), of 0.032-in. thickness, 24-in. width, and 72-in. length, as well as another sheet, "K" (17ST alloy), with 0.036-in. thickness, 24-in. width, and 96-in. length, were used for these tests. For each direction, three to four specimens were normally chosen. In order to eliminate the effect of the change of thickness across the width, the specimens were taken in such a fashion that the thickness remained as constant as possible. A check series with sheet "M" was made with at least four specimens for every direction, but, in this case, the specimens were scattered all over the whole sheet. All tests have been made with stringers of $^1/_2$-in. pitch and $^1/_2$-in. depth.

With the first series of tests on sheet "IA" of 0.032-in. thickness, the buckling load and the maximum load are fairly regular for the three specimens situated in the longitudinal and transverse direction. In the longitudinal direction, the buckle took place between 1,550 and 1,690 lbs., while the ultimate load varied between 2,480 and 2,530 lbs. (Table 4).

It is of interest to note that both these characteristics are distinctly higher for the specimens situated transverse to the rolling direction. The buckling load varies between 1,630 and 1,880 lbs., and the collapse took place between 2,570 and 2,800 lbs.

The loads carried by specimens taken at 45° are intermediate to the above two directions, varying between 2,620 and 2,770 lbs. On the other hand, the buckling loads for these specimens are the lowest and the highest in this series; they vary between 1,390 and 1,920 lbs. (specimens "IA," 9, 10, and 11).

The buckle for this and for most of the following series took place normally halfway between the grips and spread at once over the whole width of the specimen, leaving about $^1/_2$ in. at both sides of the stringers. The collapse of the specimens was always caused by an excessive deformation between the teeth of the stringers at the edges of the panels.

As shown in Table 4, similar results have been obtained with the thicker 17ST sheet "KA" of 0.036-in. thickness and 24-in. width.

The results of check tests made with sheet "M" are shown in Fig. 12. (Similar records have been made for

TABLE 4

No.	Designation of Sheet	Orientation with Rolling Direction	Buckling Load, Lbs. Min.	Buckling Load, Lbs. Max.	Average Value, Lbs.	Ultimate Load, Lbs. Min.	Ultimate Load, Lbs. Max.	Average Value, Lbs.
1	"IA 1-11"	Parallel	1,550	1,690	1,610	2,480	2,530	2,502
		Transverse	1,630	1,880	1,730	2,570	2,800	2,673
		45°	1,390	1,920	1,670	2,620	2,770	2,677
2	"KA 6-18"	Parallel	2,210	2,620	2,450	3,310	3,530	3,427
		Transverse	2,700	2,830	2,765	3,630	3,710	3,670
		45°	2,240	3,020	2,662	3,450	3,540	3,482
3	"M 1-30"	Parallel	1,630	1,920	1,830	2,800	2,930	2,855
		Transverse	1,950	2,200	2,072	3,150	3,170	3,150
		45°	1,480	2,070	1,692	2,990	3,190	3,074

every single panel tested.) These tests were made with great care and according to the final technique adopted. They confirmed the first two series of results, so that it became clear that the maximum buckling load, as well as the ultimate load, was obtained transverse to the rolling direction. Four diagrams showed a buckling load from 1,950 to 2,200 lbs. and an ultimate load of 3,150 to 3,170 lbs. The lowest values with 1,630 lbs., 1,920 lbs. and 2,800 lbs., 2,930 lbs. for the buckling and ultimate loads were again obtained in the longitudinal direction, while the 45° direction showed buckling values scattered over these two ranges with fairly high ultimate loads. The results regarding the shape of the load-deflection diagram with a maximum and minimum buckling load are in accordance with the theoretic predictions made in this field.[1-4]

Results of the Directionality Tests

These tests give conclusive evidence of the superiority of results with sheets situated in the transverse direction. The average buckling loads in the transverse direction were superior to those in the longitudinal direction (for sheet "IA" by 120 lbs., for sheet "KA" by 315 lbs., and for sheet "M" by 242 lbs.—Table 4). For the average ultimate loads, this superiority is 173 lbs. for sheet "IA," 243 lbs. for sheet "KA," and 295 lbs. for sheet "M," which means an average superiority of about 8 to 12 per cent for the buckling load and of about 7 to 10 per cent for the ultimate strength of these sheets.

The superiority of the plates situated transverse (roughly 10 per cent more resistant) may be explained by the mechanical anisotropy of the tested sheets. The anisotropy of these sheets is (because of the cold stretching of the material in the factory of about 1 to 2 per cent) fairly pronounced, and the variations from one sheet to another are great, as may be seen by the results of a special investigation of the author about this subject.* As previously stated, changes of 80 to 90 per cent of the 0.01 per cent limit (permanent deformation) in compression compared to tension have been measured. Higher changes may be expected if similar tests are conducted for the 0.001-per-cent limit, which may reach, after preliminary deformation of about 0.5 per cent in tension, values in compression, in the weakest part of the sheet, as low as 15,000 lbs. per sq.in. The cross section of the tested panels may reach, for the minimum thickness, about 0.18 sq.in., so that for a usual buckling load of 2,200 lbs. a stress of 12,200 lbs. per sq.in. can be reached. Furthermore, as, in the neighborhood of the buckling load, the stresses are irregularly distributed over the whole width of the panels, it does not seem that the influence of the mechanical anisotropy of the aluminum-alloy sheets is completely out of the question.

According to the results of these tests, it may be said that it is inadvisable to weaken the sheets in the compression direction by cold-stretching (Bauschinger effect). It is quite possible that sheets without cold-stretching will have much smaller mechanical anisotropy and, consequently, a more equal resistance both to buckling and collapse load in the longitudinal and transverse direction.

Influence of the Stringers on Buckling Results

The method of supporting the panels at their free edges to prevent premature buckling does not seem to have been sufficiently investigated. Therefore, a series of tests was made on a variable rivet pitch.

The rivet pitch was varied from 1 in. to zero (continuous stringers) in steps of $1/4$ in., and the effect was controlled on 24ST sheets ("G" and "H") of 0.032-in.

* Welter, G., "Micro-Deformation Under Tension and Compression Loads of Thin Aluminum Alloy Sheets for Aircraft Construction," presented at the 47th Annual Meeting of the American Society for Testing Materials, June 26 to 30, 1944.

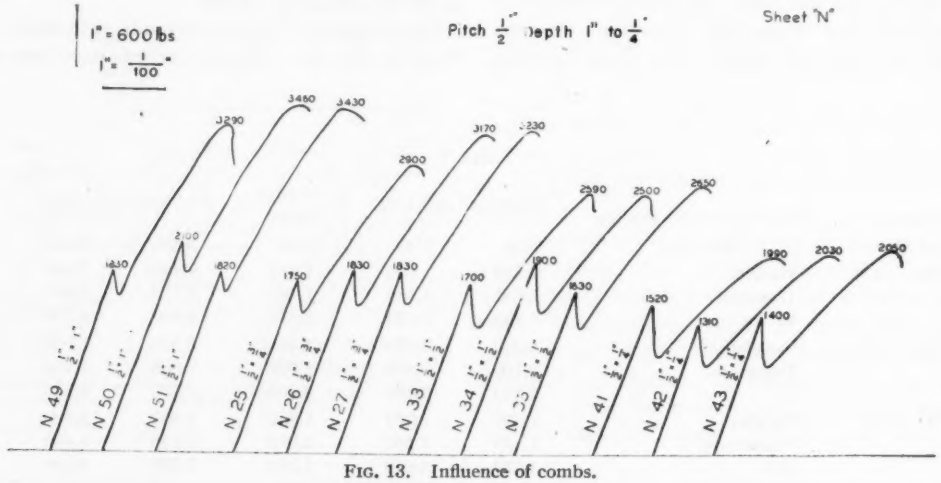

FIG. 13. Influence of combs.

thickness. The literature seems to offer no explanation for, and there have been no systematic tests on, the influence of the depth of the guiding slots on the maximum buckling load and ultimate load of the panels. In some sources, a uniform depth of the slot of 0.375 in. is given for all thicknesses of sheets between 0.02 and 0.03 in. Only the general statement that the edges parallel to the load are clamped or are simply supported is reported. The kind of clamping or details about the influence of clamping or supporting the edges on buckling results are not revealed. Also, in the theoretic consideration of Redshaw[2] concerning the development of the formula representing the maximum possible buckling load on light-alloy sheets, a clear statement about this important point is not made.

The results of a typical series are given in Fig. 13, and the average values of all series are represented in Fig. 14. The influence of this factor is so characteristic and pronounced that a simple reproduction of one series of original diagrams, represented in Fig. 13, and of the average value of the series, represented in Fig. 14, seemed sufficient. For these series, two panels for each test result were investigated under identical conditions.

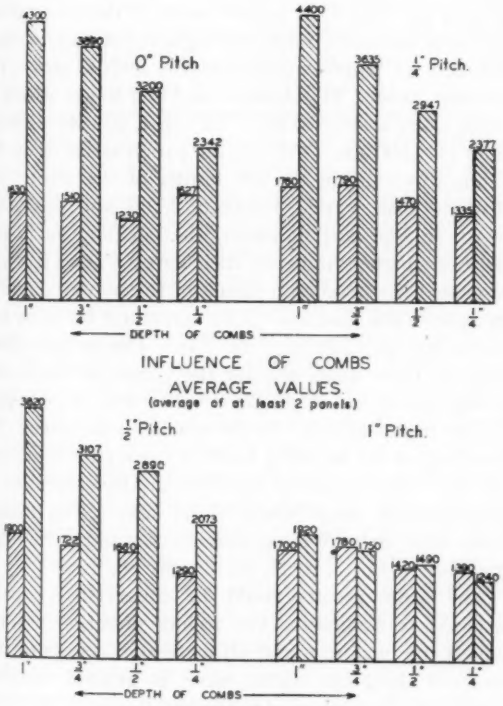

FIG. 14.

Rigid Steel Stringers Compared with Elastic Duralumin Stringers

Under the supposition that the attainment of the true buckling load is in some measure dependent on the slightest differences in initial eccentricity of the panels which may be produced during the loading process, it seemed possible that a difference in the degree of stiffness of the material restraining the edges of the panels might have a certain influence on the maximum loads attained during compression.

Tests were carried out to determine whether or not there is any difference in the behavior of light-alloy panels under compression loads with regard to the restrained edges. In one series of tests the free edges were rigidly restrained by stiff stringers having a high modulus of elasticity; in another series, with stringers made of a material with a low modulus of elasticity.

According to the test results, it seems that the variation of the buckling load and the ultimate load is much more influenced by the irregularities of the single panel and its situation in the sheet than by stringers with different moduli of elasticity. The results show that the lateral efforts of the edges of the sheets under compression are small and do not surpass a critical value; otherwise sheets with more elastically restrained edges would show an earlier eccentric loading than sheets with stringers of material with a high modulus of elasticity.

Buckling Load and Ultimate Strength on Panels of High- and Low-Resistant Aluminum Alloy

Buckling tests with soft and hard pure aluminum sheets were made. This material has practically the same Young's modulus of elasticity but a lower elastic limit and a lower yield strength than those of aluminum alloys such as 17ST or 24ST. The sheets of pure aluminum and 24ST alloy were of about the same thickness (0.032 in.), so that the stress-strain records are directly comparable.

The results of these tests are shown in Fig. 15. By comparing the graphs of the three-quarter hard, pure aluminum sheets, "L," with the 24ST alloy, "N," it may be of interest to note that the maximum buckling

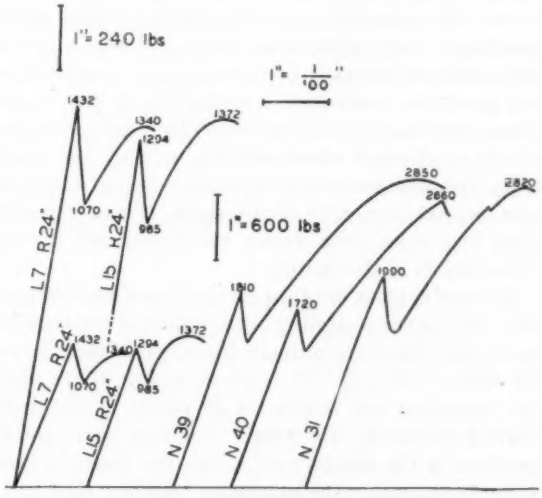

FIG. 15.

load for three-quarter hard-rolled aluminum is fairly high and reaches an average value of about 1,294 to 1,432 lbs. On the other hand, the ultimate load at collapse is rather low and, in a few cases, did not even reach the value of the maximum buckling load. While the buckling loads of hard aluminum sheets may approach minimum values of 24ST alloy, their ultimate loads are less than about 50 per cent of those of 24ST alloy. This means that pure, hard aluminum with practically the same modulus of elasticity as 24ST alloy and with a yield strength of about 17,000 lbs. per sq.in. compared to 45,000 lbs. per sq.in. for 24ST alloy, supports fairly high buckling loads that are only about 30 per cent lower than those of the high-resistant light alloys. However, failure, which is a direct function of the yield strength, is low for pure aluminum sheets.

The average ultimate loads for 24ST alloys are about 100 per cent higher than those for hard, pure aluminum sheets. Somewhat different results were obtained with soft, pure aluminum sheets (annealed at 350° during $1^1/_2$ hours). For soft aluminum with a yield strength of only about 5,000 lbs. per sq.in., the buckling of the panel did not take place. The collapse load was as low as 740 lbs. for one panel and 730 lbs. for another panel. This means that beyond the modulus of elasticity other mechanical qualities of the light alloys, such as elastic limit and yield strength, are involved in the resistance against buckling. These factors are not included in the theoretic formula of Redshaw; according to this formula, pure, soft aluminum (2 S-O) ought to have a buckling resistance of the same order as the high-resistant aluminum alloy (24ST).

Irregularities of Test Results Due to the Imperfection of the Sheets Employed

The numerous test results obtained with panels cut out of different sheets showed that, aside from the various factors investigated, there must be another factor influencing the maximum buckling loads which sometimes vary with wide limits. These strength variations are generally explained by the sensitivity of the panels to accidental irregularities in the sheets. These irregularities may be caused by a local variation of the mechanical characteristics or may be simply connected with geometric imperfections (out of roundness, eccentricity, etc.) of the sheet. These imperfections may take place during the rolling and curving of the sheets in the factory.

In order to point out the part that these imperfections may play in the scattering of the values of the buckling loads and even of the ultimate loads, a statistical survey for sheets "M" and "N" is shown in Fig. 16, in which the numerical test results for all panels, tested under normal conditions, are given. For each panel and its position in the sheets, two values are given, a lower value representing the maximum buckling load and a higher value corresponding to the collapse load of the

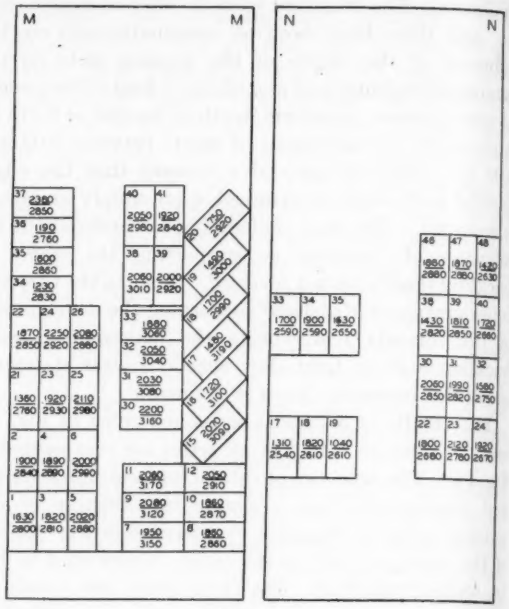

FIG. 16.

panels. As may be seen, the buckling loads are frequently the lowest for panels taken at the longitudinal border of the sheet, while the highest values have been recorded for panels situated in the middle part. For instance, sheet "M" showed buckling loads as low as 1,360, 1,630, and 1,870 lbs. ("M" 21, 1, 22), with a maximum of 1,900 lbs. ("M" 2) for panels situated in the rolling direction on the left border of the sheet. The ultimate load varied between 2,760 and 2,850 lbs. In the middle part, however, the buckling loads were distinctly higher, and even their lowest values regularly surpassed the maximum values of the border sheets by an appreciable amount. The maximum buckling load was as high as 2,110 lbs. ("M" 23). The greatest difference for these loads was for the panels at the border, as high as 540 lbs., while these values were more regular for the panels situated in the middle of the sheet. The variation of the buckling loads of these panels was only 110 lbs.—that is, about one-fifth of the values for the panels located in the border of the sheet. The ultimate loads were higher for the panels taken in the middle of the sheet ("M" 5, 6, 25, 26, 38, 39, 40, 41).

The same results could be observed for panels situated transverse to the rolling direction. For 14 panels the buckling- and ultimate-load results of those situated along the border were, in general, distinctly inferior to those situated in the middle part ("M" 34–36, 8, 10, and 30–32; "M" 33 and 37 are the only two exceptions of this test series).

Similar results were obtained with sheet "N," where 17 panels situated in the longitudinal direction were tested under identical conditions. Fig. 17 gives the maximum and minimum results for sheets "M" and "N," indicating the larger variation of the compression

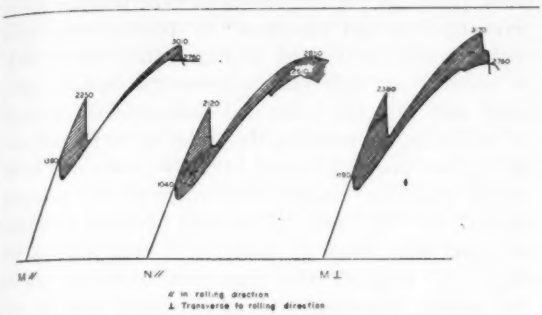

FIG. 17. Irregularities of test results of sheets "M" and "N" (maximum and minimum records).

loads in these tests. It is interesting to note that the differences of the buckling loads are especially pronounced compared to collapse loads that are more regular.

These characteristic results concerning the variations of the buckling loads in the border zones of the sheet cannot be explained only by differences in the thickness over their whole width and length as stated above. This factor may play a certain part in the scattering of the ultimate-load values in the different parts of the sheets. Concerning the variability of the buckling loads, however, there must be other factors responsible for these unsatisfactory results. Provided the test equipment works perfectly and the material tested is completely homogeneous, it should be possible to eliminate such appreciable and harmful variations of the buckling loads. Without doubt, closer control and more adequate fabrication of the sheets used for panels, as well as a true translational movement of the loading tables of the test machine, would bring about a marked amelioration in this respect.

The anisotropy of the mechanical qualities of the sheets, in combination with geometric imperfections of the curved sheet, is not without influence on the variation of the collapse loads and also of the buckling loads. As a guide, it may be stated that microplastic deformations at the elastic limit (with 0.001 per cent permanent set) were observed during recently executed microcompression tests with sheet "B" at a unit stress as low as about 22,000 lbs. per sq.in. In tension, this sheet had an elastic limit that was about 90 per cent higher (42,000 lbs. per sq.in.).* If the commercial tolerances of these sheets are taken into account, a combination of the maximum thickness of the sheet with the microplastic deformations at the elastic limit in tension can be imagined. On the other hand, the minimum thickness can be encountered in that place where the maximum compressive stresses occur. It can be calculated that differences of about 100 per cent and more in the resistance of the panels, because of variations in the properties of the sheets, can take place.

* See footnote on page 364.

Adjustment of the Sheets in the Grips

Analogous to the tests reported, the investigations of the panels under compression loads were executed with panels strongly clamped between the curved steel grips and fixed on the panels with steel bolts. However, as the results of the preliminary tests were not quite satisfactory with regard to the elastic deformations as a function of the loads, it seemed evident that by a small displacement of the panels in the grips (for instance, displacement between the clamped grips by sliding) a steadily curved stress-strain diagram can be recorded up to the maximum buckling load instead of a straight line. However, by fastening the panels over the whole length of the grips in the vertical direction so that they touched the compression tables of the testing machine over the whole width, the records became more regular and the elastic part of the diagram was represented by a straighter line. By this arrangement the panel cannot slip at all between the grips, which otherwise had to be strongly bolted to prevent slipping. The grips served in this case more as a guide for introducing and diffusing the compression loads into the thin panels. By this means the rigid clamping of the panels between the platens by friction was no longer necessary, and it became possible to study the influence of the grips on the buckling loads in relation to the clamping forces.

As shown in Fig. 18, some tests were executed with panels fastened between the grips by use of a small torque on the transverse bolts (about 5 lbs. acting on a lever of 7-in. length against 40 lbs. on the same lever for the normal adjustment). By this kind of fastening, the irregularities of the grips did not react so strongly on the panels, so that they showed appreciably higher buckling loads (2,220 to 2,480 lbs. for panels "N" 53–56) than those clamped strongly in the usual manner (1,870 to 2,120 lbs. for "N" 23, 24, 46, 47). Buckling loads as high as 2,480 lbs. could be noticed, while the ultimate loads were hardly influenced by a change of the clamping forces of the panels.

As a few other tests of this kind showed a certain relation between the clamping forces and the buckling load, it seems advisable to pay more attention to the clamping forces of the platens. In order to be sure that the panels fitted smoothly inside the grips, they were ground exactly to the desired curvature of 24 in., eliminating all irregularities of the clamping surfaces.

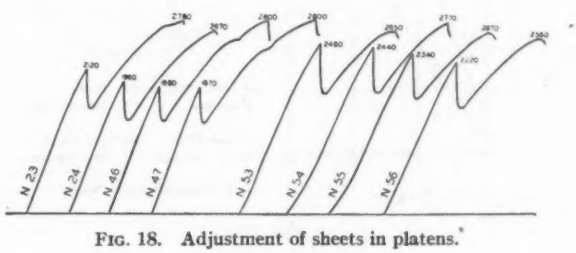

FIG. 18. Adjustment of sheets in platens.

Comparison Between Theoretic and Experimental Results (Formula of Redshaw)

As already stated, the results of these kinds of compression tests with thin light-alloy plates are influenced by: the properties of the sheets; the direction of the test specimen with the rolling direction; the shape and thickness of the stringers; an incomplete fixation of the axial edges; and the length, as well as a geometrical imperfection or local overstresses of the specimen. In spite of all these effects, it is rather astonishing that the results obtained by the buckling tests with plates of 9- to 18-in. length, tested with stiff stringers, are fairly regular and agree in a satisfactory manner with the theoretic values calculated according to the equation established by Redshaw.[2] Fig. 19 shows in curve a–b the theoretic results of that work. A value of 10.4 on the abscissa corresponds to a theoretic value of about 60–61 on the vertical axis (circle A). This value represents, for special test conditions of the preliminary tests ($b = 8$ in., $r = 24$ in., $t = 0.032$ in.), a theoretic buckling load of about 2,160 to 2,200 lbs.

Most of the tests made on plates 18 in. in length, with axial edges fixed in stiff stringers, showed an average buckling stress of 1,958 lbs. (sheet "A," seven identical tests). For these plates, cut in the rolling direction and tested with steel grips, the difference between the experimental results was hardly more than about ±6 to 7 per cent from the average value, as represented by the seven different experimental results marked by black crosses in this diagram. (The small black points of Fig. 19 represent experimental results given by Cox and Clenshaw[1] for plates tested under similar conditions.) The average value (white circle) of these seven different experimental results agrees fairly well with the value a–b calculated theoretically by Redshaw, approaching this value up to 90 per cent; the highest buckling load of 2,056 lbs., measured in the rolling direction, reaches this value to 95 per cent. Sheets "D," "B," and "E" showed buckling loads that are lower than those of sheet "A." One plate of this sheet "A," situated in a transverse direction, reached the highest buckling load (2,104 lbs.); this is only 3.5 per cent lower than the theoretic value of about 2,180 lbs.

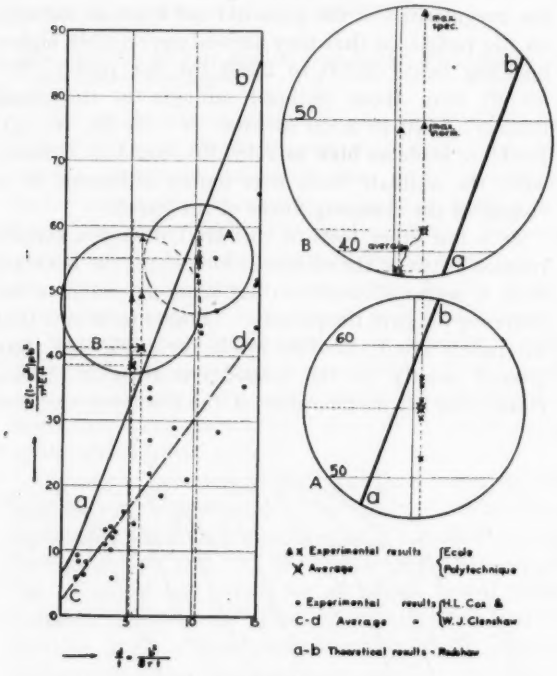

FIG. 19.

These preliminary results on buckling tests had the character of first information tests. Some of these special kinds of buckling tests were repeated in the main test series on a larger scale with different sheets and with different dimensions of the plates. Also, the influence of artificial imperfections (out of flatness) or critical eccentricity, which is presumed, according to the conclusions of Redshaw, to be the most important point for the unexplainable differences between experimental and theoretic results, have been investigated, but the results of these tests cannot yet be published. Furthermore, the directional properties of the sheets, the influence of stringers, the effect of cold-working, as well as the influence of different shapes of sheets, were studied. These investigations represent the main test series, the results of which are shown in Fig. 19B.

As already mentioned, a satisfactory agreement between theory and experiment has not yet been obtained for curved light-alloy panels, and the experimental results are in all cases appreciably lower than the theoretic values. For instance, the experimental values found by Cox and Clenshaw[1] are about half the theoretic ones. As stated by these authors, the average results are only 40 to 50 per cent of the theoretic values, and they say that the discrepancies between theoretic and experimental results remain unexplained.* It is thought that the buckling load is largely dependent on the perfection of the form of the panel, and its initial irregularities, especially the slightest eccentricity, might cause a premature buckling. If the formula of Redshaw and its graphic representation are well interpreted, the maximum theoretic buckling load for sheets 0.032 in. thick and 6 in. wide (main tests) should be, according to this formula, about 9,000 lbs. per sq.in. This means that the theoretic buckling loads or the maximum possible loads attained under ideal test conditions for panels of these dimensions cannot be higher than 1,738 lbs. (that means 36 on the vertical axis). By reviewing the numerous results measured during these main tests, it may be said that with the

* Cox[4] in a lecture read before The Royal Aeronautical Society, London, states: "Experimental realization of the theoretical buckling load is extremely improbable."

exception of a few unusual results most of the buckling loads show a value at least as high as this theoretic value. The greater part of the results surpass this theoretic load by 10 and 20 per cent. Buckling loads of 1,900 lbs., 2,000 lbs., and even 2,100 lbs. are not unusual. For sheet "M," for instance (Fig. 16), only two panels do not attain the theoretic value, while 14 panels tested in the longitudinal direction show buckling loads that are much higher than this value. The average load of these 14 panels is about 1,992 lbs. (41.5) (triangular points in circle B, Fig. 19). This means that the average value is about 15 per cent higher than the theoretic calculated value by Redshaw. However, the highest experimental value reported in the literature about this point is that of Cox, showing that in one case (see reference 4, Fig. 4, p. 235) when the panel was particularly well formed the actual buckling load was nearly 80 per cent of the theoretic value. This means that the average buckling values recorded during the present investigations on sheets 0.032 in. thick and 6 in. wide are about 45 per cent higher than the maximum experimental value recorded by Cox. On the other hand, the maximum buckling value measured on panels tested under normal conditions is, with 2,380 lbs. (49.8), more than 35 per cent higher (circle B, maximum normal, Fig. 19) than the theoretic value (a–b) calculated by Redshaw. This value has been reported as practically unattainable. The theoretic value of Redshaw (a–b) is, however, surpassed by a much higher percentage if the results of the tests concerning the amelioration of the buckling loads are taken into consideration. For instance, by cold-stretching, by changing the shape of the panel, or by other effects that cannot yet be revealed, it is possible to bring the buckling loads as high as 60 per cent over the theoretic value (circle B, maximum special 58.5, Fig. 19)—that is, about 100 per cent over the maximum experimental value of Cox.

In a similar way, the buckling results with a thicker sheet of 0.036 in. are also much higher than the theoretic value. Buckling loads of about 2,790 and 3,220 lbs. were measured for sheet "K," surpassing the value calculated by Redshaw (2,186 lbs.) by about 30 per cent and more. The maximum value measured with 3,360 lbs. (49.2) is over 50 per cent higher than the theoretic calculated value (32 compared to 49.2, Fig. 19B). It may be said that in this series (sheet "K" of 0.036 in.) by a simple mechanical change of the curved plates, which will be reported later, the maximum buckling load could be brought to about 135 per cent over the best experimental value of Cox.

The present main results of this investigation show that the buckling loads have been effectively brought up higher than the theoretic values calculated by Redshaw and that the regular average results surpass this value by about 15 per cent. Furthermore, it was possible to show that by special tests these theoretic values can be surpassed appreciably and that buckling loads of about 50 to 60 per cent higher than the theoretic values and 100 per cent higher than the maximum experimental value are not unusual. If we take into account the exceptionally high load that some of the panels tested under special conditions supported without showing any buckling, the elastic range of these panels being high, an even higher value for their resistance against compression loads has been obtained. It is felt that by more accurate test equipment, with assured translational displacement of the loading faces of the testing machine, as well as by a series of other ameliorations mentioned, still appreciably higher experimental values for buckling loads can be expected.

References

[1] Cox, H. L., and Clenshaw, W. J., *Compression Tests on Curved Panels of Thin Sheet Duralumin*, 1934 (unpublished).

[2] Redshaw, S. C., *The Elastic Stability of a Curved Plate Under Axial Thrust*, Journal of The Royal Aeronautical Society, Vol. 42, p. 536, 1938.

[3] von Kármán, Th., Dunn, L. G., and Tsien, H.-S., *The Influence of Curvature on the Buckling Characteristics of Structures*, Journal of the Aeronautical Sciences, Vol. 7, No. 7, p. 276, 1940.

[4] Cox, H. L., *Stress Analysis of Thin Metal Construction*, Journal of The Royal Aeronautical Society, Vol. 44, p. 235, and Appendix, p. 259, 1940.

[5] Gough, G. S., Elam, C. F., and de Bruyne, N. A., *The Stabilisation of a Thin Sheet by a Continuous Supporting Medium*, Journal of The Royal Aeronautical Society, Vol. 44, p. 12, 1940.

[6] Templin, R. L., and Sturm, R. G., *Some Stress-Strain Studies of Metals*, Journal of the Aeronautical Sciences, Vol. 7, No. 5, p. 189, 1940.

[7] Sechler, E., Dunn, L. G., *Airplane Structural Analysis and Design*, Galcit Aeronautical Series, John Wiley & Sons, New York, 1942.

Elementary Considerations of Longitudinal Stability

MARION THOMAS HOCKMAN*

Curtiss-Wright Corporation

SUMMARY

Increasing longitudinal stability requirements within the past few years have indicated the need for a more precise method for computing the longitudinal stability of an airplane while it is still in the design stage. A method for computing power-off stability is presented which considers the effect of the fuselage and propeller on the aerodynamic center. The use of a neutral stability c.g. position is advocated as a criterion instead of specific values of the slope dC_m/dC_L.

COEFFICIENTS AND SYMBOLS

C_m	= pitching moment coefficient
$(N_0)_w$	= aerodynamic center of wing, fraction of mean aerodynamic chord
X	= center of gravity position, fraction of mean aerodynamic chord
C_L	= lift coefficient
N_0'	= virtual aerodynamic center, fraction of mean aerodynamic chord
(ΔN_0)	= movement of aerodynamic center, fraction of mean aerodynamic chord
a_0	= slope of wing lift curve, per rad.
b	= wing span, ft.
S_w	= wing area, sq.ft.
A.R.	= aspect ratio of wing
C	= mean aerodynamic chord of wing, ft.
λ	= wing taper ratio
$d\epsilon/d\alpha$	= rate of change of down-wash angle with angle of attack
ω_f	= fuselage width at any station, ft.
X_n	= distance from leading edge of wing to nose of airplane
D	= propeller diameter, ft.
L_p	= distance from c.g. to plane of propeller, ft.
L_t	= distance from c.g. to elevator hinge line, ft.
h	= vertical distance from quarter chord of root chord to elevator hinge line, ft.
S_t	= total area of horizontal tail, sq.ft.
C_{L_t}	= tail lift coefficient
$(dC_L/d\alpha)_t$	= slope of tail lift curve, per degree
α_t	= tail angle of attack

INTRODUCTION

THE ADVENT OF THE modern high-speed, heavily loaded airplanes within the past 5 years has resulted in stability and control problems that at times have been difficult to solve. The variety of tactical uses for which military planes are now used results in many different loading conditions covering a fairly wide range of c.g. positions. It is, therefore, easily understood that it is difficult for the designer to select a tail area that will give positive stability at the most aft c.g. position without providing excessive stability at the most forward c.g. position. The problem becomes more difficult whenever full span flaps are used, since the pitching moment due to flaps may be too great for normal size elevators to overcome, and the increased elevator area necessary to land the airplane would result in excessive control sensitivity for accelerated flight with rear c.g. positions. It is thus of paramount importance that the aircraft designer fully recognize the complex nature of this problem. The ideal design condition is, of course, one in which all disposable load, whether it be fuel, ammunition, or bombs, is located at the center of gravity. This is rarely possible and it is customary for the center of gravity to move forward as the disposable load is used up.

In specifying the tail area required for a new design, it has been customary in the past to select as a criterion a tail volume equal to that of a similar plane already flying which has satisfactory longitudinal stability in the expectation that no new problems will arise which will require extensive redesign before the plane can be put into active service. The fallacy of such a method is seen in the many photographs of experimental and production airplanes which have been published in the past few years, some of which show completely new tail surfaces having entirely different areas and chord distributions. Of course, it is recognized that the effects of power may, for some designs, be a dominating factor, but no simple method has yet been devised for computation of such effects. However, there are certain basic fundamentals to which consideration must be given, and these can be most simply explained by considering only the propeller windmilling, or power-off, case.

GENERAL PITCHING MOMENT EQUATION

The total pitching moment of an airplane is the sum of the pitching moments due to wing, fuselage, propeller, and the horizontal tail surface. The equation is

$$C_m = C_{m0} + C_{m_t} \qquad (1)$$

Since the degree of stability is specified by the slope of the pitching moment curve, Eq. (1) will, for purposes of this discussion, be differentiated with respect to C_L. Thus,

Received October 21, 1944. To have been presented at the I.A.S. Thirteenth Annual Meeting, which was canceled to cooperate with a Government appeal (January, 1945) to refrain from holding conventions and meetings.

* Aerodynamics Unit Head, Columbus Plant.

$$dC_m/dC_L = dC_{m_0}/dC_L + dC_{m_t}/dC_L \qquad (2)$$

The physical aspects may best be explained by detailed consideration of the two factors on the right-hand side of Eq. (2).

The total tail-off pitching moments, C_{m_0}, is composed of the sum of the pitching moments contributed by the wing, fuselage, wing-fuselage interference and an apparent pitching moment due to the propeller, or

$$C_{m_0} = C_{m_w} + C_{m_f} + C_{m_{wf}} + C_{m_p} \qquad (3)$$

With the exception of C_{m_w}, the various factors are difficult to determine. Again, since primary consideration is given to dC_{m_0}/dC_L,

$$\frac{dC_{m_0}}{dC_L} = \frac{dC_{m_w}}{dC_L} + \frac{dC_{m_f}}{dC_L} + \frac{dC_{m_{wf}}}{dC_L} + \frac{dC_{m_p}}{dC_L} \qquad (4)$$

However, it can be shown that, since

$$C_{m_w} = C_{m_{ac}} - [(N_0)_w - X]C_L \qquad (5)$$

$$dC_{m_w}/dC_L = -[(N_0)_w - X] \qquad (6)$$

Eq. (4) can now be evaluated in terms of Eq. (6) if a virtual aerodynamic center, N_0', is used instead of $(N_0)_w$. The virtual aerodynamic center is defined as

$$N_0' = (N_0)_w + (\Delta N_0)_f + (\Delta N_0)_p \qquad (7)$$

Eq. (4) then becomes

$$dC_{m_0}/dC_L = -(N_0' - X) \qquad (8)$$

The method proposed by the use of Eqs. 7 and 8 is perfectly valid, since for fuselage-type airplanes the addition of the fuselage to a wing, plus an indeterminate wing-fuselage interference, always results in a movement of the aerodynamic center. A similar movement of the aerodynamic center also results because of the addition of a propeller.

Determination of Fuselage Effects

The difficulty in the past has been a simple evaluation of Eq. (7). Little work of a theoretic nature has been done on the aerodynamic effects of the fuselage, although it is quite logical to expect that the problem could be attacked using as a basis the theoretic analysis of airship hulls. Multhopp[1] presents such a method, based on rigorously correct theory, for the determination of fuselage moments which allows a comparatively easy evaluation of the factor $(\Delta N_0)_f$ in Eq. (7). Multhopp gives, using standard American notation,

$$(\Delta N_0)_f = -\left(\frac{1}{a_0 S_w C}\right)\left(\frac{1}{q}\right)\left(\frac{dM_R}{d\alpha}\right) \qquad (9)$$

In order to evaluate Eq. (9), it is necessary to compute the factor $(1/q)(dM_R/d\alpha)$, which is probably the most difficult computation in this discussion. As defined by Multhopp

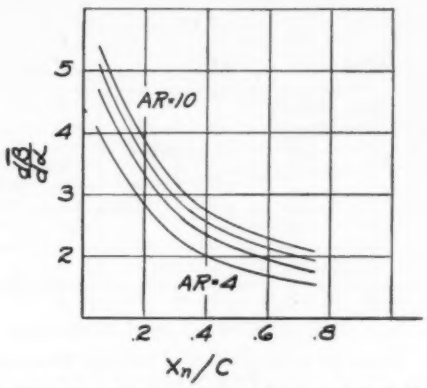

Fig. 1. Chart for determination of average values of uprush $d\beta/d\alpha$, before wing.

$$\left(\frac{1}{q}\right)\left(\frac{dM_R}{d\alpha}\right) = -\frac{\pi}{2}\int_0^l \omega_f^2\left(\frac{d\beta}{d\alpha}\right) dx \qquad (10)$$

Eq. 10 is divided essentially into two parts—i.e., the part of the fuselage forward of the wing and that part aft of the wing. The factor $d\beta/d\alpha$ is a measure of change in flow direction along the fuselage. Behind the wing, since the down-wash reduces the angle of flow along the elevator hinge line, there is obtained

$$d\beta/d\alpha = (1 - d\epsilon/d\alpha) \qquad (11)$$

and it is satisfactory to assume that $d\beta/d\alpha$ rises linearly from the wing trailing edge to this value. To estimate $d\beta/d\alpha$ before the wing, Fig. 1 is presented on which curves for various aspect ratios are shown. However, since the fuselage width ahead of the wing is substantially constant, Eq. (10) becomes

$$\left(\frac{1}{q}\right)\left(\frac{dM_R}{d\alpha}\right) = -\left(\frac{\pi}{2}\right)\bar{\omega}_f^2\left(\frac{d\bar{\beta}}{d\alpha}\right)x_n - \frac{\pi}{2}\int_{0+x_n}^{l} \omega_f^2\left(\frac{d\beta}{d\alpha}\right) dx \qquad (12)$$

Evaluation of Eq. (12) and substitution in Eq. (9) then gives the incremental forward shift in aerodynamic center due to the fuselage. Multhopp compares the shift determined from a series of wind-tunnel tests with that calculated and the agreement is shown to be remarkably good.

The full significance of Eq. (12) should not be overlooked. The effect of the fuselage varies as ω_f^2, and it would thus appear that fuselage effects could be reduced by use of narrow fuselages such as are possible only with liquid-cooled in-line engines. If this is not possible, then the fuselage should taper as rapidly as possible aft of the wing.

No attempt is made here to evaluate the effects of wing-fuselage interference on the aerodynamic center. It should be recognized that such effects do exist and may be large. However, it is possible to reduce any adverse effects to a minimum with careful fairing and filleting of the wing-fuselage juncture. This is especially true of low-wing monoplanes.

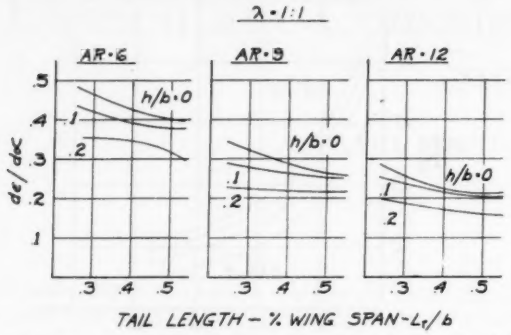

FIG. 2. Chart for determination of stability parameter $d\epsilon/d\alpha$ for $\lambda = 1:1$.

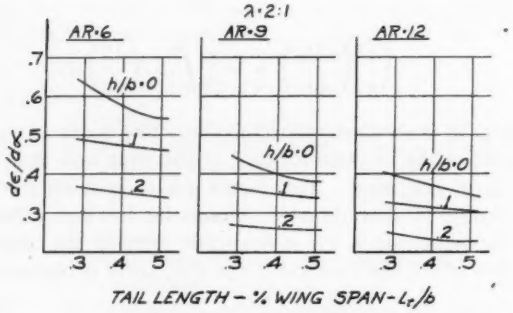

FIG. 3. Chart for determination of stability parameter $d\epsilon/d\alpha$ for $\lambda = 2:1$.

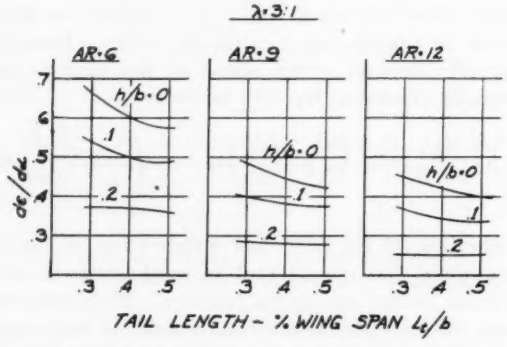

FIG. 4. Chart for determination of stability parameter $d\epsilon/d\alpha$ for $\lambda = 3:1$.

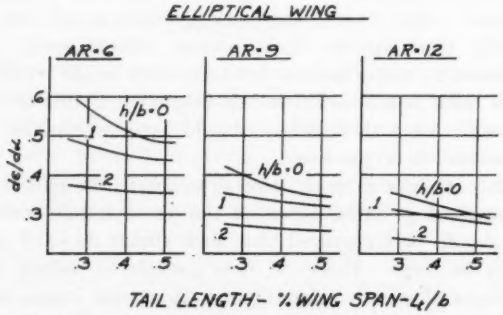

FIG. 5. Chart for determination of stability parameter $d\epsilon/d\alpha$ for elliptical wing.

DETERMINATION OF PROPELLER EFFECTS

The movement of the aerodynamic center due to the propeller cannot be computed on a theoretic basis, and it is therefore necessary to derive an empiric relationship from the available test data. From wind-tunnel tests on several different airplanes having widely different characteristics, computations indicated that the factor $(\Delta N_0)_p$ could be expressed empirically as

$$(\Delta N_0)_p = -(K/a_0)(D^2 L_p/S_w C) \tag{13}$$

where K is a factor depending on the number of blades. Evaluation of the factor K indicated that the following values are reasonable.

Number of Blades	K
3	0.065
4	0.093
6 (dual rotation)	0.400
8 (dual rotation, estimated)	0.540

The aerodynamic center of the wing may be determined from wind-tunnel tests of the wing under consideration or estimated from a spanwise lift distribution. The virtual aerodynamic center is then easily calculated from Eq. 7. It should be emphasized that, whenever the c.g. is aft of the aerodynamic center, the value of dC_{m0}/dC_L will always be positive.

DETERMINATION OF TAIL PITCHING MOMENT

Having evaluated dC_{m0}/dC_L, it next remains to determine dC_{m_t}/dC_L. For purposes of simplification, it is assumed that the ratio of velocity at the tail to free stream velocity is equal to one. The pitching moment contributed by the tail is then

$$C_{m_t} = -(L_t/C)(S_t/S_w)C_{L_t} \tag{14}$$

or

$$C_{m_t} = -(L_t/C)(S_t/S_w)(dC_L/d\alpha)_t \alpha_t \tag{15}$$

However, since

$$\alpha_t = \alpha - \epsilon \tag{16}$$

$$C_{m_t} = -(L_t/C)(S_t/S_w)(dC_L/d\alpha)_t(\alpha - \epsilon) \tag{17}$$

Differentiating with respect to C_L

$$\frac{dC_{m_t}}{dC_L} = -\left(\frac{L_t}{C}\right)\left(\frac{S_t}{S_w}\right)\left(\frac{dC_L}{d\alpha}\right)_t\left(\frac{d\alpha}{dC_L}\right)\left(1 - \frac{d\epsilon}{d\alpha}\right) \tag{18}$$

It is apparent from Eq. (18) that for a given design the factors most influencing dC_{m_t}/dC_L are $(dC_L/d\alpha)_t$ and $d\epsilon/d\alpha$. The slope of the tail lift curve may be varied by changing the aspect ratio of the tail, but since the tail length is usually fixed by weight or other design considerations, it is possible to vary $d\epsilon/d\alpha$ only by changing the height of the tail above the wing quarter chord point.

It is believed that the work necessary for a precise determination of $d\epsilon/d\alpha$ is well worth while, since only

by so doing can the effects of a change in tail height, for example, be accurately assessed. Accordingly, charts of $d\epsilon/d\alpha$ were calculated from the method given by Silverstein and Katzoff,[2] and are presented as Figs. 2 to 6. These charts were prepared for representative tail lengths and heights and a variety of wing aspect and taper ratios and therefore cover nearly all possible design combinations. Apart from being useful in these computations, Figs. 2 to 6 are also interesting because they show the importance of careful wing layout in airplane design. For wings of equal aspect ratio, it is seen that $d\epsilon/d\alpha$ increases with increase in taper ratio. The value of $d\epsilon/d\alpha$ becomes so high with large taper ratios that power on stability might be difficult to obtain with any reasonable tail area.

Stability of Complete Airplane

As given by Eqs. (8) and (18), the slope of the pitching moment curve is now

$$\frac{dC_m}{dC_L} = -(N_0' - X) - \left(\frac{L_t}{C}\right)\left(\frac{S_t}{S_w}\right)\left(\frac{dC_L}{d\alpha}\right)_t\left(\frac{d\alpha}{dC_L}\right) \times \left(1 - \frac{d\epsilon}{d\alpha}\right) \quad (19)$$

By the use of the factors previously defined, it is possible to compute the degree of power-off stability of an airplane for a given c.g. position and tail area.

It is much more important to know the c.g. position at which dC_m/dC_L equals zero because it would represent the furthest aft position at which the static power-off stability will be at least neutral, assuming a linear variation of the pitching moment curve and constant elevator effectiveness. This factor cannot be emphasized too highly, since there are airplanes flying today which have c.g. positions aft of the neutral stability position. In itself, this does not prevent an airplane from being flown, but it does make instrument or formation flying tiring to the pilot and, at the same time, is a serious source of danger in high-velocity accelerated flight unless bob weights or antibalance tabs are used for increasing the stick forces.

Placing dC_m/dC_L equal to zero and rearranging Eq. (19), the furthest aft c.g. position at which dC_m/dC_L equal zero is given by

$$X = N_0' + \left(\frac{L_t}{C}\right)\left(\frac{S_t}{S_w}\right)\left(\frac{dC_L}{d\alpha}\right)_t\left(\frac{d\alpha}{dC_L}\right)\left(1 - \frac{d\epsilon}{d\alpha}\right) \quad (20)$$

It seems wise to recommend that the c.g. position for neutral stability be at least 5 to 6 per cent aft of the furthest aft c.g. position. Power effects may reduce the static margin, although this is not always the case. Generally, speaking, the increased velocity over the tail surfaces, which tends to be stabilizing, is counteracted by the increase in $d\epsilon/d\alpha$, which is destabilizing. Unfortunately, the increase in $d\epsilon/d\alpha$ is usually greater than the increase in slipstream velocity and represents the primary source of many of the stability difficulties of present-day airplanes. As $d\epsilon/d\alpha$ approaches a value of one, it is apparent from Eq. (20) that stability would be difficult to obtain irrespective of tail area or slipstream velocity over the tail surfaces.

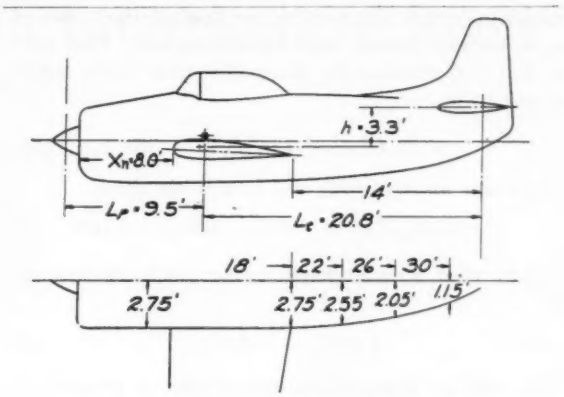

Fig. 6. Arrangement of example airplane.

Example Problem

In order to show more clearly the procedures explained in the previous discussion an example case will be presented. A drawing of the example design is shown in Fig. 6 and the following additional characteristics are tabulated.

Wing area	400 sq.ft.
Wing span	48.2 ft.
Aspect ratio	5.8
Slope of wing lift curve	4.3 per rad.
Mean aerodynamic chord	8.32 ft.
Taper ratio	2:1
Tail length	20.8 ft.
Propeller diameter	13.67 ft.
Number of blades	4
Normal c.g. position	26.5% mean aerodynamic chord
Furthest aft c.g. position	32.9% mean aerodynamic chord

From a spanwise lift distribution of the example wing the aerodynamic center $(N_0)_w$ was determined to be at 23.8 per cent mean aerodynamic chord.

From the plan view drawing of the fuselage, it is seen that the fuselage width ahead of the wing is substantially constant. Therefore, Eq. (12) may be used. From the dimensions given in Fig. 6 and by the use of Fig. 1, the factor $(\pi/2)\bar{\omega}_f^2(\overline{d\beta}/d\alpha)X_n$ is calculated.

$$(\pi/2)\bar{\omega}_f^2(\overline{d\beta}/d\alpha)X_n = 683 \quad (21)$$

Having been given the tail length, $d\epsilon/d\alpha$ may be estimated from Fig. 3 and is determined to be 0.5. From Eq. (11),

$$d\beta/d\alpha = (1 - 0.5) = 0.5 \quad (22)$$

The value of $d\beta/d\alpha$ at any point between the trailing edge of the wing and the hinge line may now be deter-

mined. From a plan view of the fuselage the values of ω_f at various stations may be determined. That part of Eq. (12) forming the integral is then easily determined to be

$$(\pi/2)\int_{0+x_n}^{l}\omega_f^2(d\beta/d\alpha)\,dx = 393 \tag{23}$$

The value of $(1/q)(dM_R/d\alpha)$ is now obtained

$$(1/q)(dM_R/d\alpha) = -683 - 393 = -1{,}076 \tag{24}$$

and the shift in aerodynamic center due to the fuselage is

$$(\Delta N_0)_f = -7.6\% \tag{25}$$

The shift in aerodynamic center due to propeller is determined as

$$(\Delta N_0)_p = -1.0\% \tag{26}$$

The virtual aerodynamic center, calculated from Eq. (7) is

$$N_0' = 23.8 - 7.6 - 1.0 = 15.2\% \text{ M.A.C.} \tag{27}$$

The calculated location of the virtual aerodynamic center is quite reasonable and is representative of the location on present-day airplanes.

The furthest aft c.g. position is given as 32.9 per cent mean aerodynamic chord, and it is desired to have a static margin of 5 per cent. In other words, the tail area should be such that neutral stability occurs at a c.g. position of 37.9 per cent mean aerodynamic chord. A tail having a moderately high aspect ratio of 4.8 is selected. The slope of the tail lift curve $(dC_L/d\alpha)_t$ is determined to be 0.044, using an efficiency factor of 0.66 determined from reference 3. Rearranging Eq. (20),

$$\frac{S_t}{S_w} = \frac{X - N_0'}{\frac{L_t}{C}\left(\frac{dC_L}{d\alpha}\right)_t\left(\frac{d\alpha}{dC_L}\right)\left(1 - \frac{d\epsilon}{d\alpha}\right)} \tag{28}$$

or, by substitution,

$$S_t/S_w = 0.322 \tag{29}$$

The tail area is then determined to be 129 sq. ft., and the tail span is 24.9 ft. These specifications for the horizontal tail are unusually severe but must be accepted if the desired stability requirements are to be met. The proportion of the total area which is to be movable will depend, as previously stated, on the control requirements necessary to make a normal three-point landing. No attempt will be made here to specify the solution to this problem.

Conclusion

It should be mentioned that one factor has been neglected—that is, the vertical location of the c.g. with respect to the aerodynamic center. Multhopp points out that the location of the wing on the fuselage has a negligible effect on $(\Delta N_0)_f$. It is also expected that $(\Delta N_0)_p$ would not be affected by wing location. Therefore, if the vertical distance of the c.g. above N_0' is great enough, the effect of the drag component on C_{m_0} will be noticeable in a variation in dC_{m_0}/dC_L. Such a variation in dC_{m_0}/dC_L will generally result in a forward movement of the neutral stability position as the lift coefficient increases.

The effects of a dynamic pressure loss at the tail can be determined by considering the forward movement of the neutral stability position to be approximately equal to the loss in dynamic pressure.

In conclusion, it is desired to point out the necessity for a similar method of general analysis which would be applicable for any power condition desired. It is believed, from a few preliminary attempts, that empiric relationships will be most satisfactory.

References

[1] Multhopp, H., *Aerodynamics of the Fuselage*, N.A.C.A. T.M. No. 1036, December, 1942.

[2] Silverstein, A., and Katzoff, S., *Design Charts for Predicting Downwash Angles and Wake Characteristics Behind Plain and Flapped Wings*, N.A.C.A. T.R. No. 648, 1939.

[3] Root, L. E., *Empennage Design with Single and Multiple Vertical Surfaces*, Journal of the Aeronautical Sciences, Vol. 6, No. 9, pp. 353-361, July, 1939.

Buckling of Plates with Intermediate Rigid Supports

ERIC REISSNER*

Massachusetts Institute of Technology

THE WRITING of the present note was suggested to the author by a paper by Saibel[1] which deals with the same subject. Mr. Saibel's aim was to express the buckling modes of the plate with intermediate supports as a combination of the known buckling modes of the plate without the intermediate supports. The coefficients of the series representing the unknown modes are to be determined by the energy method, in which the intermediate rigid supports are introduced by means of the method of the Lagrangian multiplier. Unfortunately, Mr. Saibel's use of the multiplier method is incorrect so far as two-dimensional problems are concerned; as a consequence, his paper contains conclusions that cannot be accepted. As such may be mentioned the last (unnumbered) equation on page 401 of the paper and the last two sets of equations on page 402 of the paper.[1]

In what follows it will be shown how results can be obtained for the problems under consideration which are natural extensions of the Weinstein-Trefftz procedure[2, 3] for the buckling and vibrations of the rectangular plate with clamped edges. These results are valid for rectilinear, as well as for curvilinear, rigid intermediate supports. The supports may be concentrated in a number of points along lines or distributed over portions of the plate area. Only the formal aspects of the problem are discussed here, and no actual applications of the formulas obtained are made. The difference between Saibel's and the present approach may perhaps be characterized by saying that the former assumes the constraints accurately and intends to solve the problem approximately, while in the present note constraints are assumed which approximate the real constraints and the resultant problem is solved rigorously.

It is sufficiently general for the present purpose to consider a plate that is simply supported all along its boundary and which is acted upon by a uniform thrust N in the plane of the plate. Taking coordinates x, y in the plane of the plate and letting the direction of the thrust N coincide with the x-direction, it is known that buckling modes ϕ_{ij} and corresponding buckling loads N_{ij} are obtained as the characteristic functions and characteristic values of the following variational problem:

$$\delta\left[\frac{1}{2}D\int\int(\Delta w)^2 dx\,dy - \frac{1}{2}N\int\int\left(\frac{\partial w}{\partial x}\right)^2 dx\,dy\right] = 0 \tag{1}$$

$$w_{\text{Boundary}} = 0 \tag{2}$$

Now let it be prescribed that, in addition to the boundary conditions that are satisfied by the functions ϕ_{ij}, the deflection w is subjected to the additional restrictions

$$w(x_k, y_k) = 0 \qquad k = 1, 2, \ldots n \tag{3a}$$

or

$$w[x(s), y(s)] = 0 \tag{3b}$$

or

$$w(x, y) = 0 \qquad x, y \text{ inside some region } R \tag{3c}$$

Eq. (3a) indicates intermediate rigid support in n points, Eq. (3b) indicates intermediate rigid support along a line with arc length coordinate s, and Eq. (3c) indicates intermediate support distributed over an area.

The main point of the procedure to be discussed here consists in modifying the intermediate support conditions Eqs. (3b) and (3c) in such a manner that an exact solution of the modified problem can be obtained. The modified support conditions are less stringent than the original support conditions; consequently, the buckling load of the modified problem is less than the buckling load of the original problem. A conservative estimate is thus obtained for the actual buckling load.

The modification of the support conditions, Eqs. (3b) and (3c), may be made in at least two different ways. Either Eqs. (3b) and (3c) may be replaced by n Eqs. (3a) or they may be replaced, with suitably chosen functions ψ_k, by equations of the form

$$\int w(s)\psi_k(s)\,ds = 0 \qquad k = 1, \ldots n \tag{4a}$$

$$\int_R\int w(x, y)\psi_k(x, y)dx\,dy = 0 \qquad k = 1, \ldots n \tag{4b}$$

In either case any function w satisfying Eq. (3b) or Eq. (3c) satisfies Eqs. (4a) or (4b), but the converse is not necessarily true. This shows that Eqs. (4a) and (4b) are less restrictive than Eqs. (3b) and (3c).

For the solution of the modified problem the following series is assumed:

$$w = \sum_{i=1}^{\infty}\sum_{j=1}^{\infty} a_{ij}\phi_{ij} \tag{5}$$

Received November 3, 1944.

* Assistant Professor of Mathematics. Consultant, Structures Department, Research Laboratory, Airplane Division, Curtiss-Wright Corporation.

With Eq. (5), the modified support conditions become,

$$\sum_i \sum_j a_{ij}\gamma_{ijk} = 0 \qquad k = 1, \ldots n \tag{6}$$

where the constant coefficients γ_{ijk} are given by either

$$\gamma_{ijk} = \phi_{ij}(x_k, y_k) \tag{7a}$$

or

$$\gamma_{ijk} = \int \phi_{ij}(s)\psi_k(s)\, ds \tag{7b}$$

or

$$\gamma_{ijk} = \int_R \int \phi_{ij}(x, y)\psi_k(x, y)dx\, dy \tag{7c}$$

According to the rules of the calculus of variations, the characteristic functions and values of the modified problem are obtained by multiplying the n Eqs. (6) by constant factors b_k (Lagrangian multipliers) and by replacing the minimum condition Eq. (1) by the following condition:

$$\delta\left[\frac{D}{2}\int\int (\Delta w)^2 dx\, dy - \frac{N}{2}\int\int \left(\frac{\partial w}{\partial x}\right)^2 dx\, dy + \sum_i\sum_j\sum_k a_{ij}\gamma_{ijk}b_k\right] = 0 \tag{8}$$

Let

$$\lambda_{ij} = N_{ij}/D \tag{9}$$

and let the functions ϕ_{ij} be normalized as follows:

$$\int\int (\partial\phi_{ij}/\partial x)^2 dx\, dy = 1 \tag{10}$$

It can then be shown that the functions ϕ_{ij} are orthogonal in such a manner that

$$\int\int [\Delta(\sum\sum a_{ij}\phi_{ij})]^2 dx\, dy = \sum\sum \lambda_{ij}a_{ij}^2 \tag{11a}$$

$$\int\int [(\partial/\partial x)(\sum\sum a_{ij}\phi_{ij})]^2 dx\, dy = \sum\sum a_{ij}^2 \tag{11b}$$

Substituting Eqs. (11) in Eq. (8) the minimum condition becomes

$$\delta\left[\frac{1}{2}\sum\sum \lambda_{ij}a_{ij}^2 - \frac{\lambda}{2}\sum\sum a_{ij}^2 + \frac{1}{D}\sum\sum\sum a_{ij}\gamma_{ijk}b_k\right] = 0 \tag{12}$$

which is equivalent to

$$(\lambda_{ij} - \lambda)a_{ij} + \frac{1}{D}\sum_{k=1}^{n}\gamma_{ijk}b_k = 0 \quad i, j = 1, 2, \ldots \tag{13}$$

Substituting now the terms a_{ij} from Eq. (13) into the modified intermediate support Eqs. (6), there follow n simultaneous homogeneous equations for the n multipliers b_k. Writing in Eq. (6) l instead of k, they are

$$\sum_i\sum_j \frac{\gamma_{ijl}}{(\lambda - \lambda_{ij})D}\sum_k b_k\gamma_{ijk} = 0 \qquad l = 1, \ldots n$$

or, rearranged,

$$\sum_{k=1}^{n}\left[\sum_i\sum_j \frac{\gamma_{ijl}\gamma_{ijk}}{\lambda - \lambda_{ij}}\right]b_k = 0 \qquad l = 1, \ldots n \tag{14}$$

Eqs. (14) have a solution with nonvanishing b_k only if the n-th order determinant of the system vanishes.

$$\| \sum_i\sum_j [\gamma_{ijl}\gamma_{ijk}/(\lambda - \lambda_{ij})] \| = 0 \tag{15}$$

In addition to the solutions of Eq. (15), λ may have the values λ_{ij} for those i and j for which $\gamma_{ijk} = 0$ for all values of k. The smallest value of these λ represents the required conservative estimate of the lowest buckling load of the plate. To what extent the successive numerically larger values of λ, which are roots of Eq. (15), represent approximations to the successive higher buckling loads will not be discussed here.

It is apparent that only slight modifications are necessary to obtain equivalent results for other plate buckling problems and for vibration problems of plates and membranes. Thus, for instance, the buckling loads of the rectangular clamped-edge plate[2, 3] are obtained by taking for the set ϕ_{ij} the buckling modes of the corresponding simply supported plate and by introducing the clamping condition by requiring that $\int (\partial w/\partial n)\psi_k(s)\, ds = 0$, the integral being taken along the circumference of the plate. The calculations of Weinstein and Trefftz indicate that often remarkably close approximations to the actual critical stresses and frequencies will be obtained with relatively few Eqs. (6).

Of buckling problems that are as yet unsolved and fall within the scope of the present procedure, there may be mentioned the problem of the simply supported rectangular plate with intermediate supports extending from one of two opposite edges, parallel to the remaining two edges, *part way* inside the plate.

Another problem of some interest would be to determine lower limits for the critical shear stress of rectangular plates[7] by taking for the functions ϕ_{ij} the buckling modes of the infinite strip[8, 9] and by representing the remaining boundaries of the rectangular plate by equidistant intermediate rigid supports across the width of the infinite strip.

References

[1] Saibel, E., *Buckling Loads of Beams or Plates on Continuous Supports*, Journal of the Aeronautical Sciences, Vol. 11, No. 4, pp. 399–403, October, 1944.

[2] Weinstein, A., *On a Minimal Problem in the Theory of Elasticity*, Journal, London Mathematical Society, Vol. 10, pp. 184–192, 1935.

[3] Trefftz, E., *Die Bestimmung der Knicklast gedrückter rechteckiger Platten*, Zeitschrift für angewandte Mathematik und Mechanik, Vol. 15, No. 6, pp. 339–344, December, 1935.

[4] Weinstein, A., *Étude des spectres des equations aux derivées partielles de la théorie des plaques élastiques*, Memorial des Sciences Mathematiques, Vol. 88, pp. 1–62, Paris, 1937.

[5] Levy, S., *Buckling of Rectangular Plates with Built-In Edges*, Journal of Applied Mechanics, Vol. 9, pp. A-171–A-174, 1942.

[6] Weinstein, A., and Chien, W. C., *On the Vibrations of a Clamped Plate under Tension*, Quarterly of Applied Mathematics, Vol. 1, No. 1, pp. 61–68, April, 1943.

[7] Trefftz, E., and Willers, F. A., *Die Bestimmung der Schubbeanspruchung beim Ausbeulen rechteckiger Platten*, Zeitschrift für angewandte Mathematik und Mechanik, Vol. 16, No. 6, pp. 336–344, December, 1936.

[8] Southwell, R. V., and Skan, S. W., *On the Stability under Shearing Forces of a Flat Elastic Strip*, Proceedings, Royal Society of London, Series A, Vol. 105, No. A733, pp. 582–607, May, 1924.

[9] Bergmann, S., and Reissner, H., *Neuere Probleme aus der Flugzeugstatik*, Zeitschrift für Flugtechnik und Motorluftschiffahrt, Vol. 20, No. 18, pp. 475–481, September, 1929.

I.A.S.

Special Meetings Schedule

1945

August 16–17, 1945	LOS ANGELES MEETING
October 4–5, 1945	DETROIT MEETING
October 26, 1945	WASHINGTON MEETING
November 16, 1945	DAYTON MEETING
December 17, 1945	WRIGHT BROTHERS LECTURE, Washington, D.C.

The Officers and Council of the Institute invite participation in the Technical Sessions of the Meetings of the Institute.

The Meetings Committee will consider for inclusion on the program complete papers or outlines or summaries of proposed papers.

Information for Participants

(1) Complete papers or outlines or summaries should be submitted in triplicate at least four months prior to the meeting at which it is proposed to present the paper. Outlines or summaries should not exceed 1,000 words.

(2) Each paper should be so planned that it may be presented within a time limit of 45 minutes.

(3) All papers submitted will be considered for publication in the **Journal of the Aeronautical Sciences** or the **Aeronautical Engineering Review.** While a paper should be planned to take only 45 minutes for presentation at a meeting, the written presentation may have a maximum length of approximately 15,000 words.

(4) All material received will be submitted to the Meetings Committee. Authors will be notified, in ample time to prepare the complete paper, whether or not their papers can be scheduled for presentation.

All correspondence should be addressed to

The Meetings Committee

Institute of the Aeronautical Sciences
1505 RCA Building West
30 Rockefeller Plaza
New York 20, N.Y.

SUGGESTIONS FOR CONTRIBUTORS TO THE PUBLICATIONS *of the* INSTITUTE *of the* AERONAUTICAL SCIENCES

The Institute of the Aeronautical Sciences invites both members and nonmembers from any country to submit papers for publication in the JOURNAL OF THE AERONAUTICAL SCIENCES and the AERONAUTICAL ENGINEERING REVIEW. The Institute, following the practice of other societies, does not pay for contributions.

The following directions for the preparation of papers, if followed by authors, will save correspondence, avoid the return of papers for changes, minimize the work of preparation for the printer, and save the expense due to the charges made for "author's corrections."

MANUSCRIPTS: Papers must be written in English, in original typewriting on one side only of white paper sheets, consecutively numbered, and be double or triple spaced with wide margins. Manuscripts should be prepared with great care so that they will be typographically accurate. Paragraphing should be given special attention. Papers should be written in the third person, reference to the writer being made as "the author." Avoid the use of the words "I," "we," and "you." Blueprint copies of papers are unacceptable as it is impossible to mark directions to the printer on them. Correcting, changing, or adding to papers after they are in type is costly. It is, therefore, imperative that papers submitted be in final form. Typographical errors may be corrected on proofs, but if authors wish to add material, they may do so at their own expense. In mailing, drawings may be rolled, but manuscripts should be sent flat. Send by first class mail (register if you wish for your own protection) to the Editorial Office, Institute of the Aeronautical Sciences, 1505 RCA Bldg. West, 30 Rockefeller Plaza, New York 20, N. Y. All manuscripts will be examined by the Editorial Committee and by the Editor. Authors will be advised as promptly as possible whether the paper is acceptable for publication.

TITLES: The title of the paper should be brief. The name and initials of the author should be written as he prefers. The use of the full name of an author is advocated because of the frequent duplication of initials and surnames which sometimes makes it difficult to establish the identity of the author. This is particularly important for large annual indexing and abstracting services. All titles and degrees or honors are omitted. The name of the organization with which the author is associated should be placed after his name on a separate line. The date on which the paper is received will be inserted by the Editor.

SUMMARIES OR ABSTRACTS: An abstract to be printed at the beginning should accompany each article. It should be adequate as an *index* and as a *summary*. It should contain a statement of major conclusions reached, since summaries in many cases constitute the only source of information used in compiling scientific reference indexes. Abstracts printed in other journals, especially foreign, in most cases, consist of summaries from printed papers. The summary should explain as adequately as possible the major conclusions to a nonspecialist in the subject. The summary should contain from 100 to 300 words, depending on the length of the paper.

SUBHEADINGS: Subheadings should be inserted by the author at frequent intervals. The work of editorial preparation will be simplified by the author providing many subheadings. Owing to the breaking of columns and the insertion of illustrations, some of the subheadings may have to be omitted.

SHORTENING OF PAPERS: Some papers, at the end, fill in only a portion of a page. This leaves much wasted blank space as succeeding articles are started at the top of a page. Authors should indicate by notation on the left-hand side of the page what matter may be omitted when "runovers" occur. This request is important as the Journal cannot afford in the future, as it has in its earlier issues, to have blank half pages or more at the end of papers.

MATTER USUALLY DELETED: Acknowledgments of assistance in preparation of paper, except by collaborators. Photographs or illustrations of little technical interest and not showing advances in general practice. Too detailed tabular matter (general results of such tables may be included in the text). Lengthy descriptions of materials or processes or of preliminary experiments or theories that preceded final results; salient features only are of interest.

REFERENCES AND FOOTNOTES: References should appear as footnotes only, numbered consecutively, grouped together at the end of the manuscript. The arrangement should be as follows: (for books)—[1] Durand, W. F., *Aerodynamic Theory*, 1st Edition, Vol. 1, p. 23; Julius Springer, Berlin, 1934. (For magazines)—[1] Englund, C. R., Crawford, A. B., and Mumford, W. W., *Some Results of a Study of Ultra-Short-Wave Transmission Phenomenon*, Proc. I. R. E., Vol. 20, No. 12, pp. 481 and 482, March, 1932. Please give author, title, edition, volume, page, publisher and date of publication as indicated. Omission of one required fact causes much extra editorial work and possible inaccuracies. All references are grouped at the end of the article.

ILLUSTRATIONS: Illustrations should accompany manuscripts and each should always be referred to in the text, preferably by number. Drawings or graphs should not be larger than 12 × 16 inches, and must be made with jet black India Ink on white paper or tracing cloth, the latter being preferred. *Do not use typewriter for lettering.* The smallest lettering on 8 × 10 inch figures should be no less than 1/4 inch high. Cross-section paper (white with black lines) may be used, but should not have more than 4 lines per inch. If finer ruled paper is used, the major division lines should be drawn in with black ink, omitting the finer divisions. In the case of finely ruled paper, only blue-lined paper can be accepted. *Tracing paper and blueprints* are not acceptable. Lettering and all markings must be large enough to be readable after reduction. Mail rolled or flat, never folded. Drawings that cannot be reproduced (including pencil drawings) will be returned to the author for redrawing, thus delaying publication of the paper. Photographs should be very distinct and show clear black and white contrasts. They must be on glossy white paper. Avoid round and oval photographs.

CAPTIONS AND LEGENDS: Legends or captions must accompany each drawing or photograph submitted. If written on the drawing or photograph, they should be placed below and well outside the part to be reproduced. It is better to place them on separate sheets of paper pasted to the back of the drawings or photographs. Each table should have a caption such as Table 1, Table 2, Table 3, etc. Captions should be complete in themselves so as to make the data intelligible to the reader without reference to the text. A duplicate list of captions for figures should be included as the last page of the manuscript. Use "Fig. 1" (not Figure 1), Figs. 3 and 4, etc., in both the text and the numbering of illustrations. In the text, "Eq. (1)," or "Eqs. (1) and (2)" are preferable to "Equation (1)." In captions and legends, except for "Fig." and "Eq." and table headings, write all words in full; do not abbreviate. Avoid placing explanatory written matter in the drawings; it should be in the text.

MATHEMATICAL WORK: Only the simplest formulas should be typewritten; all others should be carefully written in pen and ink, the writing to be large enough so that ample room is provided to mark mathematical matter for the printer. A considerable space for marking should be allowed above and below all equations. All complicated equations should be repeated on separate sheets with plenty of space left for marking. The solidus should be used for simple fractions appearing within the text. Make all expressions clear to the typesetter. Greek letters used in formulas should be clearly designated by name on the margin of the manuscript. All symbols should be clearly written and carefully checked. The difference between capital and lower-case letters should be clearly distinguished and care taken to avoid confusion between zero (0) and the letter (o), between the numeral (one) and the letter (ell) and the prime ('), between alpha and a, kappa and k, u and mu, v and nu, n and eta. All subscripts and exponents should be clearly marked and dots and bars over letters or mathematical expressions should be avoided. Avoid complicated exponents and subscripts. When it is necessary to repeat a complicated expression, it should be represented by some convenient symbol.

NOMENCLATURE AND ABBREVIATIONS: The National Advisory Committee for Aeronautics Nomenclature should be used in preference to any others. Standard abbreviations should be used, and it should be noted that most abbreviations are lower case, such as m.p.h., b.m.e.p., i.hp., b.hp., hp., . . . etc.

ICA-

NCES

f papers,

ce, avoid

work of

ense due

"

W., *Some*
enomenon,
rch, 1953.
lisher and
quired fact
acies. All

anuscripts
ferably by
n 12 × 18
on white
Do not use
× 10 inch
tion paper
have more
the major
nitting the
only blue-
eprints are
rge enough
never fold.
ncil draw-
s delaying
ry distinct
ust be on
s.

ist accom-
ten on the
d well out-
e them on
rawings or
n as Table
e in them-
er without
for figures
Use "Fig.
xt and the
"Eqs. (1)
otions and
ings, write
xplanatory
xt.

las should
en in pen
mple room
er. A con-
d below all
peated on
The solidus
n the text.
etters used
the margin
ritten and
and lower-
en to avoid
he numeral
pha and a,
scripts and
over letters
oid compli-
to repeat a
some con-

l Advisory
sed in pref-
d be used,
lower case,